Inclusion Studies of Metal-Organic Hosts

by

Storm Victoria Potts

Thesis presented in partial fulfilment of the requirements for the degree of Doctor of Philosophy

at

Stellenbosch University

Department of Chemistry and Polymer Science

Faculty of Science

Supervisor: Prof. Leonard. J. Barbour

Co-supervisor: Dr Delia A. Haynes

March 2012

Declaration

I, the undersigned, hereby declare that the work contained in this thesis is my own original work and that I have not previously in its entirety or in part, submitted it at any university for a degree.

_____

Signature

_____

Name

Abstract

The primary objective of the work presented in this thesis was to prepare and investigate the properties of novel inclusion complexes of metal-organic host materials. Two types of host materials were studied, namely 0D metallocycles and 3D metal-organic frameworks (MOFs).

The first section details the synthesis and characterisation of six ditopic imidazole derived ligands. These conformationally flexible ligands were reacted with a variety of transition metal salts in a systematic manner with a view to synthesising 0D metallocycles. The structures of 29 novel coordination complexes were elucidated by single-crystal X-ray diffraction and five of these were 0D metallocycles.

The thermal stability of the five metallocyclic inclusion complexes was investigated and it was found that all five of the metallocycles have remarkably high thermal stability with respect to the loss of their included volatile solvents. Indeed, in some cases the solvent is only lost when the host decomposes. This is a relatively rare phenomenon, with only a few examples of such systems reported in the literature. A computational study was undertaken in an attempt to rationalise this high thermal stability in terms of guest-guest and host-guest interaction energies. Furthermore, although the single crystals do not survive the desolvation process, all five of these systems exhibit Class II porosity (i.e. the included solvent could readily be exchanged for a different solvent guest without significant disruption to the host packing arrangement). This exchange process was monitored as a single-crystal to single-crystal transformation.

The final section reports the attempted gas-phase diffusion of two organic radicals into four porous crystalline materials. The radicals diffused into only one of the four possible host systems, thereby indicating a selective inclusion process. The structures of the two new inclusion complexes were elucidated from powder X-ray diffraction data and it was demonstrated that the properties of both the organic radical as well as the host framework are modified in the new material. Furthermore, the host framework acts as a "vessel" in which the organic radicals, which are normally highly reactive species, can be stored under ambient conditions within the channels of the host framework for a period of three months without degradation. The host framework can thus be used for controlled release of the reactive species by exposure to a suitable solvent.

Acknowledgements

Firstly, I would sincerely like to thank my supervisor Prof Len Barbour who has guided me through the past five years of my academic career. During this time I have had the privilege of working in a world-class laboratory and I have had amazing opportunities to travel and meet many of the top researchers in the field of supramolecular chemistry. He has shaped my ability conduct independent research through his open door policy and his ability to simplify the most complex of concepts, and for that I am truly grateful.

I would also like to thank my co-supervisor Dr Delia Haynes for creating an environment where I was never afraid to ask the most simplest of questions. Your encouraging smiles and genuine worry of my well-being did not go unnoticed. I will forever be indebted to you for introducing me to the world of radicals.

Then to Prof Jeremy Rawson, Dr Gareth Lloyd and Magdalene College who so graciously hosted me in Cambridge. I learnt so much during my short time there because of the many hours you both spent with me, teaching me and exposing me to new techniques and ways of thinking. I will never forget my time spent in that beautiful place.

Then to my family in the Supramolecular Materials Group, both past and present: Tia Jacobs, Leigh Loots, Charl Marais, Jan Gertenbach, Dinubanduh Das, Subhadip Neogi, Tanya le Roex, Eustina Batisai, Catharine Esterhuysen and Marlene Milani, Helene Wahl, Sean Robinson, Marike du Plessis, Ilne Grobbler, Vincent Smith, Matteo Lusi and Prashant Bhatt thank you so much for all of your helpful discussions and creating a “home-away-from-home”.

To my friends Haydn, Lisa, Lara, Leigh, Anneli and Dewald, know the support and kindness you showed me during this time got me through this experience!

Lastly I would like to thank my family for all of the love and encouragement.

Publications

1. S.V. Potts, L.J. Barbour, D.A. Haynes, J.M. Rawson and G.O. Lloyd, *J Am. Chem. Soc.*, **2011**, 133, *33*, 12948.
2. S.V. Potts and L.J. Barbour, *New J. Chem.*, **2010**, 34, 2451 (not part of this work).

Conferences

1. **Synthesis and Modeling of Advanced Materials**
   University of Liverpool, United Kingdom, 20 July 2010
   Poster presentation – *Preliminary gas sorption studies of a novel hemicarcerand.*
2. **12th International Seminar on Inclusion Compounds**
   University of Stellenbosch, South Africa 4-9 April 2009
   Poster presentation – *CRYSTAL STRUCTURE PREDICTION-PACKING POLYMORPHISM, the use of supramolecular trends to deduce molecular packing*.

Oral Presentations

1. **Laser Physics Research Group and Supramolecular Chemistry Group joint meeting**
   University of Stellenbosch, South Africa, 14 April 2011
   Radical Inclusion into a Porous Crystalline Material
2. **South African Chemical Institution (SACI) Student Symposium**
   University of Cape Town, South Africa, 9 December 2010
   Inclusion Studies of Metal-Organic Hosts

Abbreviations

0D	Zero Dimensional
1D	One Dimensional
2D	Two Dimensional
3D	Three Dimensional
ASU	Asymmetric Unit
BDTA	Benzo-1,3,2-dithiazolyl
BZ	Benzene
CIF	Crystallographic Information File
CSD	Cambridge Structural Database
CY	Cyclohexane
DCM	Dichloromethane
DFB	1,4-Difluorobenzene
DIOX	Dioxane
DSC	Differential Scanning Calorimetry
EF	Edge-to-face
EPR	Electron Paramagnetic Resonance
FF	Face-to-face
FTIR	Fourier Transform Infrared Spectroscopy
ICE	Inorganic Crystal Engineering
ILAG	Ion- and Liquid- Assisted Grinding
LC ESI-MS	Liquid Chromatography Electrospray Ionisation Mass Spectrometry
M	Metal
MBDTA	5-Methylbenzo-1,3,2-dithiazolyl
MIL	Material of Institut Lavoisier
MOF	Metal-Organic Framework
NMR	Nuclear Magnetic Resonance
OCE	Organic Crystal Engineering
OFF	Offset face-to-face
PHTP	Perhydrotriphenylene

SBU	Secondary Building Units
SCD	Single-Crystal X-ray Diffraction
SC-SC	Single-crystal to single-crystal
SOMO	Singly Occupied Molecular Orbital
TGA	Thermogravimetric Analysis
T_{on}	Onset temperature of desolvation
T_b	Boiling point
TTTA	Trithiatriazenyl
PXRD	Powder X-ray Diffraction
VT-PXRD	Variable-temperature Powder X-ray Diffraction
ZIF	Zeolitic Imidazolate Framework

Atomic Colour Key

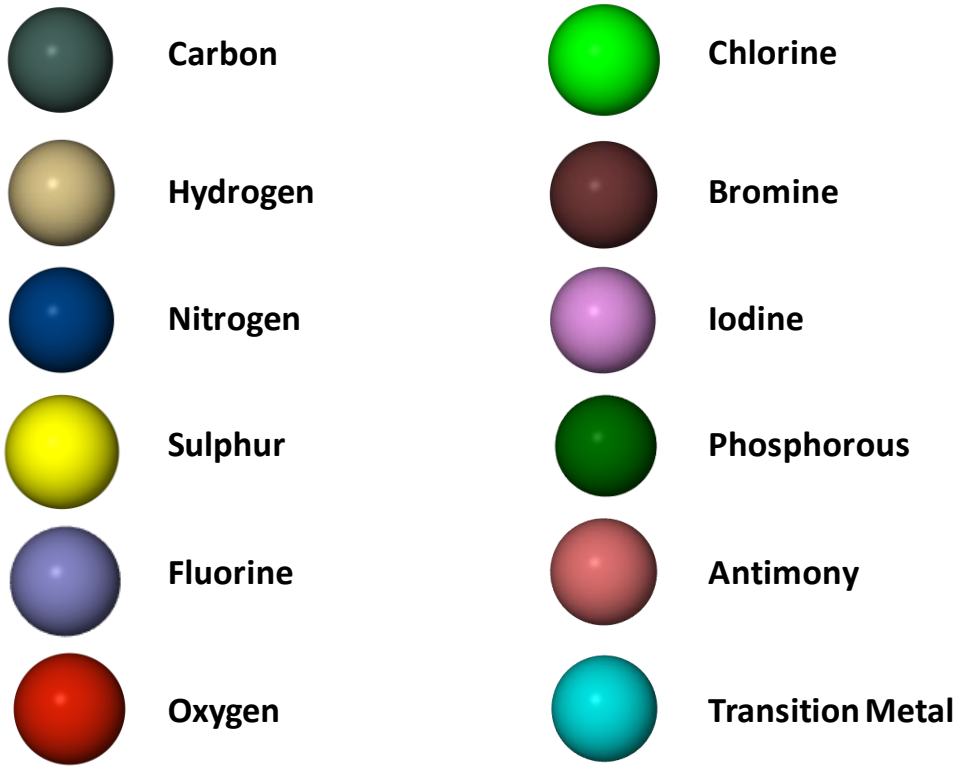

Table of Contents

CHAPTER 1

GENERAL INTRODUCTION

The past twenty years have witnessed a shift in focus of chemistry from molecular chemistry and the study of the covalent bond to, *"chemistry beyond the molecule"*[1] and the study of the weaker, non-covalent interactions that hold molecules together i.e. supramolecular chemistry. Although these weak interactions play a major role in the aggregation of molecular species in both solution and the solid state, we are particularly interested in the solid-state properties of the resulting supermolecules. Further discussion will therefore be limited to the definitions, terminology and techniques available to the solid-state chemist. This chapter presents a brief introduction to the fundamental concepts relevant to this thesis. It should be noted that this study lies at the intersection of several fields and that the partitions between the various topics can be ambiguous. Discretion has therefore been used to present information under a particular subheading rather than another.

1.1. SUPRAMOLECULAR CHEMISTRY

Supramolecular chemistry is an interdisciplinary branch of science that aims to understand, and ultimately gain control over the non-covalent interactions that govern the assembly of molecules into higher order supermolecules. This phenomenon was noted as early as 1937 when Wolf used the term *"Übermolekule"* or *"supermolecule"* to describe entities of higher order derived from the association of many coordinatively saturated chemical species such as the acetic acid dimer.[2] This field has since been described by the Nobel laureate Jean-Marie Lehn as *"... a sort of molecular sociology!"*[3] as it investigates how the intrinsic properties of individual molecules or ions influence the manner in which these components recognise, associate and interact with one another as a collective. The joint award of the Nobel Prize in 1987 to Donald Cram for his contribution to research regarding cyclophanes, spherands and carcerands, Jean-Marie Lehn for the synthesis of the first cryptands and Charles Pederson for developments in the design of macrocyclic ligands for metal cations,[4] firmly established supramolecular chemistry as a new branch of science. This field combines the expertise of the organic, physical and computational

chemists to create a new chemist who is capable of synthesising the precursors for the supramolecular entity, as well as employing various methods to understand the properties and complex behaviour of these systems.[5]

The principle recognition processes that cause molecular species to aggregate in both solution and the crystalline solid state are essentially the same and in this regard, a crystal has been viewed as the perfect supermolecule, *"a supermolecule par excellence"*.[6] For this reason much of the recent work in the area of solid-state supramolecular chemistry is referred to as the chemistry of periodic supermolecules,[7] or crystal engineering.

1.2. CRYSTAL ENGINEERING

The definition of crystal engineering in its simplest form is "making crystals by design".[7] In essence, it is a formulated and systematic approach to combining molecules into targeted supermolecules, which takes both the energetic and geometric properties of different types of intermolecular interactions into account.[8,9] A more formal definition has been proposed by Desiraju as *"... the understanding of intermolecular interactions in the context of crystal packing and in the utilisation of such understanding in the design of new solids with desired physical and chemical properties"*.[10]

The term "crystal engineering" was first introduced by Pepinsky in 1955 in an abstract entitled "Crystal Engineering: a new concept in crystallography".[11] This paper details the exploitation of complex ions in the application of specific methods for structure determination of optically active ions. This contribution was the first to introduce the concept of controlled manipulation of the molecular packing arrangement in a crystal in order to tailor the properties of a material. However, Schmidt is more commonly credited for coining the term 'crystal engineering'. In his 1971 contribution he stated *"... we shall in the present context of synthetic and mechanistic photochemistry, be able to 'engineer' crystal structures having intermolecular contact geometries appropriate for chemical reaction..."*.[12]

Different strategies have been developed for the systematic design of supramolecular architectures in the solid state. Of these, Desiraju's concept of 'supramolecular synthons'[10,13,14] is the most recognised in organic crystal engineering (OCE) and Yaghi's methodology of reticular synthesis is employed extensively in inorganic crystal engineering (ICE) (see Section 2.4.1.1).[15]

In the field of OCE the analogy proposed by Lehn, *"...supermolecules are to molecules and the intermolecular bond what molecules are to atoms and the covalent bond"*,[1,16] is most apt. In this analogy a crystal is considered the supramolecular equivalent of a molecule and, by extension, crystal engineering can be considered the supramolecular equivalent of organic synthesis.[10] The supramolecular synthon approach is based on a process in which designed combinations of intermolecular interactions are used to derive synthons. These incorporate chemical as well as geometrical recognition features of molecular fragments and are used to assemble the crystal structure. Bearing this in mind, a continuation of the above analogy is to say that the crystal becomes a retrosynthetic goal in a supramolecular retrosynthesis; a process akin to the established concept of covalent retrosynthesis. The supramolecular synthon thus performs the same role as conventional synthons do in molecular synthesis. **Figure 1** shows the relationship between a molecule, a functional group and the derived supramolecular synthon that is used to construct the supramolecular entity. Supramolecular synthons are either homosynthons, formed between self-complementary donor/acceptor groups (e.g. the carboxylic acid dimer) or they are heterosynthons formed between different, yet complementary donor/acceptor groups (e.g. between hydroxyl and pyridine moieties).[17]

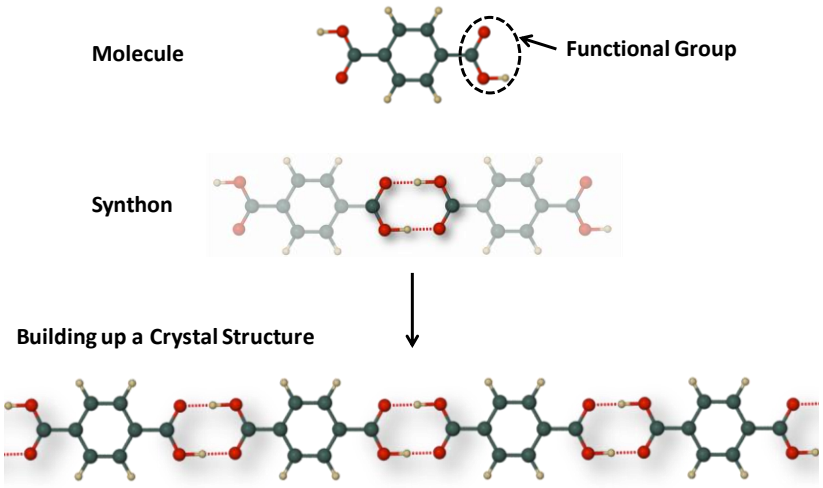

Figure 1. From molecules to crystal structures *via* supramolecular synthons. Image adapted from reference 14.

1.2.1. Intermolecular Interactions

One of the most salient features of the crystalline solid state is that molecular geometry can be studied by means of single-crystal and powder X-ray diffraction methods. The

atomic level information provided by these techniques relays important information regarding bond lengths and angles. This leads to a better understanding of intermolecular interactions and further insight into the structure/property relationships of the materials being investigated.[18] It is therefore imperative that the crystal engineer has a thorough understanding of the intermolecular forces that govern the aggregation of molecular components. Once these interactions are fully understood, the ultimate goal would be to harness this information in the purposeful design of materials with specific properties. Although we are still far from reaching this goal, many advances have already been made.

A list of common supramolecular interactions and their associated energies are shown in **Figure 2** and the following sections provide short descriptions of the interactions most relevant to the present study.

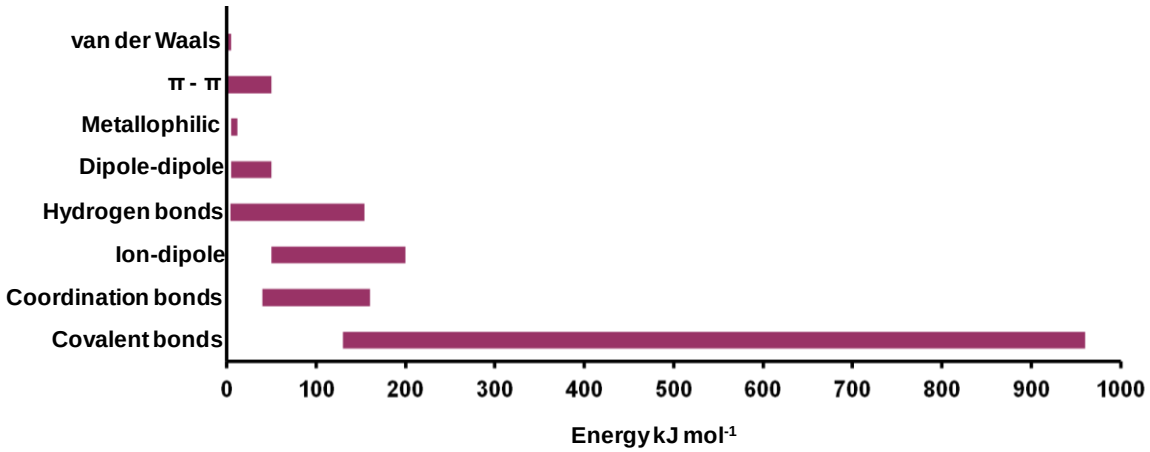

Figure 2. Supramolecular interactions and their relative strengths as compared to covalent bonds. Energy values obtained from references 4 and 33.

1.2.1.1. Van der Waals Interactions

These types of attractive electrostatic interactions are weak (< 5 kJ mol^{-1}), nondirectional interactions that are of supramolecular importance in the inclusion of small guest molecules into the voids of host materials.[4]

Van der Waals forces constitute the sum of exchange repulsion and dispersion (London terms) interactions. The attractive or dispersion forces are the result of the fact that, at a particular moment, adjacent molecules may have opposing poles and therefore attractive charge distributions. The attraction decreases with the interatomic separation r as r^{-6}, and has an approximate dependence on the size of the molecules.[9] This ubiquitous interaction has been called the "universal glue that leads to the formation of condensed

phases"[19] as dispersive forces are the major contributor to the lattice energy of a crystal, owing to the fact that all molecules are involved in this type of interaction.

The repulsive forces are important as they define molecular shape and conformation; in essence they are responsible for keeping molecules apart from one another. They follow an r^{-12} rule, which implies that at short interatomic distances the repulsion between atoms is strong, thus providing a balancing effect of dispersion forces at short range.[4] The effects of these forces decrease rapidly with increasing atomic distance.

1.2.1.2. π-π Interactions

These types of interactions prevail when aromatic systems are present in the crystal and occur in the energy range of 0–50 kJ.mol^{-1}. The aromatic hydrocarbon molecule is generally flat and contains a cyclic carbon framework capable of sustaining a π-delocalised electron density. The polarisable nature of the π-electron density enhances the stabilising dispersion interactions between adjacent aromatic molecules. The addition of high-Z heteroatoms into the aromatic system enhances this stabilising effect.[20]

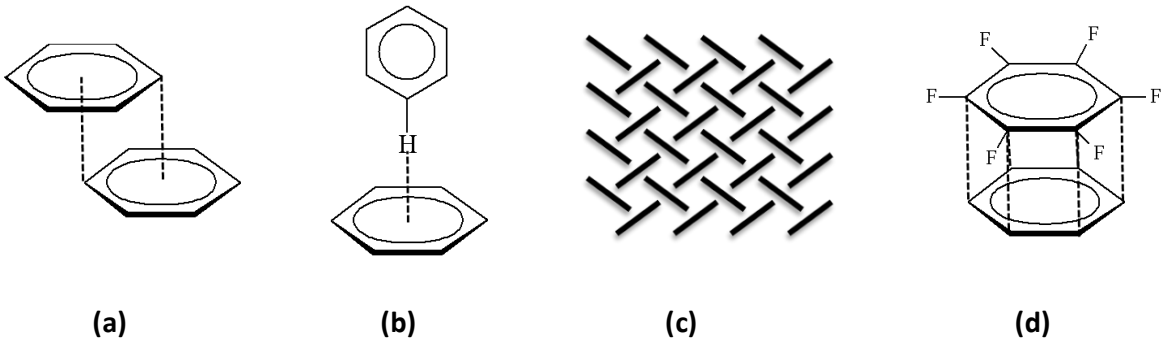

Figure 3. (a) Offset face-to-face π-π stacking motif, **(b)** Edge-to-face or T-shaped motif, **(c)** the herringbone motif formed as a result of edge-to-face interactions and **(d)** Face-to-face or eclipsed stacking.

There are two general types of π-stacking geometries: the offset face-to-face (OFF) motif and the edge-to-face (EF) motif.[4] In the former arrangement the rings are approximately parallel to each other, but offset to maximise intermolecular contacts between oppositely charge regions (**Figure 3a**). In the latter arrangement, also known as the 'T-shaped' motif, the slightly electron-deficient hydrogen atom of one ring is directed towards the central negative π-electron density of the second aromatic ring (**Figure 3b**). EF π-interactions are most often responsible for the characteristic 'herringbone' packing

formation in structures containing aromatic rings (**Figure 3c**).[4] A third geometrical relationship exists and is termed face-to-face (FF) π-stacking. In this arrangement the aromatic groups are eclipsed which, for identical aromatic groups, is a repulsive electrostatic interaction. However, for groups with complementary electron distributions, such as benzene and hexafluorobenzene, FF geometry maximises electrostatic intermolecular stabilisation (**Figure 3d**).[20]

1.2.1.3. Metallophilic Interactions

The closed-shell d^{10} metals Au(I), Ag(I) and Cu(I) have a propensity to aggregate at distances close to the sum of their van der Waals radii and thus form weak metal-metal bonds in the solid state.[21] These interactions are termed aurophilic, argentophilic and cuprophilic, respectively. The energy range of these attractive supramolecular interactions are approximately 5–7 kJ mol^{-1}, which is comparable in strength to weak hydrogen bonds.[22]

1.2.1.4. The Hydrogen Bond

The hydrogen bond is arguably the most well studied of all the intermolecular interactions. Its prominence in the field of crystal engineering can be attributed to the fact that it combines strength with directionality.[23] The first two references in the literature associated with hydrogen bonds were published in 1902 and 1910, when Werner[24] and Hantzsch[25] used the term *Nebenvalenz* (secondary valence) to describe a binding interaction in ammonia salts. However, the subject of hydrogen bonding only emerged into the chemical mainstream in 1935 when Pauling[26] used the term 'hydrogen bond' to account for the residual entropy of ice and subsequently published a chapter on hydrogen bonding in 'The Nature of the Chemical Bond'.[27]

The exact definition of a hydrogen bond has been open to a significant amount of debate. Of the many definitions that have been proposed the two most accepted are (i) that proposed by Steiner,[28] which is an augmentation of the Pimentel and McClellan definition,[29] and (ii) that recommended by the IUPAC. The Steiner definition states that: *"A D–H···A interaction is called a 'hydrogen bond', if (1) it constitutes a local bond, and (2) D–H acts as a proton donor to A."* The IUPAC definition is: *"The hydrogen bond is an attractive interaction between a hydrogen atom from a molecule or a molecular*

fragment D–H in which D is more electronegative than H, and an atom or group of atoms in the same or a different molecule, in which there is evidence of bond formation."[30]

The geometrical considerations of the hydrogen bond are shown in **Figure 4**. In this figure the hydrogen bond D–H···A comprises a donor D–H and an acceptor A. If the acceptor is extended to A–X, the entire interaction is represented by the notation *D*–H···A–X, and the following parameters have in the past been accepted to be relevant: the D–H distance or *r*, the H···A distance or *d*, the D···A distance or *Y*, the donor ∠DHA or θ and the acceptor ∠HAX or ϕ.

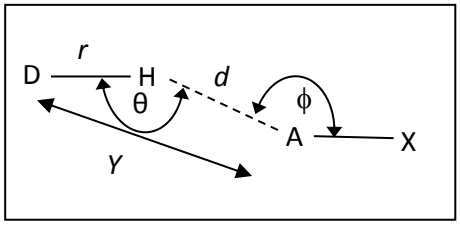

Figure 4. Definition of the historically accepted geometrical parameters *r*, *d*, *Y*, θ and ϕ for a hydrogen bond. Image adapted from reference 32.

A recent publication has cautioned reporting parameters involving the hydrogen atom.[31] The position of hydrogen atoms cannot be determined accurately using X-rays owing to the fact that this technique is based on the scattering by electrons. For lighter elements with low electron density, this leads to inaccurate locations of the nuclei. It was found that in many cases the standard hydrogen atom treatment (i.e. the placement of H according to a riding model)[32] in structures determined by X-ray diffraction leads to shorter D–H distances as compared to the 'true' values as determined by neutron data. Therefore, all hydrogen bonds in this thesis will be inferred and described *only* according to the D···A distance.

Owing to the long-range nature of the hydrogen bond, it may at any given time be simultaneously donating a hydrogen bond to more than one acceptor. In the case of two acceptors a bifurcated hydrogen bond is formed, and when there are three acceptors a trifurcated bond is formed. A situation may also arise in which an acceptor group is simultaneously hydrogen bonded to two distinct donor groups, and in this case the A–X group is called a bifurcated acceptor. These three situations are represented in **Figure 5**.

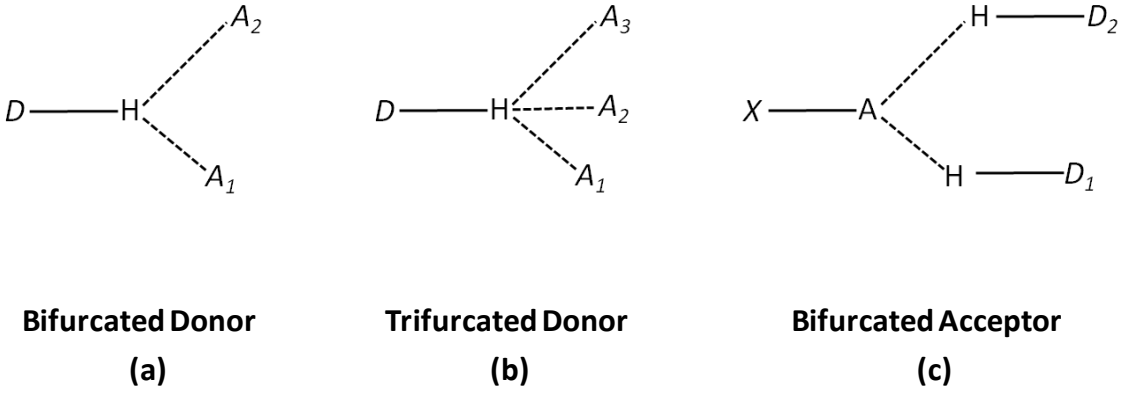

Bifurcated Donor **(a)** | **Trifurcated Donor** **(b)** | **Bifurcated Acceptor** **(c)**

Figure 5. Schematic representation of hydrogen bonds involving **(a)** a bifurcated donor, **(b)** a trifurcated donor and **(c)** a bifurcated acceptor.

It is useful in the context of crystal engineering to classify hydrogen bonds according to certain parameters. **Table 1** summarises the hydrogen bond classification system proposed by Desiraju[33] in which the hydrogen bond is considered in terms of geometric, energetic and thermodynamic properties. This system divides hydrogen bonds into three categories that span two orders of magnitude with respect to interaction energies (4–160 kJ mol^{-1}): very strong, strong and weak hydrogen bonds.

Table 1. Some properties of very strong, strong and weak hydrogen bonds (adapted from reference 32).

	Very Strong	**Strong**	**Weak**
Bond energy (kJ mol^{-1})	60-160	4-60	<4
Examples	[F···H···F]-	O–H···O=C	C–H···O
	[N···H···N]+	N–H···O=C	O–H···π
	P–OH···O=P	O–H···O–H	Os–H···O
Bond lengths	D–A ≈ D–H	H···A > D–H	H···A >>> D–H
Y(D···A) range (Å)	2.2–2.5	2.5–3.2	3.0–4.0
Bonds shorter than vdW	100%	Almost 100%	30– 80%
Effect on crystal packing	Strong	Distinctive	Variable
Utility in crystal engineering	Unknown	Useful	Partly useful
Covalency	Pronounced	Weak	Vanishing
Electrostatics	Significant	Dominant	Moderate

1.2.1.5. The Coordination Bond

A coordination bond is an ion-dipole interaction and occurs through the donation of free electrons from a ligand (usually a lone pair of electrons) to an acceptor (typically a metal ion). The strength and labililty of the bond depends on the particular combination of metal ion and ligand. The extremities of its energy range overlap with strong hydrogen bonds at

the lower end and covalent bonds at the upper end.[34] Coordination bonds are superior to most other supramolecular interactions because they are highly directional and relatively strong. They therefore tend to take precedence over the other supramolecular interactions in crystal packing, relegating these weaker interactions to being stabilising or secondary interactions in the final structure.[35] We are particularly interested in the incorporation of metal cations as structure-directing agents in the synthesis of porous metal-organic supramolecular architectures (see Section 1.4.1).

1.2.2. Self-Assembly

Self-assembly is a process in which a disordered system, comprising two or more complementary building blocks, spontaneously assembles to form a new system of higher order. This process is directed by non-covalent interactions and therefore involves all of the intermolecular forces outlined in the previous section. Owing to the labile nature of the interactions at play, the weak interactions are easily broken and reformed. This allows the system to cycle through a range of products to produce the most thermodynamically stable structure under prevailing conditions. This is a valuable tool in the formation of supramolecular assemblies.[4]

1.3. HOST-GUEST CHEMISTRY

The inception of host-guest or inclusion chemistry can be traced to the discovery of chlorine hydrate by Humphrey Davy[36] in 1810 and the subsequent assignment of its chemical formula in 1823 by Michael Faraday.[37] The foundations of host-guest chemistry are said to lie in three core concepts: fixation, recognition and coordination.[3] The first concept of *fixation* is associated with Paul Ehrlich who recognised that molecules do not act if they do not bind, and in his statement *"Corpora non agunt nisi fixata..."* he introduced the concept of the receptor in 1910.[3,38] The notion that this binding must be selective was introduced by Emil Fischer in 1894 and is depicted in his "lock and key" concept of steric fit; this model proposes that, in order for molecules to interact or 'bind', the guest must have a geometric size or shape complementary to that of the receptor, thus establishing the concept of molecular *recognition*.[3,39] The third concept is associated with the pioneering work of Alfred Werner (1893) who established his theory of *coordination*

chemistry; he showed that selective fixation requires interaction – essentially an attraction or mutual affinity must exist between the interaction partners.[3,40]

Although its history dates back to a time well before a formalised definition of supramolecular chemistry was proposed, in modern chemistry the field of host-guest chemistry is generally classed as a subfield of supramolecular chemistry. In this context, the inclusion complex or 'host-guest' complex is considered the supramolecule formed as a result of a binding, or complexation event in which a larger molecule, the 'host', binds to another smaller molecule, the 'guest'. A formalised definition of the terms host and guest has been given by Donald Cram: *"The host component is defined as an organic molecule or ion whose binding sites converge in the complex.... The guest component is any molecule or ion whose binding sites diverge in the complex."*[*] In this respect the binding site is the region of the host that can favourably interact with a reciprocal region on the guest (or vice versa) due to several reasons, some of which are correct size, correct chemical nature or complementary geometry[5] (i.e. the bulge in one of the components that can fit into the groove of the other component). It has therefore been said that molecular recognition lies at the heart of host-guest chemistry.[41]

Despite the fact that the components in a host-guest system are only associated by weak, non-covalent interactions, the applications of host-guest chemistry are far-reaching in both industry and academia. These include the separation of mixtures of closely related compounds,[42] the encapsulation of pharmaceutically active agents in dendritic hosts for specific tissue targeting and controlled release rates,[43] analyte encapsulation into a receptor-indicator host for chemical sensing,[44] the resolution of racemates, the entrapment and storage of hazardous material from the environment[45,46] and the control of particular reaction pathways by inclusion of reactants within confined vessels or channels (topochemistry).[47]

In modern chemistry, host systems are broadly classified under two categories: cavitands and clathrands (see **Scheme 1**).[48] A cavitand is a single-molecule host that forms a host-guest complex or cavitate with the guest located completely within the host. The cavity is thus an inherent feature of the molecule and as a result, cavitate formation can occur in both the solution and solid state. An example of a host-guest system in this

[*] Since this definition has been proposed, it has become necessary to remove the word 'organic' thereby creating a more generalised definition to include the plethora of inorganic hosts in the category of host-guest complexes.

category is a crown ether complex.[48] In contrast, clathrates (derived from the Latin word *clathratus*, meaning "enclosed by the bars of a grating") are lattice-type inclusion compounds existing only in the crystalline solid state. In these complexes the host molecules assemble to form a guest-accessible void located between two or more host molecules; the voids are then propagated through the material as part of the repeating motif of the crystalline lattice.[5] The majority of host-guest complexes, including those described in this thesis, belong to the clathrate family of inclusion compounds. Two examples of classical organic clathrate host systems are Dianins compound[49] and urea;[50] examples of inorganic clathrate hosts can be found in Section 1.4.1.

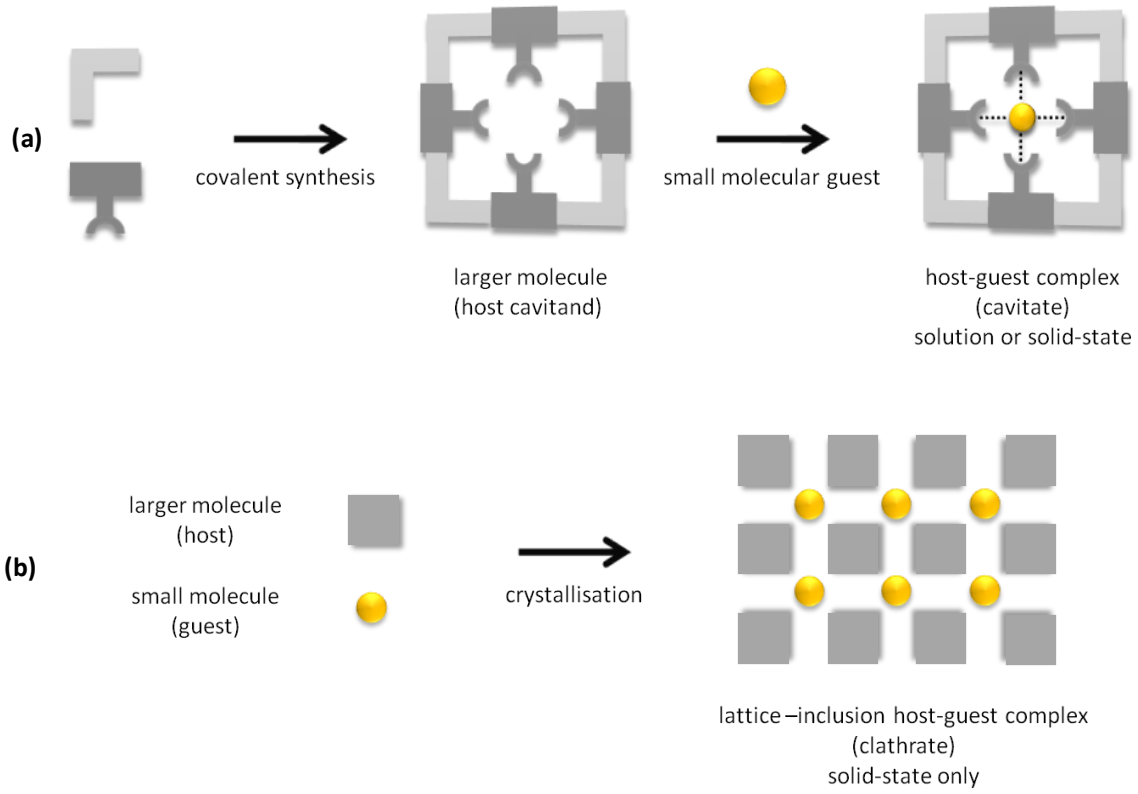

Scheme 1. (a) The formation of a host-guest cavitate complex that can exist in the solution or solid state. **(b)** The formation of a lattic-inclusion host-guest clathrate complex that can exist only in the solid state. Scheme adapted from reference 5.

The synthesis of a solid-state host-guest compound may generally be described by the following formula:

$$H_{(s,\,\alpha)} + nG_{(l \text{ or } g)} \longrightarrow H{\cdot}G_{n(s,\,\beta)}$$

where α represents the initial pure host phase H, *β* the phase of the new host-guest compound and *n* is the host-guest ratio. **Scheme 2** shows the formation of an inclusion compound comprising a multi-component host system as well as the possible phase transitions and decomposition steps that can occur when the sample is heated. The synthesis of the complex is most often carried out by dissolving the components of the host in a liquid guest and allowing the solution to concentrate – this is represented by step **a** in **Scheme 2**. During the concentration step the solvent interacts with the starting materials through weak hydrogen bonding and van der Waals interactions, thereby influencing their reactivity, availability and the nature of the inclusion product formed.[51] The effect of this host-guest interaction is seen in **a** where the host is built-up around the guest solvent molecules in solution; this phenomenon is termed the *template effect*. A non-competitive solvent is used for reactions requiring a solid guest. The formation of the *β*-phase host-guest complex resulting from the crystallisation process is shown in step **b**. The nature of the phase obtained in this step is influenced by many factors during the crystallisation process; these include the type of solvent or guest used in the reaction, the temperature of crystallisation and the pH of the solution. Steps **c**, **d** and **e** show three possible products that can be formed from heating a sample of the *β*-phase host-guest complex. The host can expel the included solvent molecules and rearrange to form a new, more densely packed, non-porous γ-host phase (step **c**). The inclusion complex can undergo a phase transformation and alter its packing mode to produce a new δ-phase (step **d**), or the host can expel the guest molecules without significant rearrangement of the host molecules to yield an empty β_o-phase apohost structure capable of absorbing new guest molecules (step **e**).

The primary method used to characterise inclusion compounds is single-crystal X-ray crystallography. However, thermoanalytical methods, such as thermogravimetric analysis (TGA) and differential scanning calorimetry (DSC) are also routinely employed to characterise and assess the strength of possible interactions between the host and guest. TGA is also used to obtain accurate host:guest ratios in cases where severe disorder of the guest impedes host:guest ratio assignment from the crystallographic data, or in cases where single crystals of the inclusion complex cannot be grown. DSC analysis provides the onset temperatures and associated enthalpy changes for thermal events such as an endothermic guest-release process.[52-54] In addition to these two standard techniques, coupled techniques such as TGA-Fourier transform infrared spectroscopy (TGA-FTIR),

TGA-mass spectrometry (TGA-MS) and DSC-Powder X-ray diffractometery (DSC-PXRD) are becoming widely used. These specialised thermal techniques enable the identification of the products formed as the material is subjected to a specific thermal program and allows for the correlation of these products with the thermal events observed in the TGA or DSC trace.[55]

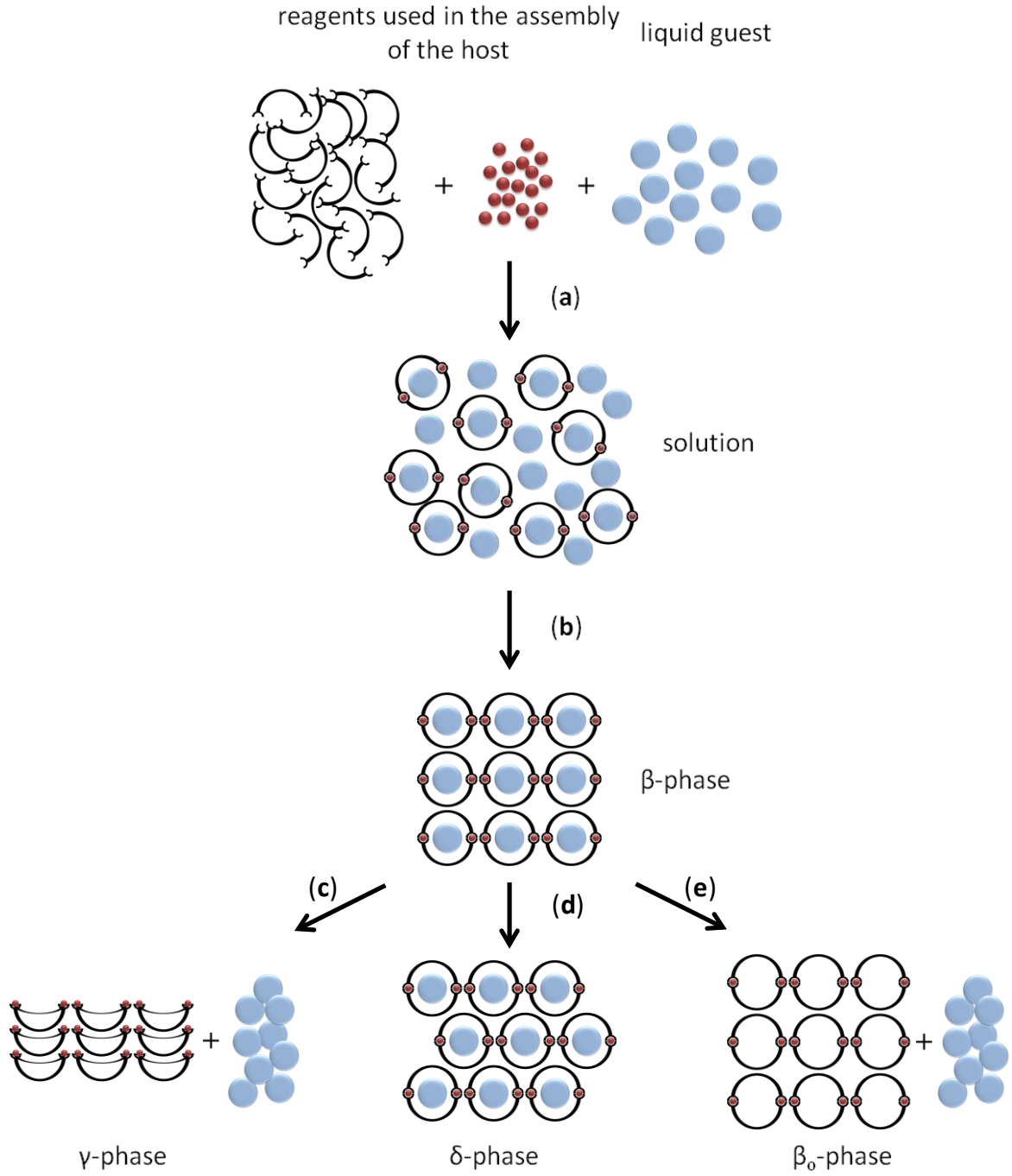

Scheme 2. The formation of an inclusion complex comprising a multi-component host system and the possible phase transitions and decomposition products that can result from heating the sample. Scheme adapted from reference 40.

1.4. POROSITY

Nanoporous crystalline materials are solids that contain interconnected pores of molecular-size dimensions (generally larger than about 25 $Å^3$).[56,57] This phenomenon counters the tendency of molecules in a crystal to maximise attractive intermolecular interactions by close packing. Consequently it is rare to find crystals with open channels or discrete voids. Solid crystalline porous materials differ from amorphous or disordered porous solids (e.g. gels and organic polymers) in that they have well defined structures and, as a consequence, the exact pore size and void volume can easily be characterised. In contrast, amorphous solids have poorly defined structure and the pores are difficult to reproduce as a result of their random arrangement in the solid.[58] In the past decade research focused on the structure and properties of both organic and inorganic nanoporous crystalline materials has increased rapidly. These research efforts are largely sustained by the potential commercial application of these materials to the sorption, storage and controlled release of gases such as hydrogen and methane.[59-63]

In the vast amount of literature available on porous materials, the definition of what exactly constitutes porosity in crystalline materials remains somewhat ambiguous and therefore requires some discussion. A simple dictionary definition of a porous substance is one that is "full of or having pores; admitting the passage of gas or liquid through pores" whilst the definition of a pore is "a small interstice admitting absorption or passage of a gas or liquid".[64] It is therefore implied that a crystalline material possesses porosity in terms of interstitial volume in relation to its mass, and demonstrates porosity if it is permeable to gases or liquids moving in or out of the material. The notion that porosity must be demonstrated has been reiterated in reports by Barbour[56] and Kitagawa.[65-67] These state that claims of porosity need to be coupled with verifiable experimental results illustrating that guest uptake has taken place e.g. gas sorption isotherms. Therefore, the formation of a material containing open spaces does not infer porosity and, in the absence of definitive proof a 'porous' material can at best be described as 'potentially porous'.[66] Another key aspect in the definition of porosity is that the guest uptake, exchange or removal process should not affect the host system to a large extent, i.e. the process should not lead to a significant rearrangement of the host molecules. For the purposes of this study, a material that forms a guest-free host phase that is capable of absorbing a new guest will be classified as a Class I porous material. A material that exchanges its original

guest for a new guest molecule will be classified as a Class II porous system – this involves mass transport of the guest through the solid host framework and therefore does not require a guest-free phase. It is also imperative that the term "porous" be associated with a specific host phase and should not be considered a property of the bulk host material.[56] In the same report by Barbour[56] three distinct categories of porosity are proposed:

1. **Virtual porosity**

In this category claims of porosity are usually created *in silico*, i.e. the crystallographic model is misrepresented in figures. This is achieved by generating figures of molecules in the capped-stick or ball-and-stick metaphor instead of space filling diagrams, thus creating a false perception of the space occupied by certain molecules. This can also be achieved by deleting judiciously selected atoms such as counter-ions or solvent molecules. These claims are rarely supported by *in situ* demonstrations of porosity.

2. **Conventional porosity**

In this form of porosity, the guest molecules are located in channels formed by the packing arrangement of the host molecules. If the guest can be removed or exchanged with another type of guest molecule without disrupting the topology of the host framework, that supramolecular phase is termed *conventionally porous*.

3. **Porosity "without pores"**

This form of porosity is also called *transient porosity*, and arises when a crystal possesses discrete voids that are not interconnected to form a continuous channel through which the guest molecules may traverse. Examples of transiently porous systems have been reported in the literature,[68-73] and in most cases the exact mechanism of the absorption process is not known. It has been postulated that a dynamic porosity must exist in which thermal motion or guest-induced motion of the host molecule facilitates the movement of guest molecules through the crystal.

1.4.1. Crystal Engineering of Porosity

There are many types of micro- and nanoporous materials and arguably the most ubiquitous of these are the open framework aluminosilicate zeolite hosts. The frameworks of these materials are constructed from AlO_4 or SiO_4 tetrahedra bridged by oxygen atoms and cations of alkali and earth alkali metals are contained within the channels of the

system to neutralise the charge of the framework.[74] The word zeolite is derived from a combination of the Greek words *zeo*, meaning "to boil" and *lithos* meaning "stone". This term was originally coined by the Swedish mineralogist Axel Fredrik Cronstedt in 1756 in accordance with the observation that the material stilbite visibly loses water when heated.[75] Zeolites occur naturally, but they can also be produced synthetically. Zeolites are generally synthesised by hydrothermal methods using reactive alkali-metal aluminosilicate gels.[76] The applications of zeolites are widespread and include ion exchange for water softening and purification, petrochemical cracking, catalysis and separation of molecular and ionic species.[77-80] Naturally occurring zeolites are often contaminated by other minerals and their industrial applications are therefore mostly limited to synthetic zeolites. Zeolites are structurally very rigid materials and access to their channels is constricted by narrow pore openings in the diameter range of 4–12 Å.[81,82] They can therefore only function as hosts to ions and small organic molecules. A further disadvantage of zeolites is the limited number of channel topologies offered by the combination of the constituents, which restricts the porous properties.[83]

Recent advances in the synthesis of materials designed to emulate the properties of zeolites have led to the use of organic bridging ligands and metal cations as building blocks in the construction of porous materials. Of particular relevance to this thesis is the self-assembly of metal cations and organic ligands from solution to yield porous 3D metal-organic frameworks (MOFs) or 0D metallocyclic complexes. A short discussion of these two classes of porous materials follows in the next two sections.

1.4.1.1. Metal-Organic Frameworks (MOFs)

Metal-organic frameworks are constructed from metal ions or clusters and rigid organic ligands. Their inception into the field of porous materials can be traced to the work of Robson and Hoskins[84,85] in the early 1990s who indicated that specific framework geometries can be synthesised by the coordination of polydentate ligands to metals.[86,87] The synthesis of MOFs is often the result of a rational design strategy, i.e. the sub-class of crystal engineering proposed by Yaghi *et al.* termed reticular synthesis.[15,88]

Reticular chemistry is informally defined as the construction of predetermined structures from molecular building blocks, which are linked together *via* strong bonds.[15] The methodology borrows the concept of secondary building units (SBUs) from zeolite analysis to construct rigid networks with permanent porosity. In these systems the metal

components, either the single cation or a metal cluster, are considered the "nodes" that are connected to one another by virtue of the organic ligand "spacers" to form an open 3D network. Owing to their ability to aggregate metal ions into M–O–C clusters (or SBUs), carboxylate linkers have been used most extensively in the construction of these porous materials (see **Figure 6** for examples of SBUs).[89] The frameworks thus created are neutral, which circumvents the problem of counter-ion clathration encountered with zeolites.[90]

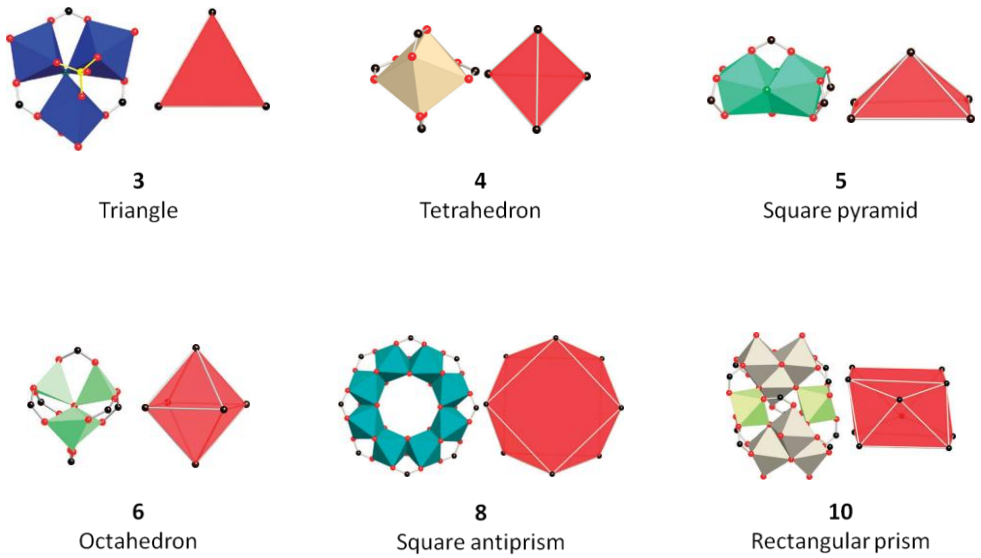

Figure 6. A selection of transition-metal carboxylate clusters that serve as SBUs. These are employed as structure directing agents in the synthesis of MOFs. The geometry and number of extension points are provided. The red shape adjacent to each SBU is the simplified representation of the unit; the vertices and edges of the net are shown as black spheres and white lines, respectively and the tiles as red surfaces. Figure adapted from reference 87.

A defining characteristic of these materials is that they have extremely high surface areas and large void volumes that are readily accessible to guests and can therefore function as hosts in the many applications that utilise porous solids.[91] One of the most well-studied MOFs is the highly porous MOF-5, which serves as a standard to which the porous properties of new MOFs can be compared.[91] This material was synthesised by Yaghi *et al.*[92] in 1999 and its discovery has laid the foundation of more than a decade of research into MOF chemistry. The structure of MOF-5 comprises benzene dicarboxylic acid (BDC) ligands coordinated to tetrahedral clusters of Zn(II) ions to form an extended cubic framework with an internal surface area of up to 4500 $m^2 g^{-1}$ (**Figure 7**).

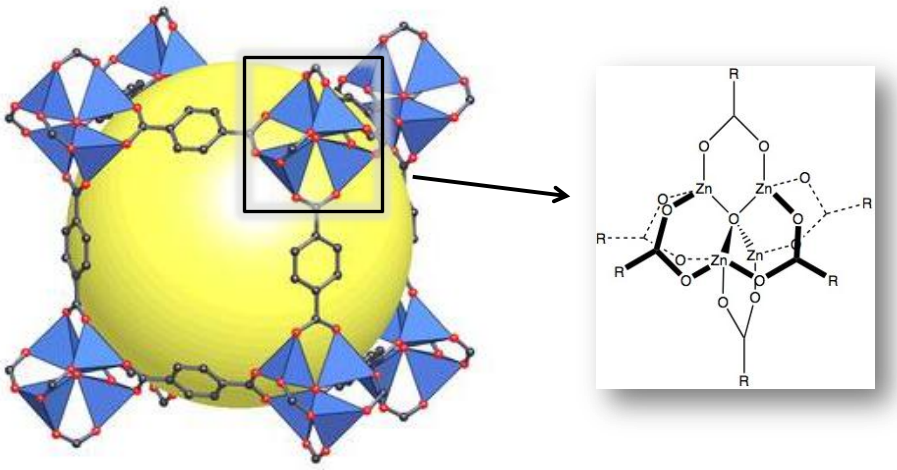

Figure 7. Structure of MOF-5. Image adapted from reference 92.

MOFs are often referred to as 'organic zeolites' as they share common structural features and some have exhibited zeolite-type porosity.[5] They are however, an attractive alternative to zeolites owing to the structural variation that can be introduced into the framework by modifying the organic spacer ligand and/or coordination geometry around the metal centre. A modification of the ligand can be effected by appending different organic substituents onto the ligand without changing the architecture of the framework. This could lead to a change in the surface properties of the channels. An example of this kind of study is shown in **Figure 8**.[93] The organic ligand in MOF-5 was modified by increasing the size of the aromatic spacer to produce an isoreticular (i.e. having the same network topology) series with increasing channel dimensions and void volumes. The BDC moieties were also altered by substituting one or two of the hydrogen atoms on the aromatic spacer for either a polar substituent, such as bromine or amine groups, or a non-polar hydrocarbon group, such as fused benzene or cyclobutane. The substituent then projects into the cavity, thereby altering the channels in the isoreticular series to increase or decrease the hydrophilicity of the material.

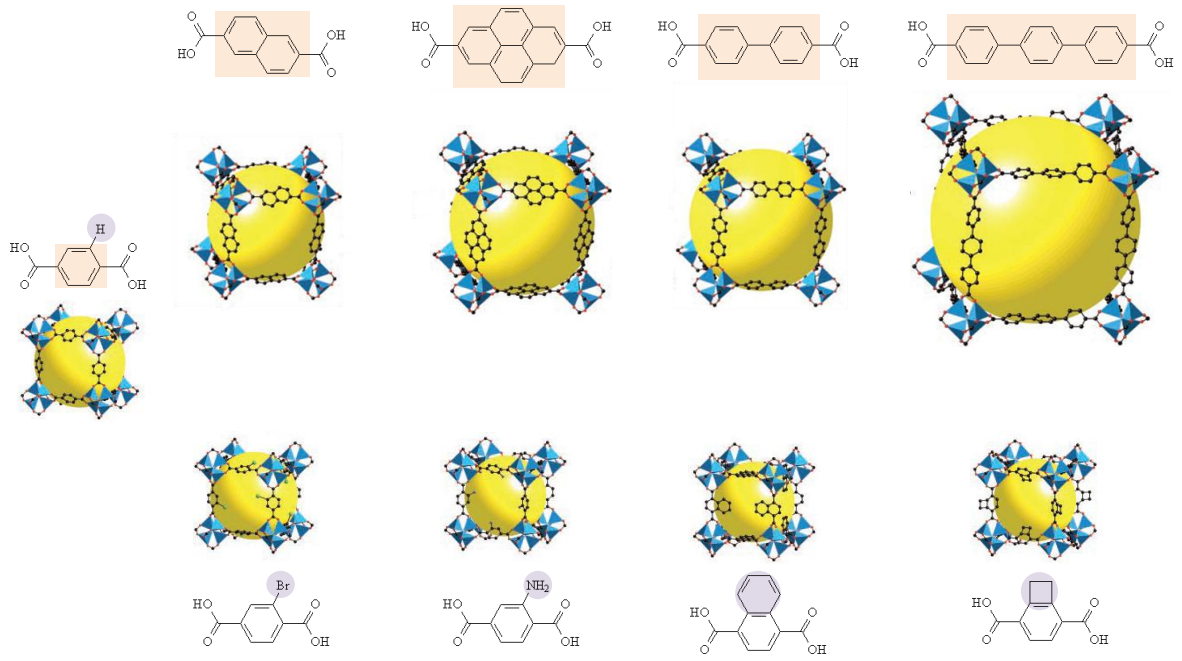

Figure 8. The isoreticular series formed by reacting Zn(II) cations with a series of organic dicarboxylate ligands. **(Top)** Increasing the length of the aromatic spacer increases the channel size and void volume. **(Bottom)** Addition of substituents onto the benzene ring that protrude into the cavity alters the hydrophilicity of the channel – becoming more hydrophilic in the case of the bromine and amine substituents and more hydrophobic for the hydrocarbon substituents. Figure has been adapted from reference 93.

Recent years have seen a shift in the focus of MOF literature from synthesis and the development of a portfolio of MOF materials to more applications-driven research. These investigations are largely associated with the porous properties of MOFs, specifically with regard to the storage of hydrogen gas.[59] They have also been recognised as nanoscale containers and reaction vessels,[94,95] and chiral MOFs have shown the ability to catalyse reactions enantioselectively.[96] Further applications include separation, sensing and purification of small molecular species.[97-101]

The two types of porous MOF materials that will feature in the current study are: the thermally, and chemically stable zeolitic imidazolate frameworks (ZIFs) developed by Yaghi,[102,103] and the structurally flexible MIL (MIL = Material of Institut Lavoisier) MOFs, which form part of a family of hybrid inorganic-organic nanoporous solids developed by Férey.[104-107] Further information on these specific host materials is available in the relevant section (Section 4.1).

1.4.1.2. 0D Metallocycles

Most of the design strategies aimed at producing porous materials yield 2D or 3D framework materials. In comparison, porous materials comprising discrete molecules or complexes have received little attention owing to the fact that they generally tend to pack efficiently in the solid state. Of the discrete porous systems reported, most consist of organic molecules.[62,63,108-110] We are, however, interested in the incorporation of coordinatively unsaturated metals into porous materials as they provide additional sorption sites for gaseous guests, thereby enhancing the sorption capability of the material.[111-113]

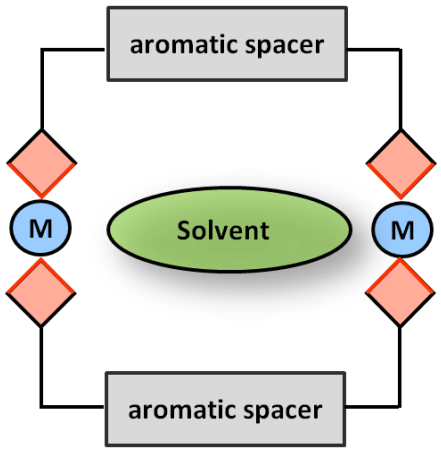

Scheme 3. Outline of a "doughnut-shaped" metal-organic complex. The grey rectangles represent a variable aromatic spacer; the red diamonds represent imidazole moieties with their imino nitrogen atoms simplified as red arrow heads. Metal ions are shown as blue ellipses and solvent molecules are represented as a green oval in the centre of the complex.

Our group's approach to the synthesis of porous materials involves the formation of discrete "doughnut-shaped" metal-organic complexes through the reaction of flexible ditopic imidazole-derived ligands with transition metal cations. These ligands comprise two imidazole moieties that are separated by a variable aromatic spacer and, *via* their imino nitrogen atoms, they doubly connect two metal centres to each another. This generates 0D metallocycles that entrap solvent molecules within the apertures of the ring-like complexes (**Scheme 3**). The metallocyclic units are necessarily shape-incompatible and accordingly preclude interdigitation and the formation of closed-packed structures. The host is defined as the entire metallocyclic unit and these stack one on top of another along a particular axis to form 1D solvent-filled channels or discrete solvent-filled pockets. Removal of the solvent molecules is achieved without significant disruption of

the host framework; therefore the packing arrangement of the metallocycles is preserved and discrete voids or empty 1D channels are formed. Using this method outlined here, our group has obtained four novel porous metallocycles.[114-117] In all four structures the occluded solvent molecules can readily be removed to yield an empty phase capable of absorbing new guests and as such all conform to the definition of Class I porous systems (see Section 2.4). Furthermore, this desolvation process generally occurs without loss in the quality of the single crystal and so the formation of the empty phase occurs as a single-crystal to single-crystal (SC–SC) transformation.

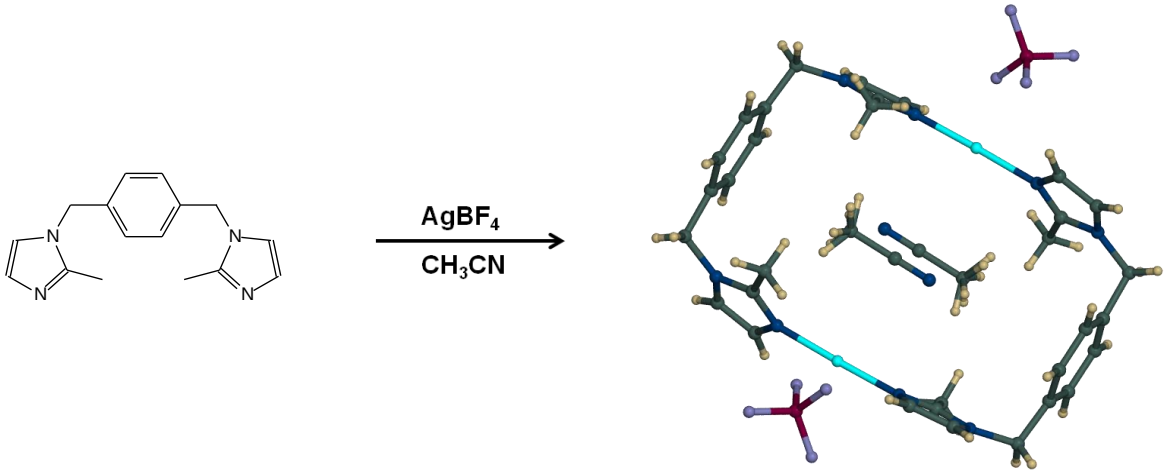

Figure 9. Formation of **M1** $[Ag_2\mathbf{A1}_2](BF_4)_2{\cdot}2CH_3CN$, where **A1** = 1,4-bis(2-methylimidazol-1-ylmethyl)benzene.

Figure 9 shows the formation of the metallocycle **M1**,[114] which consists of a rectangular cationic complex composed of two linearly coordinated silver ions doubly bridged to each other by means of two ligands **A1**. Each ring encloses two acetonitrile molecules arranged as an up-down dimeric pair. The rings stack to form 1D channels occupied by the occluded acetonitrile molecules. The BF_4^- anions are situated between adjacent columns formed by the stacking of the **M1** units. Removal of the solvent molecules was effected by heating the crystals to above 80 °C to produce an empty porous host. Gas sorption isotherms were then recorded for CO_2, N_2, CH_4 and H_2 at 30 °C using a previously described device.[118] It was found that high pressure conditions (>48 bar) favoured the sorption of the smaller gases and at lower pressures (<10 bar) the larger gases were absorbed more readily.

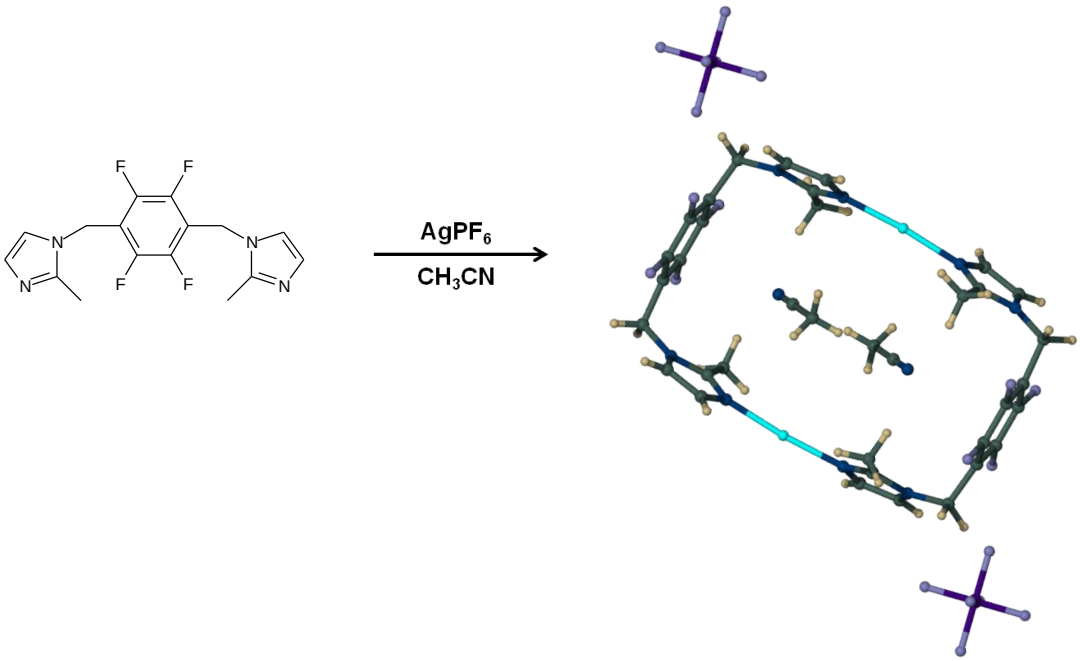

Figure 10. Formation of **M2** $[Ag_2\mathbf{A2}_2](PF_6)_2{\cdot}2CH_3CN$, where **A2** = 2,3,5,6-tetrfluoro-1,4-bis(2-methylimidazole-1-yl-methyl)benzene.

The structure of metallocycle **M2**[115] is highly reminiscent of **M1** in that a dinuclear complex is formed containing two Ag(I) centres in a linear coordination environment and each metallocycle encloses two acetonitrile molecules in an up-down dimeric arrangement (**Figure 10**). The difference in the composition of the two structures is that the counter-ion in **M1** is BF_4^-, whereas it is PF_6^- in **M2** and the aromatic spacer moiety is fluorinated at positions 2, 3, 5 and 6 in the ligand of **M2**. The metallocycles **M2** also stack to form 1D channels, but owing to additional steric constraints imposed by both the larger anion and the fluorination of the aromatic spacer in **A2**, the **M2** metallocycles are significantly more tilted to minimise repulsive interactions. As a consequence of this, the 1D channels in **M2** are not as open as they are in **M1** and consist of a series of bulges associated by smaller apertures. The packing arrangements of the metallocycles also differ: in **M1** the metallocycles form a centred rectangular arrangement, whereas in **M2** the metallocycles are linked into a rectangular arrangement by argentophilic interactions (**Figure 11**). The guest-free phase, obtained by heating crystals of **M2** to 100 °C for 30 min, was then exposed to CO_2. It was noted that, like **M1**, the empty phase of **M2** behaves as a conventionally porous material and is capable of absorbing 2.5 molecules of CO_2 per metallocycle at 0 °C and 18 bar. This is in contrast to **M1,** which can only absorb 2 CO_2 molecules per metallocycle. From this result the authors speculate that the smaller opening

between two adjacent bulges in the 1D channels could provide a further CO_2 binding site, which would account for the additional CO_2 guest molecules. Furthermore, the permeability of the solvent-free **M2** phase to acetone solvent vapours was investigated and it was found that two molecules of acetone were absorbed per metallocycle, resulting in an increase in the guest-accessible volume.

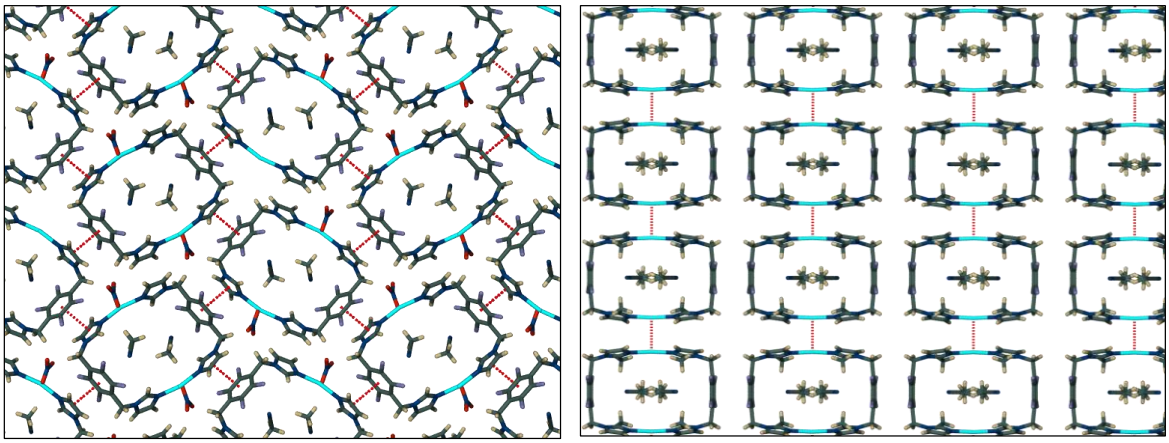

Figure 11. Packing arrangement of metallocyclic columns in **(a) M1**, viewed along [001] showing the centred rectangular arrangement and **(b) M2**, viewed along [100] showing the rectangular arrangement. Argentophilic interactions are shown as red fragmented lines and counter-ions have been omitted for clarity.

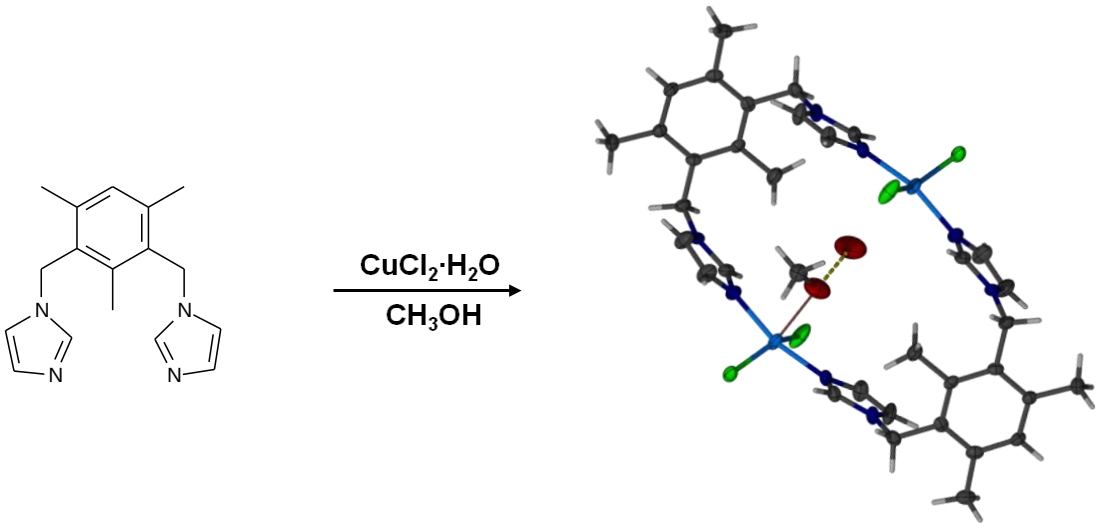

Figure 12. Formation of **M3** $[Cu_2(\mathbf{A3})_2Cl_4]\cdot CH_3OH\cdot H_2O$, where **A3** = 1,3-bis(imidazol-1-ylmethyl)-2,4,6-trimethylbenzene. The hydrogen bond between the methanol molecule and the water molecule is shown as a fragmented yellow cylinder.

Metallocycle **M3**[116] is shown in **Figure 12** and was formed from the reaction of **A3** and $CuCl_2$ in methanol. Each copper ion is in a distorted square planar coordination environment and coordinates to two ligands **A3**, located *trans* to each other, as well as two chloride anions. The metallocycles also stack linearly as in **M1** and **M2**. However, this stacking arrangement does not result in the formation of continuous channels, but rather the guest molecules are located in discrete voids. Each void contains one water molecule and one methanol molecule that can be removed by heating the crystals to 60 °C under vacuum for one hour. Gas sorption isotherms were then recorded volumetrically[118] for CO_2, N_2, CH_4 and H_2 at an initial pressure of 1.35 atm. The results indicated that the material is indeed permeable to gases and that a certain degree of selectivity exists between the different gases tested. These results show that **M3** is not porous in a conventional sense. The authors postulate that the discrete pockets become accessible to gas molecules *via* a cooperative mechanism in which the host molecules move in a concerted fashion to create temporary openings to connect adjacent pockets. Through this movement the guest is relayed through the lattice and the integrity of this transiently porous crystal is maintained.

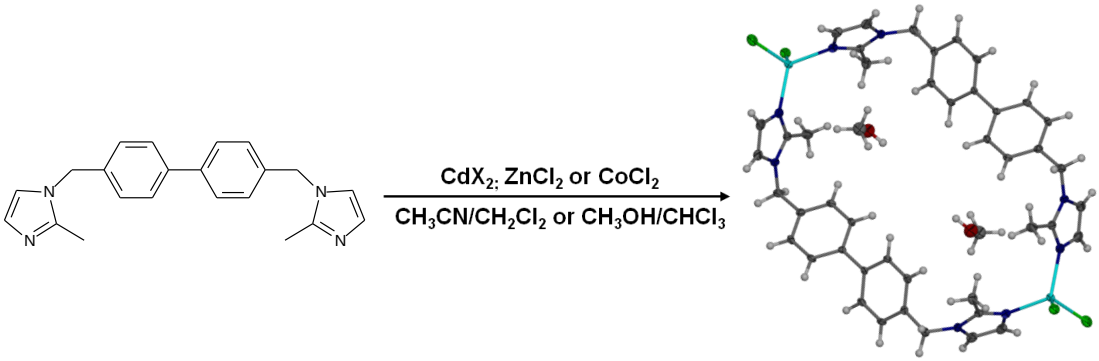

Figure 13. Formation of the **M4** metallocycle series. The specific metallocycles formed are $[Co_2\mathbf{A4}_2Cl_4]\cdot 2MeOH$ (**M4a**), $[Zn_2\mathbf{A4}_2Cl_4]\cdot 2MeOH$ (**M4b**), $[Cd_2\mathbf{A4}_2Cl_4]\cdot 2MeOH$ (**M4c**), $[Cd_2\mathbf{A4}_2I_4]\cdot CHCl_3$ (**M4d**), $[Cd_2\mathbf{A4}_2I_4]\cdot CH_2Cl_2$ (**M4e**) and $[Cd_2\mathbf{A4}_2Br_4]\cdot 2MeOH$ (**M4f**). Where **A4** = 4,4'-bis(2-methylimidazol-1-ylmethyl)biphenyl.

Figure 13 shows the final series of metallocycles; these are all formed by the reaction of **A4** with a variety of halogenated metal salts in either a CH_3CN/CH_2Cl_2 mixed solvent system or a $CH_3OH/CHCl_3$ mixed solvent system.[117] The five systems are isostructural and **M4** refers to the generalised $[M_2\mathbf{A4}_2X_2]$ unit. Each complex comprises two metal ions tetrahedrally coordinated to two halide anions and two bridging **A4**

ligands. The stacking of the metallocycles results in the formation of solvent-filled pockets between two adjacent metallocycles. Removal of the solvent is effected by heating the various materials in the temperature range of 65–140 °C for several hours. The desolvation process was followed by single-crystal X-ray diffraction and these results indicate that the conformation of the metallocycles in the **M4a** and **M4b** systems distort to yield a more efficiently packed phase that is not porous. Conversely, removal of the occluded solvent molecules in the **M4c–f** metallocycles occurs without significant disruption to the conformation or packing of the host metallocycles to yield three structurally analogous host materials with the general formula $[Cd_2\mathbf{A4}_2X_4]$ (X = Cl in **M4c**, I in both **M4d** and **M4e** and Br in **M4f**). The gas sorption capabilities of these potentially porous systems were further investigated. These results show that the nature of the electrostatic profile of the cavity (as influenced by the halide) determines the guest sorption ability of the host. The relationship in terms of most promising sorption ability for CO_2 and N_2 is X = Cl > Br > I, indicating that the decrease in sorption efficiency correlates with a decrease in electronegativity and an increase in halide size.

As part of the study of the **M4** series a miniature gas cell was developed to address the problem of maintaining an overpressure of the gaseous guest during structure determination by single-crystal X-ray diffraction. Utilising this device an investigation was made into the structural changes that occur during the guest uptake process. A single crystal of **M4c** was exposed to carbon dioxide and acetylene and a series of structures were collected at various systematically-controlled pressures for the two inclusion complexes. The high level of structural detail obtained from the single-crystal data allowed the rationalisation of the differences in sorption behaviour for the two host-guest systems.

Furthermore, the structural information obtained from the single-crystal structures of the host-guest systems was used in conjunction with statistical mechanics calculations and physico-chemical measurements of kinetic and thermodynamic parameters to postulate a plausible mechanism for gas transport through the host lattice. It was proposed that gas transport is a non-activated diffusion process aided by the dynamic motion of the framework channels, which allows adjacent pockets to merge and create ephemeral channels that allow guests to move through the host framework.

Figure 14 shows the stacking of the metallocycles **M1**–**M4** and illustrates the difference between conventionally and transiently porous materials.

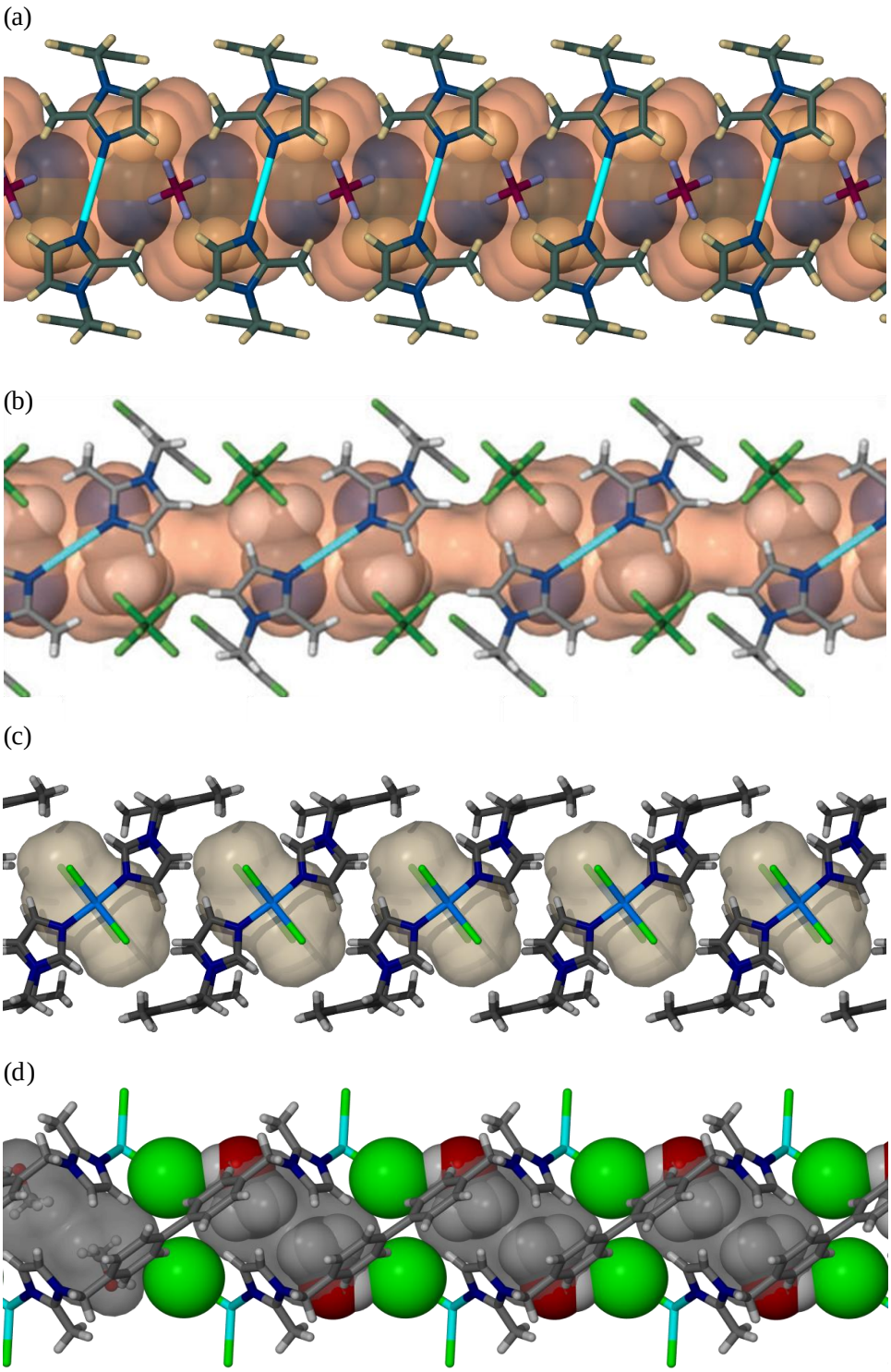

Figure 14. A comparison of conventional and transient porosity. **(a)** and **(b)** show conventionally porous systems where the metallocycles **M1** and **M2** in **(a)** and **(b)**, respectively, stack such that continuous channels are formed, allowing guest molecules to traverse the material without disrupting the host framework. **(c)** and **(d)** show transiently porous systems where the metallocycles **M3** and **M4** in **(c)** and **(d)** respectively, stack such that discrete pockets are formed. The concerted movement of the host framework creates momentary 'gaps' between the discrete voids to allow guest molecules to traverse the material.

1.5. ORGANIC RADICALS

An organic free radical is a molecular species that contains an unpaired electron in an open shell configuration. In the context of molecular orbital theory, this leads to orbitals that are singly occupied. Owing to the presence of unpaired electrons, organic radicals have been recognised as potential candidates in molecule-based conducting and magnetic materials. In the current study the organic radical assumes the role of a guest in a host-guest inclusion compound. An ultimate application would be to use this inclusion mode to alter these conductive and magnetic properties. It is therefore important that these properties are well understood.

The discovery that poly(sulphur-nitride), $(SN)_x$, a material that contains no metallic elements, exhibits superconducting properties[119] initiated an investigation into the potential properties of S-N-containing materials. In particular, this led to the development of S,N-heterocyclic radicals as species that could be utilised to emulate, and even surpass the properties of $(SN)_x$.[120,121]

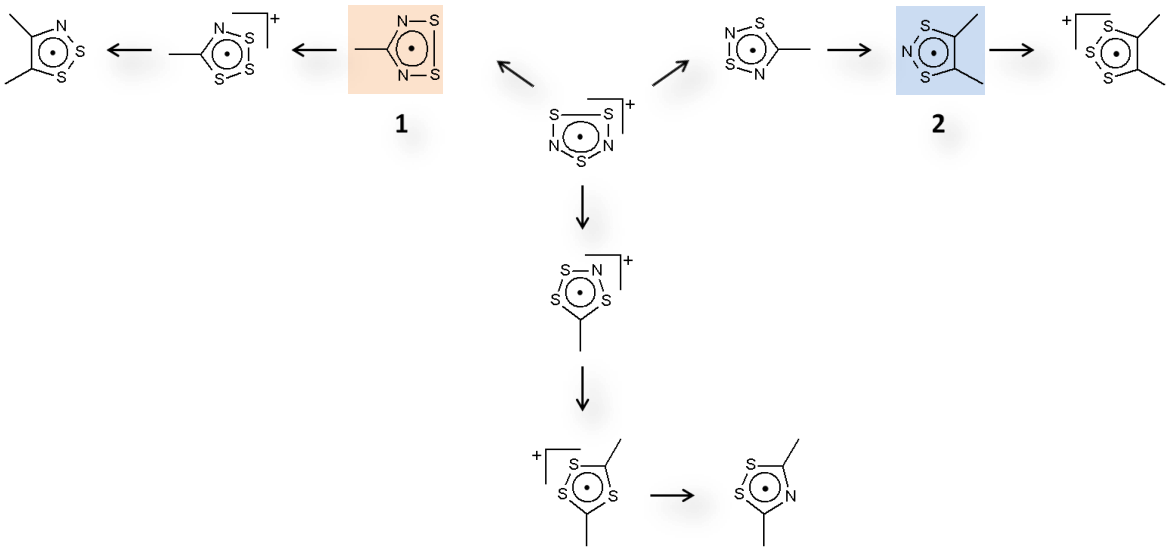

Scheme 4. Isoelectronic members of the family of five-membered heterocyclic thiazyl radicals. **1** denotes the dithiadiazolyl radical and **2** denotes the dithiazolyl radical. Scheme adapted from reference 121.

The thiazyl family of five-membered 7π heterocyclic radicals (see **Scheme 4**) has been extensively studied and their properties have been well characterised.[120-123] Of these, the dithiadiazolyl and dithiazolyl radicals have shown potential as molecular magnetic and conducting materials, and in this work we will focus on dithiazolyl radicals (denoted as **2**

in **Scheme 4**). In these organic radicals the unpaired electron resides in a π^* molecular orbital, also termed the singly occupied molecular orbital or SOMO. The SOMO is based mainly, but not exclusively in the S–N–S region of the molecule (**Figure 15**).[121,124,125] A commonly encountered phenomenon in the field of organic radicals is the efficient SOMO–SOMO overlap to produce a dimeric arrangement of molecules in the solid state; this leads to the energetically favourable spin-pairing of radical electrons and loss of conductive and magnetic properties. For this reason, many crystal engineering efforts in the field of organic radicals are aimed at manipulating the packing arrangement of the radicals in the solid state to overcome this dimerisation tendency.

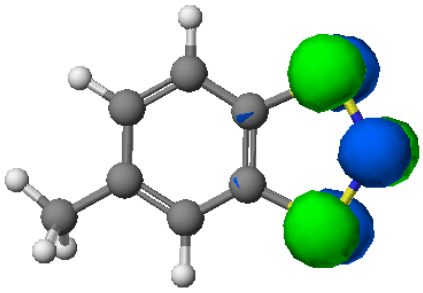

Figure 15. The SOMO of the dithiazolyl radical 5-methylbenzo-1,3,2-dithiazolyl (**MBDTA**). Figure provided by J.M. Rawson.

For a material comprising neutral π-radicals to exhibit conductive properties in the solid state, the electrons must be able to flow between the molecules when a potential difference is applied.[126] In the crystalline solid state this is achieved through close packing of the molecules into regularly spaced 1D stacks. This arrangement results in overlapping of orbitals into a set of crystal orbitals (or a band) that are delocalised over the whole structure.[127] The final result is a band structure with exactly one electron per radical being contributed to the conduction band, which gives rise to a half-filled energy band and hence conduction (**Figure 16a**). However, if the intermolecular spacing is asymmetric i.e. in the 1D stack there are alternating long and short intermolecular contacts, the electron density becomes more localised than in the ideal metallic conducting state, causing a band gap (**Figure 16b**). In the most extreme case spin-paired dimers form in the regions of short contacts, leading to a complete loss of conductive properties as the material is rendered a diamagnetic insulator. This asymmetric stacking phenomenon is termed a Peierls' distortion.[128]

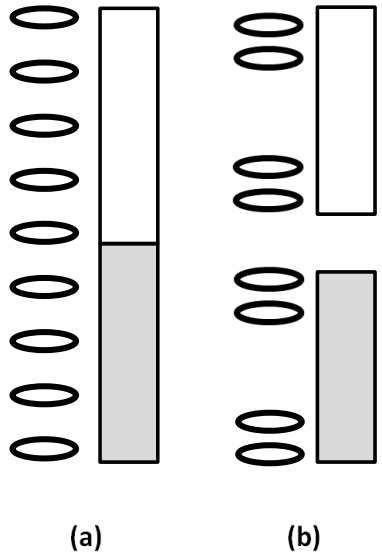

Figure 16. (a) The half-filled energy band formed as a result of a 1D array of regularly stacked radicals. **(b)** Band gap formed as a result of Peierls' distortion. Image adapted from reference 120.

The potential for the application of organic radicals as magnetic materials stems from the magnetic moments of individual electrons, which originate from two sources: its orbital motion around the nucleus, and the spin of the electron. In the second case the electron can be thought of as spinning around a particular axis in an "up" or "down" direction – this is quantified by the spin quantum number m_s. In essence, each electron can be thought of as being a small bar magnet that can interact with an applied magnetic field.

The prerequisites for an organic magnet are: (i) there must be unpaired electron spins (in the event of dimerisation this requirement cannot be met), (ii) there must be magnetic exchange interactions between these unpaired spins and (iii) a 3D magnetic exchange lattice is required.[121]

There are numerous magnetically ordered phases, the simplest of which are the ferromagnetic and anti-ferromagnetically ordered phases (**Figure 17**). If the magnetic moments align, even in the absence of a field, then the material is ferromagnetic and, if the alignment of magnetic moments between adjacent atoms is in opposite directions, then an anti-ferromagnet is formed.[129]

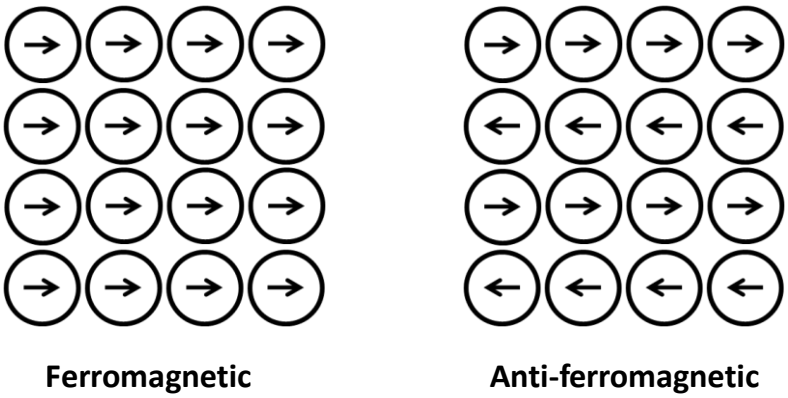

Figure 17. Schematic representation of ferromagnetic and anti-ferromagnetic ordered phases. Adapted from reference 130.

1.6. KEY ASPECTS AND AIMS OF THIS STUDY

Porous crystalline materials are attractive supramolecular target systems as they provide a platform of controlled space in which smaller molecular guests may be included. This inclusion process alters the original properties of both the host and guest components. Through crystal engineering efforts it will be possible to ultimately design and synthesise novel inclusion materials with specific properties and functions.

The main objective of this study is to investigate the properties of novel inclusion complexes. The first part of the study is concerned with the synthesis and thermal properties of 0D metallocyclic host materials and the second part of the study describes the properties of the inclusion complexes formed from the vapour-phase diffusion of organic radicals into a porous 3D MOF material.

Chapter 2 presents the synthesis and characterisation of six imidazole-derived ligands. These ligands were reacted with a variety of transition metal salts in a systematic manner with a view to synthesising 0D metallocycles. Twenty-nine single-crystal structures were obtained, including five porous metallocycles. The structures of the 24 non-metallocyclic derivatives are described in this chapter. Further aspects of this chapter include a description of a modification that could be made to the current metallocycle design strategy, as well as an outline of a high-throughput protocol that could be implemented to screen multiple reaction conditions rapidly and more efficiently than current methods.

Chapter 3 presents the single-crystal structures and thermal analyses of five metallocycles (see **Figure 18**). The thermoanalytical data reveals that all five of the

metallocycles have remarkably high thermal stability with respect to the loss of their occluded solvent molecules. The second section in this chapter describes a computational study undertaken in an attempt to rationalise this high thermal stability and the final section entails a systematic investigation of these metallocyclic host materials as Class II porous systems.

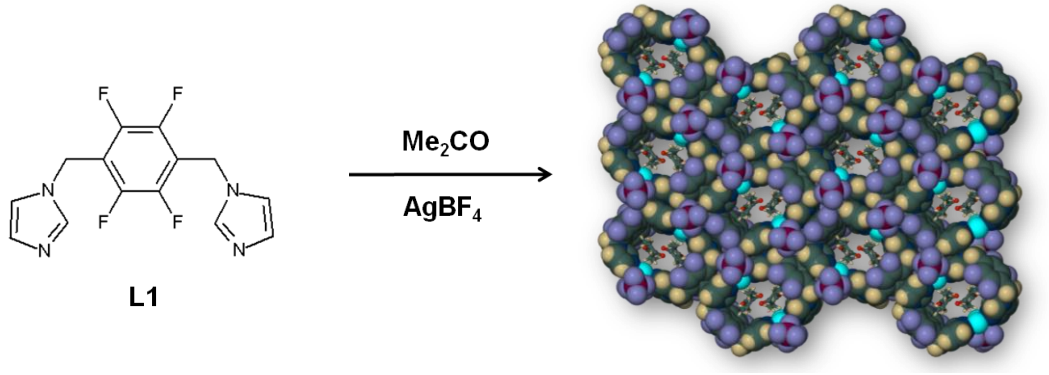

Figure 18. Formation of $[Ag(\mathbf{L1})_2](BF_4)_2$ (**L1** = 2,3,5,6-tetrfluoro-1,4-bis(imidazol-1-yl-methyl)benzene, one of the five metallocycles described in **Chapter 3**. The packing arrangement of the metallocycle is shown, with the cyclic units shown in van der Waals representation and the guest molecules in the ball-and-stick representation.

Chapter 4 describes the selective inclusion of organic radicals into the pores of a MOF (**Figure 19**). The structures of the inclusion complexes, as well as the stabilisation of the air-sensitive radical species within the porous material are discussed. **Chapter 5** presents a summary of the work contained in Chapters 2, 3 and 4.

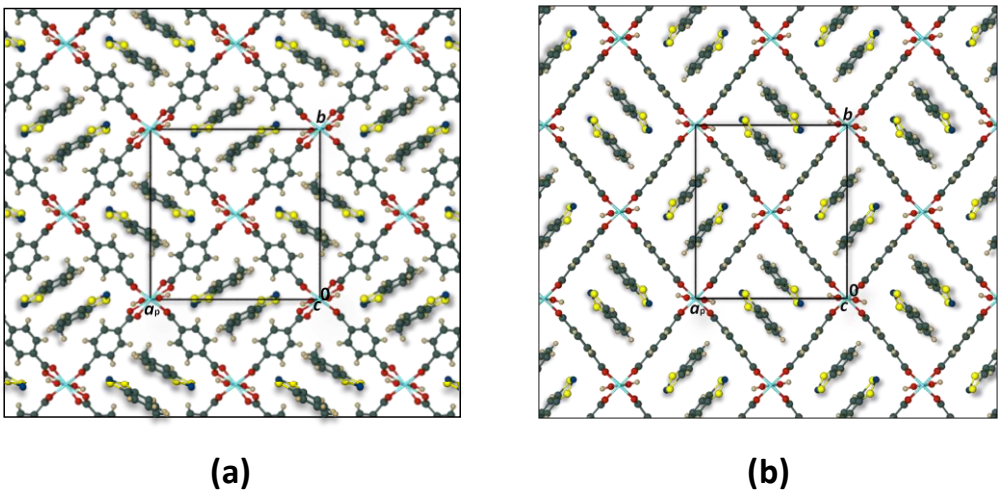

Figure 19. View along the 1D channels in the two radical inclusion complexes described in **Chapter 4** i.e. **MBDTA@MIL-53(Al) (a)** and **BDTA@MIL-53(Al) (b)**.

REFERENCES

(1) J. M. Lehn, *Angew. Chem. Int. Ed. Engl.*, **1988**, *27*, 89.

(2) K. L. Wolf; H. Frahm; H. Harms, *Z. Phys. Chem. Abt. B*, **1937**, *36*, 237.

(3) J. M. Lehn, *Supramolecular chemistry*; VCH: Weinheim ; New York, **1995**.

(4) J. W. Steed; J. L. Atwood, *Supramolecular Chemistry* John Wiley & Sons, Ltd: West Sussex, **2000**.

(5) J. W. Steed; D. R. Turner; K. J. Wallace, *Core Concepts in Supramolcular Chemistry and Nanochemistry*; Wiley: Chichester, England, **2007**.

(6) J. D. Dunitz, *Pure Appl. Chem.*, **1991**, *63*, 177.

(7) D. Braga, *Chem. Commun.*, **2003**, 2751.

(8) M. C. Etter, *J. Am. Chem. Soc.*, **1987**, *109*, 7786.

(9) G. R. Desiraju In *Comprehensive Supramolecular Chemistry*; J. L. Atwood, D. Davies, D. D. MacNicol, F. Vögtle, Eds.; Pergamon: Oxford, **1996**

(10) G. R. Desiraju, *Angew. Chem. Int. Ed. Engl.*, **1995**, *34*, 2311.

(11) R. Pepinsky, *Phys. Rev.*, **1955**, *100*, 971.

(12) G. M. J. Schmidt, *Appl. Chem.*, **1971**, *27*, 647.

(13) V. R. Thalladi; B. S. Goud; V. J. Hoy; F. H. Allen; J. A. K. Howard; G. R. Desiraju, *Chem. Commun.*, **1996**, 401.

(14) G. R. Desiraju, *J. Mol. Struct.*, **2003**, *656*, 5.

(15) O. M. Yaghi; M. O'Keefe; N. W. Ockwig; H. K. Chae; M. Eddaoudi; J. Kim, *Nature*, **2003**, *423*, 705.

(16) J. M. Lehn, *Angew. Chem. Int. Ed. Engl.*, **1990**, *29*, 1304.

(17) G. R. Desiraju, *Crystal Engineering, the Design of Organic Solids*; Elsevier: Amsterdam, **1989**.

(18) M. Kawano; M. Fujita, *Coord. Chem. Rev.*, **2007**, *251*, 2592.

(19) S. L. Price, *Intermolecular Forces - From the Molecular Charge Distribution to the Molecular Packing*; Wiley: Chichester, **1997**.

(20) I. Dance In *Encyclopedia of Supramolecular Chemistry*; J. W. Atwood, J. W. Steed, Eds.; Marcel Dekker, Inc.: New York, **2004**

(21) P. Pyykko, *Chem. Rev.*, **1997**, *97*, 597.

(22) A. N. Khlobystov; A. J. Blake; N. R. Champness; D. A. Lemenovskii; A. G. Majouga; N. V. Zyk; M. Schroder, *Coord. Chem. Rev.*, **2001**, *222*, 155.

(23) D. Braga; F. Grepioni In *Encyclopedia of Supramolecular Chemistry*; J. L. Atwood, J. W. Steed, Eds.; Marcel Dekker, Inc.: New York, **2004**

(24) A. Werner, *Liebig's Annalen der Chemie*, **1902**, *322*, 261.

(25) A. Hantzsch, *Chem. Ber.*, **1910**, *43*, 3049.

(26) L. Pauling, *J. Am. Chem. Soc.*, **1939**, *57*, 2680.

(27) L. Pauling, *The Nature of the Chemical Bond*; Cornell University Press: Ithaca, New York, **1939**.

(28) T. Steiner, *Angew. Chem. Int. Ed*, **2002**, *41*, 48.

(29) G. C. Pimentel; A. L. McClellan, *The Hydrogen Bond*; Freeman: San Francisco, **1960**.

(30) E. Arunan; G. R. Desiraju; R. A. Klein; J. Sadlej; S. Scheiner; I. Alkorta; D. C. Clary; R. H. Crabtree; J. J. Dannenberg; P. Hobza; H. G. Kjaergaard; A. C. Legon; B. Mennucci; D. J. Nesbitt, *Pure Appl. Chem.*, **2011**, *88*, 1637.

(31) M. Lusi; L. J. Barbour, *Cryst. Growth Des.*, **2011**, *11*, 5515.

(32) P. Müller, *Crystal Structure Refinement A Crystallographer's Guide to SHELXL*; Oxford University Press: Oxford, **2006**.

(33) G. R. Desiraju; T. Steiner, *The Weak Hydrogen Bond in Structural Chemistry and Biology*; Oxford University Press: Oxford ; New York, **1999**.

(34) S. Leininger; B. Olenyuk; P. J. Stang, *Chem. Rev.*, **2000**, *100*, 853.

(35) K. Kumazawa; Y. Yamanoi; M. Yoshizawa; T. Kusukawa; M. Fujita, *Angew. Chem. Int. Ed*, **2004**, *43*, 5936.

(36) H. Davy, *Philos. Trans. R, Soc. London*, **1811**, *101*, 155.

(37) M. Faraday; H. Davy, *Philos. Trans. R, Soc. London*, **1823**, *113*, 160.

(38) P. Ehrlich, *Studies on Immunity* Wiley ; New York, **1906**.

(39) E. Fischer, *Ber. Deutsch. Chem. Ges.*, **1894**, *27*, 2985.

(40) A. Werner, *Zeitschr. Anorg. Chem.*, **1893**, *3*, 267.

(41) L. R. Nassimbeni, *Acc. Chem. Res.*, **2003**, *36*, 631.

(42) Q. K. Liu; J. P. Ma; Y. B. Dong, *J. Am. Chem. Soc.*, **2010**, *132*, 7005.

(43) Y. Y. Cheng; J. R. Wang; T. L. Rao; X. X. He; T. W. Xu, *Front. Biosci-Landmrk.*, **2008**, *13*, 1447.

(44) E. V. Anslyn, *J. Org. Chem.*, **2007**, *72*, 687.

(45) E. Hughes; J. Jordan; T. Gullion, *J. Phys. Chem. B*, **2001**, *105*, 5887.

(46) S. Erdemir; M. Bahadir; M. Yilmaz, *J. Hazard Mater.*, **2009**, *168*, 1170.

(47) L. R. MacGillivray; G. S. Papaefstathiou In *Encyclopedia of Supramolecular Chemistry*; J. L. Atwood, J. W. Steed, Eds.; Marcel Dekker, Inc.: New York, **2004**

(48) G. R. Desiraju, in *Comprehensive Supramolecular Chemistry, Vol. 6*; J. Atwood, D. Davies, D. D. MacNicol, F. Vögtle, Eds.; Pergamon: Oxford, **1996**, p 1.

(49) A. P. Dianin, *J. Russ. Phys. Chem. Soc.*, **1914**, *32*, 1310.

(50) D. M. White, *J. Am. Chem. Soc.*, **1960**, *82*, 5678.

(51) H. Reuter, *Angew. Chem., Int. Ed. Engl.*, **1992**, *31*, 1185.

(52) M. R. Caira; L. R. Nassimbeni; M. L. Niven; W. D. Schubert; E. Weber; N. Dorpinghaus, *J. Chem. Soc. Perkin Trans. 2*, **1990**, 2129.

(53) S. A. Bourne; L. Johnson; C. Marais; L. R. Nassimbeni; E. Weber; K. Skobridis; F. Toda, *J. Chem. Soc. Perkin Trans. 2*, **1991**, 1707.

(54) J. J. Vittal; T. Lu, *Cryst. Growth Des.*, **2006**, *6*, 822.

(55) F. Giordano; C. Novak; J. R. Moyano, *Thermochim Acta*, **2001**, *380*, 123.

(56) L. J. Barbour, *Chem. Commun.*, **2006**, 1163.

(57) C. Lastoskie; K. E. Gubbins; N. Quirke, *J. Phys. Chem.*, **1993**, *97*, 4786.

(58) N. B. McKeown; P. M. Budd, *Chem. Soc. Rev.*, **2006**, *35*, 675.

(59) L. J. Murray; M. Dinca; J. R. Long, *Chem. Soc. Rev.*, **2009**, *38*, 1294.

(60) H. Wu; W. Zhou; T. Yildirim, *J. Am. Chem. Soc.*, **2009**, *131*, 4995.

(61) W. Zhou, *Chem. Rec.*, **2010**, *10*, 200.

(62) P. Sozzani; S. Bracco; A. Comotti; L. Ferretti; R. Simonutti, *Angew. Chem. Int. Ed*, **2005**, *44*, 1816.

(63) J. L. Atwood; L. J. Barbour; A. Jerga, *Science*, **2002**, *296*, 2367.

(64) *The American Heritage® Science Dictionary*, Published by Houghton Mifflin., **2002**

(65) S. Kitagawa; R. Kitaura; S.-I. Noro, *Angew. Chem. Int. Ed.*, **2004**, *43*, 2334.

(66) S. Kitagawa; K. Uemura, *Chem. Soc. Rev.*, **2005**, *34*, 109.

(67) S. Kitagawa; S.-i. Noro; T. Nakamura, *Chem. Commun.*, **2006**, 701.

(68) J. L. Atwood; L. J. Barbour; A. Jerga; B. L. Schottel, *Science*, **2002**, *298*, 1000.

(69) J. W. Steed, *Science*, **2002**, 976.

(70) M. Albrecht; M. Lutz; A. L. Spek; G. van Koten, *Nature* **2000**, *406*, 970.

(71) A. A. Riddle; J. C. Bollinger; D. Lee, *Angew. Chem. Int. Ed.*, **2005**, *44*, 6689.

(72) A. Deak; T. Tunyogi; Z. Karoly; S. Klebert; G. Palinkas, *J. Am. Chem. Soc.*, **2010**, *132*, 13627.

(73) S. Libri; M. Mahler; G. M. Espallargas; D. C. N. G. Singh; J. Soleimannejad; H. Adams; M. D. Burgard; N. P. Rath; M. Brunelli; L. Brammer, *Angew. Chem. Int. Ed.*, **2008**, *47*, 1693.

(74) L. D. Rollman; E. W. Valyocisk, *Inorganic Syntheses*; John Wiley and Sons: New York **1981**.

(75) T. Hertzch; J. Hulliger; E. Weber; P. Sozzani In *Encyclopedia of Supramolecular Chemistry*; 1 ed.; J. W. Atwood, J. W. Steed, Eds.; Marcel Dekker, Inc.: New York, **2004**

(76) M. E. Davis; R. F. Lobo, *Chem. Mater.*, **1992**, *4*, 756.

(77) H. S. Sherry, *Clays & Clay Minerals*, **1979**, *27*, 231.

(78) M. Choi; H. S. Cho; R. Srivastava; C. Venkatesan; D.-H. Choi; R. Ryoo, *Nat. Mater.*, **2006**, *5*, 718.

(79) J. Cejka; A. Corma; S. Zones, *Zeolites and Catalysis*; VCH: Wiley; Weinheim, **2010**.

(80) G. T. Kokotailo; S. L. Lawton; D. H. Olson; D. H. Olson; W. M. Meier, *Nature*, **1978**, *272*, 437.

(81) K. S. W. Sing; D. H. Everett; R. A. W. Haul; L. Moscou; R. A. Pierotti; J. Rouquerol; T. Siemieniewska, *Pure Appl. Chem.*, **1985**, *57*, 603.

(82) K. Egeblad; C. H. Christensen; M. Kustova; C. H. Christensen, *Chem. Mater.*, **2007**, *20*, 946.

(83) S. M. Auerbach; K. A. Carrado; P. K. Dutta, *Handbook of Zeolite Science and Technology*; CRC Press, **2003**.

(84) B. F. Hoskins; R. Robson, *J. Am. Chem. Soc.*, **1990**, *112*, 1546.

(85) B. F. Abrahams; B. F. Hoskins; D. M. Michail; R. Robson, *Nature*, **1994**, *369*, 727.

(86) Z. Y. Wu; S. Lee; J. S. Moore, *J. Am. Chem. Soc.*, **1992**, *114*, 8730.

(87) L. R. Macgillivray; S. Subramanian; M. J. Zaworotko, *J. Chem. Soc. Chem. Commun.*, **1994**, 1325.

(88) J. L. C. Rowsell; O. M. Yaghi, *Micropor. Mesopor. Mat.*, **2004**, *73*, 3.

(89) D. J. Tranchemontagne; J. L. Mendoza-Cortes; M. O'Keeffe; O. M. Yaghi, *Chem. Soc. Rev.*, **2009**, *38*, 1257.

(90) M. Eddaoudi; D. B. Moler; H. Li; B. Chen; T. M. Reineke; M. O'Keefe; O. M. Yaghi, *Acc. Chem. Res.*, **2000**, *34*, 319.

(91) A. U. Czaja; N. Trukhan; U. Muller, *Chem. Soc. Rev.*, **2009**, *38*, 1284.

(92) H. Li; M. Eddaoudi; M. O'Keeffe; O. M. Yaghi, *Nature*, **1999**, *402*, 276.

(93) M. Eddaoudi; J. Kim; N. Rosi; D. Vodak; J. Wachter; M. O'Keeffe; O. M. Yaghi, *Science*, **2002**, *295*, 469.

(94) T. Uemura; N. Yanai; S. Kitagawa, *Chem. Soc. Rev.*, **2009**, *38*, 1228.

(95) A. Poppl; B. Jee; K. Koch; L. Moschkowitz; D. Himsl; M. Hartman, *J. Phys. Chem. Lett.*, **2011**, *2*, 357.

(96) L. Q. Ma; C. Abney; W. B. Lin, *Chem. Soc. Rev.*, **2009**, *38*, 1248.

(97) F. Millange; N. Guillou; M. E. Medina; G. Ferey; A. Carlin-Sinclair; K. M. Golden; R. I. Walton, *Chem. Mater.*, **2010**, *22*, 4237.

(98) S. Bourrelly; B. Moulin; A. Rivera; G. Maurin; S. Devautour-Vino; C. Serre; T. Devic; P. Horcajada; A. Vimont; G. Clet; M. Daturi; J. C. Lavalley; S. Loera-Serna; R. Denoyel; P. L. Llewellyn; G. Ferey, *J. Am. Chem. Soc.*, **2010**, *132*, 9488.

(99) L. Hamon; C. Serre; T. Devic; T. Loiseau; F. Millange; G. Ferey; G. De Weireld, *J. Am. Chem. Soc.*, **2009**, *131*, 8775.

(100) L. Hamon; P. L. Llewellyn; T. Devic; A. Ghoufi; G. Clet; V. Guillerm; G. D. Pirngruber; G. Maurin; C. Serre; G. Driver; W. van Beek; E. Jolimaitre; A. Vimont; M. Daturi; G. Ferey, *J. Am. Chem. Soc.*, **2009**, *131*, 17490.

(101) J. T. Hupp; G. Lu, *J. Am. Chem. Soc.*, **2010**, *132*, 7832.

(102) O. M. Yaghi; K. S. Park; Z. Ni; A. P. Cote; J. Y. Choi; R. D. Huang; F. J. Uribe-Romo; H. K. Chae; M. O'Keeffe, *Proc. Natl. Acad. Sci. USA.*, **2006**, *103*, 10186.

(103) R. Banerjee; A. Phan; B. Wang; C. Knobler; H. Furukawa; M. O'Keeffe; O. M. Yaghi, *Science*, **2008**, *319*, 939.

(104) M. Maes; F. Vermoortele; L. Alaerts; S. Couck; C. E. A. Kirschhock; J. F. M. Denayer; D. E. De Vos, *J. Am. Chem. Soc.*, **2010**, *132*, 15277.

(105) T. Loiseau; C. Serre; C. Huguenard; G. Fink; F. Taulelle; M. Henry; T. Bataille; G. Ferey, *Chem.-Eur. J.*, **2004**, *10*, 1373.

(106) A. N. Neimark, A. V.; F. X. Coudert; C. Triguero; A. Boutin; A. H. Fuchs; I. Beurroies; R. Denoyel, *Langmuir*, **2011**, *27*, 4734.

(107) B. Slater; A. M. Walker; B. Civalleri; C. Mellot-Draznieks; F. Cora; C. M. Zicovich-Wilson; G. Roman-Perez; J. M. Soler; J. D. Gale, *Angew. Chem. Int. Ed.*, **2010**, *49*, 7501.

(108) R. M. Barrer; V. H. Shanson, *J. Chem. Soc. Chem. Commun.*, **1976**, 333.

(109) T. Tozawa; J. T. A. Jones; S. I. Swamy; S. Jiang; D. J. Adams; S. Shakespeare; R. Clowes; D. Bradshaw; T. Hasell; S. Y. Chong; C. Tang; S. Thompson; J. Parker; A. Trewin; J. Bacsa; A. M. Z. Slawin; A. Steiner; A. I. Cooper, *Nat. Mater.*, **2009**, *8*, 973.

(110) M. J. Bojdys; M. E. Briggs; J. T. A. Jones; D. J. Adams; S. Y. Chong; M. Schmidtmann; A. I. Cooper, *J. Am. Chem. Soc.*, **2011**, *133*, 16566.

(111) J. R. Karra; K. S. Walton, *Langmuir*, **2008**, *24*, 8620.

(112) M. J. Rosseinsky, *Micropor. Mesopor. Mat.*, **2004**, *73*, 15.

(113) J. L. C. Roswell; O. M. Yaghi, *Angew. Chem. Int. Ed*, **2005**, *44*, 4670.

(114) L. Dobrańska; G. O. Lloyd; H. G. Raubenheimer; L. J. Barbour, *J. Am. Chem. Soc.*, **2005**, *127*, 13134.

(115) L. J. Barbour; T. Jacobs; J. A. Gertenbach; D. Das, *Aust. J. Chem.*, **2010**, *63*, 573.

(116) L. Dobrzańska; G. O. Lloyd; H. G. Raubenheimer; L. J. Barbour, *J. Am. Chem. Soc.*, **2006**, *128*, 698.

(117) T. Jacobs, *PhD Thesis*; University of Stellenbosch, **2009**.

(118) J. Atwood; L. J. Barbour; P. K. Thallapally; T. B. Wirsig, *Chem. Commun.*, **2005**, 51.

(119) M. M. Labes; P. Love; L. F. Nichols, *Chem. Rev.*, **1979**, *79*, 1.

(120) D. A. Haynes, *CrystEngComm*, **2011**, *13*, 4793.

(121) A. Alberola; J. M. Rawson; A. Whalley, *J. Mater. Chem.*, **2006**, *16*, 2560.

(122) A. Alberola; R. J. Less; C. M. Pask; J. M. Rawson; F. Palacio; P. Oliete; C. Paulsen; A. Yamaguchi; R. D. Farley; D. M. Murphy, *Angew. Chem. Int. Ed.*, **2003**, *42*, 4782.

(123) J. M. Rawson; A. J. Banister; I. Lavender, *Adv. Heterocycl. Chem.*, **1995**, *62*, 137.

(124) E. G. Awere; N. Burford; R. C. Haddon; S. Parsons; J. Passmore; J. V. Waszczak; P. S. White, *Inorg. Chem.*, **1990**, *29*, 4821.

(125) G. D. McManus; J. M. Rawson; N. Feeder; F. Palacio; P. Oliete, *J. Mater. Chem.*, **2000**, *10*, 2001.

(126) R. C. Haddon, *Nature*, **1975**, *256*, 394.

(127) A. W. Cordes; R. C. Haddon; R. T. Oakley, *Adv. Mater.*, **1994**, *6*, 798.

(128) R. C. Peierls, *Quantum Theory of Solids*; Oxford University Press: London, **1953**.

(129) W. D. Callister, *Fundamentals of Materials Science and Engineering*; John Wiley & Sons: Hoboken, NJ, **2005**.

CHAPTER 2

STRUCTURAL ANALYSIS OF IMIDAZOLE-DERIVED TRANSITON METAL COMPLEXES

2.1. INTRODUCTION

In the past decade the number of self-assembled coordination compounds comprising metal centres bridged to one another by organic ligands has increased exponentially. This is undoubtedly due to the plethora of readily available metal salts and the conceptually infinite number of organic ligands that can be synthesised. The process of self-assembly has also proven to be a reliable synthetic strategy in the production of functional materials with desirable properties, especially when compared to labour intensive stepwise covalent synthesis.[1] Attempts to control the architectures derived from the self assembly of organic ligand and metal ion components fall within the realms of crystal engineering – a rapidly expanding branch of supramolecular chemistry that involves a systematic approach to the combination of molecules into targeted functional supermolecules.[2] It is important to note that crystal engineering encompasses both the *design* and the *synthesis* of targeted supramolecular assemblies.[3]

Crystal engineers often take a retrosynthetic approach to product design where the final structure is envisaged as a collective of components that can spontaneously assemble to form the required product. Therefore, building blocks are judiciously chosen based on certain intrinsic properties of the molecules, as well as their ability to favourably interact with one another to form a specific supramolecular entity.[4] The synthetic component involves tailoring the crystallisation process to obtain the optimum conditions under which the desired product can be isolated – a non-trivial task as there are many factors that can influence the process of crystallisation and, by extension, the nature of the product.[3,5-8]

Crystal engineering endeavours involving coordination compounds are largely aimed at producing porous materials, which are attractive supramolecular target systems owing to their potential applications in catalysis[9-12] and the storage,[7,13-15] separation[16-18] and sensing[19-22] of small molecular species. In this field, metal ions – typically transition metal ions and organic ligand building blocks are used to engineer solvent-templated structures of varying dimensionalities; if the solvent molecules can be extracted, or replaced by other

guest molecules without collapse of the host structure then a porous system is formed. The basic tenet in the rational design of these materials is that the coordination geometry of the metal centres can be propagated by the steric and connectivity information stored in the organic ligand. Therefore, once the metal geometry is taken into consideration the architecture of the targeted assembly is mostly dependent on the design of the ligand.[23-25]

The most fundamental aspect in the ligand design is that it needs to link two metal atoms to each other and must therefore contain at least two binding moieties that have an affinity for the chosen metal centres. These binding domains may either be locked into position in a rigid ligand or be able to rotate around fixed positions in a conformationally flexible ligand. Many research groups have had success in utilising the former, rigid type of ligands to create solvent-templated 2D and 3D coordination polymeric frameworks that retain their structural integrity upon desolvation (refer to Section 1.4.1.1). We are interested in forming similarly robust porous materials utilising a 0D (i.e. discrete) "doughnut-shaped" complex design. These systems incorporate conformationally flexible ligands to doubly connect two metal centres to each other to form a dinuclear metallocyclic coordination complex that contains solvent molecules in the aperture of the "doughnut". As is the case for many coordination polymeric frameworks, these systems are also capable of maintaining their structural integrity upon desolvation to yield porous materials. To date, our group has published four accounts of porous materials achieved using this design strategy (a review of these results is presented in Chapter 1).[26-29]

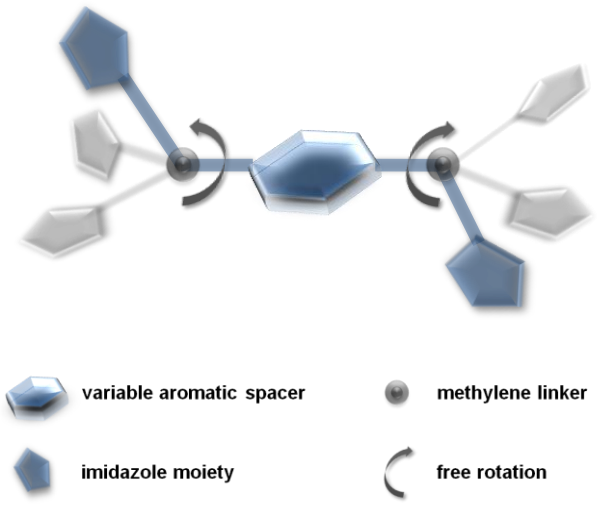

Scheme 1. Basic design principle of the ligands used in metallocycle formation.

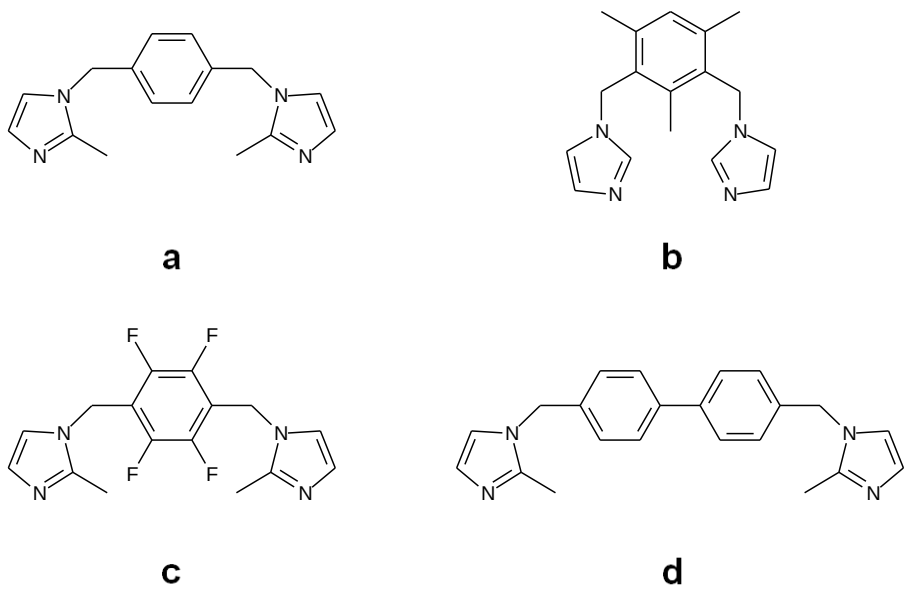

Scheme 2. The four structurally related ligands used in the construction of 0D porous metallocycles; **(a)** 1,4-bis(2-methylimidazole-1-yl-methyl)benzene,[26] **(b)** 1,3-bis(imidazol-1-ylmethyl)-2,4,6-trimethyl benzene,[27] **(c)** 2,3,5,6-tetrafluoro-1,4-bis(2-methylimidazole-1-yl-methyl)benzene[28] and **(d)** 4,4'-bis(2-methylimidazol-1-ylmethyl)biphenyl.[29]

Our success thus far has been closely tied to the specific choice of ligand, i.e. ditopic imidazole-derived ligands. The advantages of these ligands is that they can generally be synthesised and isolated in high yields from a one- or two-step synthetic procedure and the imidazole moieties have a high affinity for transition metals, which aids the self-assembly process.[30] The ligands are all based on the same simple design principle, whereby two imidazole moieties are tethered to a variable aromatic core by virtue of methylene linkages. The aromatic core thus provides a rigid building block and the methylene groups can act as hinges that will allow the ligand to alter its conformation and shift the position of the N-donor groups to suit the geometry of the metal atom (see **Scheme 1** for a representation of the ligand design principle and **Scheme 2** for the four ligands that have been successfully utilised in metallocycle formation). With regard to metallocycle formation, the optimum conformation of the ligand is a *cis* or C-shaped conformation, which places the two imidazole moieties on the same side relative to the mean plane of the aromatic spacer (this is as opposed to a *trans* conformation, which places the two imidazole groups on opposite sides of the mean plane of the aromatic spacer – see **Scheme 3**). However, as a consequence of this inherent flexibility, these ligands possess a higher degree of freedom than their rigid ligand counterparts and are therefore able to adopt many conformations, which leads to an increase in the number of

potential products; the crystallisation conditions therefore need to be carefully controlled to drive the process in the desired direction. For example, we have shown that the solution ligand-to-metal ratio influences whether metallocycles or polymeric chains are formed;[31] other factors to consider are the coordination geometry of the metal ion,[32,33] the inorganic counter-ions[34-39] and the solvent system.[40-42] In most cases many reaction conditions need to be screened and the introduction of each new permutation results in an exponential increase in the number of experiments to be carried out. It is therefore essential that a systematic approach is taken to probe the various structure directing factors. It is also important that *all* of the novel products of the various reaction conditions are characterised and entered into a database, not only those adhering to the required design principle. This effectively adds to the population of structures from which valuable statistical data regarding the occurrence of certain structural motifs, intermolecular interactions, coordination environments etc., is extracted - data that could eventually be used to formulate laws of structure prediction that will allow us to design and synthesise targeted compounds at will. Furthermore, novel coordination architectures with unique structures and topologies may lead to materials with interesting and unforeseen properties.

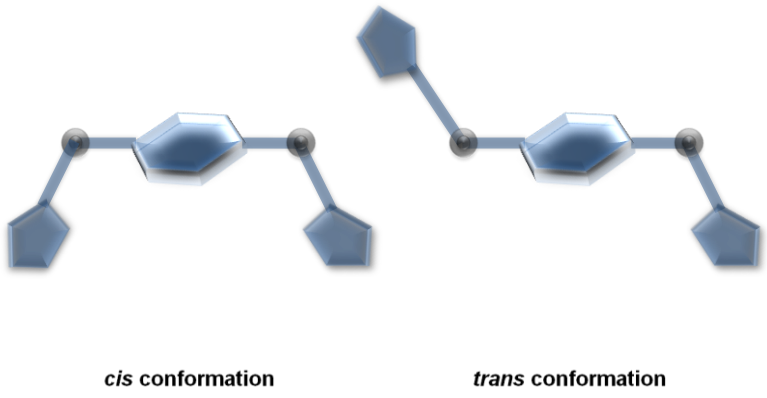

Scheme 3. The two possible conformations of the ditopic imidazole-derived ligands.

As part of our ongoing studies of metal complexes using imidazole derived ditopic ligands, the aim of the current project is to synthesise novel porous materials based on the 0D metallocycle design principle that incorporates ditopic imidazole ligands with rigid aromatic cores and transition metal salts. Six ligands have thus been prepared as part of the present study, namely 2,3,5,6-tetrafluoro-1,4-bis(imidazol-1-yl-methyl)benzene (**L1**),[43] 2,3,5,6-tetrafluoro-1,4-bis(2-isopropylimidazole-1-yl-methyl)benzene (**L2**), 1,3-bis(2-isopropylimidazole-1-yl-methyl)-2,4,6-trimethylbenzene (**L3**), 1,4-bis(4,5-dichloroimidazole-1-yl-methyl)benzene (**L4**), 4,4'-bis(4,5-dichloroimidazole-1-yl-

methyl)biphenyl (**L5**) and 4,4'-bis(2-isopropylimidazol-1-ylmethyl)biphenyl (**L6**) (**Scheme 4**). Each of the six ligands contains an aromatic core analogous to that of a ligand that has already been shown to form metallocycles (see **Scheme 2**), but differs with regard to the imidazole moiety. **L2** – **L6** were synthesised with a view to studying the effect on the resulting structure when bulky substituents are added onto the imidazole rings (i.e. the isopropyl groups on the 2' positions of **L3** and **L6**, and the Cl atoms on the 4' and 5' positions in **L4** and **L5**).

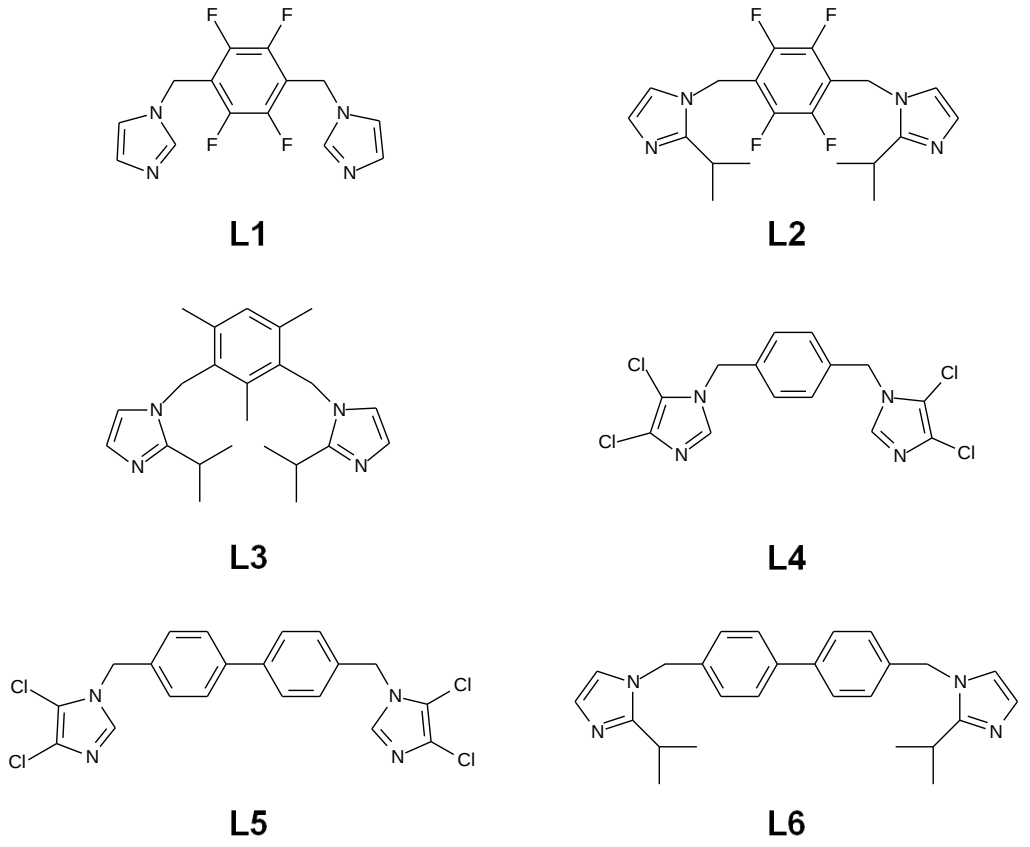

Scheme 4. Ligands synthesised as part of the current study. **(L1)** 2,3,5,6-tetrafluoro-1,4-bis(imidazol-1-yl-methyl)benzene,[43] **(L2)** 2,3,5,6-tetrafluoro-1,4-bis(2-isopropylimidazole-1-yl-methyl)benzene, **(L3)** 1,3-bis(2- isopropylimidazole-1-yl-methyl)-2,4,6-trimethylbenzene, **(L4)** 1,4-bis(4,5-dichloroimidazole-1-yl-methyl)benzene, **(L5)** 4,4'-bis(4,5-dichloroimidazole-1-yl-methyl)biphenyl and **(L6)** 4,4'-bis(2-isopropylimidazol-1-ylmethyl)biphenyl.

The six ligands were reacted with a variety of transition metal cations in a systematic manner; the solution ligand-to-metal ratio was kept constant at 1:1 in all experiments, and only the counter-ion and solvent system were varied. A total of 29 novel crystal structures were obtained under these reaction conditions, and of these five proved to be novel porous 0D metallocycles; the porous metallocycles will be treated separately in Chapter 3 and the

remaining 24 structures will be described in this chapter. To date, no coordination compounds have been obtained with ligands **L5** and **L6** and further discussion will be limited only to compounds containing **L1**–**L4**. Furthermore, Section 2.2.5 describes a modification to the current metallocycle design strategy that could be implemented to increase the probability of obtaining the desired metallocyclic host, and the final section of this chapter outlines a high throughput protocol that could be utilised as a tool to screen multiple reaction conditions rapidly and more efficiently than current methods.

2.2. RESULTS AND DISCUSSION

Ligands **L1**–**L4** were synthesised using a modified literature procedure (see section 2.4.1) and reacted with a variety of transition metal salts; for all non-Ag(I) salts the reactions were carried out in pure MeOH, as well as in mixed solvent systems of DCM/MeOH and DCM/MeCN. All reactions involving Ag(I) salts were carried out in MeOH, MeCN, acetone or DCM/MeOH (these solvent systems were specifically chosen in an attempt to mimic the reaction conditions of the metallocycles reported in the literature). In the single solvent systems 0.03 mmol of the ligand and the metal salt were dissolved in 2–3 mL of the appropriate solvent in separate vials and slowly added together in a 10 mL vial. Crystals suitable for single-crystal X-ray diffraction analysis were then obtained by slow evaporation of the solvent over a period of several days. In the mixed solvent systems diffraction quality crystals were grown by the method of layering: approximately 0.03 mmol of the metal salt was dissolved in 3 mL of either MeOH or MeCN. This solution was then carefully layered upon a solution of 0.03 mmol of the ligand dissolved in 2 mL of DCM – after several days crystals formed at the interface of the two solvent layers. The 24 novel crystal structures have been grouped by ligand and an outline of the reaction conditions used in each experiment is provided in a table at the beginning of each section. A typical entry contains three sections of information: the metal salt used in the reaction, the solvent system and a descriptor symbol for the nature of the product obtained in each vial (the key to these symbols is given in **Table 1** as well as at the bottom of each individual table). The crystallographic data and details of the structure solution and refinement procedures for **1**–**24** are given in **Table 21** at the end of the chapter. Powder X-ray diffraction patterns were measured for each of the bulk microcrystalline materials obtained in the reaction vials of **1**–**24** and compared to the simulated powder pattern from

the single-crystal structures (all diffractograms can be found in Appendix B). In most cases the single-crystal structure was representative of the bulk material; however, in a few instances several peaks corresponding to other minor phases were also present – this is not surprising, given the flexible nature of the ligands. Structures containing solvent were subjected to thermogravimetric analysis (TGA) to determine if single crystals of the solvent-free phase could be obtained; the results of the thermal analysis will be discussed in the text and the thermograms can be found in Appendix C.

Table 1. A key to the description of the nature of the products obtained in the reaction vials.

Symbol	Description
1–24	a single-crystal structure was obtained of the metal–organic complex
a	only precipitate formed in the vial
b	only polycrystalline material formed in the vial
c	unit cell measured and found to match that of the free ligand
d	unit cell measured and found to match that of the metal salt
e	single crystals formed that were too small for SCD
-	no reaction set up

2.2.1. Single-crystal structures obtained with ligand L1

Table 2. Reaction conditions used in the preparation of metal-organic complexes with Ag(I) salts and **L1**.

Metal salt	MeOH	MeCN	Acetone	DCM/MeOH
$AgNO_3$	**1_{MeOH}** – metallocycle 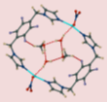 Structure in Chapter 3	**1_{MeCN}** – metallocycle 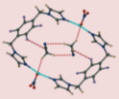 Structure in Chapter 3	**1_{AC}** – metallocycle 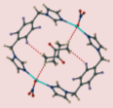 Structure in Chapter 3	**a**
$AgBF_4$	**1** – 1D chain 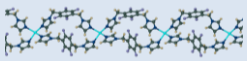	**a**	**2_{AC}** – metallocycle 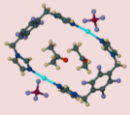 Structure in Chapter 3	**a**
$AgPF_6$	**a**	**2** – 1D strand 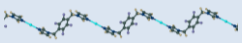	**3** – 1D strand 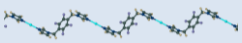	**a**
$AgSbF_6$	**a**	**a**	**a**	**a**

Table 3. Reaction conditions used in the preparation of metal-organic complexes with all non-Ag(I) salts and **L1**.

Metal salt	MeOH	DCM/MeOH	DCM/MeCN
$CdCl_2 \cdot 2.5H_2O$	**4** – 2D net 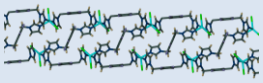	**a**	**b**
$CdBr_2$	**b**	**a**	**5** – 2D net 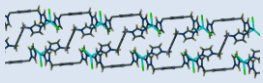
CdI_2	**e**	**a**	**6** – 1D strand 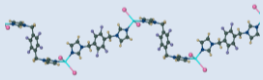
$Cd(NO_3)_2 \cdot 4H_2O$	**7** – 2D layer 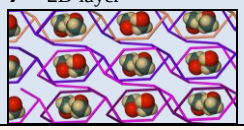	**b**	**a**
$CoCl_2$	**b**	**a**	**b**
$CoBr_2$	**e**	**a**	**a**
$Co(NO_3)_2 \cdot 6H_2O$	**b**	**b**	**8** – 2D grid 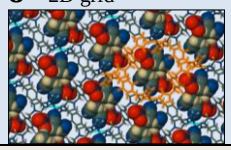
$CuCl_2$	**a**	**a**	**a**
$CuBr_2$	**b**	**a**	**a**
$Cu(NO_3)_2 \cdot 3H_2O$	**b**	**a**	**a**
$MnCl_2$	**b**	**b**	**b**
$Mn(NO_3)_2 \cdot 4H_2O$	**9** – 1D chain 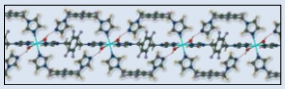	**a**	**10** – 2D layer 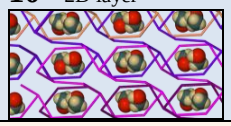
$NiCl_2$	**b**	**b**	**b**
$Ni(NO_3)_2 \cdot 6H_2O$	**b**	**d**	**c**
$ZnCl_2$	**b**	**a**	**b**
$Zn(NO_3)_2 \cdot 4H_2O$	**b**	**e**	**b**

2.2.1.1. $\{[AgL1]BF_4\}_n$ (1)

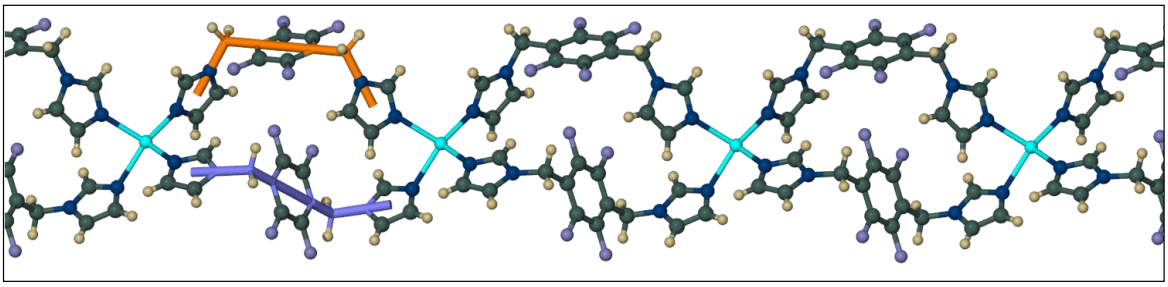

Figure 1. Ball-and-stick representation of the cationic 1D chain formed in **1**; the thick orange and blue lines emphasise the respective *cis* and *trans* conformations of the two crystallographically unique ligand **L1** molecules within the chain. Counter-ions have been omitted for clarity.

The asymmetric unit (ASU) of **1** contains one silver centre, two **L1** molecules and one BF_4^- anion disordered over two positions with site occupancy factors of 0.6 and 0.4 for the two positions. The two **L1** ligands adopt the *cis* and *trans* conformations and serve to bridge the metal centres to one another to form a 1D chain parallel to [001] (**Figure 1**); each silver centre is thus coordinated to four ligands and adopts a distorted tetrahedral coordination geometry (coordinating angles range from 93.44(4)° – 133.33(4)°). The disordered tetrafluoroborate anions lie between the chains and are associated with the cationic chains *via* several C–H···F hydrogen bonds.

2.2.1.2. $\{[AgL1]PF_6\}_n \cdot 2nCH_3CN$ (2)

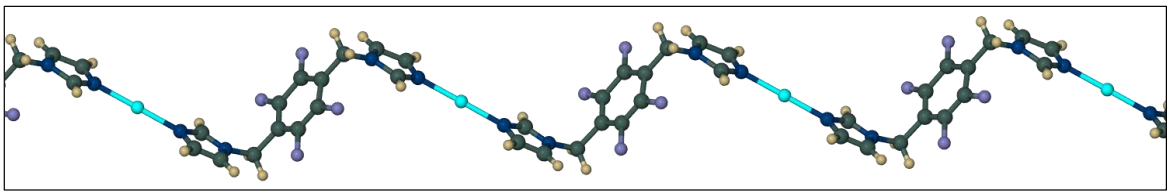

Figure 2. Ball-and-stick representation of the cationic 1D strand formed by **2**. Solvent molecules and counter-ions have been omitted for clarity.

The ASU of **2** consists of half a metal ion, half a **L1** molecule, half a PF_6 anion and one acetonitrile molecule. The Ag(I) ions are linearly coordinated by two imidazole nitrogen atoms from separate ligands, with a corresponding N–Ag–N angle of 179.4(2)°. An infinite zig-zag 1D polymeric strand running parallel to [11-1] is formed in which the metal centres are connected to one another by means of a single ligand in the *trans* conformation (**Figure 2**). **Figure 3** shows one strand is offset slightly from adjacent strands, thus creating pockets filled with the acetonitrile molecules. These pockets are

visible when the packing arrangement is viewed along [001]. The strands are aligned such that imidazole rings between adjacent strands are oriented in an offset face-to-face manner and centroid-to-centroid separations of 3.468 Å indicate the presence of π–π stacking interactions along [010]. The PF_6^- anions are located between 1D strands in the direction of the crystallographic *c* axis and interact with the polymeric strands through C–H···F hydrogen bonds involving methylene and imidazole hydrogen atoms. Thermal analysis of **2** reveals that loss of solvent occurs as a single step process from room temperature to *ca.* 90 °C, with a corresponding weight loss percentage of 9.9% – a value of 12.7% is expected for the loss of the solvent molecules. Such a large discrepancy in these two values can be attributed to the fact that the crystals had been removed from the mother liquor and had been exposed to atmospheric conditions for several days before the TGA was carried out.

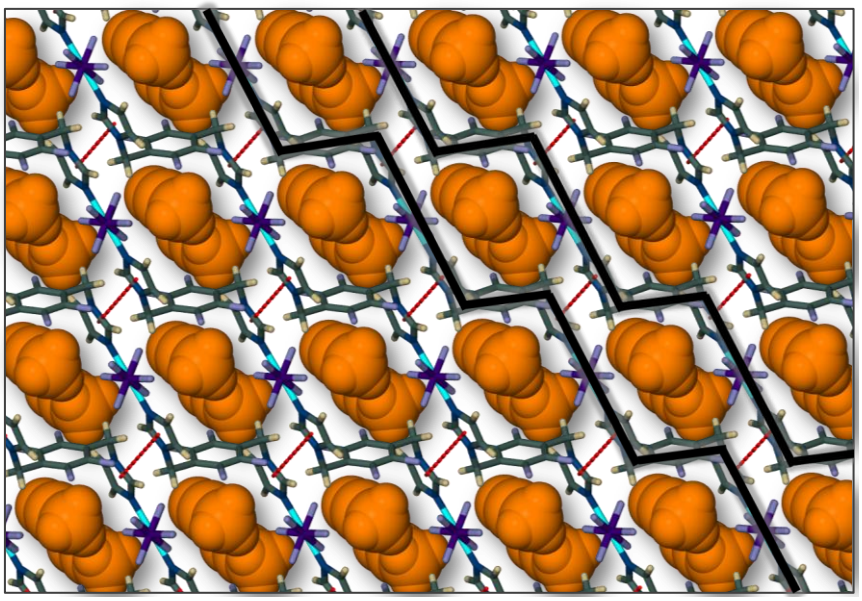

Figure 3. Capped-stick packing arrangement of the solvent-filled pockets created by the association of the 1D strands in **2**. Solvent molecule are shown as orange molecules in van der Waals representation. The thick black lines are shown to emphasise the zig-zag character of the strands. π–π stacking interactions are shown as red fragmented lines between the centroids of the imidazole rings.

2.2.1.3. $\{[AgL1]PF_6\}_n \cdot n(CH_3)_2CO$ (3)

The ASU of **3** consists of one metal ion, two independent half molecules of **L1**, each located on an inversion centre, two independent half molecules of PF_6^-; each situated on an inversion centre and an acetone molecule. The packing of **3** is highly reminiscent of **2** (**Figure 4**) in that zig-zag 1D strands are formed that associate by means of π–π stacking interactions between imidazole rings (centroid separation = 3.487 Å). The PF_6^- anions can

also be found in a similar environment in **3** as they are in **2** i.e. between 1D strands in the direction of the crystallographic *c* axis, and interacting with the polymeric strands through C–H···F hydrogen bonds. Only a few single crystals of **3** were harvested from the reaction vial and these did not prove to be sufficient for thermal analysis.

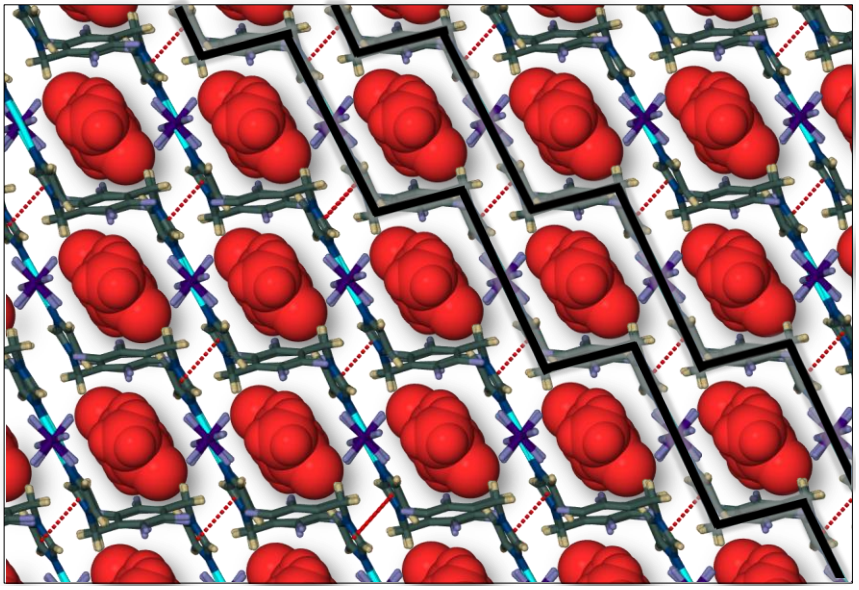

Figure 4. Capped-stick packing arrangement of the solvent-filled pockets created by the association of the 1D strands in **3**. Solvent molecules are shown as red molecules in van der Waals representation. The thick black lines emphasise the zig-zag character of the strands. π–π stacking interactions are shown as red fragmented lines between the centroids of the imidazole rings.

2.2.1.4. $\{Cd(L3)_{1.5}Cl_2\}_n$ (4)

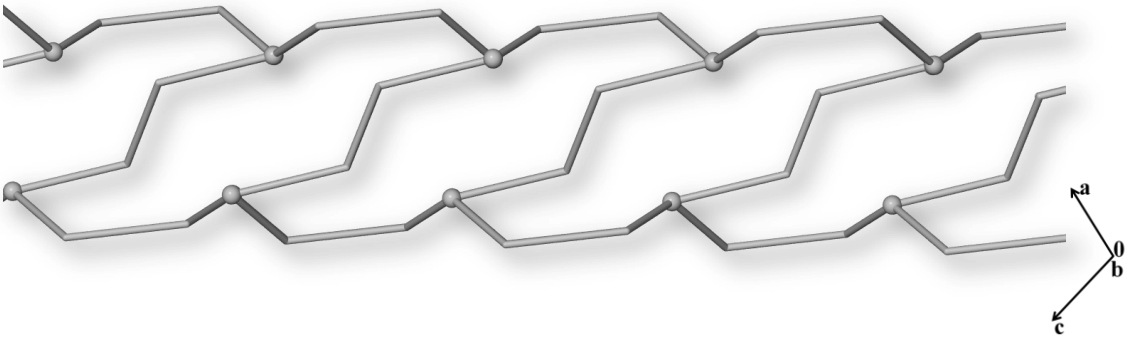

Figure 5. A schematic projection of the 2D nets formed in **4** viewed along [010]; Cd atoms are shown as grey spheres and the ligands connecting the Ag(I) centres to one another are represented as grey pipes.

The ASU of **4** consists of a Cd(II) centre, two ligated chloride ions, one complete ligand in the *cis* conformation and one half of a ligand – the second half of this ligand is generated by inversion symmetry and the ligand thus adopts the *trans* conformation. Each Cd(II)

centre is coordinated by two chloride ions and three imidazole groups in a trigonal bipyramidal coordination environment: the two chloride ions (Cd–Cl = 2.5274(5) and 2.4892(5) Å) and a nitrogen atom from an imidazole group (Cd–N = 2.284(2) Å) occupy the equatorial positions, and the apical positions are occupied by nitrogen atoms from the remaining imidazole groups (Cd–N = 2.349(2) and 2.308(2) Å). The ligands in the *cis* conformation serve to link the metal centres to one another along [101], whilst the ligands in the *trans* conformation link the metal ions to one another along [1-23] and, as such, the structure forms a 2D net; **Figure 5** shows a schematic of the net as viewed parallel to the plane of propagation. The nets stack one on top of another, as shown in **Figure 6**, and the aryl cores of each net are aligned. However, the distance between the centroids (5.16 Å) is too great for this to be considered π–π stacking.

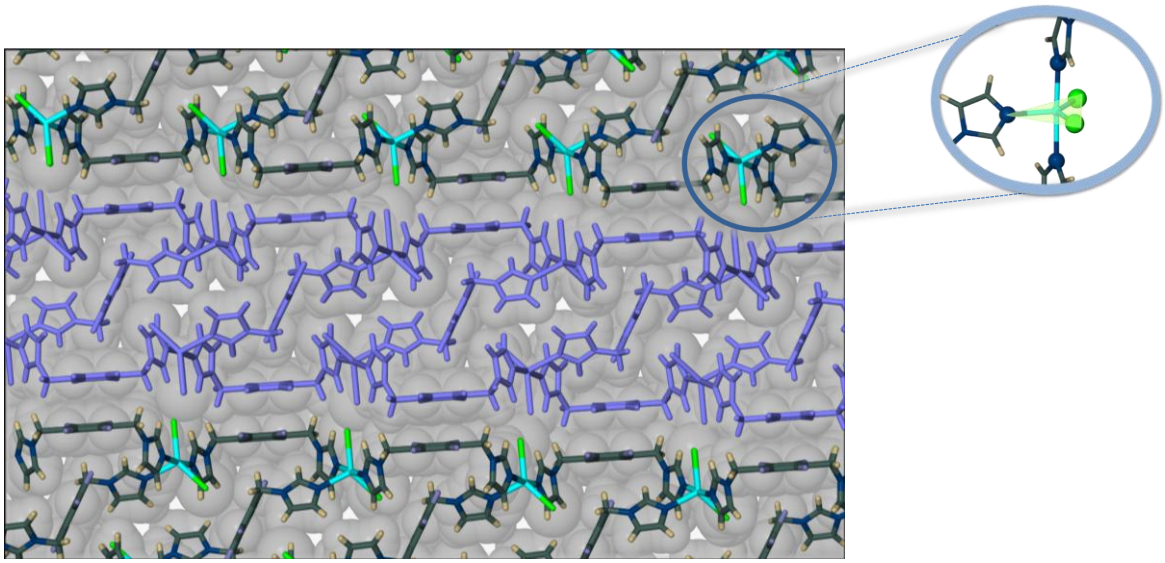

Figure 6. Packing arrangement of **4** as viewed along [010]. A capped-stick representation has been superimposed on a space-filled representation of the molecules to convey the connectivity of the atoms as well as the space filling of the packing arrangement. A single 2D net has been coloured blue for clarity and the insert to the right of the image is of the immediate environment around a Cd(II), which has been oriented to bring the trigonal bipyramidal coordination environment into full view– coordinated atoms are shown as spheres (chloride anions in green and nitrogen atoms in blue).

2.2.1.5. $\{Cd(L3)_{1.5}Br_2\}_n$ (5)

The structure of **5** is similar to that of **4**; indeed, the unit cell parameters and space group are sufficiently similar that **4** and **5** can be considered to be isostructural (in a non-rigorous sense) (see **Table 21**), and a packing diagram is therefore not provided. The unique coordination distances are Cd–Br = 2.6100(5) and 2.5839(4) Å and Cd–N = 2.273(3) Å for

the atoms occupying the equatorial positions and Cd–N = 2.350(3) and 2.399(3) Å for the two apical coordination sites.

2.2.1.6. $\{CdL1I_2\}_n$ (6)

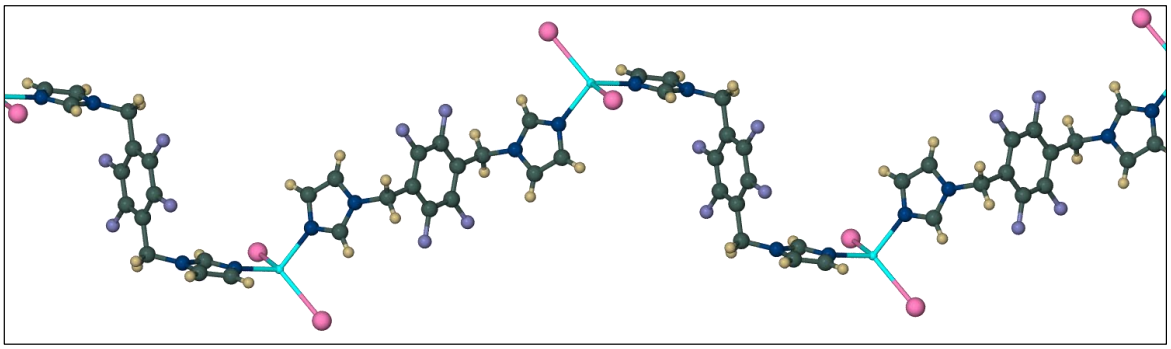

Figure 7. Ball-and-stick representation of the 1D strands formed in **6**.

The ASU of **6** consists of one Cd(II) ion, two independent half molecules of **L1**, each located on an inversion centre, and two ligated iodine atoms. Both of the ligands adopt the *trans* conformation and link successive metal centres to one another along [0-21] to form a 1D strand (**Figure 7**). Each Cd(II) ion is in a tetrahedral coordination environment and is coordinated by two nitrogen atoms from separate ligands and two iodide ions (see **Table 4**). One of the ligated iodine atoms accepts a hydrogen bond from an adjacent strand ($C_{donor}\cdots I_{acceptor}$ = 3.868(4) Å) to connect the 1D strands into an open 2D grid in the (001) plane (**Figure 8**). The grids stack one on top of another in an offset ...*ABCD*... fashion; i.e. the atoms of the first layer are directly placed over the atoms of the fifth layer and as a result, the vertices of one grid align with the voids of the grid directly below, thereby negating the potential for porosity.

Table 4. Selected geometric parameters for **6** (Å, °).

Complex **6**			
Cd–I1	2.7111(5)	Cd–N1	2.246(3)
Cd–N3	2.217(3)	Cd1–I2	2.7350(5)
N3–Cd1–N1	105.83(1)	N3–Cd1–I2	115.65(9)
N3–Cd1–I1	105.15(9)	N1–Cd1–I2	98.61(9)
N1–Cd1–I1	107.07(9)	I1–Cd1–I2	122.84(2)

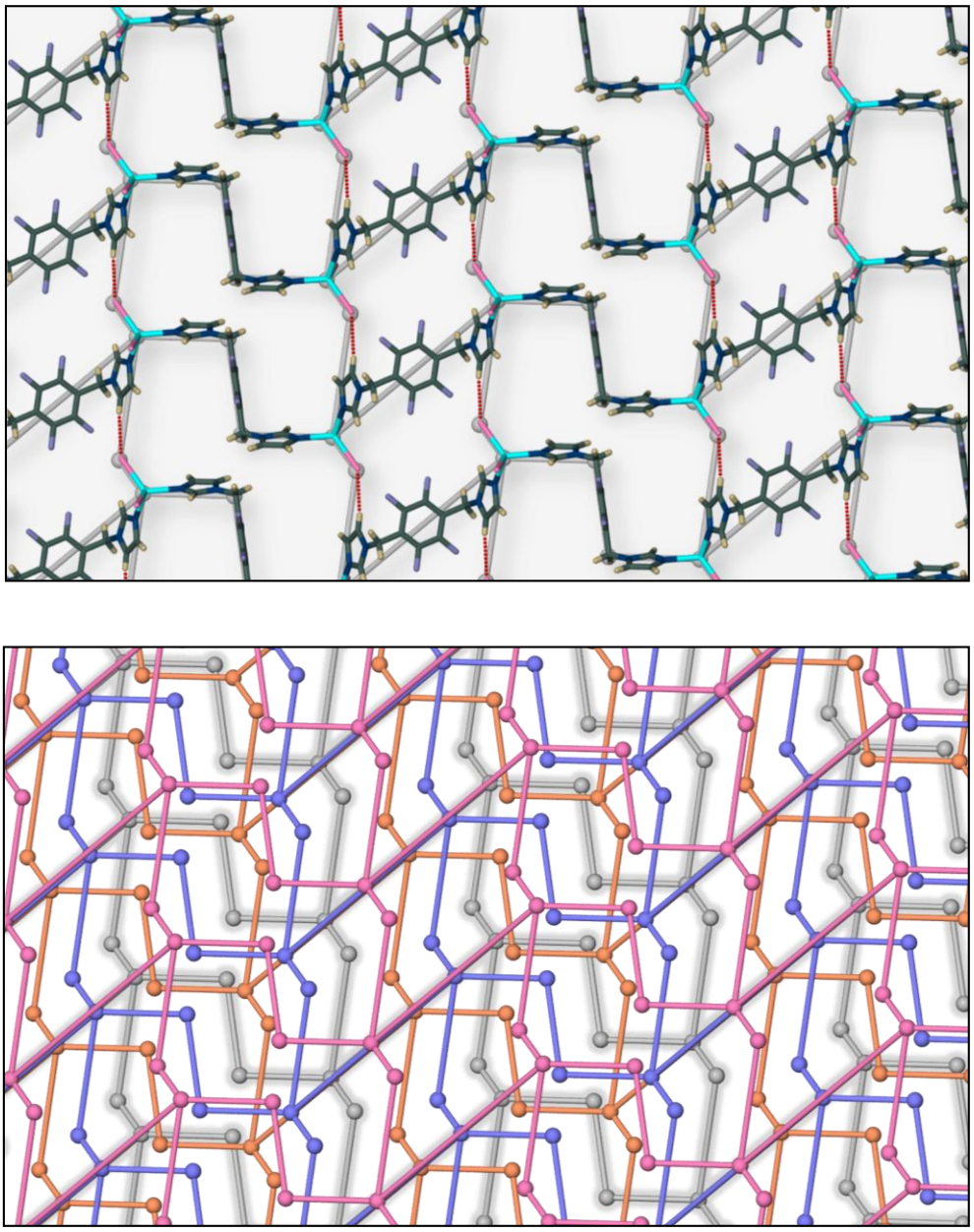

Figure 8. (Top) Packing arrangement of the 2D grid formed by **6** as viewed perpendicular to (001); a simplification of the grid is superimposed on a capped-stick representation of the grid. Hydrogen bonds are shown as red fragmented lines. **(Bottom)** A schematic representation of the ...*ABCD*... packing of the 2D grids in **6** as viewed perpendicular to (001); the individual grids are coloured pink, grey, orange and blue to distinguish them from one another. Nodes are shown as spheres and connections are indicated as pipes.

2.2.1.7. $\{Cd(L1)_{1.5}(\mu\text{-}NO_3)_2\}_n \cdot nCH_3OH$ (7)

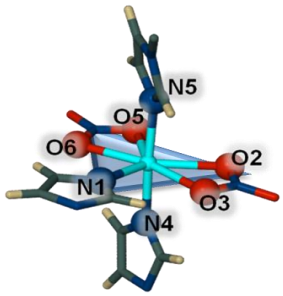

Figure 9. The pseudo-trigonal bipyramidal coordination environment of the Cd(II) centres in **7**. Coordinated atoms are shown as spheres.

The ASU of **7** consists of one Cd(II) centre, one complete ligand in the *cis* conformation and one half of a ligand (the second half of this ligand is generated by inversion symmetry and thus the ligand adopts a *trans* conformation), two nitrate anions and one methanol molecule. Each Cd(II) centre is 7-coordinate and coordinates to two bidentate nitrate anions and three **L1** ligands in a pseudo-trigonal bipyramidal coordination environment; the two bidentate nitrate anions and one imidazolate nitrogen occupy the vertices of a trigonal planar arrangement and the remaining two imidazole groups occupy the apical positions (see **Table 5** for the geometric coordination parameters) (**Figure 9**). Two *cis* ligands and one *trans* ligand serve to connect three metal centres into an S-shaped complex that propagates perpendicular to the *ac*-plane to form a canted 'hour-glass' shaped 2D layer.

Table 5. Selected geometric parameters for **7** (Å, °).

Complex **7**			
Cd–N1	2.302(3)	Cd–N4^{i}	2.246(3)
Cd–N5	2.239(3)	Cd1–O2	2.482(3)
Cd1–O3	2.460(3)	Cd1–O5	2.495(3)
Cd1–O6	2.485(3)		
N5–Cd1–N4^{i}	172.0(1)	N4^{i}–Cd1–O6	89.4(1)
N5–Cd1–N1	91.9(1)	N1–Cd1–O6	81.3(9)
N4^{i}–Cd1–N1	95.7(1)	O3–Cd1–O6	164.0(9)
N5–Cd1–O3	95.7(1)	O2–Cd1–O6	143.48(8)
N4^{i}–Cd1–O3	87.6(1)	N5–Cd1–O5	84.8(1)
N1–Cd1–O3	83.3(1)	N4^{i}–Cd1–O5	88.3(1)
N5–Cd1–O2	91.1(1)	N1–Cd1–O5	133.0(1)
N4^{i}–Cd1–O2	85.2(1)	O3–Cd1–O5	143.69(9)
N1–Cd1–O2	135.2(1)	O2–Cd1–O5	91.85(9)
O3–Cd1–O2	51.86(9)	O6–Cd1–O5	51.83(8)
N5–Cd1–O6	89.4(1)		

Symmetry code: (*i*) $x - {}^{1}/_{2}, -y + {}^{3}/_{2}, z + {}^{1}/_{2}$.

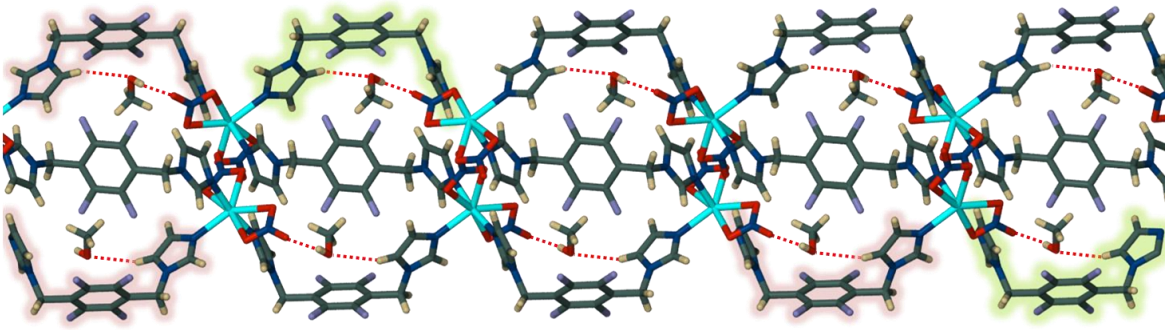

Figure 10. Capped-stick representation of the S-shaped complexes formed in **7**; atoms shown in CPK colours are in the *ac*-plane, green ligands propagate further into the plane and the pink ligands propagate out of the plane. Hydrogen bonds are shown as red fragmented lines.

Figure 10 shows five consecutive S-shaped complexes in the *ac*-plane. The green and pink ligands are shown uncoordinated to provide an unobstructed view but in reality they are coordinated to metal centres into and out of the page respectively (i.e. perpendicular to the *ac*-plane). The methanol molecules are located within the S-shaped conformation of each complex. They are stabilised by hydrogen bonding interactions with an oxygen atom of a ligated nitrate anion ($O_{donor}\cdots O_{acceptor}$ = 3.052(4) Å) and an imidazolate carbon ($C_{donor}\cdots O_{acceptor}$ = 3.533(5) Å). Thus in the 2D model they are located in the bulges of the 'hour-glass' shape. The 2D layers stack one on top of another with adjacent layers related to one another by an *n*-glide operation (**Figure 11**).

Thermal analysis of **7** shows that the sample is stable to *ca.* 270 °C and then rapidly starts to decompose beyond this temperature i.e. the loss of the methanol molecules occurs concurrently with decomposition.

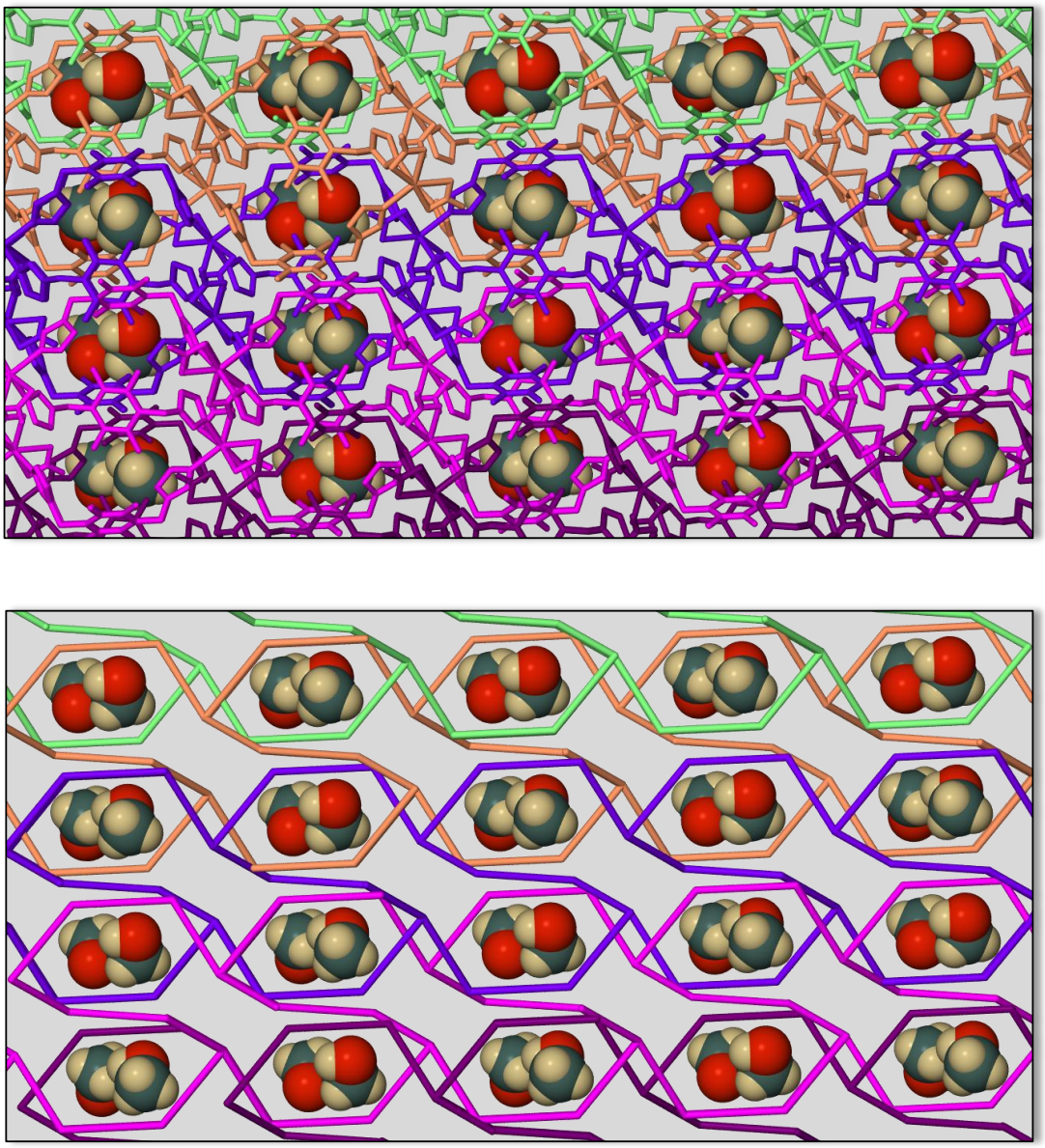

Figure 11. (Top) Capped-stick representation of the packing arrangement of **7** as viewed perpendicular to (010); the 2D layers have been coloured green, orange, violet, pink and mauve to distinguish them from one another. Hydrogen atoms of the ligands have been omitted for clarity and the methanol molecules are shown in space-filled representation. **(Bottom)** Schematic representation of the packing arrangement of **7**; the connections are simplified as pipes in the same colour scheme as above. Solvent molecules are shown in van der Waals representation.

2.2.1.8. $\{[Co(L1)_2(CH_3CN)_2](NO_3)_2\}_n \cdot 2nCH_3CN$ (8)

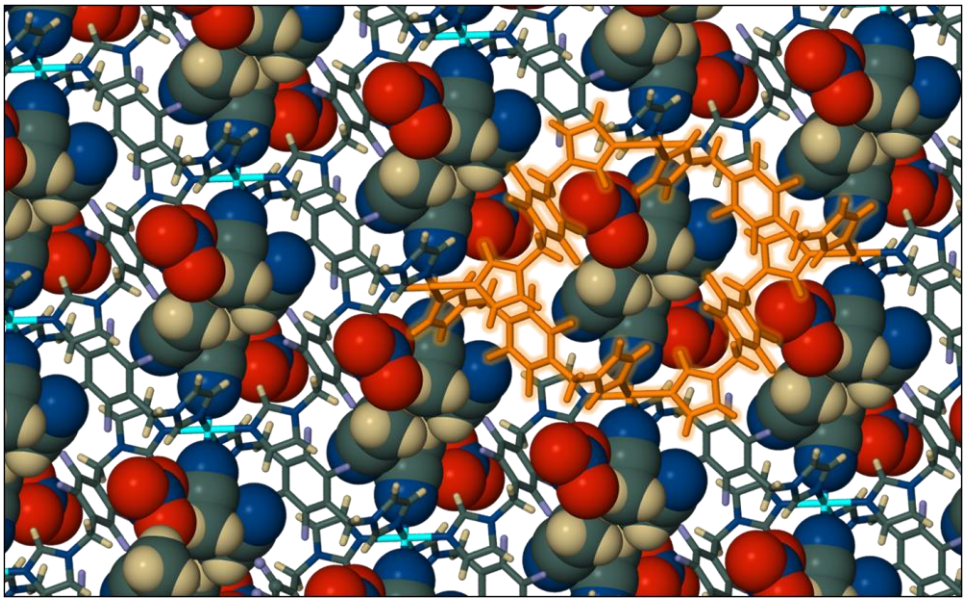

Figure 12. Capped-stick representation of the packing arrangement of **8** to form a 2D grid, as viewed down [100]. A single unit of the grid is highlighted in orange for clarity; solvent molecules and nitrate anions are shown in van der Waals representation within the apertures of the grid.

The ASU of **8** contains a Co(II) centre, a nitrate anion, a ligated acetonitrile molecule, a lattice acetonitrile molecule and two independent half molecules of **L1**, each located on an inversion centre – the two ligands thus adopt the *trans* conformation. Each cobalt ion is in an octahedral coordination environment; two symmetry-related acetonitrile molecules occupy the apical positions (Co–N = 2.149(1) Å) and two unique imidazole groups occupy the equatorial positions, with the remaining two positions generated by symmetry (Co–N = 2.110(1) and 2.126(1) Å). The Co(II) ions thus act as 4-connected nodes and propagation from these centres results in the formation of an open 2D grid in the (100) plane (**Figure 12**). The apertures of the 2D grid accommodate both the ligated and the lattice acetonitrile molecules, as well as the nitrate ions. The solvent molecules and counter-ions all interact with one another and the coordinated imidazole groups through a series of hydrogen bonding interactions, as shown in **Figure 13** (see **Table 6** for hydrogen bonding parameters). Unfortunately, a meaningful TGA could not be obtained for **8** as PXRD analysis indicated the presence of more than one phase in the vial from which single crystals of **8** were harvested.

Table 6. Hydrogen bond geometry for **8** (Å).

D*–H···*A	***D*···*A***
C8–H8···N6	3.464(3)
C9–H9···N6^{i}	3.307(3)
C17–H17C···O2^{ii}	3.290(3)
C15–H15A···O1	3.298(3)

Symmetry codes: (*i*) -*x* + 1, -*y*, -*z*; (*ii*) -*x* + 2, -*y* + 1, -*z*.

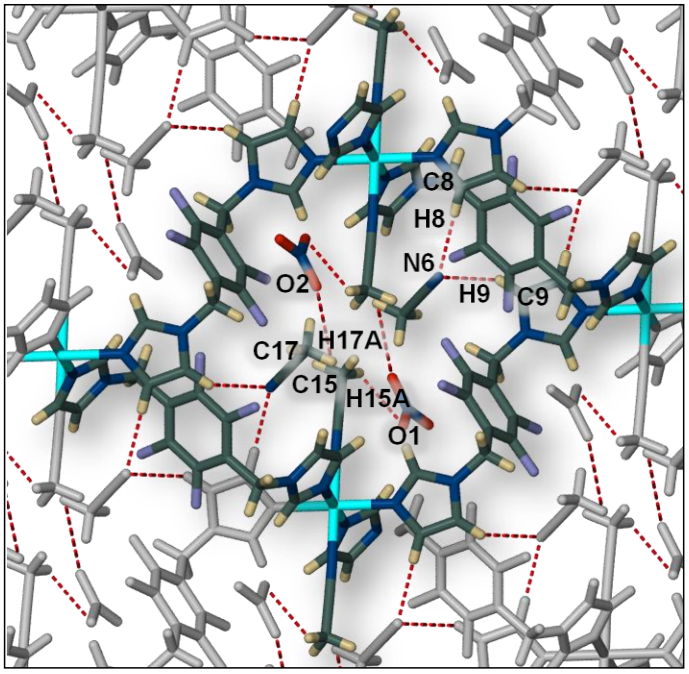

Figure 13. Capped-stick representation of the hydrogen bonding interactions evident in the structure of **8**. A single component of the 2D grid is shown in CPK colours and the remaining molecules are shown in grey; hydrogen bonds are indicated as dashed red lines.

2.2.1.9. {[Mn(L1)$_3$(H$_2$O)$_2$](NO$_3$)$_2$}$_n$·nH$_2$O·nCH$_3$OH (9)

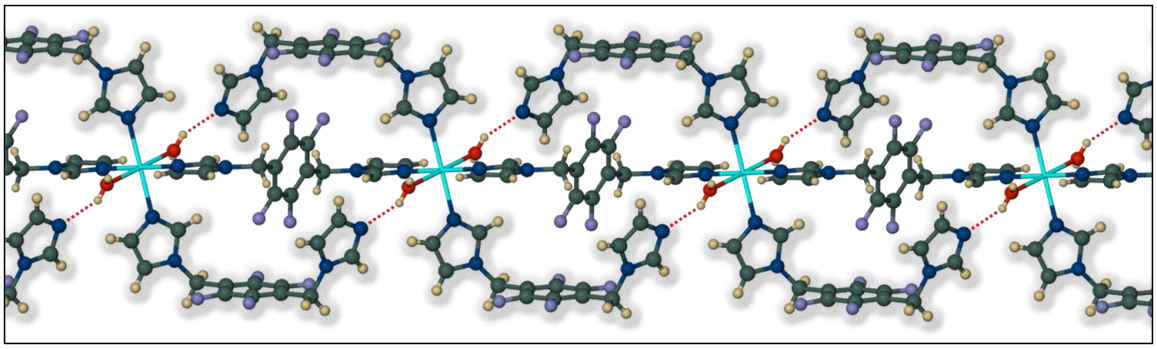

Figure 14. Ball-and-stick representation of the 1D chain formed in **9**; **L1** molecules in the *cis* conformation are highlighted in grey. Hydrogen bonds are shown as red fragmented lines and lattice solvent molecules and nitrate anions are omitted for clarity.

The ASU of **9** consists of a Mn(II) ion situated on an inversion centre, one nitrate anion, a ligated water molecule, a partially occupied water molecule (SOF = 0.5), a partially occupied methanol molecule (SOF = 0.5), one complete ligand **L1** in the *cis* conformation and one half of a ligand **L1** – the second half of this ligand is generated by inversion symmetry and the ligand thus adopts a *trans* conformation. In the structure of **9** the two lattice solvent molecules cannot co-exist as they are located on equivalent sites; either the water molecule is present or the methanol molecule is present. The manganese ions are in an octahedral coordination environment: imidazole groups are situated at the vertices of the square plane (unique Mn–N = 2.239(1) and 2.279(1) Å) and the apical positions are occupied by ligated water molecules (Mn–O = 2.186(1) Å). The *cis* and *trans* ligands assume two distinct roles in connecting successive Mn(II) ions to one another to form a 1D chain running parallel to [111]; a single ligand in the *trans* conformation is coordinated to Mn(II) ions at both ends of the ligand and thus serves to directly link the manganese centres to one another (...Mn–**L1**$_{trans}$–Mn...), whilst the *cis* ligands are only coordinated to the Mn(II) centres at one end of the ligand – the second imidazole moiety is hydrogen bonded to the ligated water molecule ($O_{donor}\cdots N_{acceptor}$ = 2.740(2) Å) and by virtue of symmetry the Mn(II) centres are additionally, but indirectly, linked to one another by a double stranded ligand/water hydrogen bonded motif (...Mn–$H_2O\cdots$**L1**$_{cis}$–Mn...) (see **Figure 14**). The 1D chains are connected to one another in 3D through a system of hydrogen bonding interactions between the ligated water molecules, the nitrate anions and the lattice solvent molecules. The structure of **9** is highly reminiscent of a structure obtained previously[43] by the reaction of $Cd(NO_3)_2$ and **L1** in methanol (CSD refcode – **ECALOK**) and differs only in the respect that both water and methanol molecules are present in **9**, whereas only lattice water molecule is evident in the Cd(II) structure; aside from this difference the unit cell parameters and space group are sufficiently similar such that the two could be considered isostructural in a non-rigorous sense. We were unable to obtain a TGA for complex **9** as only a few single crystals were harvested from the reaction vial and these did not prove to be sufficient for thermal analysis.

2.2.1.10. $\{Mn(L1)_{1.5}(\mu\text{-}NO_3)_2\}_n \cdot nCH_3CN$ (10)

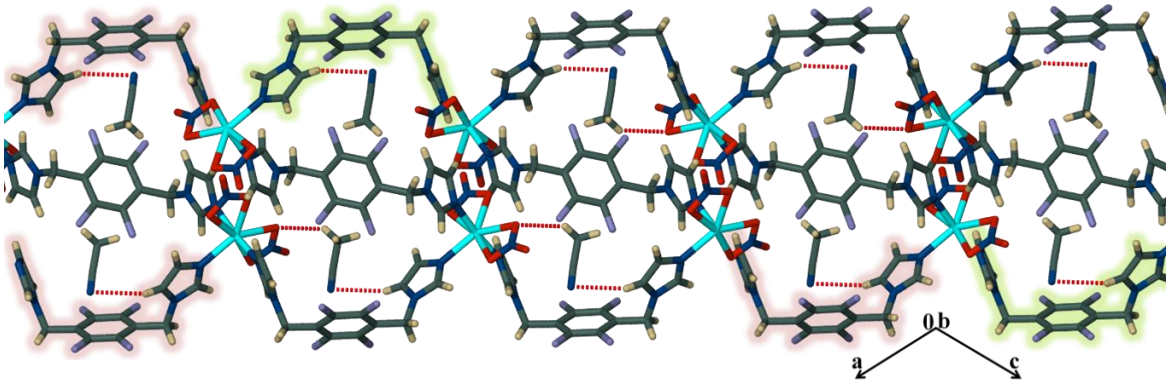

Figure 15. Capped-stick representation of the S-shaped complexes formed in **10**; atoms shown in CPK colours are in the *ac*-plane, green ligands propagate further into the plane and the pink ligands propagate out of the plane. Hydrogen bonds are shown as red fragmented lines.

The structure of **10** is similar to that of **7** (see unit cell parameters in **Table 21**), but differs in that the metal cation is Mn(II) and not Cd(II) (see **Table 7** for the unique coordination geometric parameters) and an acetonitrile molecule, rather than a methanol molecule, is located within the S-shaped conformation of each complex. As in **7**, the solvent molecule is stabilised by hydrogen bonding interactions with an oxygen atom of a ligated nitrate anion ($O_{donor}\cdots C_{acceptor}$ = 3.326(5) Å) and an imidazolate carbon ($C_{donor}\cdots N_{acceptor}$ = 3.606(4) Å). The packing arrangement of **10** is similar to that of **7** and a packing diagram is therefore not provided. The TGA trace of **10** indicates that the sample rapidly loses solvent from room temperature to *ca* 80 °C. A theoretical weight loss percent of 5.9% is expected for the loss of one molar equivalent of acetonitrile per metal centre and an experimental value of 5.4% was obtained; as some solvent is already lost at ambient temperature this discrepancy can be attributed to the time taken for the sample to be loaded into the TGA instrument.

Table 7. Selected geometric parameters for **10** (Å, °).

Complex **10**			
Mn–N1	2.235(2)	Mn–N4^{i}	2.193(2)
Mn–N5	2.193(2)	Mn–O2	2.308(2)
Mn–O4	2.392(2)	Mn–O5	2.495(3)
Mn–O6	2.485(3)		
N5–Mn1–N4^{i}	174.99(7)	N4^{i}–Mn1–O1	90.86(7)
N5–Mn1–N1	93.08(7)	N1–Mn1–O1	136.96(6)
N5–Mn1–O2	93.18(7)	O3–Mn1–O1	54.99(5)
N4^{i}–Mn1–O2	89.69(7)	N5–Mn1–O4	86.93(6)
N1–Mn1–O2	82.05(6)	N4^{i}–Mn1–O4	91.35(7)
N5–Mn1–O5	85.37(6)	N1–Mn1–O4	83.07(6)
N4^{i}–Mn1–O5	89.81(7)	O3–Mn1–O4	165.10(5)
N1–Mn1–O5	137.26(7)	O2–Mn1–O4	54.19(5)
O3–Mn1–O5	140.69(6)	O6–Mn1–O4	139.82(5)
N5–Mn1–O1	87.44(6)		

Symmetry code: (*i*) $x - {}^{1}/_{2}, -y + {}^{1}/_{2}, z + {}^{1}/_{2}$.

2.2.1.11. Comparison of the crystal structures obtained for L1

A total of 15 single-crystal structures of transition metal coordination complexes containing **L1** were obtained. Analysis of the Ag(I)-containing structures reveals a number of interesting features. In $\mathbf{1_{MeOH}}$, $\mathbf{1_{MeCN}}$, $\mathbf{1_{AC}}$ and $\mathbf{2_{AC}}$ the ligand adopts a *cis* conformation, which leads to the formation of metallocyclic structures (see Chapter 3), whereas in **2** and **3** the ligand adopts a *trans* conformation and 1D polymeric strands are formed. It is noteworthy that despite the difference in the conformation of the ligand in these two sets of compounds, the preferred linear coordination geometry of the Ag(I) ion is preserved in all cases.[44] In addition, the role of the solvent appears to be different in the two classes of compounds; for the metallocycles it presumably serves as a template for the formation of the dinuclear discrete structures, and in **2** and **3** it performs a space-filling role as the molecules are located in pockets between the stacking of the zig-zag 1D strands. The structures **2** and **3** differ only with respect to the identity of the solvent, i.e. acetonitrile in **2** and acetone in **3** and are therefore considered solvates. In contrast, the Ag(I) ion is in a tetrahedral coordination environment in **1** and the ligand assumes both the *cis* and *trans* conformations in connecting successive Ag centres to one another to form a 1D chain. There are also no solvent molecules present in the lattice of **1**.

Four crystal structures were obtained by the reaction of **L1** and Cd(II) salts; three of these structures (**4**, **5** and **7**) form 2D networks with a solid-state metal:ligand (M:L) ratio of 2:3 and the final structure forms 1D strands with a M:L ratio of 1:1 (complex **6**). It is

interesting to compare the structures obtained from the Cd(II)-halide salts with one another; complexes **4** and **5** are isostructural and were obtained by the reaction of **L1** with $CdCl_2$ and $CdBr_2$, respectively. Both structures feature the Cd(II) in a trigonal bipyramidal coordination environment and propagation from these metal centres by ligands in both the *cis* and *trans* conformation results in the formation of 2D nets. In contrast the reaction of **L1** with the larger CdI_2 facilitates the formation of 1D strands, with the Cd(II)-ions in a tetrahedral coordination environment and connected to one another by a single ligand in the *trans* conformation. It is unclear whether the solvent system is a major driving force in the product formation for these systems as **4** and **5** are isostructural and were obtained using different solvent systems. Furthermore, the structure of **6** is different to that of **4** and **5**, yet it was obtained using the same solvent system as that of **5**. The third Cd(II)-containing 2D network was formed by the reaction of **L1** and $Cd(NO_3)_2$; the nitrate anions coordinate in a bidentate fashion and, along with three imidazole rings, form a pseudo-trigonal bipyramidal coordination environment around the Cd-centres. As a consequence of the bulky nature of the coordinated nitrate anion, the network in **7** is not as densely packed as that of the other 2D structures and an open network is formed which contains methanol molecules located in discrete pockets within the 2D layers – the net comprises ligands in both the *cis* and *trans* conformations.

Complex **10** is similar to **7** (see **Table 21** for the unit cell parameters and space group) and differs only in that Mn(II) ions replace the Cd(II) ions at the centre of the pseudo-trigonal bipyramidal coordination sphere, and acetonitrile molecules, not methanol molecules, are located in the discrete pockets of the framework. A similar situation arises for structure **9** and a structure reported in the literature[43] (CSD refcode : **ECALOK**). In both structures the metal ions are connected to one another by virtue of a single *trans* ligand, as well as a double stranded ligand/water hydrogen bonded motif, to form 1D chains. The structures are almost identical to one another, the major difference being that **9** contains Mn(II) ions and disordered water/methanol lattice solvents and the literature structure contains Cd(II) ions and only lattice water molecules. These four structures pose an interesting question from a classification perspective. The relationship between **7** and **10** is not that of solvato supramolecular isomerism, a term that is interchangeable with "pseudopolymorphic supramolecular isomerism" which is defined as "frameworks constructed from the same molecular components but with different noninteracting guest molecules giving rise to different topologies",[45] owing to the fact that the frameworks are

not comprised of the same building blocks, i.e. Cd(II) ions in **7** and Mn(II) ions in **10**. Furthermore, the two structures cannot be considered isostructural as one contains methanol and the other acetonitrile; however, if the solvent molecules are not taken into account the atomic arrays of the 2D networks of **7** and **10** are superimposable, and therefore isostructural[46] – it has been suggested that the term "isoskeletal" be used to describe this scenario.[47] Similarly, **9** and **ECALOK** can also be considered "isoskeletal" as the host packing of the two structures are superimposable.

The final structure obtained in this series was isolated from a vial containing a nitrate salt. In **8** the ligand molecules assume the *trans* conformation and link the Co(II) ions into an open 2D grid, with the nitrate anions located in the apertures of the grid.

2.2.2. Single-crystal structures obtained with ligand L2

Table 8. Reaction conditions used in the preparation of metal-organic complexes with Ag(I) salts and **L2**.

Metal salt	MeOH	MeCN	Acetone	DCM/MeOH
$AgNO_3$	**a**	**a**	3_{AC} 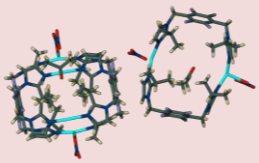 Structure in Chapter 3	**b**
$AgBF_4$	**a**	**a**	**a**	**b**
$AgPF_6$	**a**	**a**	**a**	**b**
$AgSbF_6$	**a**	**a**	**a**	**b**

Table 9. Reaction conditions used in the preparation of metal-organic complexes with all non–Ag(I) salts and **L2**.

Metal salt	MeOH	DCM/MeOH	DCM/MeCN
$CdCl_2·2.5H_2O$	**a**	**a**	**b**
$CdBr_2$	**b**	**b**	**b**
CdI_2	**11** – 1D strand 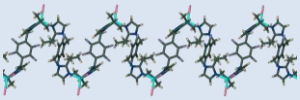	**11**	**11**
$Cd(NO_3)_2·4H_2O$	**c**	**e**	**b**
$CoCl_2$	**b**	**b**	**b**
$CoBr_2$	**b**	**b**	**b**
$Co(NO_3)_2·6H_2O$	**c**	**c**	**a**
$CuCl_2$	**c**	**a**	**a**
$CuBr_2$	**c**	**a**	**a**
$Cu(NO_3)_2·3H_2O$	**c**	**a**	**a**
$MnCl_2$	**c**	**a**	**a**
$Mn(NO_3)_2·4H_2O$	**a**	**b**	**a**
$NiCl_2$	**c**	**b**	**12** – 1D strand 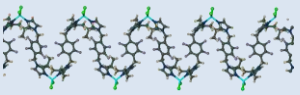
$Ni(NO_3)_2·6H_2O$	**c**	**e**	**b**
$ZnCl_2$	**e**	**b**	**b**
$Zn(NO_3)_2·4H_2O$	**c**	**c**	**b**

2.2.2.1. $\{CdL2I_2\}_n·nCH_3OH$ (11)

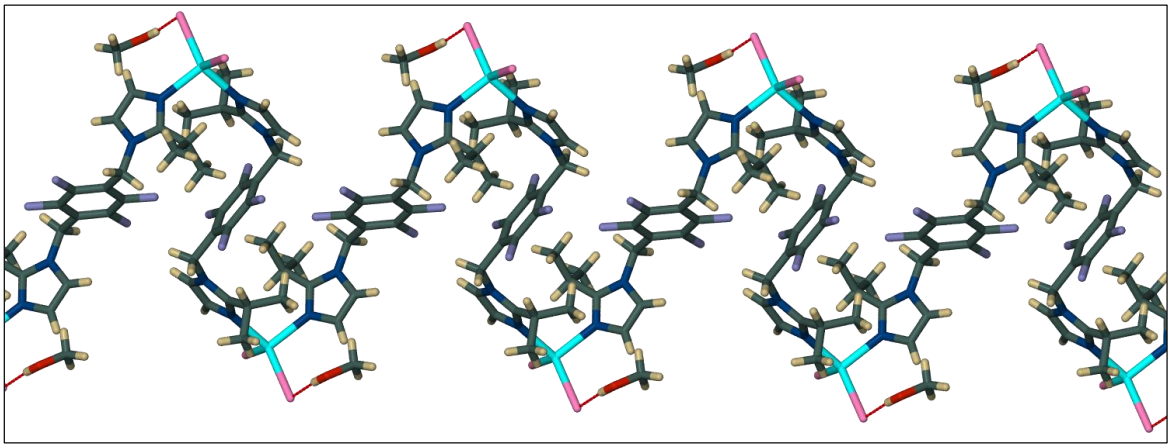

Figure 16. Capped-stick representation of the 1D strands formed in **11**; hydrogen bonds are shown as fragmented red lines. Solvent molecules are omitted to provide an unobstructed view.

The ASU of **11** contains a Cd(II) centre, two ligated iodide anions, two independent halves of **L2** ligands and a methanol molecule; the remaining halves of the **L2** ligands are

generated by inversion symmetry. Both of the ligands adopt the *trans* conformation and serve to link successive metal centres to one another along [001] to form a 1D strand (**Figure 16**). Each Cd(II) ion is thus in a tetrahedral coordination environment and is coordinated by two nitrogen atoms from separate ligands and two iodide ions (coordinating angles range from 100.4(1)° – 120.95(7)°). One of the ligated iodine atoms accepts a hydrogen bond from an isopropyl substituent on an adjacent strand to connect the 1D strands into a corrugated 2D layer in the (010) plane (**Figure 17**). Each methanol molecule is associated by means of a hydrogen bond to a ligated iodine atom (see **Table 10** for hydrogen bonding parameters). The TGA trace of **11** indicates that the sample is stable to *ca.* 280 °C and then rapidly starts to decompose beyond this temperature i.e. the loss of the methanol molecules occurs concurrently with decomposition.

Table 10. Hydrogen bond geometry for **11** (Å, °).

D*–H···*A	***D*···*A***
O1–H1···I1	3.650(6)
C9–H9C···I2^{i}	4.279(5)

Symmetry codes: (*i*) -*x* + 1, -*y* + 1, -*z* + 1.

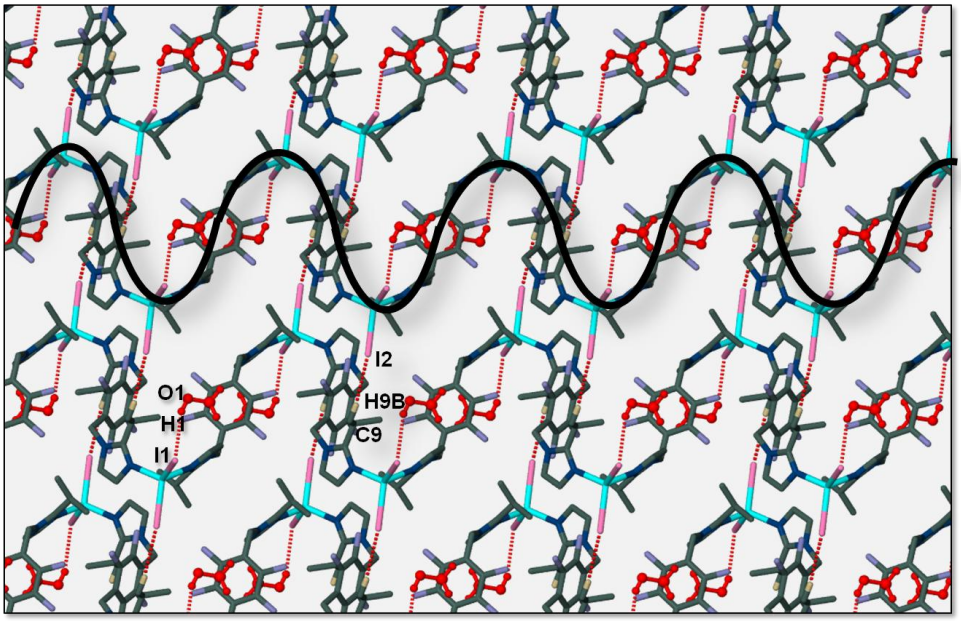

Figure 17. Capped-stick representation of the corrugated 2D layers formed in **11**, as viewed in the (010) plane; the thick black line has been superimposed on a single 1D strand to emphasise the corrugated nature of the layer. Hydrogen atoms not participating in hydrogen bonds have been omitted for clarity and methanol molecules are shown in red in the ball-and-stick metaphor. Atoms participating in hydrogen bonds have been labelled (refer to **Table 10** for hydrogen bonding parameters).

2.2.2.2. $\{NiL2Cl_2\}_n$ (12)

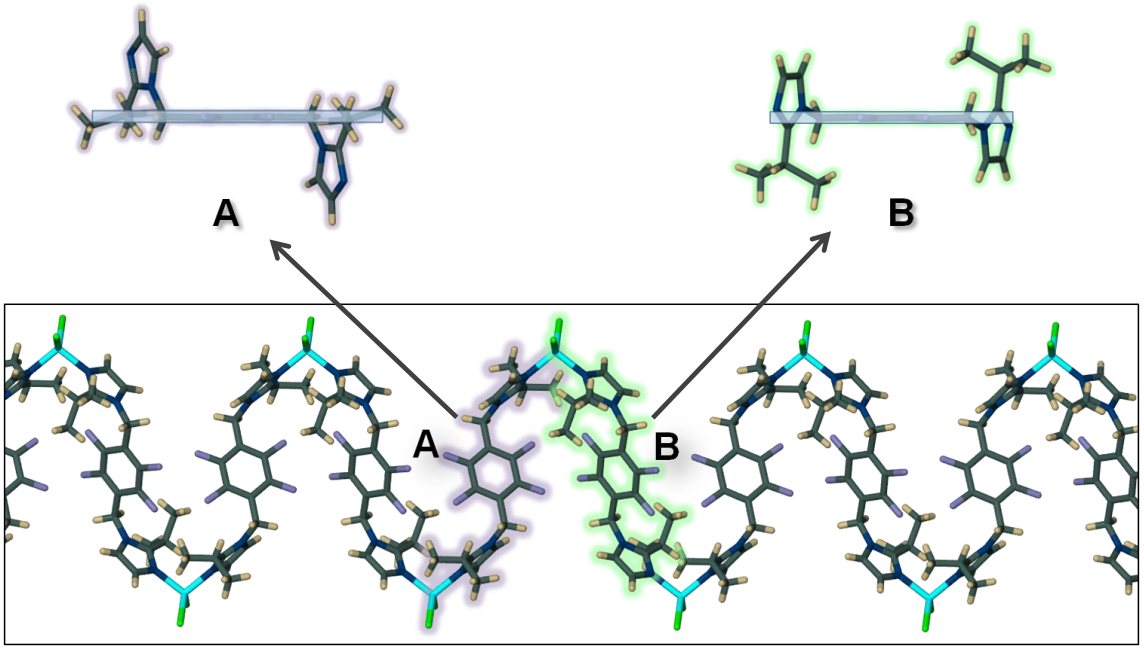

Figure 18. Capped-stick representation of the 1D strands formed in **12** viewed down [11-1], the two unique **L2** molecules, **A** and **B**, have been highlighted in purple and green, respectively. The conformation of the two ligands as a function of the displacement of the imidazole moieties relative to the aryl plane (transparent blue rectangle) are shown above the image.

The ASU of **12** is similar to that of **11** in that it contains a metal centre, two ligated halide anions and two independent halves of **L2** ligand, with the remaining halves generated by symmetry (the two crystallographically unique ligand molecules are labelled **A** and **B**, respectively in **Figure 18**). The ligands are both in the *trans* conformation, however the displacement of the imidazole moieties relative to the aryl plane in ligand **A** is more pronounced than in ligand **B**. The complex also forms 1D strands similar to those of **11** – each metal centre is linked to its neighbour by means of one ligand **L2**, and is in a tetrahedral coordination environment (coordinating angles range from 102.0(3)° – 116.9(2) °). However, in **12** π–π stacking interactions between imidazole rings (centroid–centroid distance = 3.775 and 3.928 Å) link the strands to one another in the formation of a 2D sheet running parallel to (1-10) (**Figure 19**). It must be noted that the data obtained for **12** is not of high quality and an attempt was made to process the data as a non-merohedral twin. Using the program *cell_now* it was determined that the crystal contained two domains (one major and one minor) and the data were processed accordingly, with the final structure converging to an $R1$ = 10.1 %.

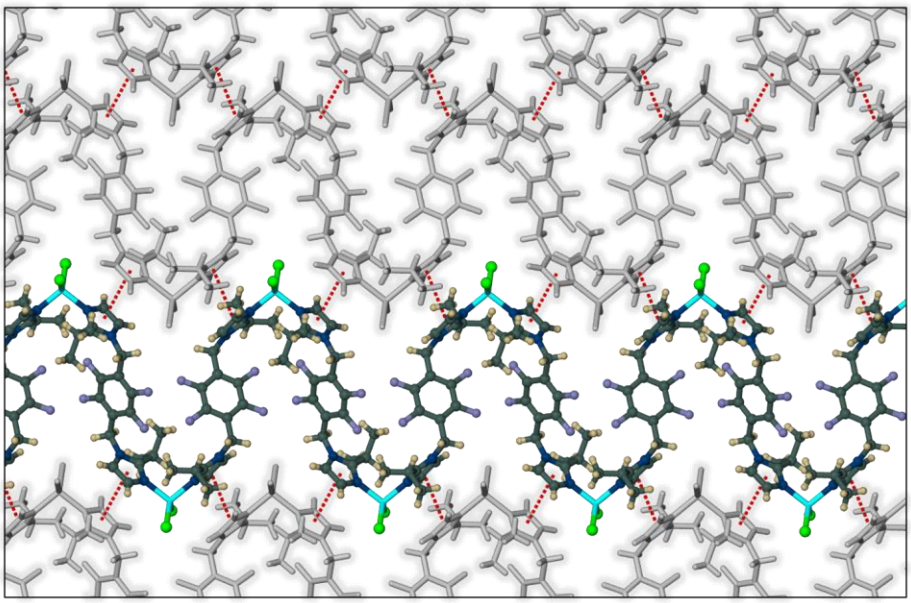

Figure 19. Packing arrangement of **12** to form 2D layers, as viewed perpendicular to (1-10). A single 1D strand has been shown in the ball-and-stick metaphor in CPK colours and the remaining strands are shown as grey capped-sticks; π–π interactions are shown as red fragmented lines between the centroids of neighbouring imidazole rings.

2.2.2.3. Comparison of the crystal structures obtained for L2

It is evident that the conditions of crystallisation of **L2** and transition metal salts need to be explored beyond the experimental approach in this project; only three crystal structures of transition metal complexes were obtained from the conditions outlined in **Table 8** and **Table 9**. In most cases a precipitate formed in the vial or single crystals of the free ligand formed before complexation – this is particularly true for reactions utilising methanol as the reaction solvent. In $\mathbf{3_{AC}}$ the ligand assumes a *cis* conformation and discrete metallocyclic complexes are formed (see Chapter 3). In contrast, both **11** and **12** form 1D polymeric strands with the ligand in the *trans* conformation. The crystal structure of **11** indicates that the 1D strands are linked into a 2D layer *via* the donation of a hydrogen bond from an isopropyl substituent to a ligated iodide ion, whereas π–π stacking interactions between imidazole rings in adjacent strands serve this purpose in the structure of **12**.

2.2.3. Single-crystal structures obtained with ligand L3

Table 11. Reaction conditions used in the preparation of metal-organic complexes with Ag(I) salts and **L3**.

Metal salt	MeOH	MeCN	Acetone	DCM/MeOH
$AgNO_3$	**a**	**a**	**b**	**b**
$AgBF_4$	**a**	**a**	**b**	**c**
$AgPF_6$	**b**	**b**	**a**	**b**
$AgSbF_6$	**b**	**b**	**b**	**b**

Table 12. . Reaction conditions used in the preparation of metal-organic complexes with Ag(I) salts and **L3**.

Metal salt	MeOH	DCM/MeOH	DCM/MeCN
$CdCl_2 \cdot 2.5H_2O$	**c**	**13** – 0D salt 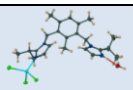	**b**
$CdBr_2$	**b**	**a**	**14** – 1D strand 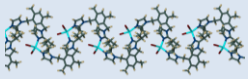
CdI_2	**15** – 1D strand 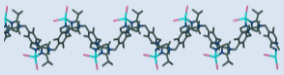	**15**	**b**
$Cd(NO_3)_2 \cdot 4H_2O$	**b**	**a**	**b**
$CoCl_2$	**c**	**a**	**a**
$CoBr_2$	**a**	**a**	**a**
$Co(NO_3)_2 \cdot 6H_2O$	**a**	**a**	**a**
$CuCl_2$	**b**	**a**	**a**
$CuBr_2$	**b**	**a**	**b**
$Cu(NO_3)_2 \cdot 3H_2O$	**c**	**a**	**b**
$MnCl_2$	**c**	**a**	**a**
$Mn(NO_3)_2 \cdot 4H_2O$	**a**	**a**	**a**
$NiCl_2$	**c**	**c**	**a**
$Ni(NO_3)_2 \cdot 6H_2O$	**a**	**a**	**a**
$ZnCl_2$	**16** – 1D strand 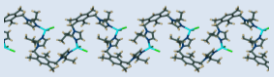	**16**	**a**
$Zn(NO_3)_2 \cdot 4H_2O$	**c**	**a**	**a**

2.2.3.1. $[CdL3Cl_3]\cdot H_2O$ (13)

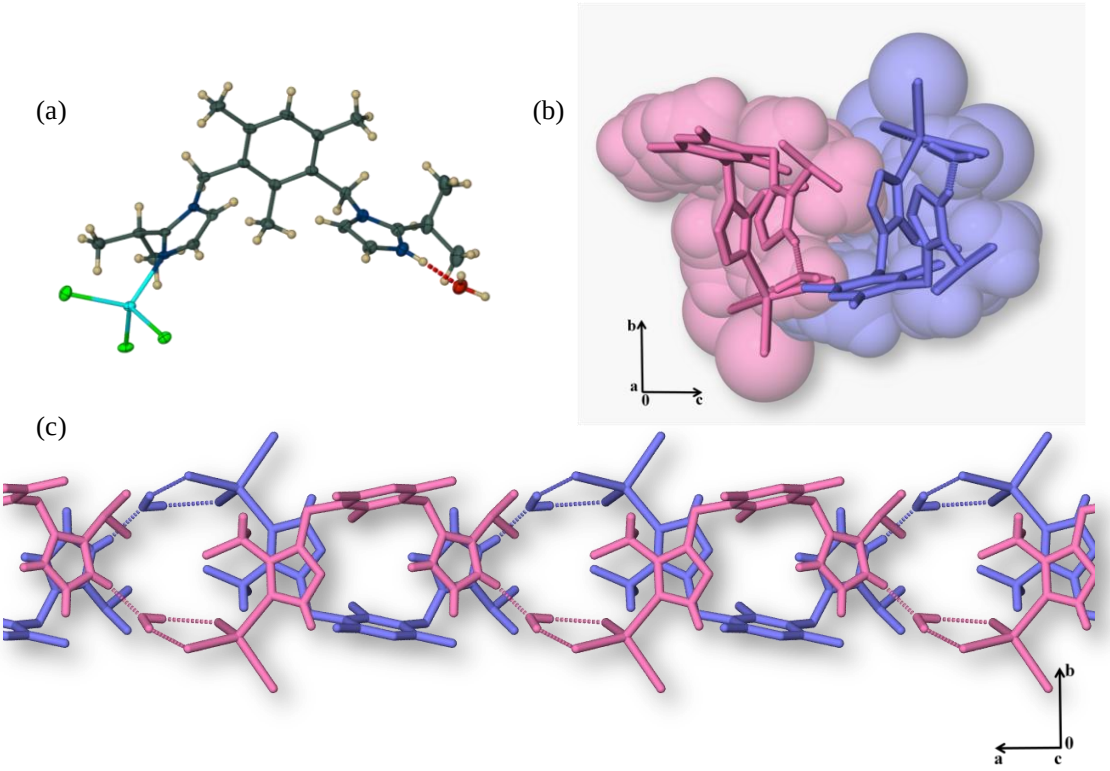

Figure 20. (a) Atomic displacement (50% probability) plot showing the ASU of complex **13**. Hydrogen atoms are shown as spheres of arbitrary radius. **(b)** Capped-stick metaphor superimposed on a space-filled representation of the shape-complementary double strand motif formed in **13**, as viewed down [100]; the individual strands are coloured pink and blue respectively and hydrogen atoms not participating in hydrogen bonding interactions have been omitted for clarity. **(c)** Capped-stick representation of double stranded motif viewed down [001], hydrogen bonds are shown as fragmented lines in the same colour as the atoms of their respective 1D strands and hydrogen atoms not participating in hydrogen bonding interactions have been omitted to provide an unobstructed view of the double strand.

The ASU of **13** consists of one protonated ligand **L3** in the *cis* conformation, a cadmium(II) ion, three chloride ions and a water molecule (**Figure 20a**). The two imidazole moieties of the ligand point upwards such that the ligand assumes an approximate U-shape. At one end of the ligand the imidazole group is coordinated to a cadmium ion, which is in a tetrahedral coordination environment – the remaining three coordination sites are occupied by chloride ions. The second imidazole group is protonated at the nitrogen site to balance the overall charge of the complex. The amino nitrogen donates a hydrogen bond to the water molecule ($N_{donor}\cdots O_{acceptor}$ = 2.720(4) Å) which, in turn, donates two hydrogen bonds to two of the coordinated chloride ions in an adjacent complex ($O_{donor}\cdots Cl_{acceptor}$ = 3.258(3) and 3.250(3) Å) and collectively these

hydrogen bonds serve to connect the discrete units into a 1D strand running parallel to [100]. The strands form a shape-complementary double strand motif in which the two strands interact by van der Waals interactions only, and are related to one another by means of a glide operation parallel to the direction of propagation (**Figure 20b** and **Figure 20c**). The TGA trace of **13** indicates that the sample gradually loses mass from room temperature to 270 °C and then more rapidly above this temperature. It is presumed that the former step is a solvent loss process coupled with the initiation of decomposition, which is taken to completion above 270 °C.

2.2.3.2. $\{CdL3Br_2\}_n \cdot nCH_2Cl_2$ (14)

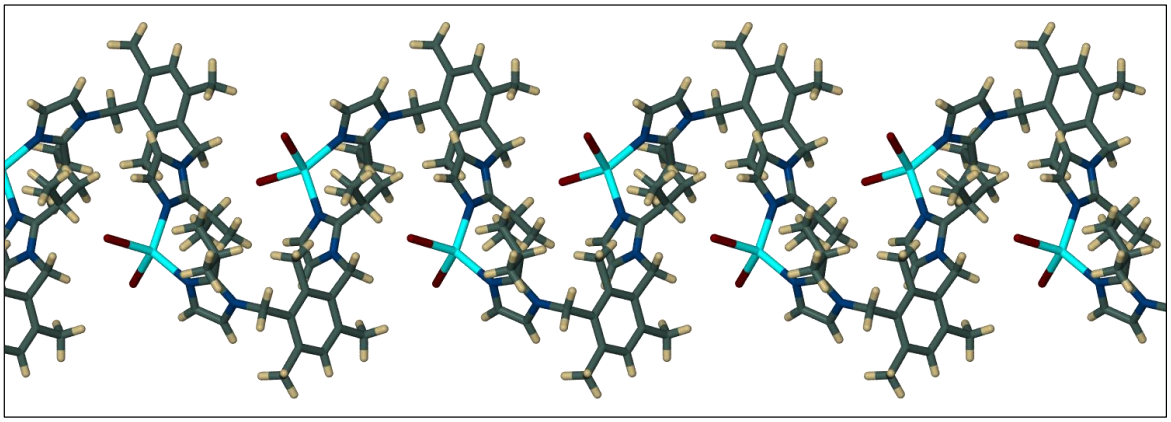

Figure 21. Capped-stick representation of the 1D strands formed in **14**. Solvent molecules have been omitted for clarity.

Complex **14** forms a 1D strand propagating along [010] (**Figure 21**). Adjacent Cd(II) ions are connected by means of a single ligand molecule in the *trans* conformation. Each metal centre is coordinated by two bromide ions and two nitrogen atoms from distinct ligand molecules and is in a distorted tetrahedral coordination environment (coordinating angles range from 100.3(1)° – 116.3(1)°). In addition to the constituents that form part of the 1D strand, the ASU also contains one dichloromethane molecule, which participates in weak hydrogen bonding interactions with the ligated bromide ions in one strand ($C_{donor}\cdots Br_{acceptor}$ = 3.586(7) Å) and an imidazolate hydrogen on an adjacent strand ($C_{donor}\cdots Cl_{acceptor}$ = 3.800(6) Å). By virtue of these hydrogen bonds, adjacent 1D strands are connected to one another to form 2D sheets in the (10-1) plane as shown in **Figure 22**. Thermal analysis of **14** reveals that loss of solvent occurs as a single step process from room temperature to *ca* 190 °C, with a corresponding weight loss percentage of 11.9% – a theoretical value of 12.1% is expected for the loss of the solvent molecules. It was not

possible to obtain a structure of the solvent-free phase as the heating process resulted in extensive fracturing of the formerly discrete crystals into a polycrystalline powder.

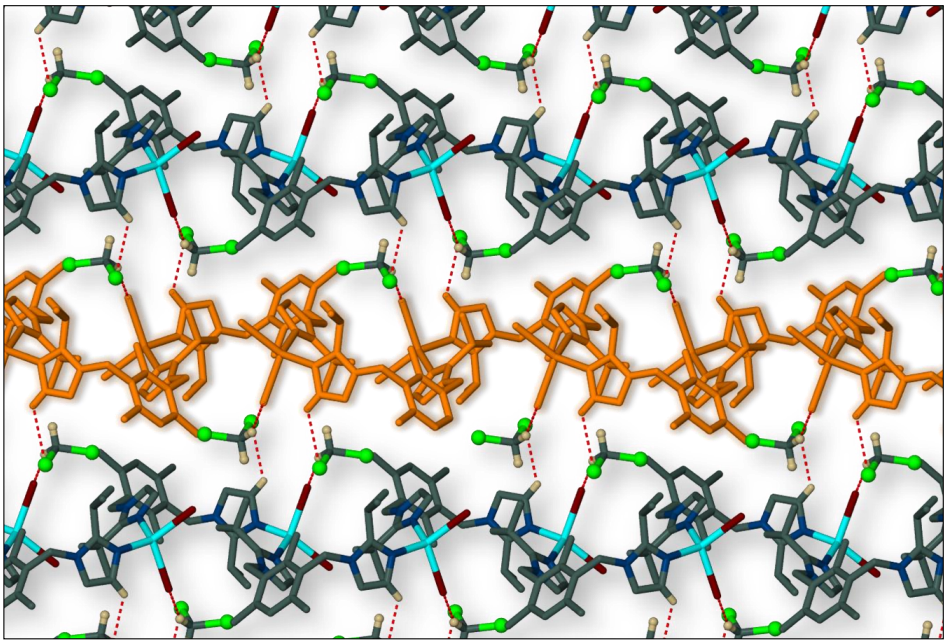

Figure 22. Capped-stick representation of the packing arrangement of **14** to form 2D sheets, as viewed perpendicular to the (10-1) plane. Ligand hydrogen atoms not involved in hydrogen bonding have been omitted for clarity and hydrogen bonds are indicated by fragmented red lines. A single 1D strand has been highlighted in orange and all solvent molecules are shown in the ball-and-stick metaphor.

2.2.3.3. $\{CdL3I_2\}_n$ (15)

Complex **15** forms 1D strands similar to those of **14** in that each metal centre is linked to its neighbour by means of one ligand **L3** in the *trans* conformation and is in a tetrahedral coordination environment coordinated by two imidazole moieties from separate ligands and two halide ions (coordinating angles range from 99.0(1)° – 121.59(7)°). There are no lattice solvent molecules in **15** and weak hydrogen bonds between a ligated iodine atom and a methyl hydrogen on the isopropyl substituent ($C_{donor}\cdots I_{acceptor}$ = 3.934(3) Å) serve to link adjacent 1D strands to one another to form a 2D sheet parallel to the (001) plane. Furthermore, the sheets stack one on top of another along [001] in an ...*ABAB*... stacking arrangement and are connected by means of offset face-to-face π–π interactions between neighbouring aryl rings (centroid-centroid distance = 3.481 Å). **Figure 23** shows the progressive formation of this stacking arrangement.

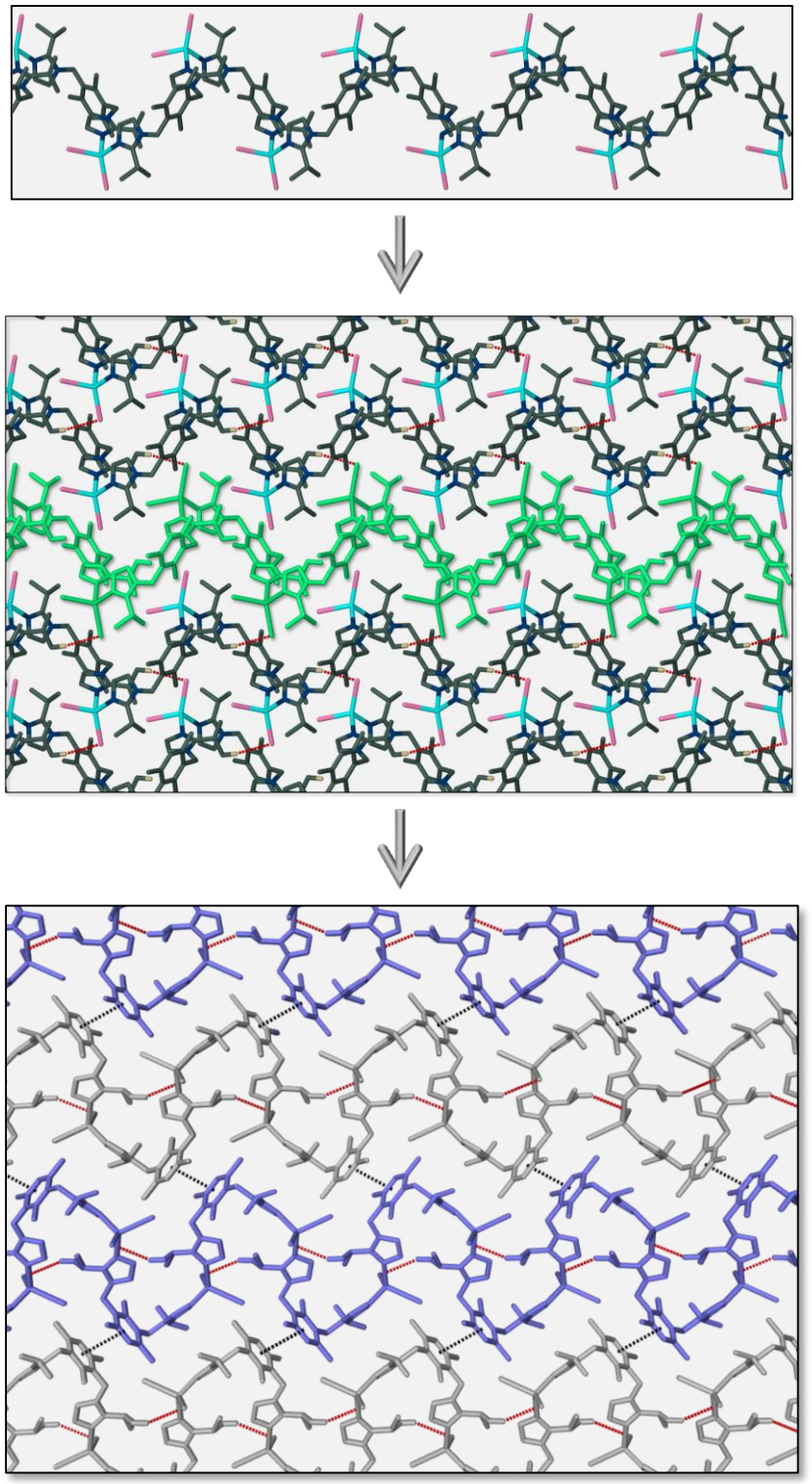

Figure 23. (Top) A single 1D strand of **15** running parallel to [010]. **(Middle)** A view perpendicular to (001) of the 2D sheet formed by hydrogen bonding, one 1D strand has been highlighted in green. **(Bottom)** The ...*ABAB*... stacking arrangement of the 2D sheets as viewed down [100]; alternating layers are shown in silver and blue. Hydrogen atoms not participating in hydrogen bonding have been omitted to provide an unobstructed view; hydrogen bonds are shown as fragmented red lines and stacking interactions are shown as dashed black lines between the centroids of the aryl rings in adjacent sheets. All molecules are shown in the capped-stick metaphor.

2.2.3.4. $\{Zn_2(L3)_2Cl_4\}_n \cdot 2nCH_3OH$ (16)

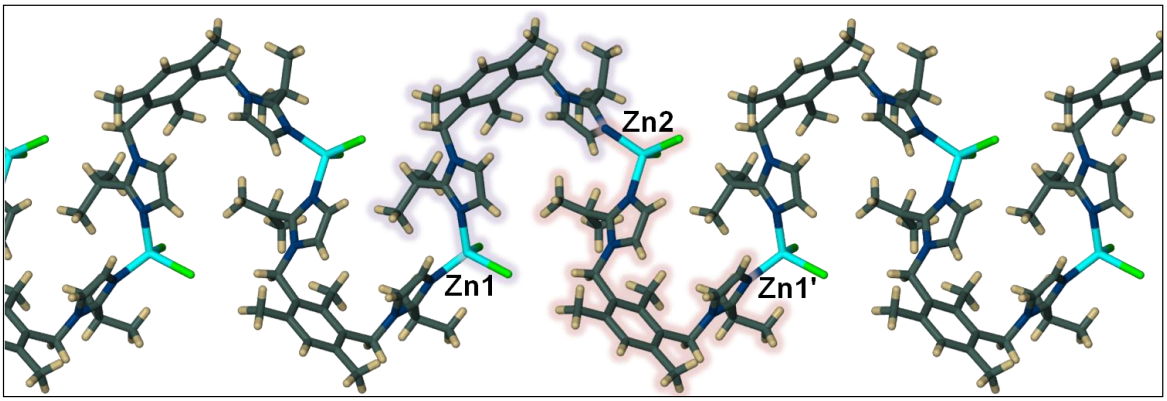

Figure 24. Capped-stick representation of the 1D strands formed in **16** viewed down [100]. The two unique **L3** molecules have been highlighted in purple and pink, respectively – the purple ligand connects Zn1 to Zn2 and the pink ligand connects Zn2 to a symmetry related Zn1'. Solvent molecules have been omitted to provide an unobstructed view of the strand.

The ASU of complex **16** consists of two metal ions, two **L3** molecules, four ligated chloride ions and two methanol molecules. The structure consists of 1D strands running parallel to [010] (**Figure 24**). The two unique ligand molecules are both in the *trans* conformation and serve to connect the metal centres to one another i.e. the first ligand connects Zn1 to Zn2, and the second ligand connects Zn2 to a symmetry related Zn1. Both metal Zn(II) ions are in a tetrahedral coordination environment coordinated by two imidazole nitrogen atoms and two chloride ions. The MeOH molecules contribute to a system of hydrogen bonds with the ligated chloride ions and imidazole protons, and by virtue of these hydrogen bonds and inversion symmetry each 1D strand is connected to one other strand (see **Table 13** for hydrogen bonding parameters). This association creates solvent filled channels along [010] (**Figure 25**). Thermal analysis of **16** indicates that solvent loss is concurrent with decomposition.

Table 13. Hydrogen bond geometry for **16** (Å, °).

D*–H···*A	***D*···*A***
O1–H1···Cl1	3.165(4)
O2–H2A···O1	2.764(4)
C25–H25···O2^{i}	3.244(4)

Symmetry codes: (*i*) *-x*, *-y* + 2, *-z*.

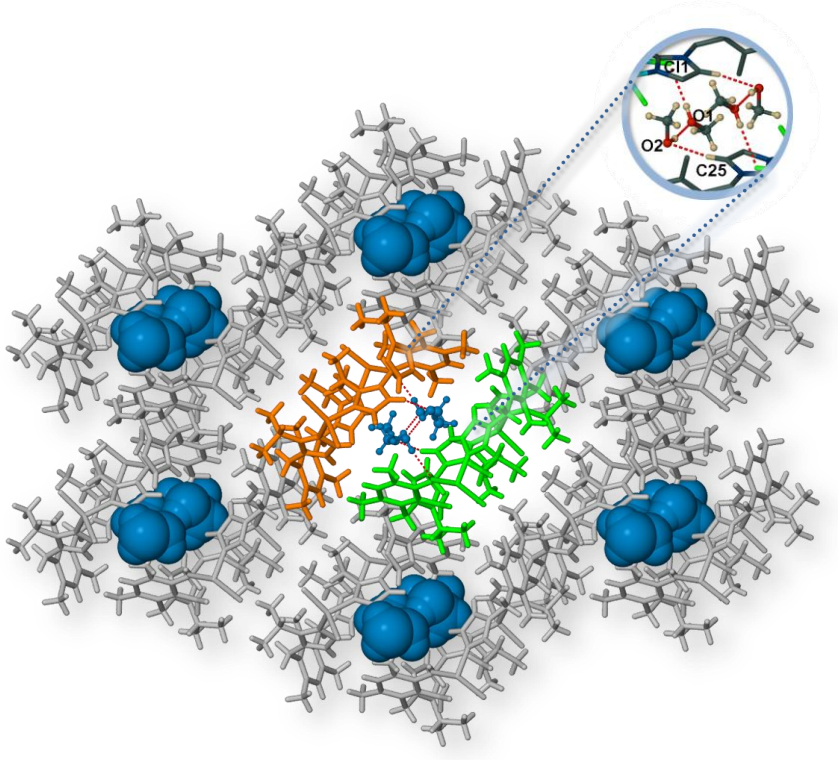

Figure 25. View along [010] of the solvent-filled channels created by the association of two 1D strands in **16**. All methanol molecules are shown in blue and are represented in the ball-and-stick metaphor in the central channel and in van der Waals representation in the remaining channels. All 1D strands are shown in capped-stick representation in grey, except the two strands in the centre of the image that are coloured orange and green to distinguish them from each other. The insert above the image highlights the hydrogen bonding interactions between the methanol molecules and the 1D strands – refer to **Table 13** for details of the hydrogen bonding parameters.

2.2.3.5. Comparison of the crystal structures obtained for L3

Four structures were elucidated from the reaction of **L3** with a variety of transition metal salts – one discrete metal–ligand salt and three 1D polymeric strands. In all four cases the solution M:L ratio of 1:1 is reflected in the solid-state structures. Three of the four structures form a series containing Cd(II)-halides. It must, however, take into consideration that the structures are not directly comparable as they were isolated from different solvent systems. In complex **13** the Cd(II) ion is coordinated by an imidazole nitrogen atom and three chloride anions to form a discrete metal-organic salt. The discrete units are U-shaped and are connected to one another to form a 1D strand *via* a series of hydrogen bonds involving lattice water molecules. In contrast the structures containing $CdBr_2$ and CdI_2, both form 1D polymeric strands. The two structures share similarities; the Cd(II) ions are both in a tetrahedral coordination environment coordinated by two ligated halide anions and two ligands and the Cd-centres are connected to one another by a single

ligand in the *trans* conformation. They differ in that the structure of **14** contains DCM molecules that participate in hydrogen bonding interactions that link the 1D strands to one another to form a 2D layer, whereas weak hydrogen bonds between an isopropyl substituent and a ligated bromide ion connect the strands to one another in **15**. Complex **16** is formed by the reaction of **L3** and $ZnCl_2$; the Zn(II) ions are connected to one another by a single ligand in the *trans* conformation and, like **14**, this structure also contains solvent molecules. **16** is the most interesting of the 1D polymeric structures in that each strand associates with one other strand through a series of hydrogen bonds involving the lattice solvent molecules to form solvent-filled channels.

2.2.4. Single-crystal structures obtained with ligand L4

Table 14. Reaction conditions used in the preparation of metal-organic complexes with Ag(I) salts and **L4**.

Metal salt	MeOH	MeCN	Acetone	DCM/MeOH
$AgNO_3$	**a**	**a**	**a**	**a**
$AgBF_4$	**b**	**a**	**a**	**b**
$AgPF_6$	**17** – 2D network 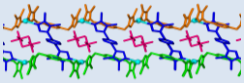 **18** – 2D layer 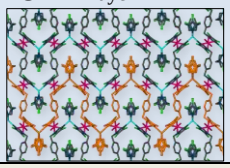	**a**	**b**	**a**
$AgSbF_6$	**a**	**a**	**a**	**a**

Table 15. Reaction conditions used in the preparation of metal-organic complexes with all non–Ag(I) salts and **L4**.

Metal salt	MeOH	DCM/MeOH	DCM/MeCN
$CdCl_2 \cdot 2.5H_2O$	**b**	**e**	**b**
$CdBr_2$	**a**	**a**	**19** – 2D network 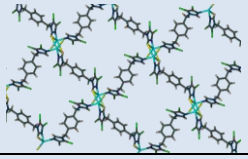
CdI_2	**a**	**a**	**20** – 0D metallocycle 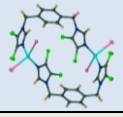
$Cd(NO_3)_2 \cdot 4H_2O$	**a**	**b**	**a**
$CoCl_2$	**b**	**e**	**a**
$CoBr_2$	**b**	**e**	**a**
$Co(NO_3)_2 \cdot 6H_2O$	**a**	**a**	**21** – 1D strand 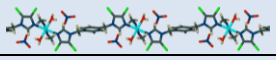
$CuCl_2$	**b**	**a**	**22** – 1D strand 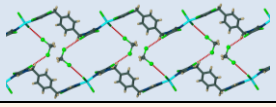
$CuBr_2$	**23** – 1D chain 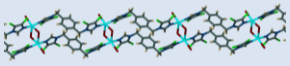	**b**	**b**
$Cu(NO_3)_2 \cdot 3H_2O$	**a**	**a**	**a**
$MnCl_2$	**e**	**b**	**a**
$Mn(NO_3)_2 \cdot 4H_2O$	**b**	**b**	**b**
$NiCl_2$	**e**	**b**	**a**
$Ni(NO_3)_2 \cdot 6H_2O$	**e**	**b**	**b**
$ZnCl_2$	**24** – 1D strand 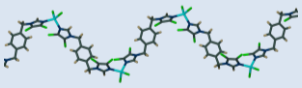	**b**	**a**
$Zn(NO_3)_2 \cdot 4H_2O$	**b**	**b**	**b**

2.2.4.1. $\{[Ag_2(L4)_3](PF_6)_2\}_n$ (17)

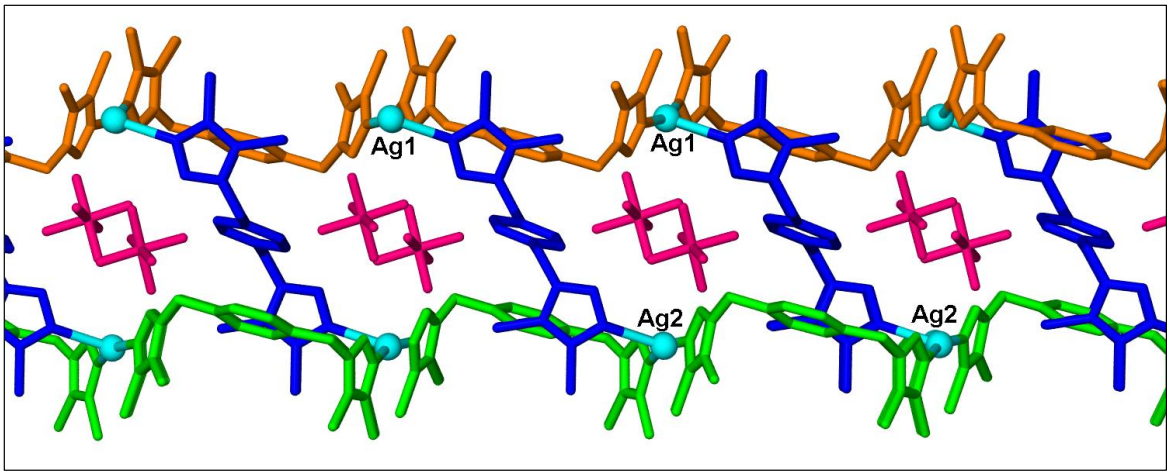

Figure 26. Packing arrangement of **17** viewed along [001] to form 2D layers containing channels occupied by PF_6 anions (pink capped-stick molecules). The three unique **L4** molecules are coloured orange (**A**), green (**B**) and blue (**C**). Ligand molecules are shown as capped-sticks, the Ag centres are shown as spheres and all hydrogen atoms have been omitted for clarity.

The ASU of **17** consists of two Ag(I) ions, three ligands **L4** (**A**, **B** and **C**) and two PF_6^- anions. Two of the ligands, **A** and **B**, represented as the orange and green molecules, respectively, in **Figure 26** are in the *cis* conformation, and **C** is in the *trans* conformation (blue molecules in **Figure 26**). The Ag1 centres are connected to one another by virtue of a single **A** molecule and similarly, the Ag2 centres are connected to one another by a single **B** molecule. The **C** molecules serve to connect the two crystallographically independent Ag(I) centres to each other, resulting in the formation of an open 2D network containing channels running parallel to [010]; the PF_6^- anions occupy the spaces within the channels. Each Ag(I) centre is thus coordinated by three **L4** ligands in a distorted T-shaped coordination environment (see **Table 16** for the coordination geometric parameters).

Table 16. Selected geometric parameters for **17** (Å, °).

Complex **17**			
Ag1–N1^{i}	2.151(4)	Ag2–N12^{ii}	2.149(4)
Ag1–N4	2.157(4)	Ag2–N9	2.168(4)
Ag1–N5	2.447(4)	Ag2–N8	2.461(4)
N1^{i}–Ag1–N4	164.1(2)	N12^{ii}–Ag2–N9	164.6(2)
N1^{i}–Ag1–N5	97.8(1)	N12^{ii}–Ag2–N8	94.9(1)
N4–Ag1–N5	97.1(1)	N9–Ag2–N8	99.1(1)

Symmetry codes: (*i*) $x + {}^1/_2, -y, z$, (*ii*) $x - {}^1/_2, -y + 1, z$.

2.2.4.2. $\{[Ag(L4)_2]PF_6\}_n$ (18)

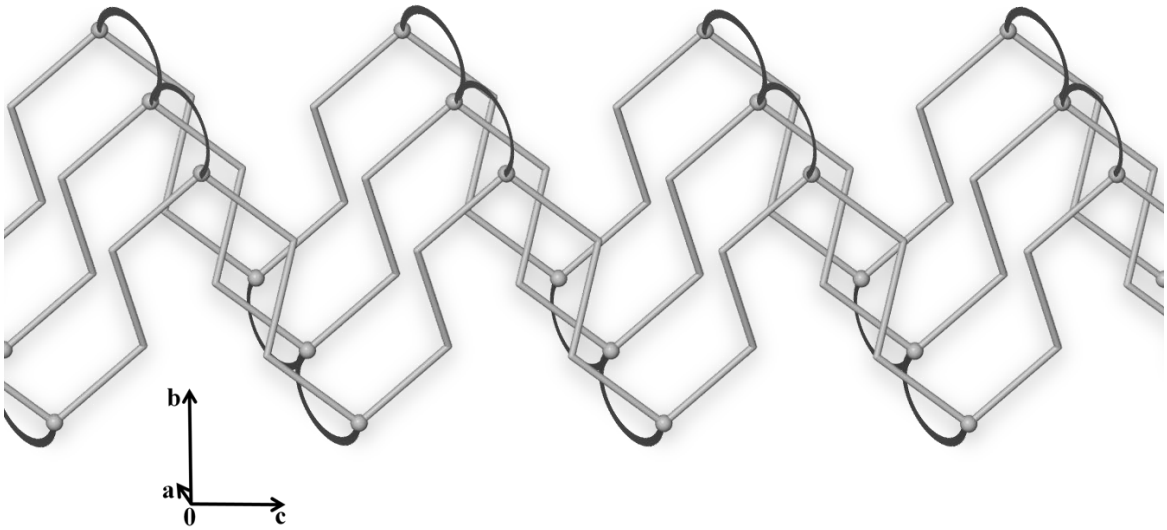

Figure 27. A schematic projection of the 2D nets formed in **18**; Ag atoms are shown as grey spheres, the ligands connecting the Ag centres to one another in the 1D strands are represented as grey pipes and the ligands bridging the strands to one another are indicated as black bows.

In the structure of **18**, each Ag(I) metal centre is in a tetrahedral coordination environment and is linked to an adjacent centre along (100) by means of a single ligand **L4** in the *trans* conformation, thus forming undulating 1D strands propagating in this plane. The Ag(I) centres are further linked to one another in the [100] direction through a shared coordination to a single ligand **L4**, which functions as a bridge connecting the 1D strands into a 2D layer (**Figure 27**). The 2D layers interdigitate in the direction of the *b* axis (**Figure 28**), and the PF_6^- anions are located between adjacent nets, weakly hydrogen bonded to the imidazolate hydrogen atoms from separate nets ($C_{donor}\cdots F_{acceptor}$ = 3.384(4) and 3.462(5) Å). Both **17** and **18** were isolated from the same reaction vial.

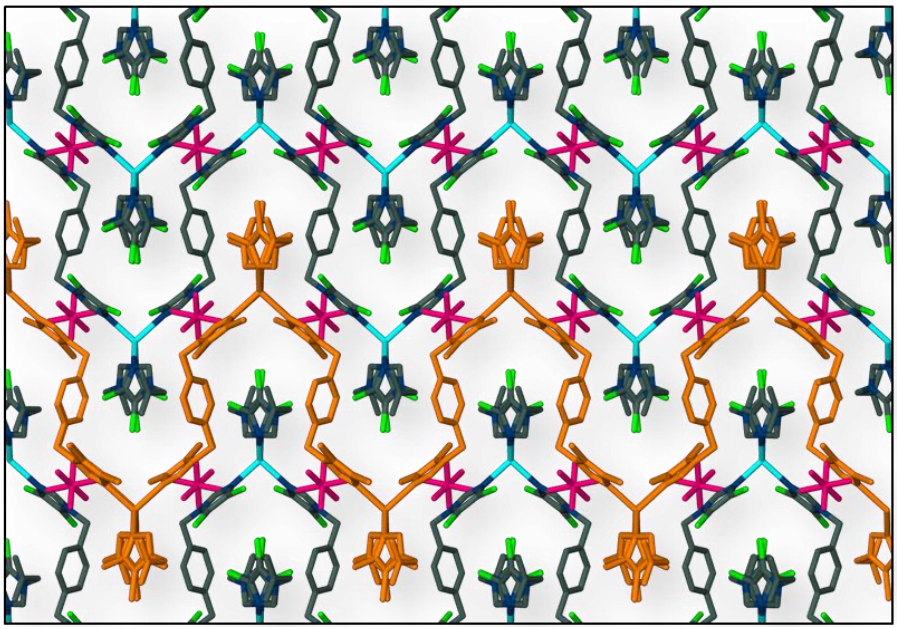

Figure 28. Packing arrangement of **18** as viewed along [100]. Molecules are shown as capped-sticks. Hydrogen atoms have been omitted for clarity, PF_6^- anions are shown in pink and a single 2D net is coloured orange for clarity.

2.2.4.3. {CdL4(μ-Br)Br}$_n$ (19)

The ASU of **19** consists of two unique half molecules of **L4** (each ligand is situated about an inversion centre and thus adopts the *trans* conformation), one Cd(II) ion and two bromide ions, with each Cd(II) ion in a distorted square-based pyramidal coordination environment. The vertices of the square consist of two imidazole nitrogen atoms (Cd–N = 2.235(2) and 2.264(2) Å) situated *cis* with respect to each other, a terminal bromide ion (Cd–Br = 2.5440(2) Å) and one of two bridging bromide ions (Cd–Br = 3.1066(3) Å); the apical position of the pyramid is occupied by the second bridging bromide ion (Cd–Br = 2.6004(3) Å) (see **Table 17** for the coordination geometric parameters). Owing to the bridging bromide ions and the arrangement of ligands around the metal centres, a four-connected node comprising two Cd(II) ions is created. Propagation of the ligands from these nodes results in the formation of a 2D net, containing corrugated diamond-shaped apertures along [100] (**Figure 29**–top). The 2D layers stack in an ...*ABAB*... fashion, i.e. atoms in the first layer are placed over atoms in the third layer (**Figure 29**–bottom), where the layers are shifted such that the vertices of the *A* layer are placed over the void of the *B* layer, and *vice versa*.

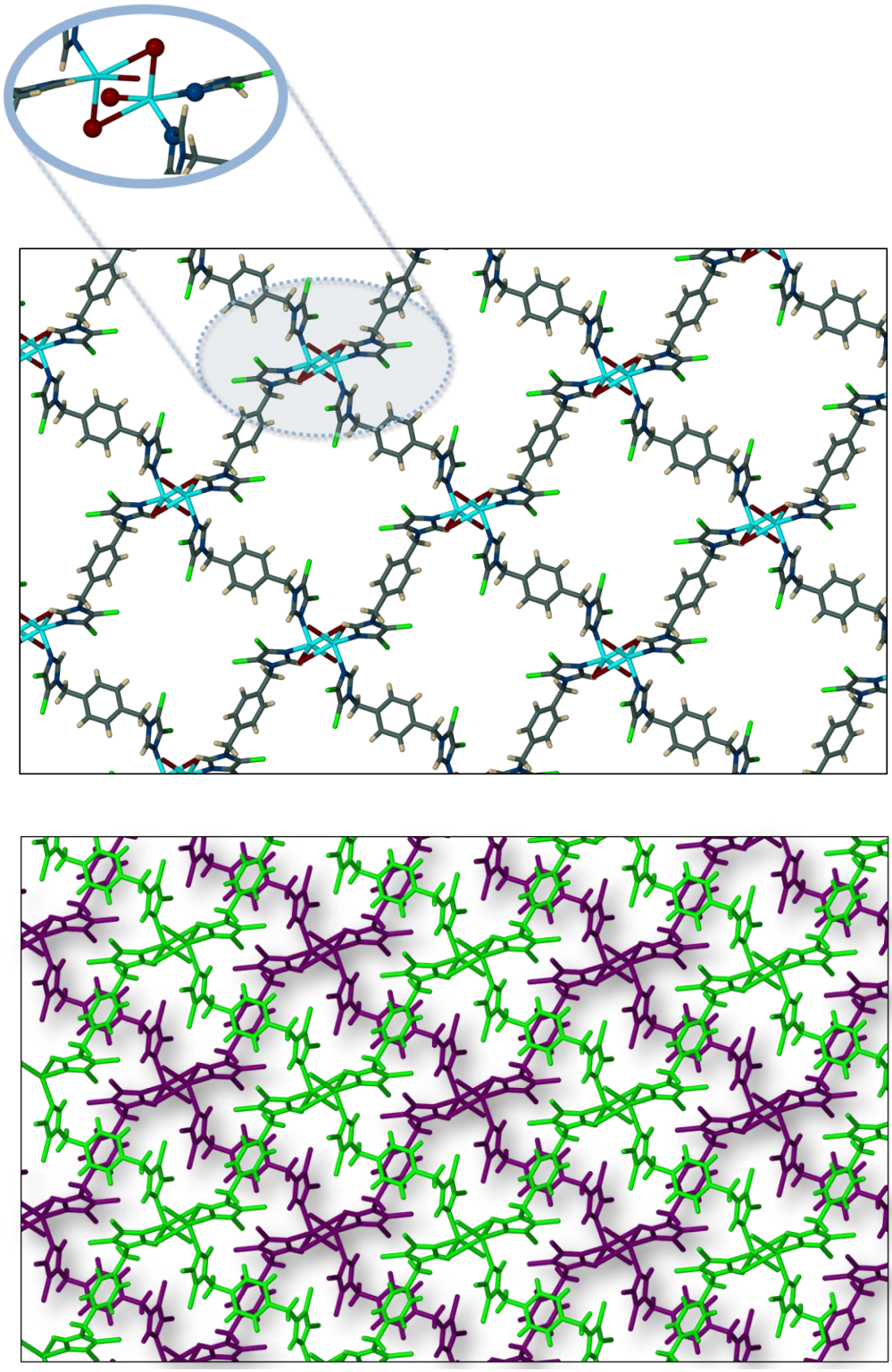

Figure 29. (Top) Capped-stick representation of the 2D nets formed in **19**; the insert above the image is of a dinuclear, four-connected node that has been slightly re-oriented to highlight the coordination mode of the Cd(II) ions; coordinated atoms are shown as spheres. **(Bottom)** The ...*ABAB*... stacking arrangement of the 2D nets, the individual nets have been coloured purple and green for clarity.

Table 17. Selected geometric parameters for **19** (Å, °).

Complex **19**			
Cd1–N2	2.264(2)	Cd1–Br1	2.6004(3)
Cd1–N3	2.325(2)	Cd1–Br1^{i}	3.1066(3)
Cd1–Br2	2.5440(2)	Br1–Cd1^{i}	3.1066(3)
N2–Cd1–N3	96.27(6)	N2–Cd1–Br1^{i}	74.97(4)
N2–Cd1–Br2	140.13(4)	N3–Cd1–Br1^{i}	164.56(4)
N3–Cd1–Br2	92.98(4)	Br2–Cd1–Br1^{i}	86.267(8)
N2–Cd1–Br1	98.57(4)	Br1–Cd1–Br1^{i}	93.616(7)
N3–Cd1–Br1	100.34(4)	Cd1–Br1–Cd^{i}	86.384(7)
Br2–Cd1–Br1	117.759(9)		

Symmetry codes: (*i*) -*x* + 1, -*y* + 2,-*z* + 1.

2.2.4.4. $[Cd_2(L4)_2I_2]$ (20)

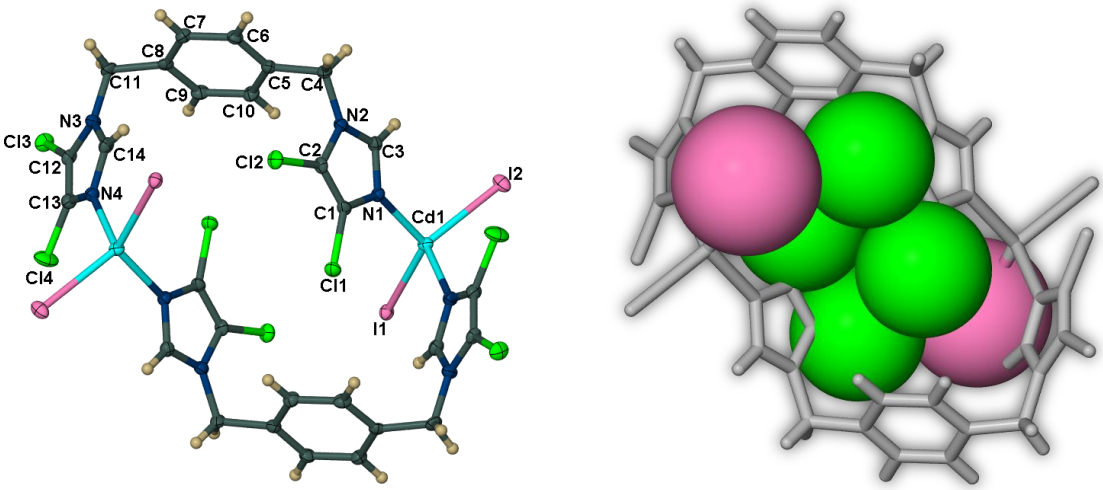

(a) (b)

Figure 30. (a) Atomic displacement (50% probability) plot showing the molecular structure of complex **20**. Unlabelled atoms are related to the labelled atoms by the symmetry operator 1 – *x*, 1 – *y*, 1 – *z*. **(b)** White capped-stick representation of the cyclic complex **20**; the iodide ions and chlorine substituents of the imidazole rings that protrude into the centre of the ring are shown in CPK colours in van der Waals representation.

Complex **20** consists of a discrete dinuclear complex with each Cd(II) ion tetrahedrally coordinated to two iodide anions and two bridging **L4** ligands in the *cis* conformation. The molecule is situated on a crystallographic inversion centre and the ASU consists of half a

complex (**Figure 30a**). The ligands assume an approximate C-shape in the cyclic complex but are sufficiently distorted such that the chlorine substituents from one of the imidazole rings and a coordinated iodide ion protrude into the centre of the ring and, as a consequence, there are no interstitial voids in the structure of **20** (**Figure 30b**).[*] The complexes pack in the well-known herringbone motif and this arrangement is further stabilised by weak π–π interactions between phenylene and imidazole rings as shown in **Figure 31** (centroid–centroid distance = 3.502 Å).

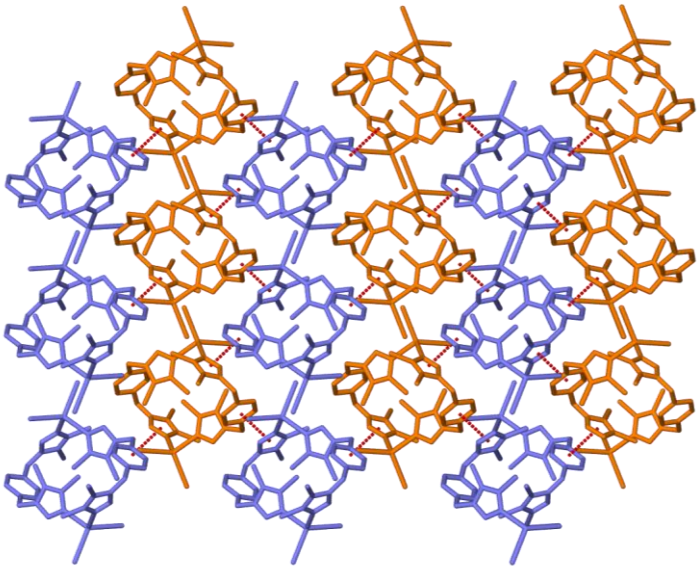

Figure 31. Capped-stick representation showing the packing arrangement of **20** as viewed along [100]. Hydrogen atoms have been omitted for clarity and adjacent columns of the herringbone pattern are coloured blue and orange to distinguish them from one another. π–π stacking interactions are shown as segmented red lines from the centroid of the aryl ring to the centroid of the imidazole ring.

2.2.4.5. $\{CoL4(CH_3CN)_2(H_2O)_2\}_n \cdot 2nNO_3$ (21)

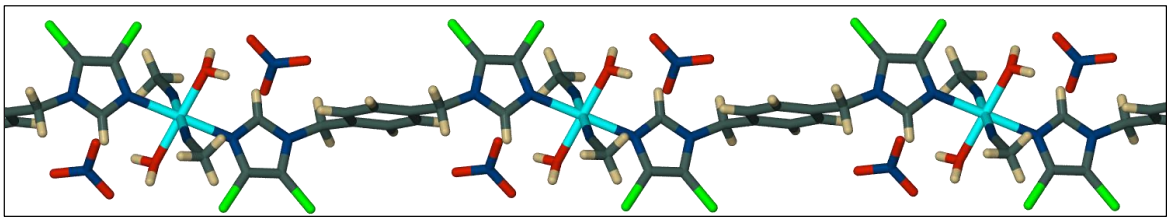

Figure 32. Capped-stick representation of the 1D strand formed in **21** as viewed perpendicular to the [001] direction.

[*] MSRoll was used to verify the absence of interstitial voids and it was found that there are no guest-accessible surfaces in the structure of **4**, even to a probe of radius 1.1 Å.

Complex **21** forms infinite 1D strands running parallel to [001] (**Figure 32**). Each metal centre is linked to an adjacent metal centre by means of one ligand **L4** in the *trans* conformation. The cobalt ions are in an octahedral coordination environment and coordinate to two symmetry-related imidazole groups located *trans* with respect to each other and two symmetry-related acetonitrile molecules, which occupy the vertices of an almost ideal square plane (see **Table 18** for coordination geometric parameters); the apical positions of the octehedra are occupied by ligated water molecules. Furthermore, nitrate counter-ions are present in the structure and accept hydrogen bonds from the ligated water molecules ($O_{donor}\cdots O_{acceptor}$ = 2.723(1) and 2.789(2) Å) to connect the 1D strands into a 3D hydrogen bonded network (**Figure 33**). The TGA trace of **21** reveals that loss of the coordinated acetonitrile and water molecules occurs as a single step process in the temperature range of 70 – 130 °C, with a corresponding weight loss of 16.9% – a theoretical value of 17.4% is expected for the loss of the solvent molecules. It was not possible to obtain a structure of the solvent-free phase as the heating process resulted in extensive fracturing of the formerly discrete crystals into a polycrystalline powder.

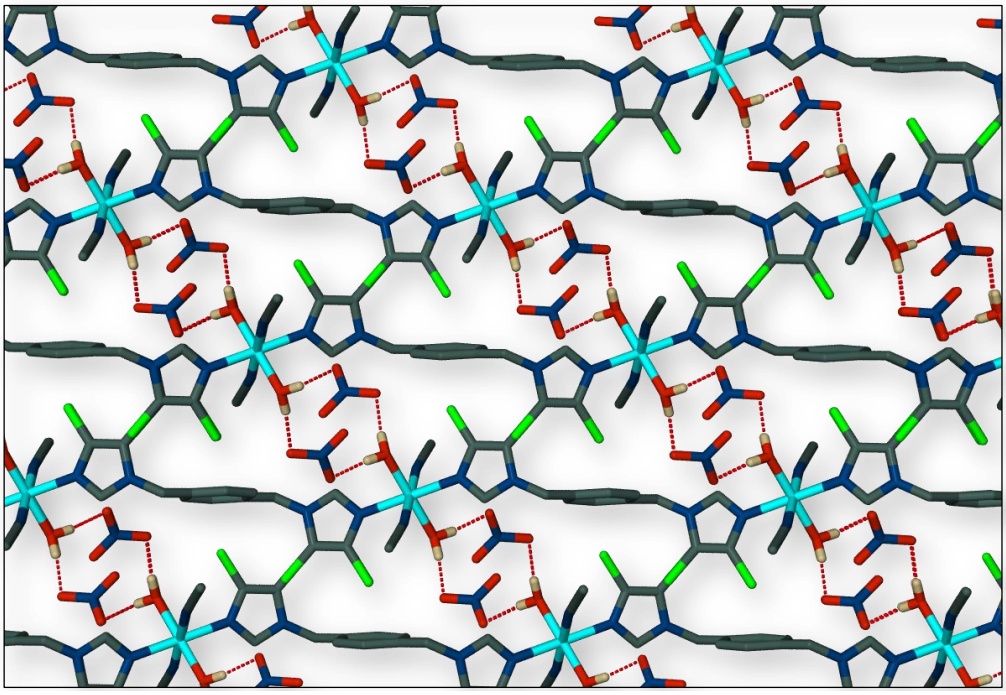

Figure 33. Capped-stick representation of the 3D array formed by hydrogen bonding in **21**, as viewed along [010]. Hydrogen atoms not involved in hydrogen bonding have been omitted for clarity.

Table 18. Selected geometric parameters for **21** (Å, °).

Complex **21**			
Co1–O1	2.0455(9)	Co1–N1	2.6004(3)
Co1–O1^{i}	2.0455(9)	Co1–N1^{i}	3.1066(3)
Co1–N3^{i}	2.145(1)	Co1–N3	2.145(1)
O1–Co1–O1^{i}	180.00(7)	N3^{i}–Co1–N1	90.44(4)
O1–Co1–N3^{i}	87.91(4)	N3–Co1–N1	89.56(4)
O1^{i}–Co1–N3^{i}	92.08(4)	O1–Co1–N1^{i}	91.22(4)
O1–Co1–N3	92.09(4)	O1^{i}–Co1–N1^{i}	88.78(4)
O1^{i}–Co1–N3	87.91(4)	N3^{i}–Co1–N1^{i}	89.56(4)
N3^{i}–Co1–N3	180.00	N3–Co1–N1^{i}	90.44(4)
O1–Co1–N1	88.78(4)	N1–Co1–N1^{i}	180.00
O1^{i}–Co1–N1	91.22(4)		

Symmetry codes: (*i*) *-x, -y, -z*.

2.2.4.6. $\{CuL4Cl_2\}_n \cdot nCH_2Cl_2$ (22)

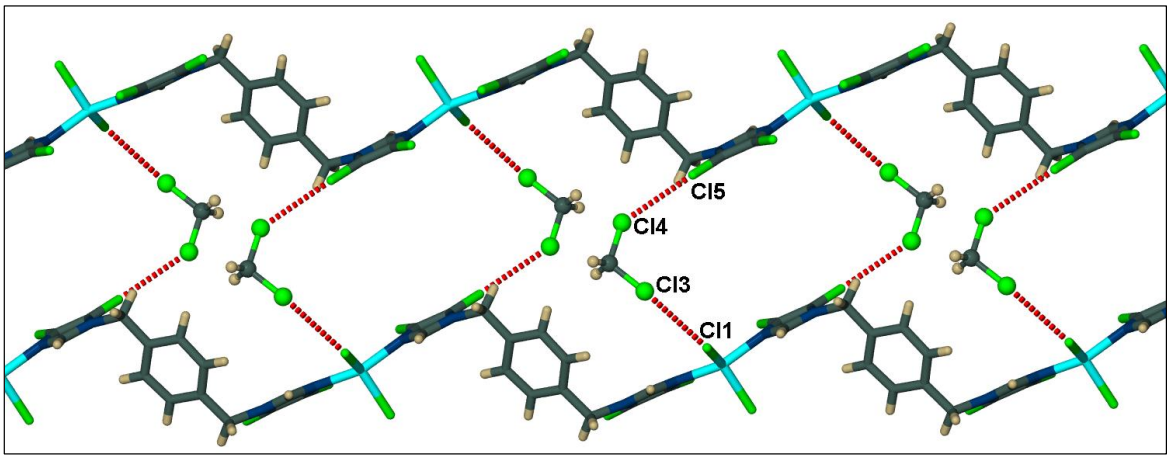

Figure 34. Capped-stick representation of the 1D strands formed in **22**. The DCM molecules are shown in the ball-and-stick metaphor and Cl···Cl interactions are shown as fragmented red lines.

The ASU of **22** consists of a single ligand **L4** in the *trans* conformation, a Cu(II) ion, two ligated chloride ions and a DCM molecule. The Cu(II) centres are connected to one another by means of a single bridging ligand to form 1D strands along [-110]. The Cu(II) ions are in a distorted square planar coordination environment with the imidazole groups located *trans* to one another (see **Table 19** for the geometric coordination parameters). The DCM molecules are situated between two 1D strands and as can be seen in **Figure 34**; Cl···Cl halogen interactions are observed between the chlorine atoms of the DCM molecules and both a ligated chloride ion (Cl3···Cl1 = 3.496(4) Å), as well as a chlorine substituent of an imidazole ring (Cl4···Cl5 = 3.359(5) Å). Thermal analysis of **22** indicates

that the sample rapidly loses solvent from room temperature to *ca* 60 °C and then starts to gradually decompose from approximately 150 °C. Once the crystals are removed from the mother liquor, conversion to a polycrystalline powder occurs within several minutes, even at ambient temperatures.

Table 19. Selected geometric parameters for **22** (Å, °).

Complex **22**			
Cu1–N4^{i}	1.964(4)	Cu1–Cl8	2.250(1)
Cu1–N5	1.975(4)	Cu1–Cl7	2.250(1)
N4^{i}–Cu1–N5	155.1(2)	N4^{i}–Cu1–Cl7	94.0(1)
N4^{i}–Cu1–Cl8	92.3(1)	N5–Cu1–Cl7	97.0(1)
N5–Cu1–Cl8	95.13(1)	Cl8–Cu1–Cl7	136.07(6)

Symmetry codes: (*i*) *x* - 1, *y* + 1, *z*.

2.2.4.7. {CuL4(μ-Br)Br}$_n$ (23)

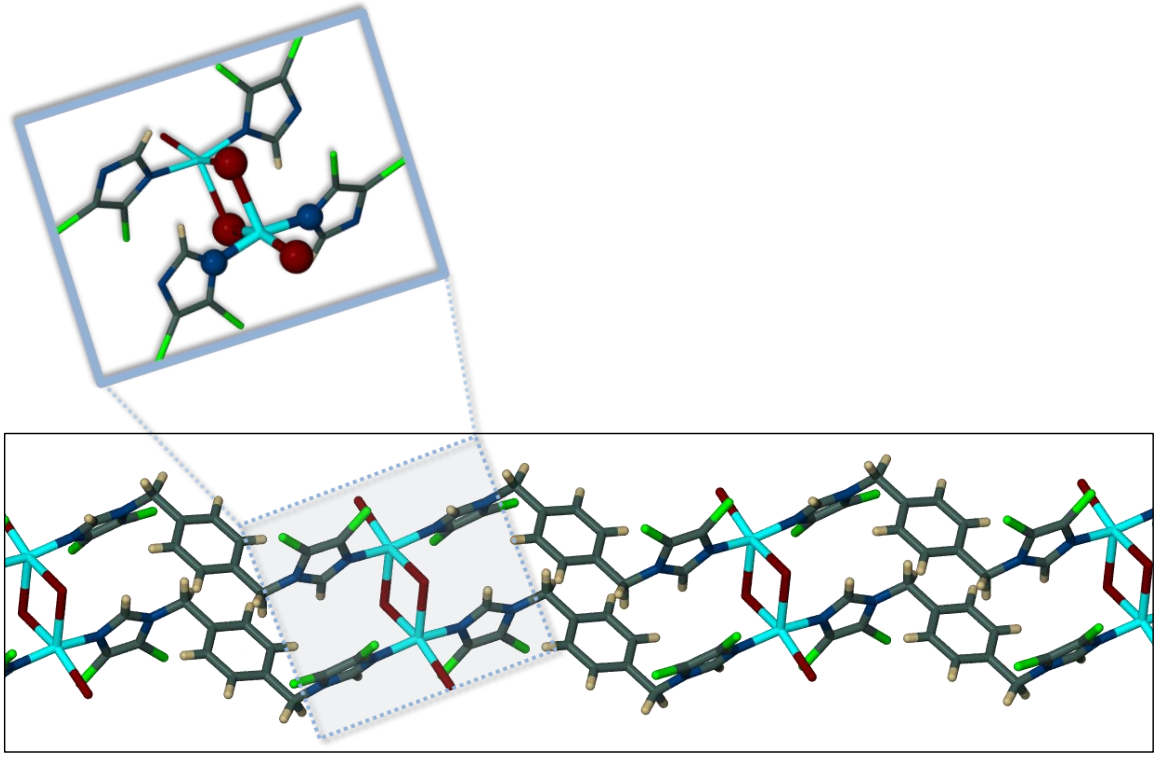

Figure 35. Capped-stick representation of the double stranded 1D chains formed in **23**; the insert above the image highlights the square pyramidal coordination mode of the Cu(II) centres – coordinated atoms are shown as spheres (bromide anions in brown and nitrogen atoms in blue).

The structure of **23** consists of double-stranded 1D chains running along the crystallographic *b* axis. The Cu(II) centres are connected to one another parallel to the

[010] direction another *via* a single ligand **L4** in the *trans* conformation and through two bridging bromide ions perpendicular to [010]. The coordination environment about each Cu(II) is thus square pyramidal, with two imidazole nitrogen atoms (Cu–N = 1.973(3) and 1.974(3) Å) situated *trans* with respect to each other, a terminal bromide ion (Cu–Br = 2.439(5) Å) and one of the two bridging bromide ions (Cu–Br = 2.524(6) Å) occupy the vertices and the second bridging bromide ion is situated at the apex (Cu–Br = 2.6847(6) Å) (**Figure 35**, also see **Table 20** for the coordination geometric paramaters). The terminal bromide ions act as bifurcated hydrogen bond acceptors and accept hydrogen bonds from both the imidazole hydrogen and a methylene hydrogen in adjacent chains; these interactions effectively connect the chains to one another in three dimensions.

Table 20. Selected geometric parameters for **23** (Å, °).

Complex **21**			
Br1–Cu1^{i}	2.5254(6)	Cu1–N1	1.974(3)
Br1–Cu	2.6847(6)	Cu1–Br2	2.4392(6)
Cu1–N4^{ii}	1.973(3)	Cu1–Br1^{i}	2.5254(6)
Cu1^{i}–Br1–Cu1	88.39(2)	Br2–Cu1–Br1^{i}	161.35(2)
N4^{ii}–Cu1–N1	163.8(1)	N4^{ii}–Cu1–Br1	101.32(8)
N4^{ii}–Cu1–Br2	90.47(8)	N1–Cu1–Br1	94.10(8)
N1–Cu1–Br2	89.84(8)	Br2–Cu1–Br1	106.96(2)
N4^{ii}–Cu1–Br1	87.41(8)	Br1^{i}–Cu1–Br1	91.61(2)
N1–Cu1–Br1^{i}	87.13(8)		

Symmetry codes: (*i*) –*x* + 2, - *y* + 2, -*z*; (*ii*) *x*, *y* + 1, *z*.

2.2.4.8. $\{ZnL4Cl_2\}_n$ (24)

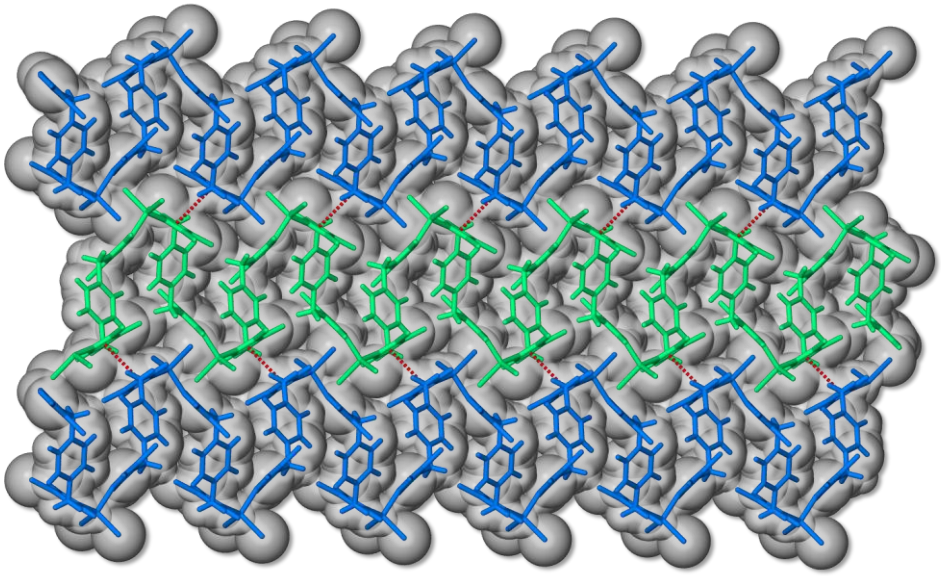

Figure 36. Packing arrangement of **24** as viewed along [100]; the ...*ABAB*... stacking of the 1D polymeric strands is indicated by the alternating blue and green colours of the strands. A capped-stick representation has been superimposed on a space-filled representation of the molecules to convey the connectivity of the atoms as well as the space filling nature of the packing arrangement. π–π stacking interactions are indicated as dashed red lines between the centroids of the imidazole rings.

The ASU of **24** consists of one ligand **L4** in the *trans* conformation, a zinc(II) ion and two chloride ions. The zinc ions are in a tetrahedral coordination environment, and coordinate to two imidazole groups from distinct ligands and two unique chloride ions. The metal centres are linked to one another by means of a single bridging ligand to form a 1D polymeric strand running parallel to [201]. Each polymeric strand is associated with one other strand along (100) by virtue of inversion symmetry, this results in an ....*ABAB*... stacking arrangement in this plane (**Figure 36**). The 1D strands are further connected to one another in this plane by face-to-face π–π stacking interactions between imidazole rings (centroid–centroid distance = 3.550 Å) and form a 2D layer as a result of these interactions.

2.2.4.9. Comparison of the crystal structures obtained for L3

Eight single-crystal structures were elucidated from the reaction conditions outlined in Tables 14 and 15. Complex **17** crystallises concomitantly with complex **18** from the vial containing **L4** and $AgPF_6$ in MeOH. The coordination number of the Ag(I) ions and the

conformation of the ligands differ in the two structures. In **17**, the Ag(I) ions are coordinated by three unique ligands, two in the *cis* conformation and one in the *trans* conformation, and assume a T-shaped coordination environment; in **18** the Ag(I) centres are in a tetrahedral coordination environment and are connected to one another by virtue of ligands in the *trans* conformation. The dimensionality of the two structures is the same, i.e. they both form 2D network structures. However, **17** forms an open 2D network that contains channels occupied by the PF_6^- anions and in **18**, interdigitated 2D layers are formed with the PF_6^- anions located between the layers weakly hydrogen bonded to the imidazolate hydrogen atoms from separate nets.

It is convenient to group the remaining structures by dimensionality. The reaction of **L4** with $Co(NO_3)_2$, $CuCl_2$, $CuBr_2$ and $ZnCl_2$ (structures **21**, **22**, **23** and **24**), respectively, results in the formation of 1D polymeric structures. Not surprisingly, the Co(II) ions assume octahedral coordination environments in **21** with the coordination sphere consisting of two ligated water molecules, two acetonitrile molecules and two imidazole nitrogen atoms; it appears therefore that under these conditions of crystallisation the cobalt binds more readily to both acetonitrile and water than to the nitrate anions. A single ligand in the *trans* conformation serves to link the Co(II) centres to one another and the ligated water molecules participate in a system of hydrogen bonds with the lattice nitrate anions to connect the 1D strands into a 3D network. **22** is similar to **21** in that solvent molecules are present in the structure and a single ligand in the *trans* conformation serves to link the metal centres to one another. However, the Cu(II) ions are in a distorted square planar coordination environment and each 1D strand is only associated with one other strand by virtue of hydrogen bonding interactions with the DCM solvent molecules. In contrast to **22**, the Cu(II) centres in **23** assume a square pyramidal coordination environment and are coordinated by two imidazole nitrogen atoms, a terminal bromide ion and two bridging bromide ions; as a consequence of the bridging anions a double stranded 1D chain is formed. The terminal bromide ions participate in hydrogen bonds that connect the chains to one another in 3D. The final 1D structure consists of Zn(II) ions (in a tetrahedral coordination environment) connected to one another by a single ligand in the *trans* conformation. The imidazole rings in adjacent strands are oriented such that π–π stacking interactions between these aromatic heterocycles is possible, and by virtue of this interaction the 1D strands are connected into a 2D layer.

Only one 2D network formed in this series of structures i.e. complex **19**. The Cd(II) centres in **19** are in a similar coordination environment to that of **23** (i.e. a square pyramidal coordination environment consisting of two imidazole nitrogen atoms, a terminal bromide ion and two bridging bromide ions). However, unlike **23**, propagation of the ligands from these metal centres results in the formation of an open 2D net, not a 1D chain. The 2D nets stack one on top of another such that the vertices of one layer are placed over the voids of the layers directly above and below.

The only discrete complex obtained in this reaction series is complex **20**. This structure is particularly interesting as it essentially conforms to our 0D dinuclear metallocycle design principle; it consists of two Cd(II) metal centres doubly bridged to each other by two ligands in the *cis* conformation. However, the metallocycle is canted such that the chlorine substituents from one of the imidazole rings and a ligated iodide anion protrude into the centre of the ring and, as a consequence, there are no voids present in the structure of **20**.

2.2.5. Pre-organisation of the metal binding sites – a future study

The synthesis of the metallocyclic complexes occurs *via* a self-assembly process of flexible organic ligands and metal salts, and this is a process over which the synthetic chemist has very little control. The inherent flexibility of organic ligands and multiple coordination modes of the metal salts render both of these building blocks *divergent* units i.e. the components promote binding in multiple directions (as opposed to the concept of *convergent* components that promote binding sites towards a central point).[48] We have seen in the preceding section that a direct consequence of this divergent nature means that the combination of the ligands and metal salts can result in a multitude of possible products ranging from discrete dinuclear products (in ideal cases) or extended polymeric networks (**Scheme 5a**). One way to increase the level of predictability in the resulting product is to pre-organise the binding sites of the components so that they are already well-defined and complementary to one another prior to the reaction (**Scheme 5b**). In the case of the ligand component this is normally achieved by utilising rigid ligands in complex formation where the coordinating groups are covalently bonded to an inflexible, normally aromatic, moiety. As ligand flexibility is crucial to dinuclear metallocycle formation, further efforts should rather be aimed at synthesising convergent metal centres

as a means of pre-organising the components, to increase the probability of obtaining the desired metallocyclic host.[48]

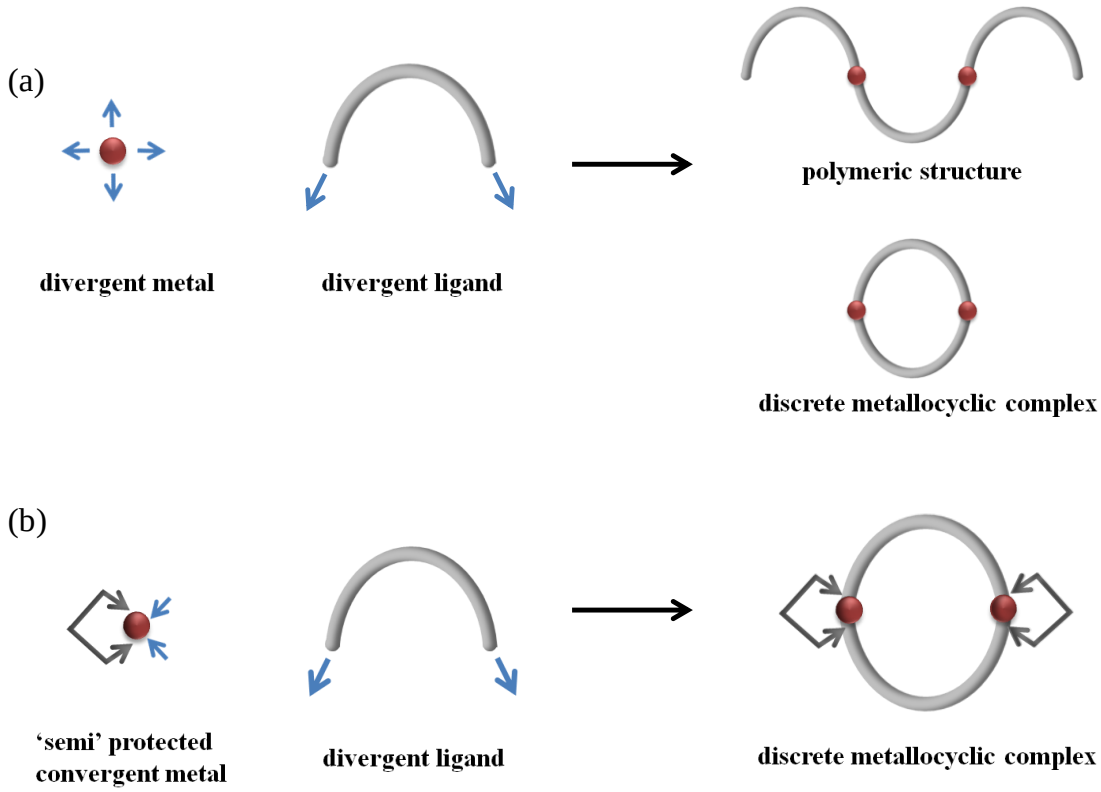

Scheme 5. Cartoon representation of **(a)** the combination of a divergent metal with a divergent ligand to give either a polymeric structure or a discrete metallocyclic complex or **(b)** a 'semi'-protected convergent metal is pre-organised to combine with a divergent ligand to yield a discrete metallocyclic complex. Picture adapted from reference 48.

In two separate reports by Zhao *et al.*[49] and Sun *et al.*[50] dinuclear metallocyclic complexes were synthesised by first reacting a Zn(II) metal with a dicarboxylate chelating moiety thereby forming a 'semi-protected' metal cation in which part of the coordination sphere is already occupied by the spectator chelate ligand (**Scheme 6**). The metal centre is thus pre-organised and reaction with a divergent ligand is more likely to yield the desired discrete species. Based on these structures we suggest future work aimed at synthesising discrete dinuclear metallocyclic complexes should entail an additional step whereby the metal cation is first reacted with a suitable chelating ligand and then only reacted with the ditopic ligand. Several examples of possible chelating ligands are suggested in **Scheme 7**. Furthermore, it is anticipated that the added rigidity might provide support to the host framework and reduce the chance of ligand rearrangement upon desolvation.

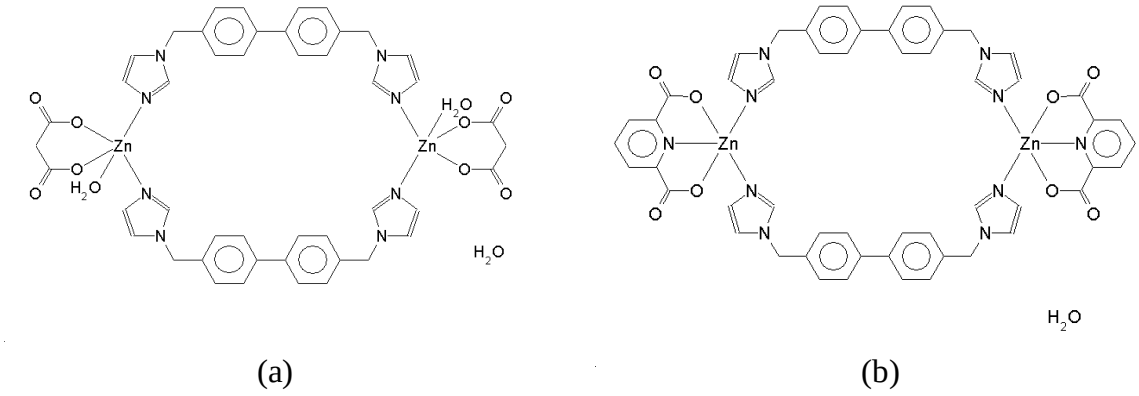

(a) (b)

Scheme 6. (a) Complex synthesised by Zhao *et al.*[49] utilising malonic acid as a chelating moieity (CSD refcode: **IZIPAI**). **(b)** Complex synthesised by Sun *et al.*[50] utilising pyridine-2,6-dicarboxylate as a chelating moiety (CSD refcode: **PEVJIK**).

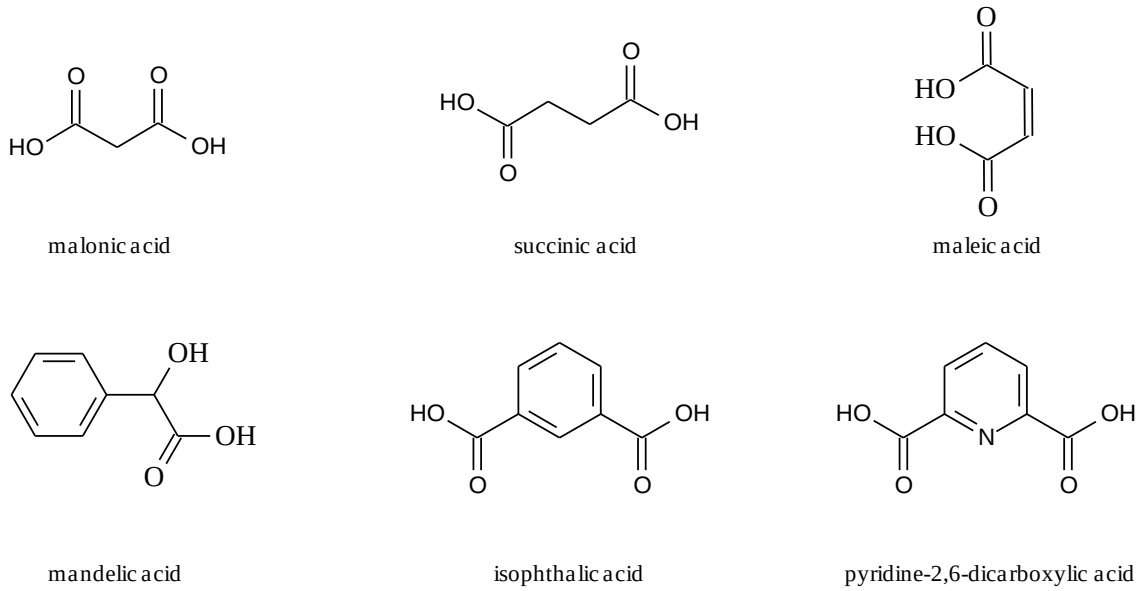

malonic acid succinic acid maleic acid

mandelic acid isophthalic acid pyridine-2,6-dicarboxylic acid

Scheme 7. Possible chelating di-acids that could be used in the synthesis of discrete metallocycles.

2.2.6. Towards the development of a high-throughput approach to the synthesis of novel 0D porous metallocycles

As previously mentioned, the synthesis of new or targeted crystalline compounds occurs *via* a systematic study of the experimental parameter space; this involves varying the composition and molar ratios of the starting products as well as the conditions of crystallisation e.g. temperature, pH, reaction time etc. Experimental arrays intended to probe the effects of only one parameter are reasonably undemanding in terms of time.

However, simultaneous investigations of many parameters increases the number of potential experiments to a value that is often impractical and not feasible within the time contraints of a typical project. With a view to addressing these issues, combinatorial and high-throughput (HT) methods have been suggested as a rapid and systematic method in which a wide range of experimental conditions can be investigated in a short period of time.[51-55]

Combinatorial chemistry involves the synthesis and characterisation of large numbers of distinct, yet structurally related compounds, and is usually carried out using HT-methods.[56] Historically, combinatorial and HT-techniques have been used in the pharmaceutical industry to specifically improve the time-to-market aspect of drug development, and it is only over the past decade that this field has expanded to include inorganic-organic hybrid compounds. To date, most of the inorganic-organic hybrid systems investigated by HT-methods have been studied with the ultimate goal of forming 3D framework structures[52,54,55] and, as yet, there are no reports in the literature that utilise HT-techniques to screen reaction conditions aimed at producing discrete porous systems. Of particular relevance to this study is the HT-method reported by Yaghi and co-workers in the synthesis of the 3D porous zeolitic imidazolate frameworks (ZIFs), utilising Zn(II)/Co(II) and imidazolate-derived links.[55] In that study, a HT protocol is described in which 25 different ZIF crystals were isolated from 9600 microreactions in a 3 month period; prior to the date of that publication only 24 ZIF structures had been reported in the preceding 12 year period. Whilst the isolation of 25 products is in itself a prodigious result, if the number of individual microreactions is taken into account this is only a 0.26% success rate, i.e. only 1 in every 384 experiments produced the desired product. Given the low success rate it is likely that a project of this kind would have been abandoned in the timeframe it would have taken to manually set up this many reactions and analyse the resulting products. We believe that an adaptation of the HT-methods documented in Yaghi's study could be applied to improve the efficiency and productivity of future work aimed at producing 0D porous metallocycles.

2.2.6.1. Development of a HT-protocol

The first step in the development of a HT-protocol is the construction of an in-house database containing all relevant information regarding experiments carried out within the group; only once this database is fully functional should a HT-protocol be employed. In

the following section the salient features of this database will be discussed and an outline of a HT protocol that could be implemented within our laboratory is provided. The four major aspects to consider in the development of HT-techniques are: design of the experiment, synthesis, characterisation and data evaluation. Each step will be described and the advantages and disadvantages of the HT-technique will be discussed in relation to our current methodologies. A work-flow chart is provided at the end of the section.

2.2.6.1.1. Database

The Cambridge Structural Database (CSD) is an invaluable resource available to crystal engineers; one of its many functions is to provide information that will prevent the collection of full single-crystal datasets of already published work. The obvious limitation to this tool is that it only contains structures documented in the literature and does not provide information regarding previous experimental conditions and unpublished structures obtained within a specific research group. The ready availability of this information acquired by prior members of our group is vital to the successful implementation of a HT-protocol aimed at producing novel porous materials – therefore it is imperative that, at the outset of the project, an in-house database should be constructed to contain all relevant information of previously studied systems. A typical entry should include: reaction parameters, conditions of crystallisation, the nature of the product obtained (i.e. single crystals or powder), as well as providing access to any diffraction data such as experimental and simulated powder patterns and crystallographic information files. The database should also have a built-in search function allowing the user to browse the entries by multiple criteria. Finally, this database should be available to all members of the group and it should be routinely updated.

2.2.6.1.2. Design of the experiment

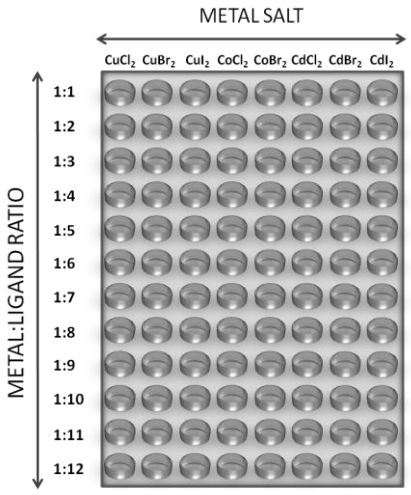

Figure 37. A schematic representation of a 96-well set-up that could be used in our laboratory.

It is imperative that the experimental design allows for the parallel investigation of many reaction parameters. This is most optimally achieved by taking a combinatorial chemistry approach. In a typical set up of this type, 96-well glass plates or a multi-autoclave unit are used as the reaction vessel and each vessel allows for 0.300 mL of reactant volume. The next step in the experimental design entails establishing which of the reaction parameters should be varied and which should remain constant, as well as deciding the method of crystallisation, e.g. solvothermal or slow evaporation etc. Stock solutions of the respective metal salt component and organic ligand are then prepared and dispensed by means of a programmed liquid handler in the required molar quantities. **Figure 37** shows an example of a 96-well plate that could potentially be used in our laboratory to screen for 0D metallocyclic compounds utilising the method of slow evaporation. The autoclave described in HT-method reported by Yaghi and co-workers[55] would be more suited for solvothermal crystallisations. In this hypothetical experiment, the ligand, temperature profile, solvent, concentration of the reagents and method of crystallisation are kept constant and the metal ion, metal-to-ligand solution ratio and counter-ion are varied.

2.2.6.1.3. Synthesis

In this step the actual method of crystallisation is carried to completion, and has with it an associated ‘ageing’ time – for solvothermal methods this would be the time taken for the heating and cooling process to occur, and for slow evaporation experiments this would be

the time allowed for enough solvent to evaporate to saturate the solution sufficiently such that, in the best case scenario, crystals are formed. This 'ageing' time is an important parameter and should be noted.

2.2.6.1.4. Characterisation

After the reaction time has lapsed, all vessels need to be visually inspected under a microscope, preferably an automated high speed optical microscope, and the phase of the sample i.e. powder or single crystals, must be recorded. The products of the different reaction vessels then need to be isolated and characterised by X-ray diffraction methods – this should be done in two stages. First, the vials containing single crystals need to be subjected to single crystal X-ray diffraction – the unit cells must be determined and checked against the CSD and the in-house database. If the unit cell is new then a full dataset must be collected. In the second stage, all products must be characterised by powder X-ray diffraction – this is accomplished by utilising a HT horizontal *x-y* stage attachment in the PXRD instrument. Isolation of the sample array is achieved in parallel by sonication and transfer of the solid to the PXRD multiple sample holder. All powder data should be collected using a standard program and checked against the database in order to determine if the material under study is a new phase or one that has already been characterised. All new PXRD data must be logged into the in-house database.

2.2.6.1.5. Data evaluation

This step involves structural elucidation from the diffraction data to determine if a novel material adhering to the design principle was formed. At present this information is predominantly attained from single-crystal data. However, with the advances in high quality powder diffraction data and the availability of user friendly software, structural elucidation from powder is rapidly attaining routine status in many research groups. In the next step, all new structures, even those not adhering to the design principle, must be entered into the database. The products of successful experiments (i.e. 0D metallocyclic complexes), or indeed the products of unsuccessful experiments that may have yielded systems that are potentially interesting for other applications, should be investigated further. If the experiment does not yield any useful results, the reaction conditions should be re-evaluated and the parameters for the next experiment should be established.

2.2.6.1.6. Advantages and disadvantages

The successful implementation of a HT method has many advantages associated with it. In the experimental setup the stock solutions of the requisite ligand and metals salt are dispensed in 0.300 mL quantities. This avoids errors associated with manually weighing out accurate milligram quantities of reagents and ensures reproducibility as well as preventing uneconomical consumption of large volumes of solvent. In the synthesis step the 'ageing' or reaction time is carefully noted and carried out for an entire batch of reactions, the obvious advantage is again that of consistency and ease of reproducibility of the reaction conditions. The combinatorial approach allows the simultaneous and rapid investigation of many different parameters and the products of these reactions can be quickly characterised by diffraction methods and screened against libraries of published and unpublished data contained within the in-house database. As a consequence of this, an experiment that would normally take months or even years to complete can be accomplished in a matter of weeks. The in-house database will also allow access to experimental design strategies utilised by prior members of the group. This is advantageous as it will prevent unnecessary replication of reaction conditions. Furthermore, once the database contains a significant number of entries it will be possible to determine reaction trends, which will lead to a better understanding of the relationship between reaction conditions and the nature of the product formed. This will contribute substantially to the further development of crystal engineering of metallocycles. The most obvious disadvantage of the HT method is the high initial cost of the tools required to execute each step in the workflow. This may be somewhat offset by the improved efficiency of the HT-system and a reduction in the number of redundant data collections.

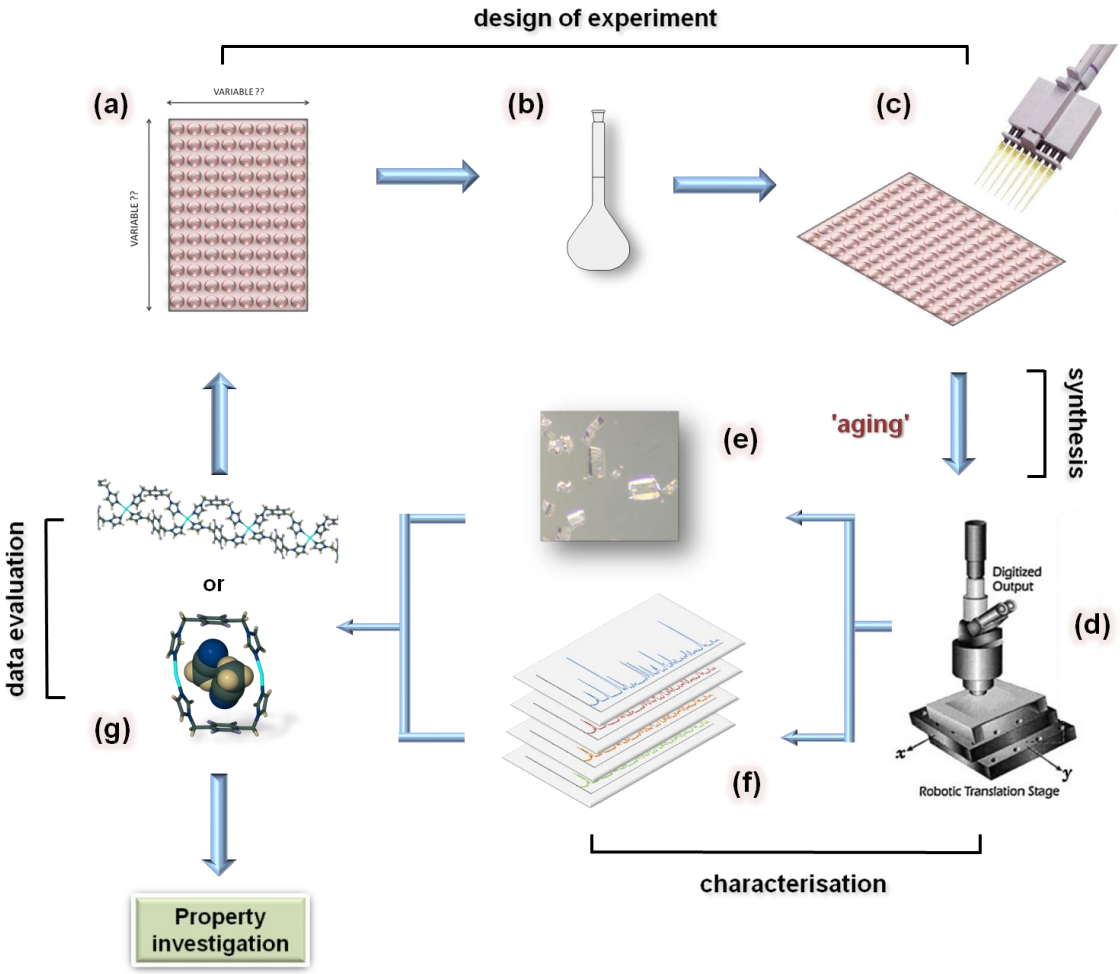

Figure 38. A workflow for a HT-protocol. The experimental information and data obtained during each step should be carefully recorded and entered into the database; **(a)** decide on the reaction variables, **(b)** prepare stock solutions of reagents, **(c)** dispense solutions of reagents by means of a programmed liquid handler in required molar quantities, **(d)** once the synthesis is complete, visually inspect the contents of vials using a high speed optical microscope, **(e)** single crystals must be subjected to singe-crystal X-ray diffraction – determine unit cell – if novel, collect structure, **(f)** all products must be characterised by PXRD utilising a HT horizontal *x-y* stage attachment and **(g)** structural elucidation from the diffraction data – products from successful experiments should be investigated further, if the experiment did not yield useful results – re-evaluate and determine the parameters for the next experiment.

2.3. CONCLUSION

The aim of the present study was to synthesise novel porous materials based on a 0D "doughnut-shaped" metallocycle design principle. This type of structure requires two ligand molecules in the *cis* conformation to complex to two metal cations to form a discrete closed-ring structure. The ligands employed in the synthesis of these compounds must therefore be flexible and contain functional groups capable of coordinating to metal cations. To this end, four flexible ditopic imidazole ligands **L1** – **L4** were synthesised; each comprises two imidazole moieties tethered to a variable aromatic core by means of methylene linkers. The rationale behind this ligand design is that the methylene linkers can act as hinges facilitating the rotation of the coordinating imidazole groups around the rigid aromatic spacer. As a consequence of this flexibility the ligands are able to adopt many conformations that broadly fall into one of two categories – *cis* or *trans*. The four ligands were then reacted with a variety of transition metal salts in a systematic manner. The structures of 29 novel coordination complexes were elucidated by means of single- crystal X-ray diffraction: fifteen complexes contain **L1**, three contain **L2**, four contain **L3** and eight contain **L4**. Of the 29 coordination complexes elucidated, 5 porous metallocycles were isolated and these structures are treated separately in Chapter 3.

With the exception of complex **13** (a 0D metal-ligand salt) and **20** (a 0D non-porous dinuclear metallocycle) the remaining structures all formed extended polymeric structures. 14 structures were classified as 1D strands – where the metal centres are directly connected to one another by virtue of one or two bridging ligands and 8 structures were classified as 2D network structures. The dimensionality of all of these structures can be increased when other non-covalent interactions such as hydrogen bonding and π–π stacking interactions are taken into account.

An attempt was made to analyse the thermal behaviour of all structures containing lattice or coordinated solvent molecules. Unfortunately, we were not able to obtain a single-crystal structure for the solvent-free phase in any of these cases as thermal analysis revealed that either solvent loss occurs concurrently with the decomposition of the sample, or thermal release of solvent from the lattice resulted in fracturing of the crystals into a polycrystalline material.

In one case, concomitant crystallization of two different crystal forms was observed i.e. the reaction of **L4** with $AgPF_6$ in methanol yielded complexes **17** and **18**. It is

surprising that only one example of this kind was found given that the PXRD data indicated the presence of more than one phase in the bulk crystalline material obtained in several of the reaction vials. This may be due to the fact that the different forms cannot be distinguished based purely on visual inspection of the crystals, i.e. they may be similar in colour and morphology.

A comparison of the structures of **7** and **10** with each other leads to an interesting note on classification; the 2D frameworks of **7** and **10** are identical apart from the fact that **7** contains Cd(II) ions and **10** contains Mn(II) ions. However, the two structures cannot be considered isostructural as the solvents contained within the frameworks differ. It was therefore suggested that the term 'isoskeletal' be used to describe the relationship between **7** and **10**. The same is true for structure **9** and the literature structure **ECALOK** (CSD refcode); in both structures identical 1D chains are formed, except that in **9** the **L1** molecules connect Mn(II) ions to one another and in **ECALOK** the **L1** molecules connect Cd(II) ions to one other. Again different solvent molecules are present in the lattice of each; therefore **9** and **ECALOK** are also classed as 'isoskeletal'.

It was further suggested that future efforts regarding the synthesis of dinuclear metallocycles could be aided by pre-organisation of the metal centres via the reaction of the metal cation with a suitable chelating moiety, prior to the reaction of the metal with the organic ligand. Several organic di-acids were suggested as possible spectator chelating ligands.

In the final section of this chapter a high-throughput protocol was outlined that could potentially be implemented in our laboratory to streamline further studies aimed at producing porous metallocyclic materials. It was concluded that a combinatorial approach, coupled with HT methods would be an efficient and systematic means of exploring a wide parameter space in a short period of time. We believe that a successful implementation of these methods could aid in reducing redundant data collections, as part of this process is the development of an in-house database that contains all relevant information regarding experimental conditions carried out by previous members of the group. A further advantage of the in-house database is that, once sufficient data have been collected, it should be possible to identify trends that will allow us to gain insight into the relationship between reaction conditions and the nature of the product formed, thereby limiting the role of serendipity in the discovery of novel porous materials.

2.4. EXPERIMENTAL

2.4.1. Synthesis and characterisation

2.4.1.1. 2,3,5,6-Tetrafluoro-1,4-bis(imidazol-1-yl-methyl)benzene (L1)

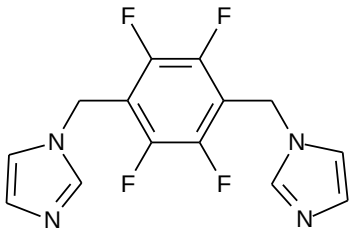

L1 was synthesised by the method of Gao *et al.*[43] A solution containing imidazole (3.40 g, 50.0 mmol) and 1,4-bis(chloromethyl)-2,3,5,6-tetrafluorobenzene (1.23 g, 5.00 mmol) in 60 mL MeOH was heated under reflux for 18 hours. Removal of the solvent under reduced pressure left a colourless oil that was dissolved in aqueous K_2CO_3 (6.5 g, 100 mL). Upon standing, this solution yielded crystalline **L1**, which was filtered, washed with H_2O (3 × 20 mL) and dried *in vacuo* for 24 hours. Yield: 89.1%; ^{1}H–NMR ($CDCl_3$, 400 MHz): δ 5.21 (4H, s), 6.96 (2H, s), 7.04 (2H, s), 7.57 (2H, s); ^{13}C–NMR ($CDCl_3$, 75.5 MHz): δ 37.6 (m), 115.8 – 116.0 (m), 118.8, 130.3, 137.2, 142.8–143.2 (m), 146.2–146.2 (m); ^{19}F–NMR ($CDCl_3$, 282 MHz): δ –143.6. These values agree well with those obtained in the literature.

2.4.1.2. 2,3,5,6-Tetrafluoro-1,4-bis(2-isopropylimidazole-1-yl-methyl)benzene (L2)

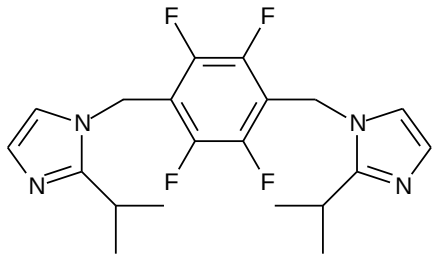

A solution containing isopropylimidazole (3.00 g, 27.0 mmol) and 1,4-bis(bromomethyl)-2,3,5,6-tetrafluorobenzene (0.932 g, 2.70 mmol) in 60 mL MeOH was heated under reflux for 18 hours. Removal of the solvent under reduced pressure left a colourless oil that was dissolved in aqueous K_2CO_3 (6.5 g, 100 mL). Upon standing, this solution yielded crystalline **L2**, which was filtered, washed with H_2O (3 × 20 mL) and dried *in vacuo* for 24 hours. Yield: 65.7%; m.p.: 99 – 104 ºC; IR (golden–gate accessory): νmax 3230, 2971, 1665, 1485, 1465, 1367, 1269, 1103, 1072, 1016, 924, 862, 768, 735, 688 cm^{-1}; ^{1}H–NMR ($CDCl_3$, 400 MHz): δ 1.32 (12H, d, J = 6.8 Hz), 3.143 (2H, m), 5.16 (4H, s), 6.79 (2H, s), 6.93 (2H, s); ^{13}C–NMR ($CDCl_3$, 75.5 MHz): δ 21.8, 25.6, 36.7, 115.4–116.1 (m), 118.5, 127.9, 142.9–143.4 (m), 146.4–146.8 (m), 153.1; ^{19}F–NMR ($CDCl_3$, 282 MHz)): δ –144.0; MS (ESI$^+$): m/z 395 (40%, M^+), 353 (20%, M^+ – isopropyl), 286 (10%, M^+ – isopropylimidazole).

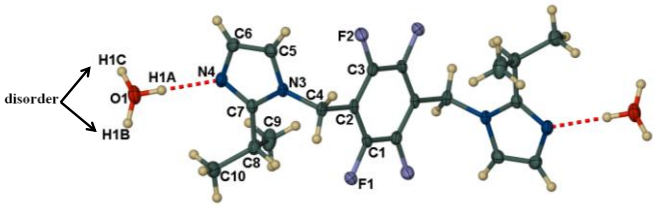

Figure 39. The molecular structure of **L2**; displacement ellipsoids are drawn at the 50% probability level and H atoms are shown as spheres of arbitrary radius. Atoms of the ASU have been labelled.

Single crystals of **L2** were obtained by slow evaporation of a methanolic solution of the ligand. **L2** crystallises in the monoclinic space group $P2_1/c$ (see **Table 21**). The ASU consists of half a ligand molecule situated about an inversion centre and a water molecule in a general position. The ligand therefore adopts the *trans* conformation with the two imidazole groups located on opposite sides relative to the central aromatic plane. **Figure 39** displays a perspective view of the molecular structure of **L2**. The ligand molecules are connected to one another through a series of hydrogen bonds to form a 2D sheet; one of the hydrogen atoms of the water molecule participates in a hydrogen bond with the imino nitrogen of the imidazole group ($O_{donor}\cdots N_{acceptor}$ = 2.900(2)Å) and is locked in position. The second hydrogen atom participates in a hydrogen bond with an adjacent water molecule ($O_{donor}\cdots O_{acceptor}$ = 2.960(3)Å), but is disordered over two sites of equal occupancy. Three columns of hydrogen bonding motifs are represented in **Figure 40**; the central column represents the disordered model and the left and right columns represent possible hydrogen bonding scenarios – in these scenarios H1B and H1C alternate along the hydrogen bonded chain.

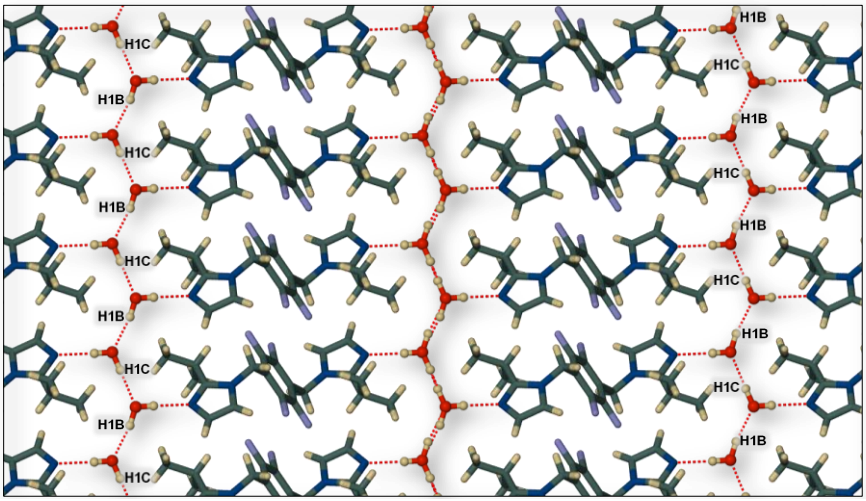

Figure 40. Packing arrangement of **L2** as viewed down [100]. Three hydrogen bonding columns are shown. The central column represents the disordered model and the left and right columns show possible hydrogen bonding scenarios. Ligand molecules are shown as capped sticks and water molecules in the ball-and-stick metaphor.

2.4.1.3. 1,3-Bis(2- isopropylimidazole-1-yl-methyl)-2,4,6-trimethylbenzene (L3)

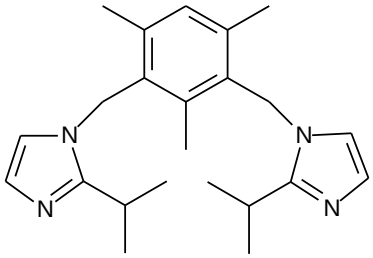

Isopropylimidazole (1.37 g, 12.5 mmol), 2,4-bis(chloromethyl)-1,3,5-trimethylbenzene (1.09 g, 5.00 mmol) and K_2CO_3 (4.45 g, 32.5 mmol) were suspended in 60 mL acetonitrile. The reaction was then stirred under reflux for 18 hours. The reaction mixture was an orange solution, over a beige precipitate. The precipitate was removed by filtration and the solvent was then removed under reduced pressure to produce a dark orange oil. The product was then precipitated by slowly adding the oil to water and filtered. Yield: 66.7%; m.p.: 124 – 126 ºC; IR (golden–gate accessory): νmax 3380, 2960, 1603, 1492, 1426, 1384, 1337, 1261, 1223, 1097, 929, 889, 847, 756 cm^{-1}; ^{1}H–NMR ($CDCl_3$, 400 MHz): δ 1.39 (12H, d, *J* = 6.8Hz), 2.08 (3H, s), 2.28 (6H, s), 3.16 (2H, m), 5.00 (4H, s), 6.82 (4H, s), 7.04 (1H, s); ^{13}C-NMR ($CDCl_3$, 75.5 MHz): δ 15.2, 19.8, 21.5, 26.3, 43.8, 116.9, 126.7, 130.2, 131.2, 137.8, 138.5, 152.6; MS (ESI^+): m/z 365 (100%, M^+).

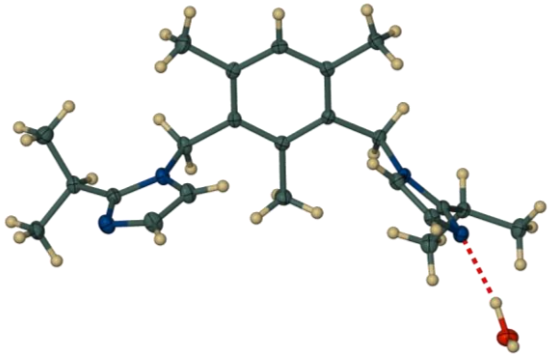

Figure 41. The ASU of **L3**; displacement ellipsoids are drawn at the 50% probability level and H atoms are shown as spheres of arbitrary radius.

Single crystals of **L3** were obtained by slow evaporation of a methanolic solution of the ligand. **L3** crystallises in the monoclinic space group $P2_1/c$ (see **Table 21**). The ASU consists of one molecule of **L3** in the *cis* conformation and one water molecule (**Figure 41**). The water molecules are hydrogen bonded to two imino nitrogens from separate ligand molecules ($O_{donor}\cdots N_{acceptor}$ = 2.937(2) and 2.940(1) Å). This serves to connect the ligand molecules into a 1D spiral running parallel to [010] (**Figure 42**). **Figure 43** shows the final packing arrangement in which the 1D spirals interdigitate along [010].

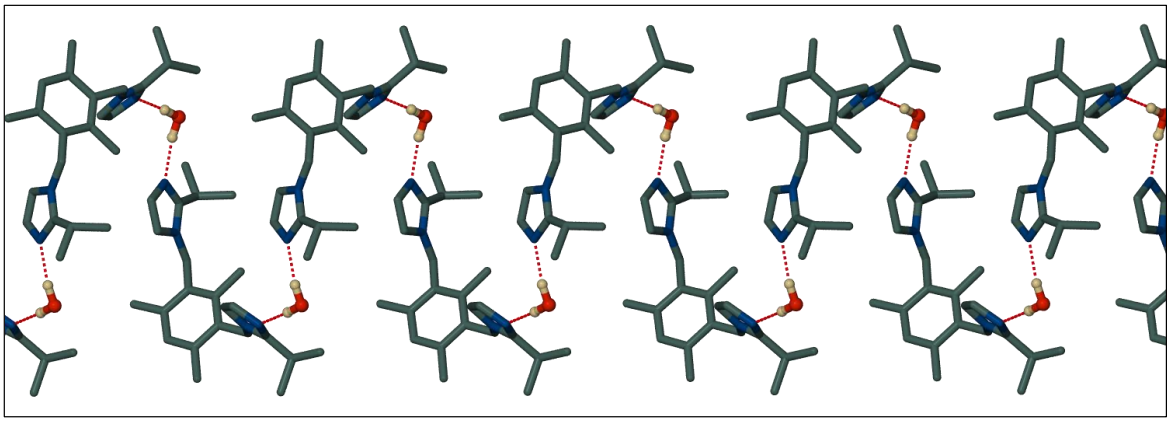

Figure 42. The 1D spirals formed in **L3** as viewed perpendicular to [010]; ligand molecules are shown as capped-sticks and water molecules are shown in the ball-and-stick metaphor. Hydrogen atoms of the ligand molecules have been omitted for clarity.

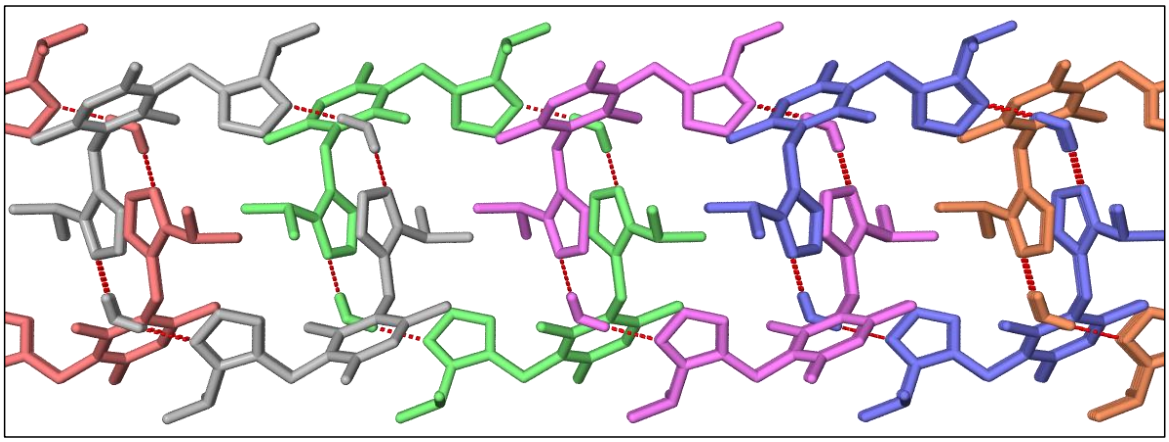

Figure 43. Packing arrangement of **L3** showing the interdigitation of the 1D spirals as viewed down [010]. The 1D spirals have all been represented in a different colour to distinguish them from one another. Molecules are shown in capped-stick representation and hydrogen atoms of the ligand molecules have been omitted for clarity.

2.4.1.4. 1,4-Bis(4,5-dichloroimidazole-1-yl-methyl)benzene

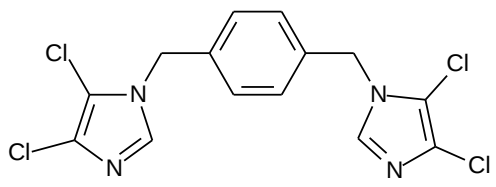

4,5-Dichloroimidazole (0.500 g, 3.65 mmol), α-α'-dibromo-*p*-xylene (0.389 g, 1.46 mmol) and K_2CO_3 (1.31 g, 9.50 mmol) were suspended in 60 mL acetonitrile. The reaction was then stirred under reflux for 18 hours. After this the reaction mixture was a pink solution over a beige precipitate. The precipitate was removed by filtration and the solvent was then removed under vacuum to produce a dark orange oil. The crude product was then taken up in 20 mL chloroform and washed with water. The chloroform layer was then isolated and the solvent removed under reduced pressure to yield a white solid.

Yield: 73.2 %; m.p.: 157 – 159 ºC; IR (golden–gate accessory): νmax 3099, 1612, 1517, 1482, 1427, 1389, 1347, 1313, 1251, 1211, 1178, 1113, 981, 853, 807, 746 cm^{-1}; ^{1}H–NMR ($CDCl_3$, 400 MHz): δ 5.09 (4H, s), 7.18 (4H, s), 7.42 (2H, s); ^{13}C–NMR ($CDCl_3$, 75.5 MHz): δ 49.2, 113.6, 126.6, 128.0, 134.4, 134; MS (ESI^+): m/z 377 (100%, M^+), 239 (8%, M^+ – 4,5–dichloroimidazole). Unfortunately we were not able to obtain a single-crystal structure for **L4**.

2.4.2. Crystallographic data

Table 21. Crystallographic data for complexes **1**–**24** and free ligands **L2** and **L3**.

	1	**2**	**3**	**4**	**5**
Empirical formula	$C_{28}H_{20}AgBF_{12}N_8$	$C_{18}H_{16}AgF_{10}N_6P$	$C_{31}H_{26}Ag_2F_{20}N_8OP_2$	$C_{21}H_{15}CdCl_2F_6N_6$	$C_{21}H_{15}Br_2CdF_6N_6$
Formula weight	815.20	645.21	1184.28	648.69	737.61
Temperature (K)	100(2)	100(2)	100(2)	100(2)	100(2)
Wavelength (Å)	0.71073	0.71073	0.71073	0.71073	0.71073
Crystal system	triclinic	triclinic	triclinic	monoclinic	monoclinic
Space group	$P\bar{1}$	$P\bar{1}$	$P\bar{1}$	$P2_1/n$	$P2_1/n$
a (Å)	10.7356(13)	7.9988(6)	8.1094(8)	16.2571(10)	16.5376(10)
b (Å)	11.6853(15)	8.1450(6)	8.2490(8)	8.1935(5)	8.4810(5)
c (Å)	12.6996(16)	8.7644(6)	17.3009(16)	18.3308(11)	18.5386(12)
α (°)	68.4900(10)	86.1910(10)	84.0800(10)	90	90
β (°)	82.6040(10)	81.8680(10)	84.4450(10)	104.0480(10)	105.1330(10)
γ (°)	83.4180(10)	81.8790(10)	84.1030(10)	90	90
V (Å^3)	1465.9(3)	558.96(7)	1140.72(19)	2368.7(2)	2510.0(3)
Z	2	1	1	4	4
D_c (g/cm^3)	1.847	1.917	1.724	1.819	1.952
Absorption coefficient	0.802	1.077	1.046	1.218	4.121
F_{000}	808	318	580	1276	1420
Reflections collected	17176	6127	12120	13580	15965
Independent reflections	6898 [R_{int} = 0.0113]	2422 [R_{int} = 0.0125]	4865 [R_{int} = 0.0174]	5146 [R_{int} = 0.0185]	5989 [R_{int} = 0.0257]
Goodness-of-fit on F^2	1.036	1.042	1.091	1.025	1.017
Final R indices [I>2σ(I)]	$R1$ = 0.0192, $wR2$ = 0.0501	$R1$ = 0.0199, $wR2$ = 0.0533	$R1$ = 0.0373, $wR2$ = 0.1097	$R1$ = 0.0232, $wR2$ = 0.0562	$R1$ = 0.0324, $wR2$ = 0.0678
R indices (all data)	$R1$ = 0.0203, $wR2$ = 0.0508	$R1$ = 0.0201, $wR2$ = 0.0534	$R1$ = 0.0398, $wR2$ = 0.1125	$R1$ = 0.0277, $wR2$ = 0.0591	$R1$ = 0.0532, $wR2$ = 0.0751

	6	**7**	**8**	**9**	**10**
Empirical formula	$C_{14}H_{10}CdF_4I_2N_4$	$C_{22}H_{19}CdF_6N_8O_7$	$C_{36}H_{32}CoF_8N_{14}O_6$	$C_{43}H_{38}F_{12}MnN_{14}O_{10}$	$C_{23}H_{18}F_6MnN_9O_6$
Formula weight	676.46	733.85	967.69	1193.81	685.40
Temperature (K)	100(2)	100(2)	100(2)	100(2)	100(2)
Wavelength (Å)	0.71073	0.71073	0.71073	0.71073	0.71073
Crystal system	triclinic	monoclinic	triclinic	triclinic	monoclinic
Space group	$P\bar{1}$	$P2_1/n$	$P\bar{1}$	$P\bar{1}$	$P2_1/n$
a (Å)	9.4653(15)	13.968(3)	8.4117(10)	10.2241(11)	13.8611(15)
b (Å)	9.6553(15)	14.829(3)	10.7777(13)	11.6828(12)	15.0751(17)
c (Å)	10.8463(17)	14.451(3)	12.7316(15)	12.0433(13)	14.3181(16)
α (°)	103.072(2)	90	68.2570(10)	104.0330(10)	90
β (°)	100.717(2)	116.696(3)	71.9180(10)	103.2990(10)	111.9130(10)
γ (°)	92.036(2)	90	87.9480(10)	112.5160(10)	90
V (Å^3)	945.6(3)	2674.1(10)	1015.1(2)	1202.6(2)	2775.7(5)
Z	2	4	1	1	4
D_c (g/cm^3)	2.376	1.823	1.583	1.648	1.640
Absorption coefficient	4.461	0.918	0.525	0.395	0.573
F_{000}	624	1460	493	607	1384
Reflections collected	11160	16388	11876	14277	17359
Independent reflections	4496 [R_{int} = 0.0282]	6375 [R_{int} = 0.0531]	4780 [R_{int} = 0.0244]	5719 [R_{int} = 0.0184]	6591 [R_{int} = 0.0387]
Goodness-of-fit on F^2	1.022	0.997	1.035	1.034	1.038
Final R indices [$I>2\sigma(I)$]	$R1$ = 0.0314, $wR2$ = 0.0640	$R1$ = 0.0439, $wR2$ = 0.0916	$R1$ = 0.0374, $wR2$ = 0.0933	$R1$ = 0.0398, $wR2$ = 0.1024	$R1$ = 0.0445, $wR2$ = 0.0970
R indices (all data)	$R1$ = 0.0397, $wR2$ = 0.0666	$R1$ = 0.0668, $wR2$ = 0.1027	$R1$ = 0.0448, $wR2$ = 0.0970	$R1$ = 0.0448, $wR2$ = 0.1056	$R1$ = 0.0672, $wR2$ = 0.1063

	11	**12**	**13**	**14**	**15**
Empirical formula	$C_{21}H_{26}CdF_4I_2N_4O$	$C_{20}H_{22}Cl_2F_4N_4Ni$	$C_{23}H_{35}CdCl_3N_4O$	$C_{24}H_{34}Br_2CdCl_2N_4$	$C_{23}H_{32}CdI_2N_4$
Formula weight	792.66	524.03	602.30	721.67	730.73
Temperature (K)	100(2)	100(2)	100(2)	100(2)	100(2)
Wavelength (Å)	0.71073	0.71073	0.71073	0.71073	0.71073
Crystal system	triclinic	triclinic	monoclinic	monoclinic	monoclinic
Space group	$P\bar{1}$	$P\bar{1}$	$P2_1/c$	$P2_1/n$	$P2_1/c$
a (Å)	10.0405(10)	9.545(5)	15.228(7)	14.324(4)	8.2520(5)
b (Å)	10.6157(10)	9.746(5)	15.588(7)	13.005(3)	13.0199(7)
c (Å)	12.7169(13)	13.137(7)	11.177(5)	15.901(4)	23.8576(13)
α (°)	77.8250(10)	70.601(7)	90	90	90
β (°)	85.9620(10)	70.145(7)	93.987(7)	107.565(3)	94.1370(10)
γ (°)	81.2110(10)	81.368(7)	90	90	90
V (Å^3)	1308.4(2)	1083.2(10)	2647(2)	2823.9(12)	2556.6(2)
Z	2	2	4	4	4
D_c (g/cm^3)	2.012	1.607	1.512	1.697	1.898
Absorption coefficient	3.243	1.192	1.150	3.812	3.286
F_{000}	756	536	1232	1432	1408
Reflections collected	15379	5274	14496	15405	14627
Independent reflections	6181 [R_{int} = 0.0161]	5274 [R_{int} = 0.0873]	6183 [R_{int} = 0.0484]	6492 [R_{int} = 0.0462]	5842 [R_{int} = 0.0182]
Goodness-of-fit on F^2	1.028	1.059	1.028	1.036	1.152
Final R indices [$I>2\sigma(I)$]	$R1$ = 0.0278, $wR2$ = 0.0737	$R1$ = 0.1076, $wR2$ = 0.3141	$R1$ = 0.0427, $wR2$ = 0.0930	$R1$ = 0.0492, $wR2$ = 0.1153	$R1$ = 0.0290, $wR2$ = 0.0725
R indices (all data)	$R1$ = 0.0296, $wR2$ = 0.0748	$R1$ = 0.1688, $wR2$ = 0.3371	$R1$ = 0.0713, $wR2$ = 0.1048	$R1$ = 0.0902, $wR2$ = 0.1307	$R1$ = 0.0304, $wR2$ = 0.0732

	16	**17**	**18**	**19**	**20**
Empirical formula	$C_{48}H_{72}Cl_4N_8O_2Zn_2$	$C_{42}H_{29}Ag_2Cl_{12}F_{12}N_{12}P_2$	$C_{28}H_{20}AgCl_8F_6N_8P$	$C_{14}H_{10}Br_2CdCl_4N_4$	$C_{28}H_{20}Cd_2Cl_8I_4N_8$
Formula weight	1065.68	1632.85	1004.96	648.28	1484.52
Temperature (K)	100(2)	100(2)	100(2)	100(2)	100(2)
Wavelength (Å)	0.71073	0.71073	0.71073	0.71073	0.71073
Crystal system	triclinic	orthorhombic	monoclinic	triclinic	monoclinic
Space group	$P\bar{1}$	$Pca2_1$	$C2/c$	$P\bar{1}$	$P2_1/n$
a (Å)	12.3361(12)	20.2171(11)	13.8786(11)	9.6310(6)	11.9242(6)
b (Å)	13.6482(14)	9.9408(5)	19.7169(15)	10.1437(6)	10.9177(6)
c (Å)	16.6486(17)	28.7979(15)	15.1423(12)	10.4487(6)	16.9470(9)
α (°)	93.8640(10)	90	90	92.1400(10)	90
β (°)	110.7620(10)	90	105.1160(10)	92.5520(10)	110.0520(10)
γ (°)	96.3970(10)	90	90	100.5850(10)	90
V (Å^3)	2587.4(5)	5787.6(5)	4000.2(5)	1001.33(10)	2072.50(19)
Z	2	4	4	2	2
D_c (g/cm^3)	1.368	1.874	1.669	2.150	2.379
Absorption coefficient	1.179	1.371	1.139	5.620	4.554
F_{000}	1120	3204	1984	616	1376
Reflections collected	30945	32363	11496	11907	12985
Independent reflections	12257 [R_{int} = 0.0559]	11407 [R_{int} = 0.0407]	4291 [R_{int} = 0.0224]	4741 [R_{int} = 0.0193]	4938 [R_{int} = 0.0226]
Goodness-of-fit on F^2	1.046	1.024	1.042	1.040	1.029
Final R indices [$I>2\sigma(I)$]	$R1$ = 0.0506, $wR2$ = 0.1065	$R1$ = 0.0383, $wR2$ = 0.0864	$R1$ = 0.0359, $wR2$ = 0.0887	$R1$ = 0.0189, $wR2$ = 0.0427	$R1$ = 0.0225, $wR2$ = 0.0477
R indices (all data)	$R1$ = 0.0917, $wR2$ = 0.1235	$R1$ = 0.0466, $wR2$ = 0.0914	$R1$ = 0.0441, $wR2$ = 0.0941	$R1$ = 0.0210, $wR2$ = 0.0434	$R1$ = 0.0284, $wR2$ = 0.0501

	21	**22**	**23**	**24**	**L2**	**L3**
Empirical formula	$C_{18}H_{20}Cl_4CoN_8O_8$	$C_{15}H_{12}Cl_8CuN_4$	$C_{14}H_{10}Br_2Cl_4CuN_4$	$C_{14}H_{10}Cl_6N_4Zn$	$C_{20}H_{26}F_4N_4O_2$	$C_{23}H_{34}N_4O$
Formula weight	677.15	595.43	599.42	512.33	430.45	382.54
Temperature (K)	100(2)	100(2)	100(2)	100(2)	100(2)	100(2)
Wavelength (Å)	0.71073	0.71073	0.71073	0.71073	0.71073	0.71073
Crystal system	monoclinic	triclinic	monoclinic	monoclinic	monoclinic	monoclinic
Space group	$P2_1/n$	$P\bar{1}$	$P2_1/n$	$P2_1/c$	$P2_1/c$	$P2_1/c$
a (Å)	11.5863(10)	9.2922(6)	9.3114(17)	10.0786(8)	12.108(4)	12.862(2)
b (Å)	8.0466(7)	10.9551(7)	13.917(3)	20.6907(17)	5.3872(18)	10.595(2)
c (Å)	14.8088(12)	11.1363(8)	14.799(3)	9.3213(8)	16.127(5)	15.837(3)
α (°)	90	80.9230(10)	90	90	90	90
β (°)	104.7080(10)	77.0820(10)	99.405(2)	91.6750(10)	106.453(4)	94.581(2)
γ (°)	90	87.0380(10)	90	90	90	90
V (Å^3)	1335.4(2)	1090.96(13)	1892.0(6)	1943.0(3)	1008.9(6)	2151.2(7)
Z	2	2	4	4	2	4
D_c (g/cm^3)	1.684	1.813	2.104	1.751	1.417	1.181
Absorption coefficient	1.102	1.991	5.949	2.094	0.118	0.074
F_{000}	686	590	1156	1016	452	832
Reflections collected	7816	11987	11827	10981	5703	12925
Independent reflections	3166 [R_{int} = 0.0150]	4725 [R_{int} = 0.0190]	4433 [R_{int} = 0.0345]	4248 [R_{int} = 0.0197]	2364 [R_{int} = 0.0251]	5100 [R_{int} = 0.0215]
Goodness-of-fit on F^2	1.072	1.059	1.014	1.098	1.027	1.046
Final R indices [$I>2\sigma(I)$]	$R1$ = 0.0240, $wR2$ = 0.0619	$R1$ = 0.0596, $wR2$ = 0.1819	$R1$ = 0.0303, $wR2$ = 0.0590	$R1$ = 0.0244, $wR2$ = 0.0601	$R1$ = 0.0423, $wR2$ = 0.1076	$R1$ = 0.0396, $wR2$ = 0.0937
R indices (all data)	$R1$ = 0.0267, $wR2$ = 0.0633	$R1$ = 0.0642, $wR2$ = 0.1871	$R1$ = 0.0457, $wR2$ = 0.0640	$R1$ = 0.0255, $wR2$ = 0.0608	$R1$ = 0.0487, $wR2$ = 0.1119	$R1$ = 0.0506, $wR2$ = 0.1004

REFERENCES

(1) C. Y. Su; Y. P. Cai; C. L. Chen; M. D. Smith; W. Kaim; H. C. Z. Zoye, *J. Am. Chem. Soc.*, **2003**, *125*, 8595.

(2) M. C. Etter, *J. Am. Chem. Soc.*, **1987**, *109*, 7786.

(3) D. Braga; F. Grepioni; G. R. Desiraju, *Chem. Rev.*, **1998**, *98*, 1375.

(4) V. R. Thalladi; B. S. Goud; V. J. Hoy; F. H. Allen; J. A. K. Howard; G. R. Desiraju, *Chem. Commun.*, **1996**, 401.

(5) M. J. Zaworotko, *Cryst. Growth Des.*, **2007**, *7*, 4.

(6) J.-P. Zhang; X.-M. Chen, *Chem. Commun.*, **2006**, 1689.

(7) O. M. Yaghi; M. O'Keefe; N. W. Ockwig; H. K. Chae; M. Eddaoudi; J. Kim, *Nature*, **2003**, *423*, 705.

(8) A. J. Blake; N. R. Champness; P. Hubberstey; W. S. Li; M. A. Withersby; M. Schroder, *Coord. Chem. Rev.*, **1999**, *183*, 117.

(9) N. M. Okun; T. M. Anderson; K. I. Hardcastle; C. L. Hill, *Inorg. Chem.*, **2003**, *42*, 6610.

(10) D. Farrusseng; S. Aguado; C. Pinel, *Angew. Chem. Int. Ed.*, **2009**, *48*, 7502.

(11) M. Ranocchiari; J. A. v. Bokhoven, *Phys. Chem. Chem. Phys.*, **2011**, *13*, 6388.

(12) F. Vermoortele; R. Ameloot; A. Vimont; C. Serre; D. De Vos, *Chem. Commun.*, **2011**, *47*, 1521.

(13) M. Meilikhov; K. Yusenko; R. A. Fischer, *Dalton Trans.*, **2009**, 600.

(14) M. Meilikhov; K. Yusenko; R. A. Fischer, *Dalton Trans.*, **2010**, 10990.

(15) C. E. Willans; S. French; L. J. Barbour; J.-A. Gertenbach; P. C. Junk; G. O. Lloyd; J. W. Steed, *Dalton Trans.*, **2009**, 6480.

(16) S. Couck; J. F. M. Denayer; G. V. Baron; T. Remy; J. Gascon; F. Kapteijn, *J. Am. Chem. Soc.*, **2009**, *131*, 6326.

(17) F. X. Coudert; C. Mellot-Draznieks; A. H. Fuchs; A. Boutin, *J. Am. Chem. Soc.*, **2009**, *131*, 11329.

(18) L. Hamon; P. L. Llewellyn; T. Devic; A. Ghoufi; G. Clet; V. Guillerm; G. D. Pirngruber; G. Maurin; C. Serre; G. Driver; W. van Beek; E. Jolimaitre; A. Vimont; M. Daturi; G. Ferey, *J. Am. Chem. Soc.*, **2009**, *131*, 17490.

(19) H. G. Zheng; Z. Z. Lu; R. Zhang; Y. Z. Li; Z. J. Guo, *J. Am. Chem. Soc.*, **2011**, *133*, 4172.

(20) J. T. Hupp; G. Lu, *J. Am. Chem. Soc.*, **2010**, *132*, 7832.

(21) M. Melegari; M. Suman; L. Pirondini; D. Moiani; C. Massera; F. Ugozzoli; E. Kalenius; P. Vainiotalo; J.-C. Mulatier; J.-P. Dutasta; E. Dalcanale, *Chem.-Eur. J.*, **2008**, *14*, 5772.

(22) Y. Takashima; S. Furukawa; S. Kitagawa, *CrystEngComm*, **2011**, *13*, 3360.

(23) P. Baxter; J. M. Lehn; A. Decian; J. Fischer, *Angew. Chem., Int. Ed. Engl.*, **1993**, *32*, 69.

(24) P. N. W. Baxter; J. M. Lehn; B. O. Kneisel; G. Baum; D. Fenske, *Chem.-Eur. J.*, **1999**, *5*, 113.

(25) D. P. Funeriu; J. M. Lehn; K. M. Fromm; D. Fenske, *Chem.-Eur. J.*, **2000**, *6*, 2103.

(26) L. Dobrańska; G. O. Lloyd; H. G. Raubenheimer; L. J. Barbour, *J. Am. Chem. Soc.*, **2005**, *127*, 13134.

(27) L. Dobrzańska; G. O. Lloyd; H. G. Raubenheimer; L. J. Barbour, *J. Am. Chem. Soc.*, **2006**, *128*, 698.

(28) L. J. Barbour; T. Jacobs; J. A. Gertenbach; D. Das, *Aust. J. Chem.*, **2010**, *63*, 573.

(29) T. Jacobs, *PhD Thesis*; University of Stellenbosch, **2009**.

(30) L. Dobrańska; G. O. Lloyd; T. Jacobs; I. Rootman; C. L. Oliver; M. W. Bredenkamp; L. J. Barbour, *J. Mol. Struct.*, **2006**, *796*, 107.

(31) L. Dobrańska; D. J. Kleinhans; L. J. Barbour, *New. J. Chem.*, **2008**, *32*, 813.

(32) C. L. Cahill; D. T. de Lill; M. Frisch, *CrystEngComm*, **2007**, *9*, 15.

(33) L. Rulisek; J. Vondrasek, *J. Inorg. Biochem.*, **1998**, *71*, 115.

(34) L. Dobrańska, *CrystEngComm*, **2011**, *13*, 2303.

(35) L. Carlucci; G. Ciani; D. M. Proserpio; S. Rizzato, *CrystEngComm*, **2002**, 413.

(36) L. Carlucci; G. Ciani; D. M. Proserpio; S. Rizzato, *CrystEngComm*, **2002**, 121.

(37) K. J. Wei; J. Ni; M. Gao; Y. Z. Liu; Q. L. Liu, *Eur. J. Inorg. Chem.*, **2007**, 3868.

(38) M. O. Awaleh; A. Badia; F. Brisse, *Cryst. Growth Des.*, **2005**, *5*, 1897.

(39) J. S. Fleming; K. L. V. Mann; C. A. Carraz; E. Psillakis; J. C. Jeffery; J. A. McCleverty; M. D. Ward, *Angew. Chem. Int. Ed.*, **1998**, *37*, 1279.

(40) K. Salorinne; O. Lopez-Acevedo; E. Nauha; H. Hakkinen; M. Nissinen, *CrystEngComm*, **2011**.

(41) C. P. Li; M. Du, *Chem. Commun.*, **2011**, *47*, 5958.

(42) L. Dobrańska; G. O. Lloyd; L. J. Barbour, *New. J. Chem.*, **2007**, *31*, 669.

(43) J. M. Shreeve; Y. Gao; B. Twamley, *Inorg. Chem.*, **2006**, *45*, 1150.

(44) A. N. Khlobystov; A. J. Blake; N. R. Champness; D. A. Lemenovskii; A. G. Majouga; N. V. Zyk; M. Schroder, *Coord. Chem. Rev.*, **2001**, *222*, 155.

(45) M. Schröder; N. Champness In *Encyclopedia of Supramolecular Chemistry*; 1 ed.; J. L. Atwood, J. W. Steed, Eds.; Marcel Dekker, Inc.: New York, **2004**

(46) M. R. Caira In *Encyclopedia of Supramolecular Chemistry*; 1 ed.; J. W. Atwood, J. W. Steed, Eds.; Marcel Dekker, Inc.: New York, **2004**

(47) G. O. Lloyd; J. Alen; M. W. Bredenkamp; E. J. C. de Vries; C. Esterhuysen; L. J. Barbour, *Angew. Chem. Int. Ed.*, **2006**, *45*, 5354.

(48) J. W. Steed; D. R. Turner; K. J. Wallace, *Core Concepts in Supramolcular Chemistry and Nanochemistry*; Wiley: Chichester, England, **2007**.

(49) W. Zhao; J. Fan; T.-a. Okamura; W.-Y. Sun; N. Ueyama, *J. Solid State Chem.*, **2004**, *177*, 2358.

(50) X. Z. Sun; M. H. Zeng; B. Wang; B. H. Ye; X. M. Chen, *J. Mol. Struct.*, **2007**, *828*, 10.

(51) P. Maniam; N. Stock, *Z. Anorg. Allg. Chem.*, **2011**, *637*, 1145.

(52) N. Stock; T. Bein, *Angew. Chem. Int. Ed.*, **2004**, *43*, 749.

(53) S. Norbert, *Micropor. Mesopor. Mat.*, **2010**, *129*, 287.

(54) S. Bauer; N. Stock, *Angew. Chem. Int. Ed.*, **2007**, *46*, 6857.

(55) R. Banerjee; A. Phan; B. Wang; C. Knobler; H. Furukawa; M. O'Keeffe; O. M. Yaghi, *Science*, **2008**, *319*, 939.

(56) D. C. Webster, *Macromol. Rapid Comm.*, **2008**, *209*, 237.

CHAPTER 3

INVESTIGATION OF HIGH THERMAL STABILITY IN A SERIES OF SOLVATES

3.1. INTRODUCTION

Solvates are crystalline materials in which one component is the solute and the second component necessarily consists of solvent molecules from which the solvate is crystallised.[1] If the term "solvate" is placed within the context of host-guest inclusion chemistry, the solute comprises the "host" component of the system and the solvent molecules the "guest". The guest molecules are usually associated by means of non-covalent interactions to the host framework structure and are most often located within discrete cavities or channels created by the packing mode of the host molecules. Owing to the weak nature of the interactions that confine the guest molecules within the host, loss of solvent from the framework can often be effected by prolonged exposure of the sample to atmospheric conditions or, depending on the specific guest, by heating. Although the included guests no longer retain properties of the bulk liquid, there are numerous accounts in the literature that indicate the temperature at which the guest molecules are expelled from the host is closely correlated to the boiling point of the solvent i.e. desolvation generally occurs either below the boiling point or at temperatures approximating the boiling point of the solvent. In this regard, Nassimbeni has indicated that a useful parameter to assess the relative stability of an inclusion compound is the difference between the onset temperature of an endothermic guest-release reaction and the boiling point of the solvent ($T_{on} - T_b$); [2,3] for most inclusion compounds $T_{on} < T_b$ and as a consequence $T_{on} - T_b$ is normally a negative number.

Systems that exhibit a positive $T_{on} - T_b$ value are rare, and may find potential applications as storage materials in high temperature environments. To date there are only a few examples of such systems reported in the literature and these can be conveniently divided into two categories; those that show remarkable thermal stability of host-guest systems involving *gas* molecules and those involving volatile *solvent* molecules. In the former category Ripmeester *et al*. have demonstrated that the host *p-tert*-butylcalix[4]arene is capable of absorbing NO, air, SO_2 and Xe and retaining these guest

molecules at temperatures well above their boiling points (**Figure 1a** and **b**).[4] Similarly, Atwood *et al*. have reported that the discrete lattice voids formed by the hexagonal close-packed calix[4]arene occlude a range of freons, as well as methane at temperatures exceeding their boiling points (the inclusion of small liquid guests was also reported).[5] In both cases, the guest molecules were trapped within the host interstices with no channels being present for guest transport, and stabilisation of the guest molecules was achieved solely by van der Waals interactions (**Figure 1c**). The latter category comprises two reports that show high thermal stability of diethyl ether channel inclusion compounds in which the stabilisation of the Et_2O molecules is achieved through O–H···O^- hydrogen bonds. The first instance was reported by Barbour *et al*. and involves an organic diol host compound, 9,9'-dihydroxy-9,9'-di(4-*tert*-butylphenyl)-9,9'-dihydroanthracene, which retains ether to 29.8 °C above its normal boiling point.[6] In the second report, Vittal *et al*. described a series of lanthanide complexes that are able to retain Et_2O up to approximately 80 °C.[7]

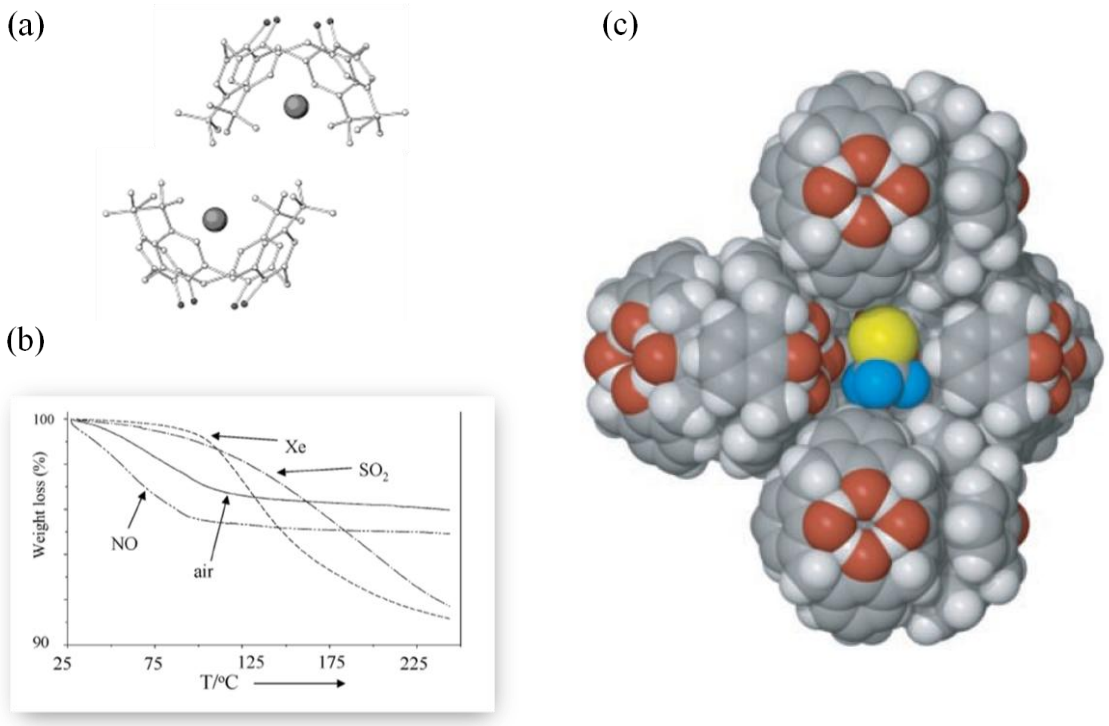

Figure 1. (a) The host compound *p-tert*-butylcalix[4]arene shown in capped-sticks with the guest Xe molecules indicated as spheres trapped within the host interstices.[4] **(b)** Thermogravimetric analysis of *p-tert*-butylcalix[4]arene host-guest compounds for NO, air, SO_2 and Xe, indicating that the guest molecules are retained within the host compound well above the boiling point of the guest.[4] **(c)** Space-filling representation of the guest freon (CF_3Br) located in the interstitial void of the calix[4]arene host lattice. One guest molecule is surrounded by 5 trimeric host units – one unit has been omitted for clarity.[5]

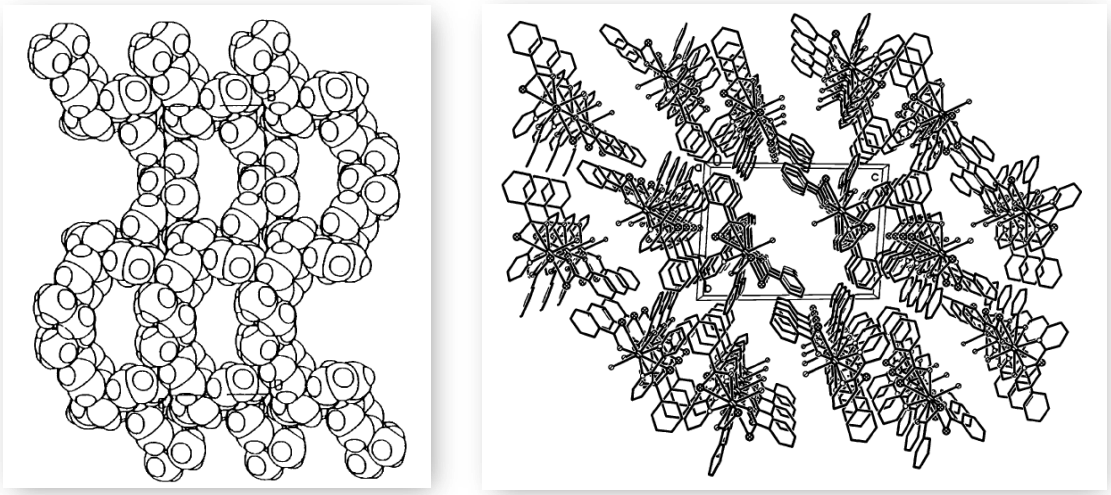

(a) (b)

Figure 2. (a) Arrangement of the diol host, 9,9'-dihydroxy-9,9'-di(4-*tert*-butylphenyl)-9,9'-dihydroanthracene along [100]; molecules are drawn with van der Waals radii. Image adapted from reference 6. **(b)** Packing of $[La(2,2'\text{-bpy})SC\{O\}Ph)_3(H_2O)]\cdot Et_2O$ along [100]. The diethyl ether solvate molecules have been omitted from both **(a)** and **(b)** to emphasise the channels formed by the arrangement of the host molecules. Image adapted from reference 7.

Porosity can be classified into three categories – conventional porosity, porosity "without pores" and virtual porosity[8] (the conditions of these three categories have been discussed in detail in Section 1.4). Conventionally porous materials are generally grown as solvates and permeability is established in one of two ways; either the parent solvent molecules are removed completely from the host framework, yielding an apohost phase that is capable of absorbing new guest molecules, or the parent solvent molecules can be exchanged for another guest – this involves mass transport of guests through a solid medium without there being a need for a guest-free phase;[8] however, in both instances an essential requirement is that the topology of the host framework should remain relatively unaffected by the process. In the context of this study, materials that conform to the former situation will be referred to as Class I porous systems and the latter as Class II porous systems.

Research efforts in our group are largely concerned with the synthesis and characterisation of the properties of novel crystalline porous materials. In particular, we are interested in the encapsulation of molecular species within the apertures of dinuclear metallocyclic coordination host complexes. We have shown that the formation of these metallocycles is solvent templated[9] and that removal of the solvent from the apertures can occur without significant disruption to the host structure,[10-12] resulting in the formation of

a Class I porous material that is capable of absorbing a variety of guests.* Much of our success thus far has involved the use of flexible ditopic imidazole ligands as integral components in metallocycle formation and porous materials achieved by this design principle have utilised a variety of transition metal salts – of particular relevance to this study are the Ag(I)-containing metallocycles.[10,12] The synthesis of four ditopic imidazole ligands is presented in Chapter 2; these ligands were reacted in a systematic manner with a variety of transition metal salts with a view to synthesising novel 0D porous metallocycles. Under the reaction conditions outlined in Chapter 2, a total of 29 novel coordination complexes were isolated and characterised by single-crystal X-ray diffraction methods. Twenty-four of these structures were described in detail in Chapter 2 and the remaining 5 structures were classified as porous Ag(I) metallocycles and are the subject of the current chapter.

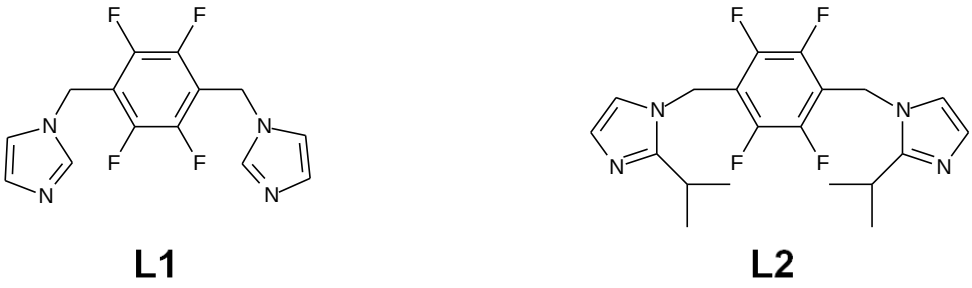

Scheme 1. (**L1**) 2,3,5,6-tetrafluoro-1,4-bis(imidazol-1-yl-methyl)benzene[13] and (**L2**) 2,3,5,6-tetrafluoro-1,4-bis(2-isopropylimidazole-1-yl-methyl)benzene.

In this chapter, solvates of 5 Ag(I) metallocycles are reported. They are $[Ag_2(\mathbf{L1})_2](NO_3)_2{\cdot}2CH_3OH{\cdot}H_2O$ ($\mathbf{1_{MEOH{\cdot}H2O}}$), $[Ag_2(\mathbf{L1})_2](NO_3)_2{\cdot}2CH_3CN$ ($\mathbf{1_{MeCN}}$), $[Ag_2(\mathbf{L1})_2](NO_3)_2{\cdot}2(CH_3)_2CO$ ($\mathbf{1_{AC}}$), $[Ag_2(\mathbf{L1})_2](BF_4)_2{\cdot}2(CH_3)_2CO$ ($\mathbf{2_{AC}}$) and $([Ag_2(\mathbf{L2})_2NO_3)(Ag_2(\mathbf{L2})_2(NO_3)_2)([Ag_2(\mathbf{L2})_2](NO_3)_2){\cdot}3(CH_3)_2CO$ ($\mathbf{3_{AC}}$) (refer to Scheme 1 for the identity of **L1** and **L2**). The structures are all channel inclusion compounds with no appreciably strong host–guest interactions. The initial aim of the study was to determine if it is possible to thermally remove the solvent from the respective inclusion complexes and obtain single crystals of the apohost phase. While retention of monocrystallinity is not essential for further sorption studies it is vital if we intend characterising future inclusion compounds of the original host by means of single-crystal diffraction methods. In the first part of the study the single-crystal structures and thermal analysis of the 5 solvates is

* A review of the porous metallocycles synthesised in our group has been given in Section 2.4.1.2.

presented. The thermoanalytical data presented in Section 3.2.1 reveal that all 5 solvates have remarkably high thermal stability for their occluded volatile solvents and the single crystals do not survive the desolvation process; in fact, in some cases the solvent is only lost when the host decomposes. This is in stark contrast to the thermal behaviour exhibited by analogous metallocyclic host complexes reported in the literature – thermogravimetric analysis of these systems indicates that solvent loss occurs readily from room temperature, and complete removal of the solvent from the apertures of the cyclic complexes can be effected by gently heating the samples under vacuum, with the discrete nature of the crystals preserved in all cases. It would therefore be interesting to compare one of these literature structures with one of the inclusion complexes in this study to determine if it is possible to correlate the structure of the inclusion compounds at the molecular level with its thermal stability at the macro level. In order to make a valid comparison, the two structures would have to be similar in composition, and for this reason $\mathbf{1}_{\mathbf{MeCN}}$ and the literature structure $\mathbf{M2}_{\mathbf{MeCN}}$[12] ($[Ag_2(\mathbf{A2})_2](PF_6)\cdot 2CH_3CN$, where **A2** = 2,3,4,6-tetrafluoro-1,4-bis(2-methylimidazole-1-ylmethyl)benzene) were chosen as the subjects of a computational study aimed at investigating the various intermolecular interaction energies in the two structures. The results of this study are discussed in Section 3.2.1.6.

In a further effort to obtain single crystals of the apohost phases of the complexes, a liquid-solvent exchange was attempted; in this type of experiment the 'parent' solvent is replaced by a more volatile solvent that can generally be removed under milder heating conditions. To this end, single crystals of $\mathbf{1}_{\mathbf{MeOH\cdot H2O}}$, $\mathbf{1}_{\mathbf{MeCN}}$, $\mathbf{1}_{\mathbf{AC}}$, $\mathbf{2}_{\mathbf{AC}}$ and $\mathbf{3}_{\mathbf{AC}}$, were immersed in DCM. Remarkably, the single crystals survived the guest exchange process intact and it was possible to obtain single-crystal structures of the new inclusion complexes. The structures indicated that the parent solvent molecules had been replaced by DCM molecules without significant rearrangement of the host metallocycle. Attempts to remove the DCM from the host lattice resulted in extensive fracturing of the formerly single crystals into a polycrystalline material, and while this is disconcerting with regard to our aim of obtaining single crystals of the guest-free structure, this result is interesting in itself. The facile exchange of the initial solvent for DCM is not entirely intuitive given that the solvent cannot readily be removed by heating; this prompted us to explore the exchange capabilities of these host materials as Class II porous systems. Therefore, in the second part of this study we investigated the permeability of $\mathbf{1}_{\mathbf{MeOH\cdot H2O}}$, $\mathbf{1}_{\mathbf{MeCN}}$, $\mathbf{1}_{\mathbf{AC}}$ and $\mathbf{2}_{\mathbf{AC}}$ to a variety of common solvents and monitored this exchange by single-crystal X-ray

diffraction. If the diffraction data indicated that exchange had successfully taken place, the material was subjected to thermogravimetric analysis (TGA) and differential scanning calorimetry (DSC) to assess the thermal stability of the new inclusion complex; the thermal stability of all inclusion complexes exhibiting a discrete endothermic desolvation step were additionally evaluated using the $T_{on} - T_b$ parameter. These results are presented in Section 3.2.2. and are discussed in Section 3.2.4.

Unfortunately, it was not possible to synthesise further single crystals of $\mathbf{3_{AC}}$ beyond those contained in the original reaction vial. Numerous crystallisation attempts mimicking the conditions used in the original experiment merely resulted in the formation of polycrystalline material or crystals of such poor quality that it was not possible to obtain reliable single-crystal data. While the powder X-ray diffraction (PXRD) data indicate that the phase of the bulk material is that of $\mathbf{3_{AC}}$, single crystals of high quality are necessary to elucidate the products of the exchange experiments. Therefore, although our investigations of the thermal stability and exchange properties of $\mathbf{3_{AC}}$ are not as extensive as those of $\mathbf{1_{MeOH{\cdot}H2O}}$, $\mathbf{1_{MeCN}}$, $\mathbf{1_{AC}}$ and $\mathbf{2_{AC}}$, we feel it would be remiss to ignore the results obtained thus far, and these have thus been reported in a separate section (Section 3.2.3).

3.2. RESULTS

3.1.1 Structure determinations of $\mathbf{1_{MeOH{\cdot}H2O}}$, $\mathbf{1_{MeCN}}$, $\mathbf{1_{AC}}$ and $\mathbf{2_{AC}}$ from single-crystal X-ray diffraction

The ligand 2,3,5,6-tetrafluoro-1,4-bis(imidazole-1-ylmethyl)benzene (**L1**) was synthesised by the method of Gao *et al.*[13] (see Section 2.4.1.1) and a series of four metallocycles with general formula $[Ag_2\mathbf{L1}_2](X)_2{\cdot}nG$ were prepared. These entities are self-assembled from Ag(I) salts and **L1** in a particular solvent, and each of the four metallocycles contains a different anion (X) and guest (G) combination. For the purposes of this study the metallocyclic host structures obtained using $AgNO_3$ are indicated as **1**, the host structure obtained using $AgBF_4$ is indicated as **2**, and the guest species is denoted as a subscript following the host number. The four inclusion complexes investigated were thus $\mathbf{1_{MeOH{\cdot}H2O}}$, $\mathbf{1_{MeCN}}$, $\mathbf{1_{AC}}$ and $\mathbf{2_{AC}}$ (**Scheme 2**). The structure of $\mathbf{1_{MeOH{\cdot}H2O}}$ has been described previously.[13] However, the thermal stability of the compound has not been reported in the literature. In each case, the structure was determined by means of single-crystal X-ray diffraction and suitable crystals were grown by slow evaporation of an equimolar solution

of the appropriate ligand and metal salt in the relevant solvent. The crystallographic data and details of the structure solution and refinement procedures for the crystal structures are given in **Table 4** at the end of the chapter. PXRD was used to assess whether the structures obtained for the single-crystals of $\mathbf{1}_{\mathbf{MeOH\cdot H2O}}$, $\mathbf{1}_{\mathbf{MeCN}}$, $\mathbf{1}_{\mathbf{AC}}$ and $\mathbf{2}_{\mathbf{AC}}$ were indeed representative of the bulk sample, and in each case the experimental PXRD patterns of the bulk samples matched those simulated from their respective single-crystal structures (see Appendix B).

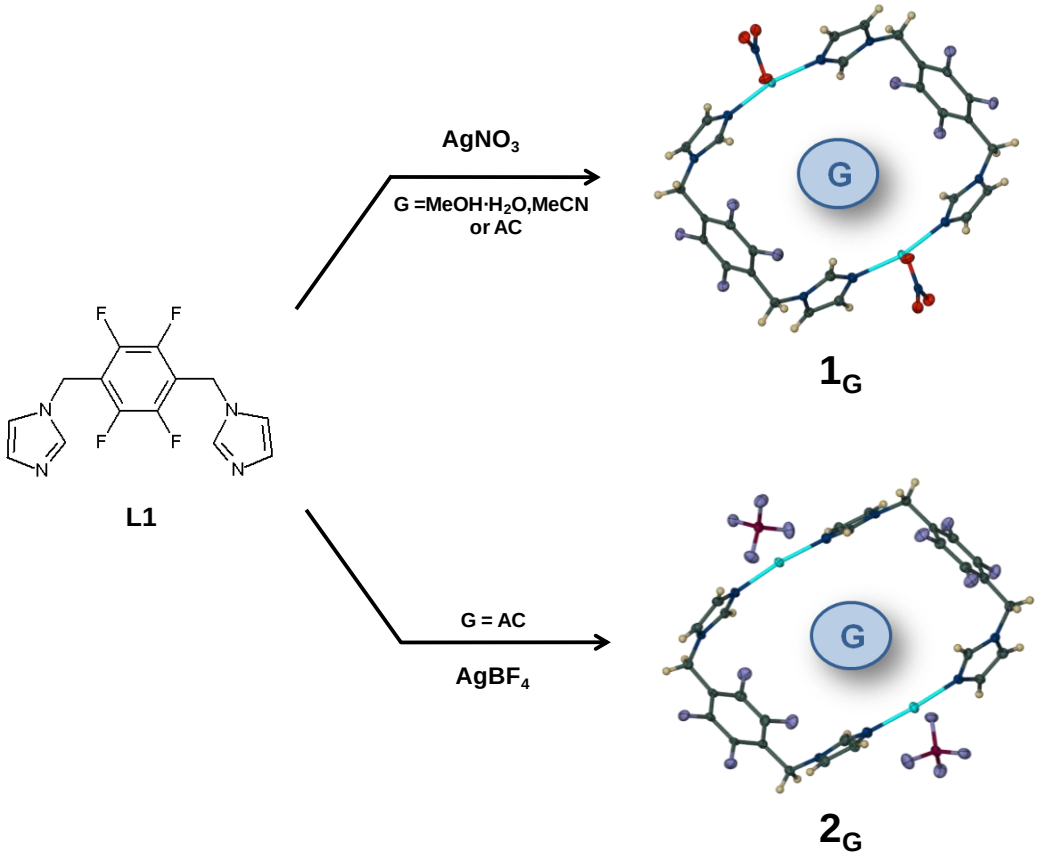

Scheme 2. Formation of $[Ag_2\mathbf{L1}_2](NO_3)_2{\cdot}2MeOH{\cdot}H_2O$ ($\mathbf{1}_{\mathbf{MEOH\cdot H2O}}$), $[Ag_2\mathbf{L1}_2](NO_3)_2{\cdot}2CH_3CN$ ($\mathbf{1}_{\mathbf{MeCN}}$), $[Ag_2\mathbf{L1}_2](NO_3)_2{\cdot}2(CH_3)_2CO$ ($\mathbf{1}_{\mathbf{AC}}$) and $[Ag_2\mathbf{L1}_2](BF_4)_2{\cdot}2(CH_3)_2CO$ ($\mathbf{2}_{\mathbf{AC}}$).

Single-crystal analyses of $\mathbf{1}_{\mathbf{MeOH\cdot H2O}}$, $\mathbf{1}_{\mathbf{MeCN}}$, $\mathbf{1}_{\mathbf{AC}}$ and $\mathbf{2}_{\mathbf{AC}}$ reveal the formation of discrete dinuclear metallocyclic complexes comprised of two linearly coordinated Ag(I) ions doubly bridged to each other by means of two **L1** ligands, with intra-metallocycle Ag···Ag separations of 8.841(3), 8.703(2), 9.004(3) and 7.864(6) Å, respectively. $\mathbf{1}_{\mathbf{MeOH\cdot H2O}}$, $\mathbf{1}_{\mathbf{MeCN}}$ and $\mathbf{1}_{\mathbf{AC}}$ crystallise in the monoclinic space group $P2_1/n$ with the metallocycles situated on a site of 2/*m* symmetry; this requires only half of the metallocycle to be present in the ASU. In addition to half of the metallocyclic complex and a nitrate anion, the ASU of $\mathbf{1}_{\mathbf{MeOH\cdot H2O}}$, $\mathbf{1}_{\mathbf{MeCN}}$ and $\mathbf{1}_{\mathbf{AC}}$ also respectively contain: one

methanol molecule and a half of a water molecule, one fully occupied MeCN molecule and a half occupied acetone molecule.

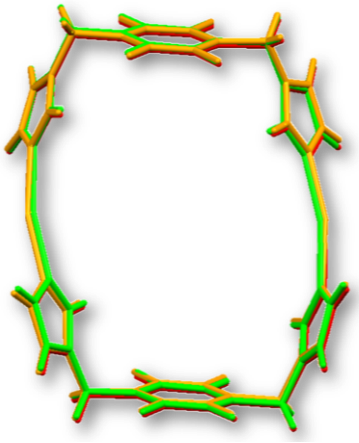

Figure 3. Overlay of the $\mathbf{1_G}$ host metallocycles (guest and anions omitted); $\mathbf{1_{MeOH{\cdot}H2O}}$ is indicated in red, $\mathbf{1_{MeCN}}$ in green and $\mathbf{1_{AC}}$ in orange.

As can be seen in the structural overlay provided in **Figure 3**, the molecular structures of three host metallocycles are superimposable and, taken in conjunction with the unit cell parameters in **Table 4** at the end of the chapter, it is apparent that $\mathbf{1_{MeOH{\cdot}H2O}}$, $\mathbf{1_{MeCN}}$ and $\mathbf{1_{AC}}$ are in fact 'isoskeletal'[14] i.e. the structures of $\mathbf{1_{MeOH{\cdot}H2O}}$, $\mathbf{1_{MeCN}}$ and $\mathbf{1_{AC}}$ are isostructural with regard to the packing of the host, but differ with respect to the identity of the guest. Bearing this in mind, the following description of the host packing arrangement applies equally to all the $\mathbf{1_G}$ structures. The metallocycles stack one on top of another in columns along the crystallographic *a* axis to form 1D channels that accommodate the reaction solvent guest molecules (**Figure 4**). The angle between each complex and the general channel direction[†] is ~87° – this almost upright orientation of the metallocycles causes the fluorinated aryl spacer to tilt by ~60° relative to the mean plane of the metallocycle in order to minimise F–F repulsive interactions between adjacent metallocycles (refer to **Figure 5** for the method used to calculate the 'metallocycle tilt' angle as well as the 'aromatic tilt' angle). Within each column the stacking periodicity is equal to the crystallographic *a* axis.

$\mathbf{2_{AC}}$ crystallises in the monoclinic space group $P2_1/c$, with one metallocycle ('aromatic tilt' angles of ~44° and ~68°) and two acetone molecules per ASU. The two solvent molecules are not related by symmetry; this results in a doubling of the *a*-axis and a shift of the 2/*m* site symmetry from the centre of the metallocycle to between two successive metallocycles resulting in an …*ABAB*… stacking arrangement within each metallocycle column (i.e. atoms of the first metallocycle are placed directly over the atoms of the third metallocycle along [100], **Figure 4**d) and two 'metallocycle tilt' angles of ~96° and ~99°. $\mathbf{2_{AC}}$ therefore has the largest packing periodicity of the four complexes.

[†] This measurement is based on the observation that the inter-metallocycle Ag···Ag vectors run parallel to the channel direction.

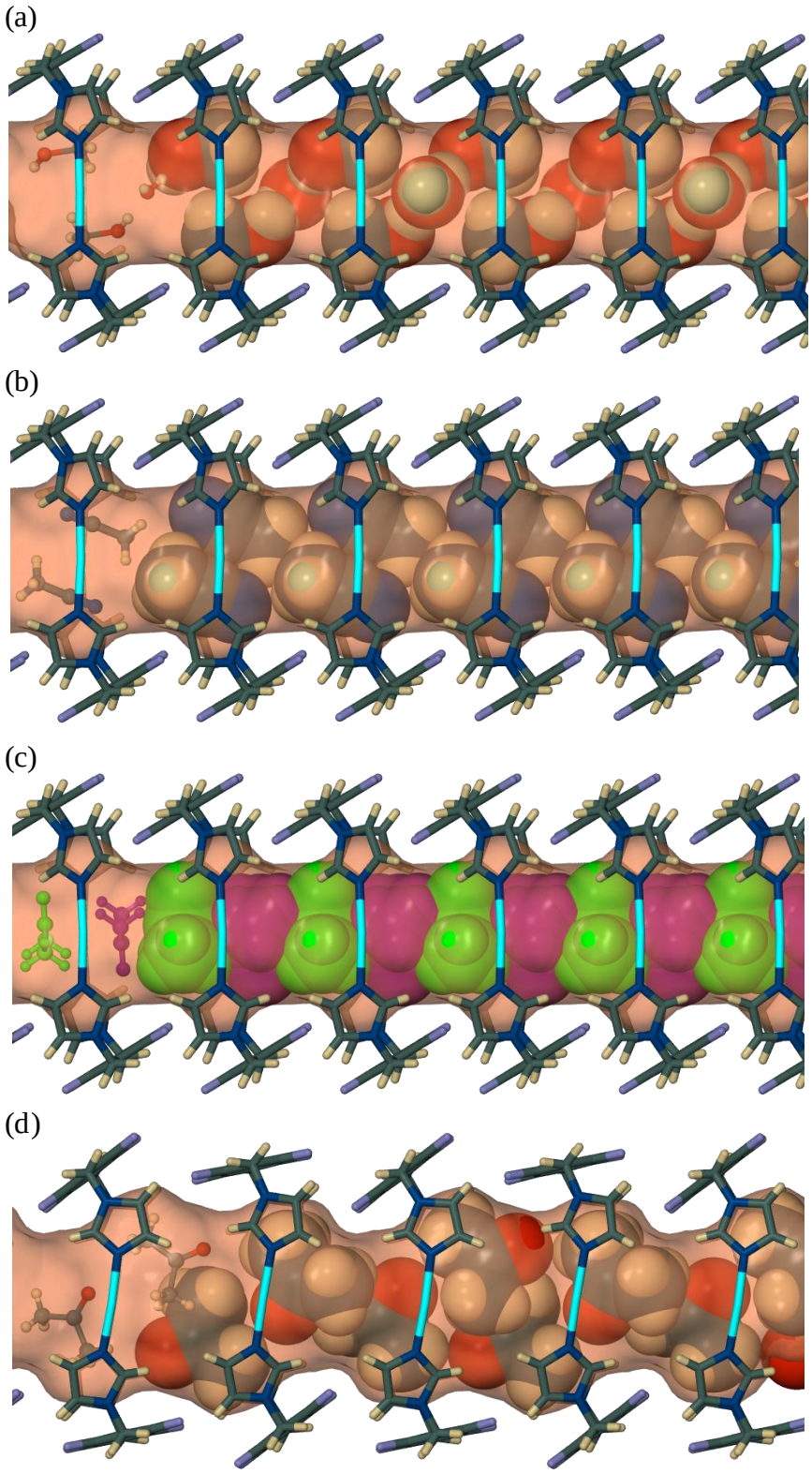

Figure 4. Columnar stacking of **(a)** $\mathbf{1}_{\mathbf{MeOH\cdot H2O}}$, **(b)** $\mathbf{1}_{\mathbf{MeCN}}$, **(c)** $\mathbf{1}_{\mathbf{AC}}$ and **(d)** $\mathbf{2}_{\mathbf{AC}}$ along [100] (horizontal direction) as viewed along [010]. The metallocyclic complexes are shown as capped-sticks and the counter-ions have all been omitted for clarity. Within the channels the first set of guest molecules (from the left) are shown in ball-and-stick and the remaining guests in van der Waals representation – the acetone guests in **(c)** are shown disordered over two equivalent positions and the model therefore shows

overlapping molecules, indicating that either the green molecules or the purple molecules, but not both, can be present within the channels. The solvent channels passing through the stacked metallocycles are shown as semitransparent pink Connolly surfaces (using a probe radius of 1.4 Å). Guest molecules protrude from certain areas of their respective surfaces in order to take part in hydrogen bonding interactions with atoms located in positions external to the surface; for **(a)** – **(b)** these interactions involve the NO_3^- counter-ions and in **(d)** these interactions involve the BF_4^- counter-ions, as well as the imidazole groups (see text for a detailed analysis of these interactions).

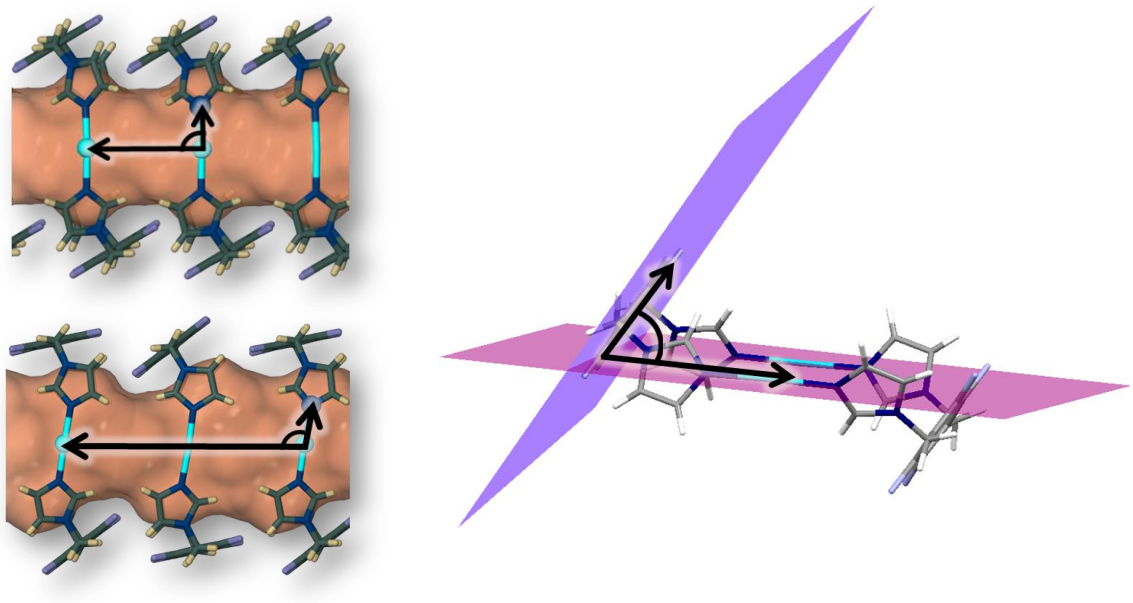

(a) (b)

Figure 5. (a) Columnar stacking of $\mathbf{1_G}$ (top) and $\mathbf{2_G}$ (bottom) as viewed perpendicular to the channel direction. The angle at which the metallocycles are canted relative to the general channel direction (the 'metallocycle tilt' angle is determined as the $\angle N_{im}$–Ag···Ag angle formed between two successive symmetry-related metallocycles. Therefore $\mathbf{2_G}$ will have two 'metallocycle tilt' angles associated with it owing to the ...*ABAB*... stacking of the metallocycles within a column – only one has been shown here. The metallocycles are shown in capped-sticks and the channel is represented as a semi-transparent orange surface. **(b)** A side view of a metallocyclic complex indicating the 'aromatic tilt' angle, i.e. the angle between the least-squares plane through the metallocycle ring (defined by the N_{im} and Ag atoms on either side of the ring) and the fluorinated aromatic spacer of the ligand. These planes are shown as the blue and purple surfaces, respectively.

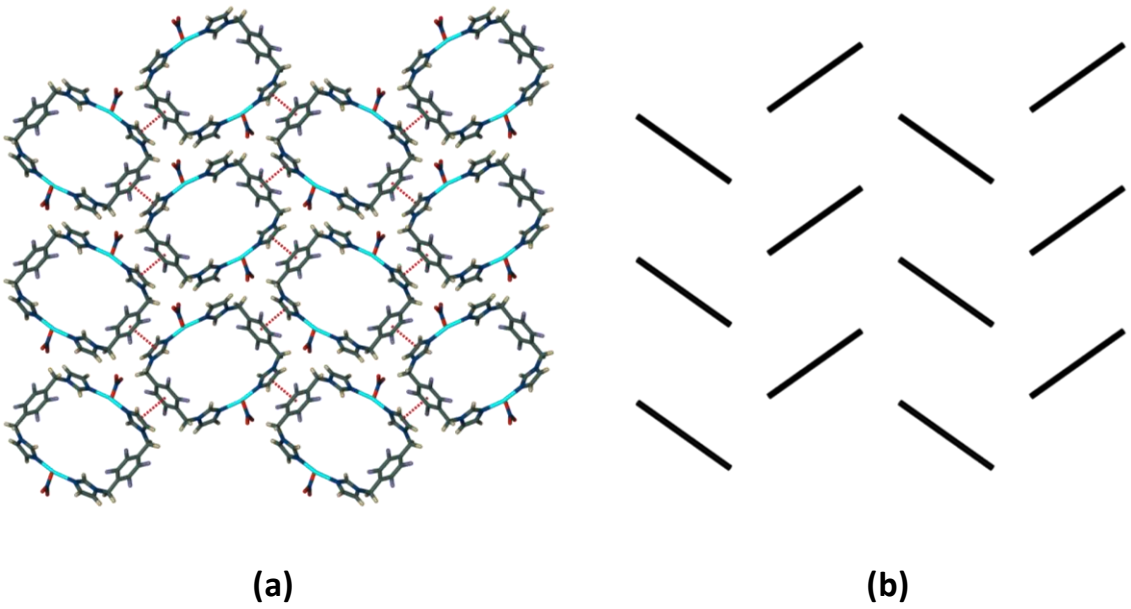

Figure 6. (a) Capped-stick arrangement of columns of metallocycles in $\mathbf{1_G}$ viewed along [100]. The face-to-face π–π stacking interactions are shown as fragmented red lines between the centroids of the aromatic rings and solvent molecules are omitted for clarity. **(b)** A simplification of the arrangement of the metallocyclic columns as viewed along [100] in order to highlight the herringbone packing motif of the columns. Each solid black line represents one metallocycle stack and extends between the centroids of the two aryl rings contained within one metallocycle. The arrangement of the metallocycle columns in $\mathbf{2_{AC}}$ is very similar to that of $\mathbf{1_G}$ therefore only one figure has been provided.

Each metallocycle column is surrounded by six identical columns in an arrangement similar to the hexagonal packing of tubes (**Figure 6a**). The metallocyclic columns adjacent to one another in the direction parallel to [010] are all in the same orientation within the crystal and are related to neighbouring columns in the (011) direction by a 2_1 screw axis and an *n*-glide plane. This packing arrangement results in a classical herringbone packing motif when viewed down [100] (**Figure 6b**) and is further stabilised by intermolecular face-to-face (FF) π-π stacking interactions between the imidazole rings in one column and the fluorinated benzene rings in an adjacent column (centroid-centroid separation = 3.599 Å). The NO_3^- anions in $\mathbf{1_{MeOH\cdot H2O}}$, $\mathbf{1_{MeCN}}$ and $\mathbf{1_{AC}}$ and the BF_4^- anions in $\mathbf{2_{AC}}$ occupy general positions in the unit cell and are located between the metallocycle columns. These anions are associated with the coordinated Ag(I) ions by virtue of weak electrostatic interactions. The $\angle N_{im}AgN_{im}$ angle in the structures containing NO_3^- deviate substantially from linearity ($\angle N_{im}–Ag–N_{im}$ = 166.54(5)°, 165.12(9)°, 162.97(9)° for $\mathbf{1_{MeOH\cdot H2O}}$, $\mathbf{1_{MeCN}}$ and $\mathbf{1_{AC}}$ respectively) and we therefore infer that the interaction between the anions and the Ag(I) cations are much stronger in these systems than in the system

containing BF_4^-. The fluorine atoms are only weakly associated with the Ag centres in **2**$_{AC}$, resulting in more linear ∠N_{im}–Ag–N_{im} angles of 175.19(2)° and 172.16(2)°.

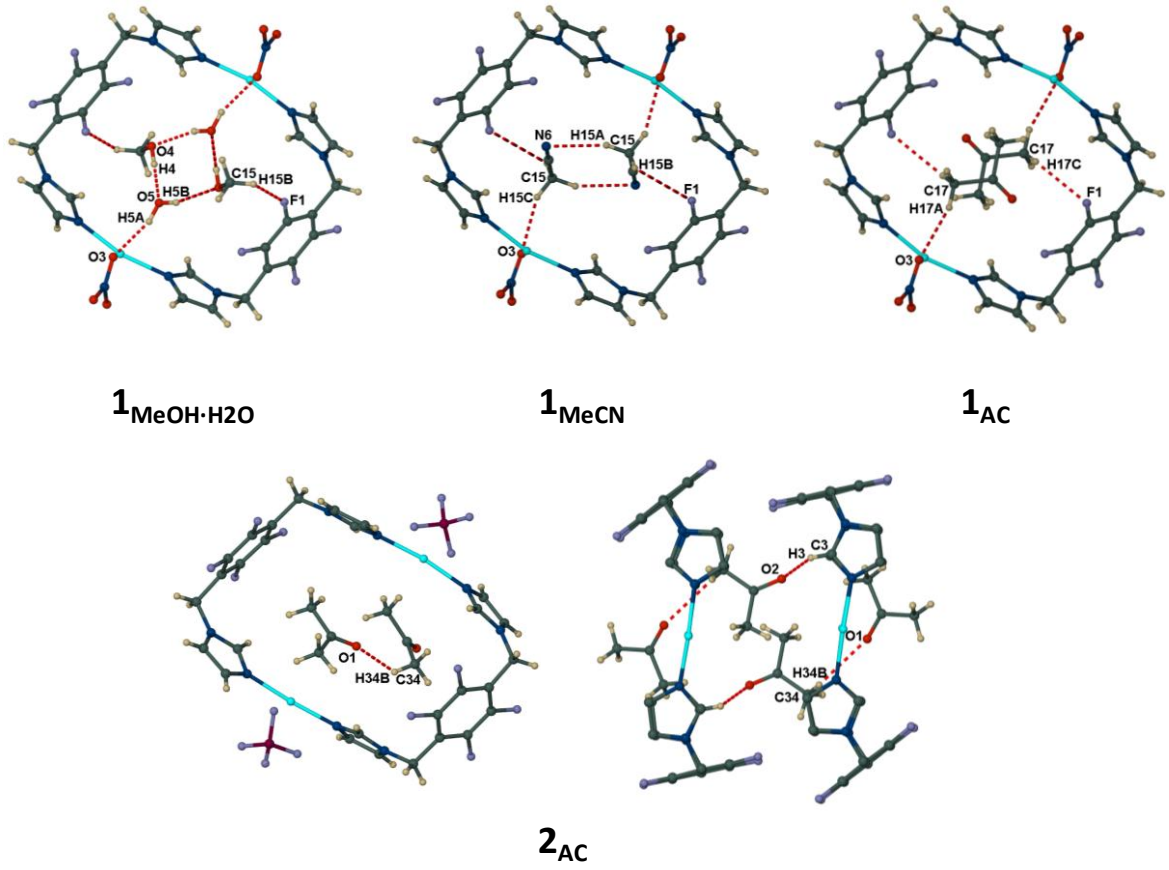

Figure 7. Ball-and-stick representations of **1**$_{MeOH·H2O}$, **1**$_{MeCN}$, **1**$_{AC}$ and **2**$_{AC}$ indicating the host:guest and guest:guest hydrogen bonding interactions. Hydrogen atoms not participating in hydrogen bonds, and the BF_4^- anions have been omitted from the bottom right image of **2**$_{AC}$ for the sake of clarity.

As stated above, each metallocycle accommodates reaction solvent guest molecules that are held in place by a system of weak hydrogen bonds (**Figure 7**). In the case of **1**$_{MeOH·H2O}$, two methanol molecules and one water molecule are present per metallocycle. These form a cooperative system of hydrogen bonds in which the two types of solvent molecules act as both hydrogen bond donors as well as hydrogen bond acceptors. The water molecule is located in two positions, with each position having a site occupancy factor of 0.5. The methanol molecules donate a hydrogen bond *via* the sp^3 carbon atom to the aromatic fluorine atom located closest in proximity to each methanol molecule (C15···F1 = 3.332(7) Å), and to the water molecule through the hydroxyl oxygen atom (O5···O4 = 2.756(5) Å). The water molecule, in turn, donates a hydrogen bond to the second methanol molecule (O4···O5 = 2.756(5) Å), as well as the nitrate anion (O4···O3 =

2.907(6) Å). In $\mathbf{1_{MeCN}}$, each host metallocycle encloses a pair of acetonitrile guest molecules, which are hydrogen bonded to each other (C···N = 3.482(5) Å), and by virtue of these hydrogen bonds they assume a head-to-tail dimeric formation within the channels (**Figure 4b**). The solvent molecules are further stabilised within the channels *via* the donation of hydrogen bonds from the sp^3 carbon of the solvent molecules to both the uncoordinated nitrate counter-ions (C15···O3 = 3.351(4) Å) and an aromatic fluorine atom located closest in proximity to the acetonitrile molecule (C15···F1 = 3.240(4) Å). The aperture of each metallocycle in $\mathbf{1_{AC}}$ houses a single acetone molecule disordered equally over two positions across a crystallographic inversion centre. From inspection of the space-filling projection of the acetone molecules within the channels it is apparent that the two symmetry-related guest molecules cannot co-exist, thus only one acetone molecule in a particular orientation can be present per host metallocycle within a stacked column (i.e. in **Figure 4d** only the green molecules or the purple molecules can be present in the channel at any given time). Only one of the two sp^3 carbons of an acetone molecule is in a favourable position to participate in hydrogen bonding, and donates hydrogen bonds to both the nitrate counter-ion (C17···O3 = 3.465(2) Å) and an aromatic fluorine atom (C17···F1 = 3.327(1) Å). The acetone molecules therefore do not occupy the centre of the aperture, but are situated on either side in order to take part in these interactions. In contrast to $\mathbf{1_{AC}}$, two acetone molecules of full occupancy are present per metallocycle in $\mathbf{2_{AC}}$. One acetone molecule donates a hydrogen bond to the second acetone molecule (C34···O1 = 3.379(9) Å), while the latter simultaneously accepts a hydrogen bond from an imidazolate carbon in an adjacent metallocycle (C3···O2 = 3.244(7) Å).

3.2.1. Thermal analyses of $\mathbf{1_{MeOH\cdot H2O}}$, $\mathbf{1_{MeCN}}$, $\mathbf{1_{AC}}$ and $\mathbf{2_{AC}}$

TGA, DSC and hot stage microscopy were used in conjunction with one another to assess the thermal behaviour of the inclusion complexes, as well as to determine if the single crystals of the complexes survive the desolvation process. For the TGA and DSC analyses, samples of the as-grown crystals of $\mathbf{1_{MeOH\cdot H2O}}$, $\mathbf{1_{MeCN}}$, $\mathbf{1_{AC}}$ and $\mathbf{2_{AC}}$ were filtered off from the mother liquor and left to dry on the filter paper for two hours to ensure removal of any residual solvent adhered to the surface of the crystals. The dried crystals were then heated at a rate of 10 °C min^{-1} and the resulting thermograms were recorded as a function of temperature. Onset temperatures (T_{on}) of guest release were only noted for complexes in

which the thermoanalytical data indicated a distinct endothermic desolvation step.‡ For the hot stage microscopy single crystals were selected, placed on a glass slide, covered with silicone oil and heated at a rate of 10 °C min^{-1}. Finally, variable temperature powder X-ray diffraction (VT-PXRD) was used to investigate the samples for which a T_{on} value was recorded in order to determine whether a phase change had occurred as a result of the desolvation process.

3.2.1.1. Thermal analysis of $\mathbf{1_{MeOH\cdot H2O}}$

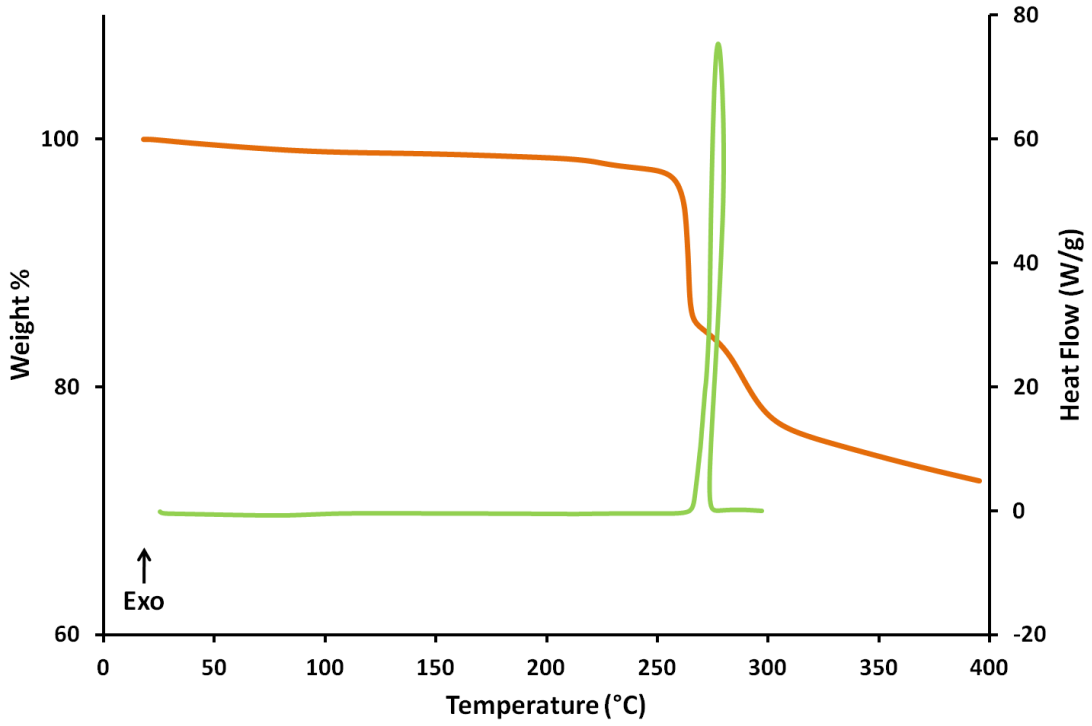

Figure 8. Thermoanalytical data for $\mathbf{1_{MeOH\cdot H2O}}$; the TGA and DSC traces are orange and green, respectively.

The TGA trace for $\mathbf{1_{MeOH\cdot H2O}}$ indicates that the inclusion complex is stable to *ca.* 240 °C, after which the sample decomposes rapidly (**Figure 8**). As care was taken to ensure all surface solvent had been removed prior to the analysis, we postulate that the gradual weight loss observed in the thermogram from room temperature up to the decomposition step is due to the loss of solvent molecules from a small percentage of the sample and not

‡ When considering the TG and DSC traces collectively, it is important to note that the system geometries are different for the two techniques; i.e. the TG experiments were carried out in an open aluminium pan, whereas the DSC experiments were performed with the sample in a crimped, vented aluminium pan. As a consequence of this the onset temperatures for the two techniques may not always coincide.

due to surface solvent. This conjecture is supported by the results obtained by hot stage microscopy: these images (shown in **Figure 9**) indicate that solvent, appearing in the form of bubbles in the oil surrounding the single crystals of $\mathbf{1}_{\mathbf{MeOH\cdot H2O}}$, emerge only as the crystals start to decompose (i.e. turn brown), thereby indicating that loss of solvent is concomitant with the decomposition of the crystals. The final decomposition step is a highly exothermic process as inferred from the sharp peak on the DSC trace in **Figure 8** (onset temperature of *ca* 260 °C). The exothermic peak is not symmetrical; this could be an indication that the nature of the decomposition step is complex and may occur too rapidly for the heating rate of 10 °C min^{-1} (a slower heating rate may result in a more symmetrical exotherm).

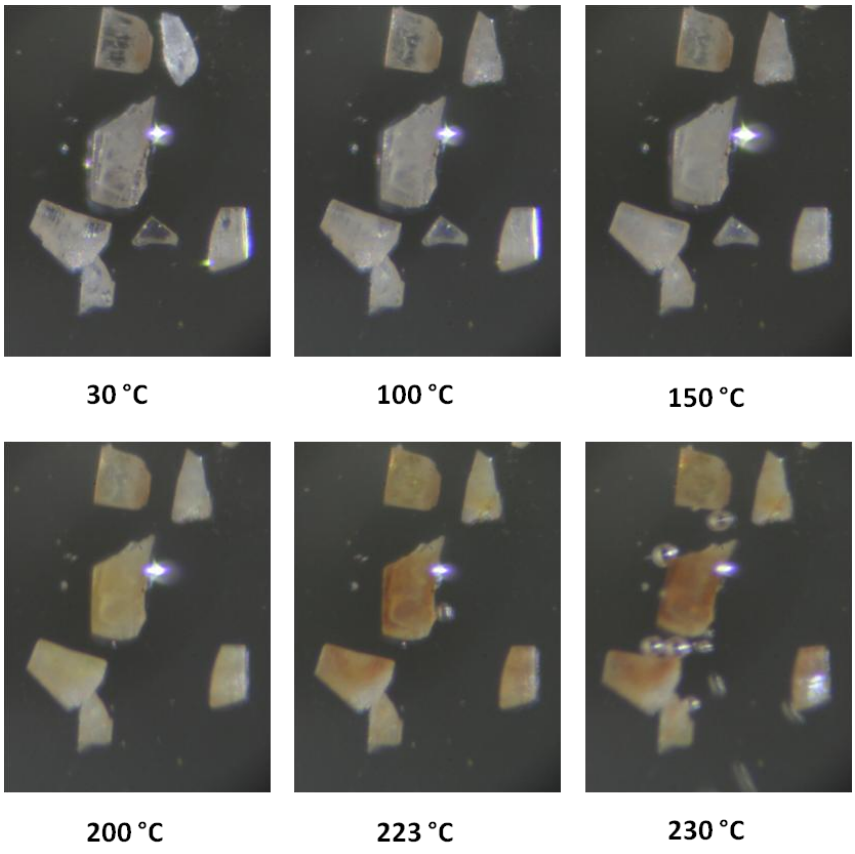

Figure 9. Hot stage microscopy images obtained for $\mathbf{1}_{\mathbf{MeOH\cdot H2O}}$. A sample was heated from room temperature to 230 °C. Bubbles corresponding to solvent loss appear in the oil surrounding the crystals only as they become brown and start to decompose.

3.2.1.2. Thermal analysis of $\mathbf{1}_{\mathbf{MeCN}}$

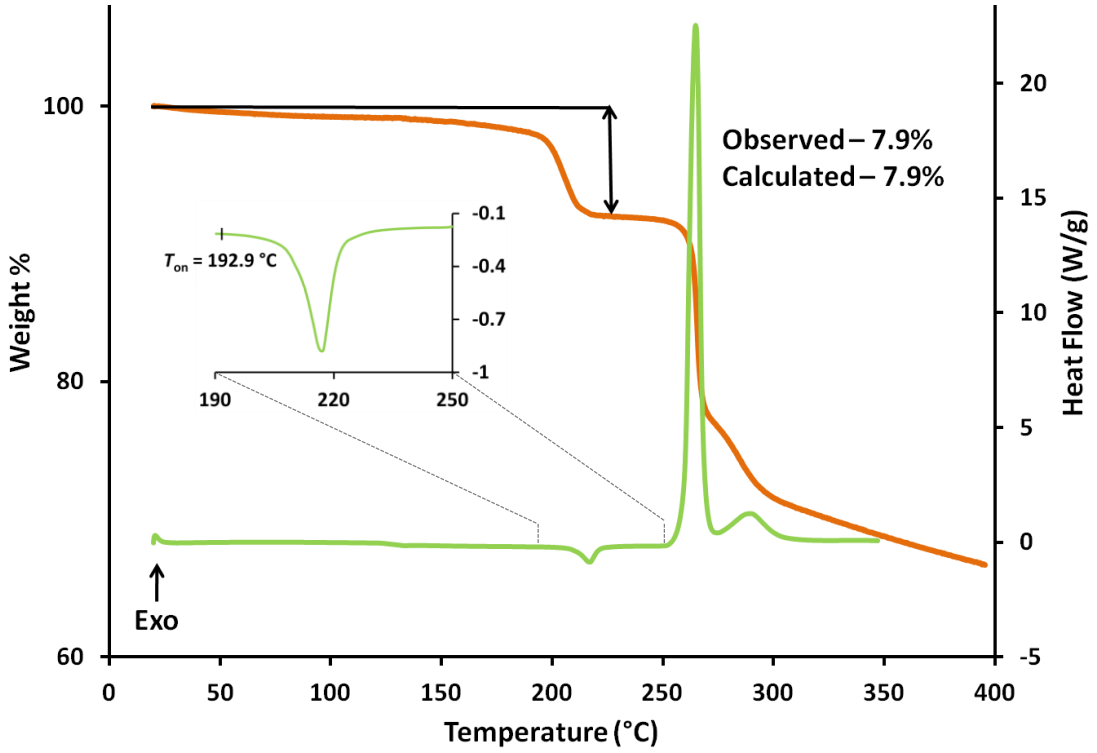

Figure 10. Thermoanalytical data for $\mathbf{1}_{\mathbf{MeCN}}$; the TGA and DSC traces are orange and green, respectively and the insert highlights the endothermic desolvation step on the DSC trace.

Figure 10 shows that the loss of guest molecules in $\mathbf{1}_{\mathbf{MeCN}}$ is a single-step process occurring in the temperature range 180–220 °C. The sample is then stable up to *ca* 250 °C after which it starts to decompose. As was observed for $\mathbf{1}_{\mathbf{MeOH{\cdot}H2O}}$, a gradual weight loss that can be attributed to solvent loss from a small percentage of the sample is seen from room temperature up to the major desolvation step in the TGA. A theoretical value of 7.9% is expected for two equivalents of acetonitrile per metallocycle and a 7.9% weight loss is indeed observed. The DSC trace reveals an endotherm coinciding with the guest release from the host metallocycles at an onset temperature of 192.9 °C – this corresponds to a $T_{on} - T_b$ value of 111.3 °C. The resulting desolvated phase appears to be stable from 230–250 °C after which the sample decomposes. The decomposition of $\mathbf{1}_{\mathbf{MeCN}}$ is a two-step process as is evidenced by the two closely spaced exotherms in the DSC trace at onset temperatures of approximately 250 and 275 °C. The nature of the desolvated phase was investigated by means of VT-PXRD; an initial measurement of the guest-included phase was taken, and **Figure 11** shows a good match between the powder pattern of the bulk sample of $\mathbf{1}_{\mathbf{MeCN}}$ and that simulated from the single-crystal guest-included structure. A

powder pattern was then recorded at various intervals from 30 to 227 °C (the upper limit of the VT cryostat). **Figure 11** shows that the experimental patterns are closely correlated to that of the guest-included phase until the start of desolvation at ~190 °C, where several peaks appear to shift slightly and new peaks emerge. We therefore conclude that the desolvation process must lead to a subtle rearrangement of the host molecules to a more densely packed phase. In order to test whether the original solvated phase could be recovered, the powder of the high temperature (HT) phase was submerged in MeCN overnight and, as can be seen in the bottom PXRD pattern in **Figure 11**, the diffraction pattern appears to regain characteristics of the original solvated $\mathbf{1}_{\mathbf{MeCN}}$ phase.

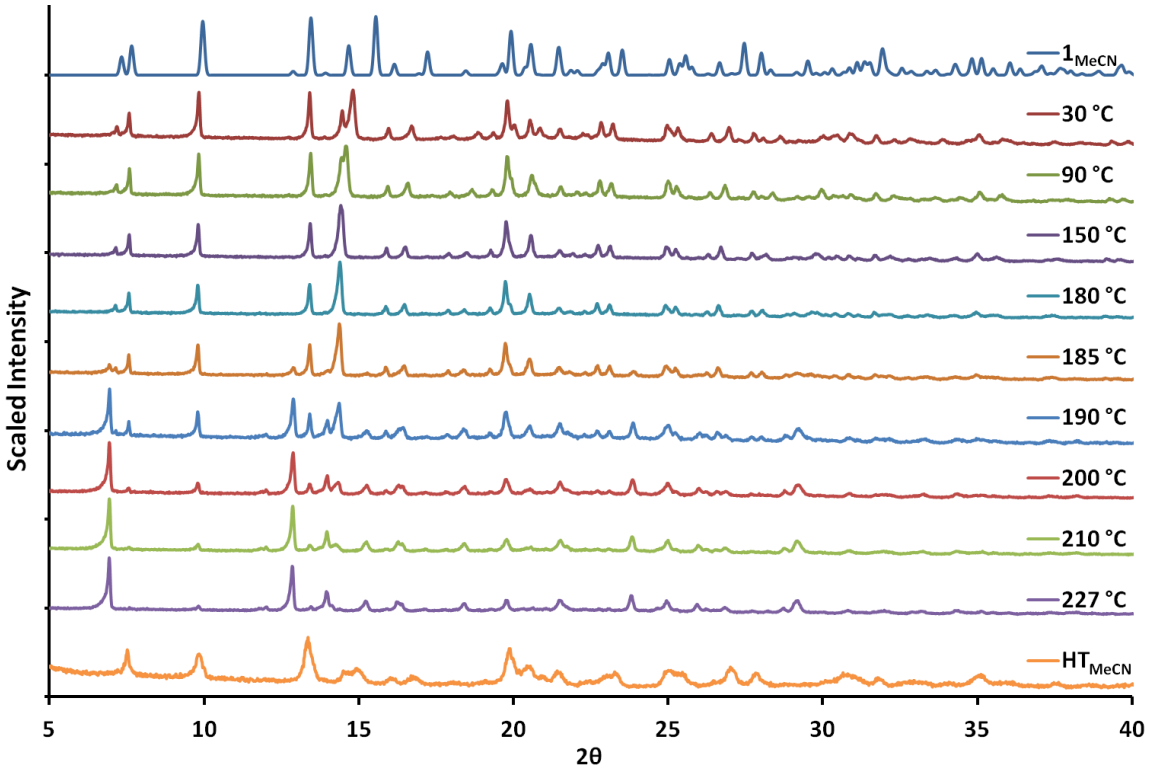

Figure 11. PXRD patterns of $\mathbf{1}_{\mathbf{MeCN}}$ recorded at various intervals from 30–227 °C. The top PXRD pattern (blue line) was simulated from the single-crystal structure of $\mathbf{1}_{\mathbf{MeCN}}$ and the bottom pattern (orange line) is the experimental diffractogram recorded after the high temperature phase (i.e. the phase obtained at 227 °C) had been immersed in MeCN overnight.

Unfortunately, the desorption of $\mathbf{1}_{\mathbf{MeCN}}$ cannot be followed as a single-crystal to single-crystal transformation because the crystals become opaque as the solvent is released and they eventually convert to a polycrystalline powder; this can clearly be seen from the images obtained by hot stage microscopy shown in **Figure 12**. Furthermore, the PXRD data were not of sufficient quality for elucidation of the crystal structure.

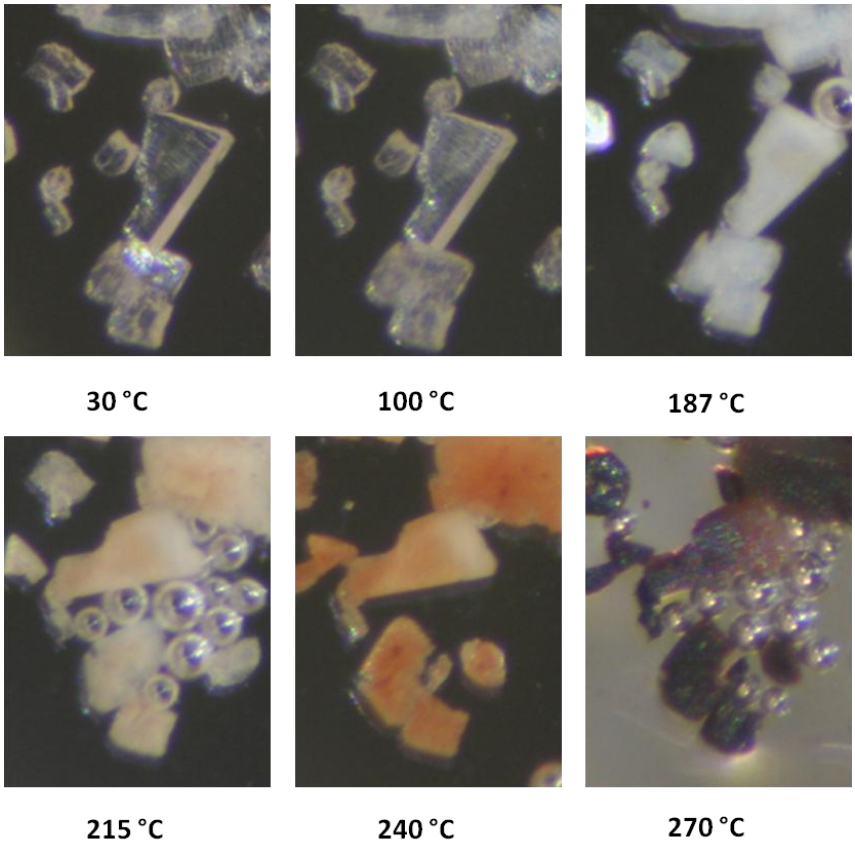

Figure 12. Hot stage microscopy images obtained for $\mathbf{1}_{\mathbf{MeCN}}$. The sample was heated from room temperature to 270 °C. Bubbles in the oil surrounding the crystals correspond to solvent loss in the approximate temperature range of 180–220 °C. As the solvent is lost the crystals become opaque and are no longer suitable for single-crystal diffraction. A stable intermediate phase is obtained between desolvation and decomposition, during which the crystals gradually discolour (i.e. change from an off-white colour to a dark brown colour).

3.2.1.3. Thermal analysis of $\mathbf{1}_{\mathbf{AC}}$

The thermal stability of $\mathbf{1}_{\mathbf{AC}}$ is similar to that of $\mathbf{1}_{\mathbf{MeOH{\cdot}H2O}}$ in that the loss of solvent occurs simultaneously with decomposition of the sample. The thermoanalytical data in **Figure 13** and the hot stage images in **Figure 14** indicate that the inclusion complex is stable to *ca* 240 °C, after which the sample rapidly starts to decompose in a multi-step process. The images also show that the crystals do not lose solvent before decomposition, and the weight loss steps before the major decomposition step are therefore due to decomposition and not desolvation. The sharp exothermic peak in the DSC trace coincides with the major weight-loss step of decomposition, and is sufficiently intense that the minor decomposition steps are lost in the baseline.

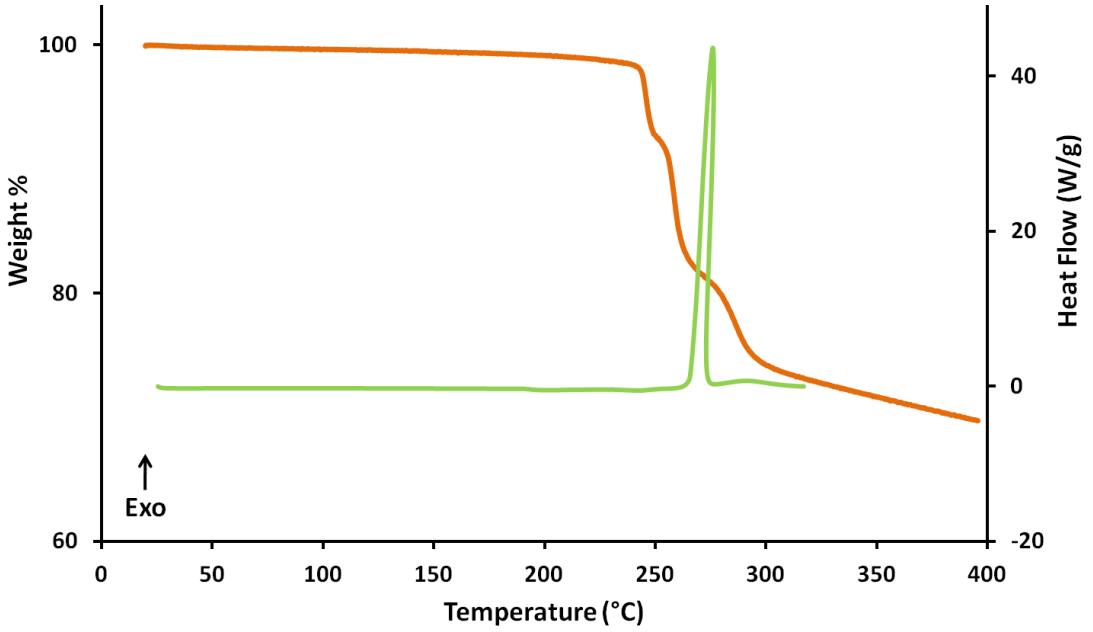

Figure 13. Thermoanalytical data for $\mathbf{1}_{AC}$; the TGA and DSC traces are orange and green, respectively.

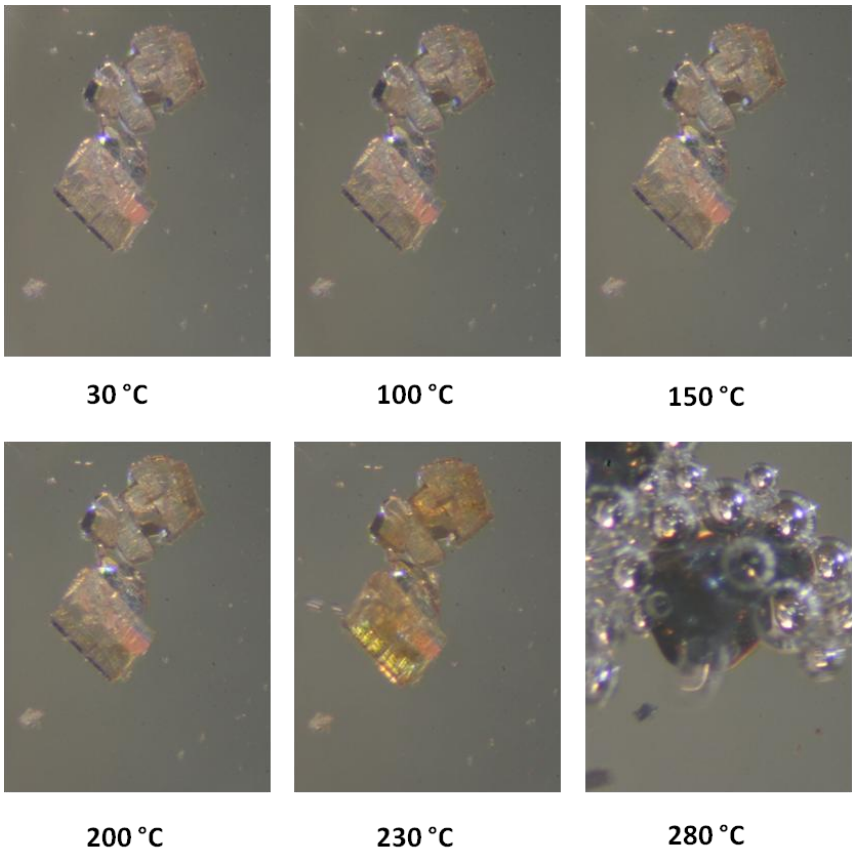

Figure 14. Hot stage microscopy images obtained for $\mathbf{1}_{AC}$. The sample was heated from room temperature to 280 °C. The crystals proceed directly to decomposition without a distinct desolvation step.

3.2.1.4. Thermal analysis of $\mathbf{2_{AC}}$

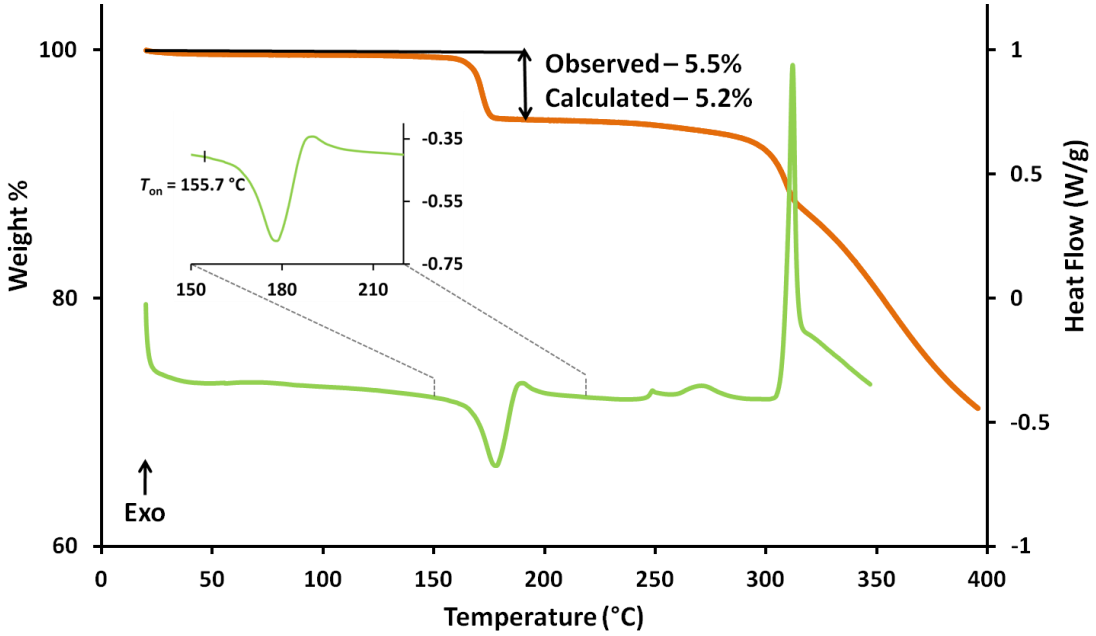

Figure 15. Thermoanalytical data for $\mathbf{2_{AC}}$; the TGA and DSC traces are orange and green, respectively and the insert highlights the endothermic desolvation step followed immediately by an exothermic event on the DSC trace.

Thermogravimetric analysis of $\mathbf{2_{AC}}$ shows a weight loss of 5.5% in the temperature range 160–190 °C, which corresponds to the loss of only a single acetone molecule per metallocycle (a theoretical mass loss of 5.2% is expected for the loss of one acetone molecule per host metallocycle). This is followed by a plateau region until *ca* 230 °C, after which the sample gradually starts to decompose (**Figure 15**). These findings are interesting considering that the single-crystal structure of $\mathbf{2_{AC}}$ has two molecules of acetone per metallocycle. This indicates that the sample does not fully desolvate before it decomposes. As was observed for $\mathbf{1_{MeCN}}$, an endotherm coinciding with the loss of the guest molecules is observed in the DSC trace of $\mathbf{2_{AC}}$ (T_{on} = 155.7 °C, with a corresponding $T_{on} - T_b$ of 99.4 °C), but unlike $\mathbf{1_{MeCN}}$, this is immediately followed by an exotherm. In order to determine if a phase change occurred upon desolvation a sample was subjected to VT-PXRD – an initial measurement of the guest-included phase correlated well with the simulated pattern from the single-crystal guest-included structure. A powder pattern was then recorded at various intervals from 30 to 227 °C. **Figure 16** shows that the removal of the single acetone molecule per metallocycle indeed induces a phase change in the sample (see patterns recorded above 150 °C); it is presumed that this phase change leads to a more

densely packed form. Unfortunately a single-crystal structure of the partially desolvated phase could not be determined as the heating process results in a loss of single crystallinity. This can be seen in the images obtained by hot stage microscopy (**Figure 17**). These images show that, once solvent loss occurs, the crystals darken and become opaque. Owing to peak broadening and a reduction in peak intensity on the powder diffractogram it was also not possible to elucidate the structure from the powder data. Furthermore, an attempt was made to recover the initial solvated $\mathbf{2_{AC}}$ phase by immersing the HT sample in liquid acetone over a period of several days. Interestingly, the HT phase persisted, which is in contrast to what was observed for $\mathbf{1_{MeCN}}$.

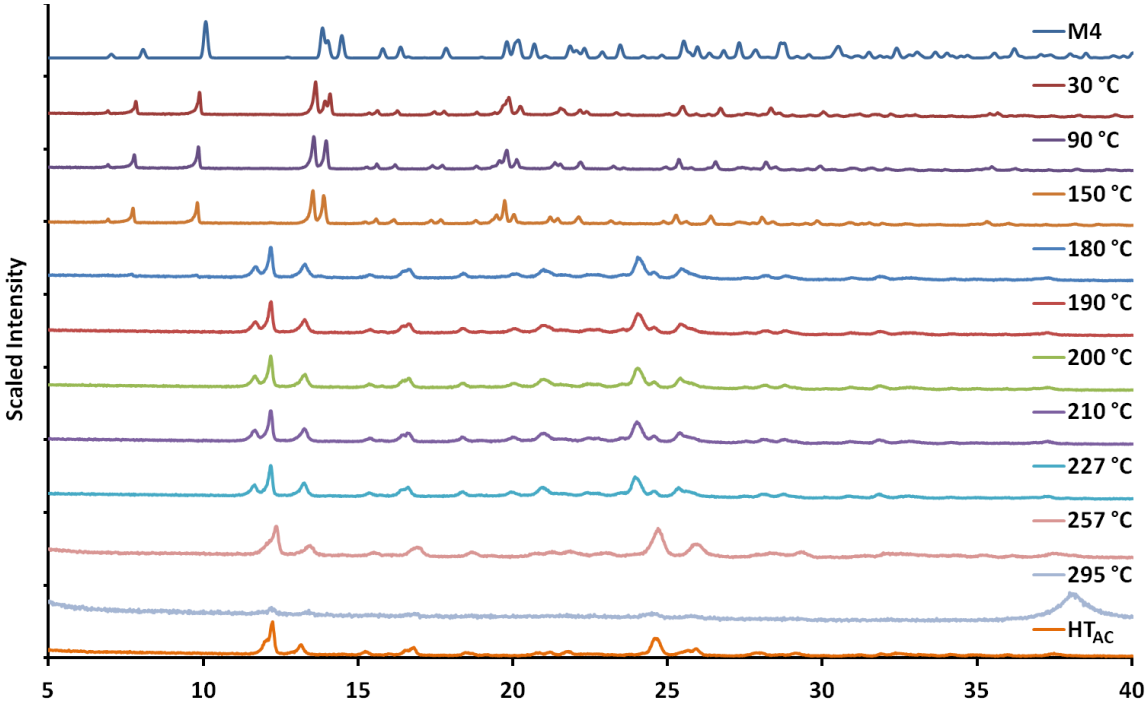

Figure 16. PXRD patterns of $\mathbf{2_{AC}}$ recorded at various intervals from 30–227 °C as part of the VT-PXRD program. The diffractograms at 257 and 295 °C were recorded using two separate samples, each heated in the TGA to the specific temperatures indicated in the legend. The top PXRD pattern (blue line) is was simulated from the single-crystal structure of $\mathbf{2_{AC}}$, whilst the bottom pattern (orange line) is the experimental diffractogram recorded after the high temperature phase (i.e. the phase obtained at 227 °C) had been immersed in liquid acetone for several days.

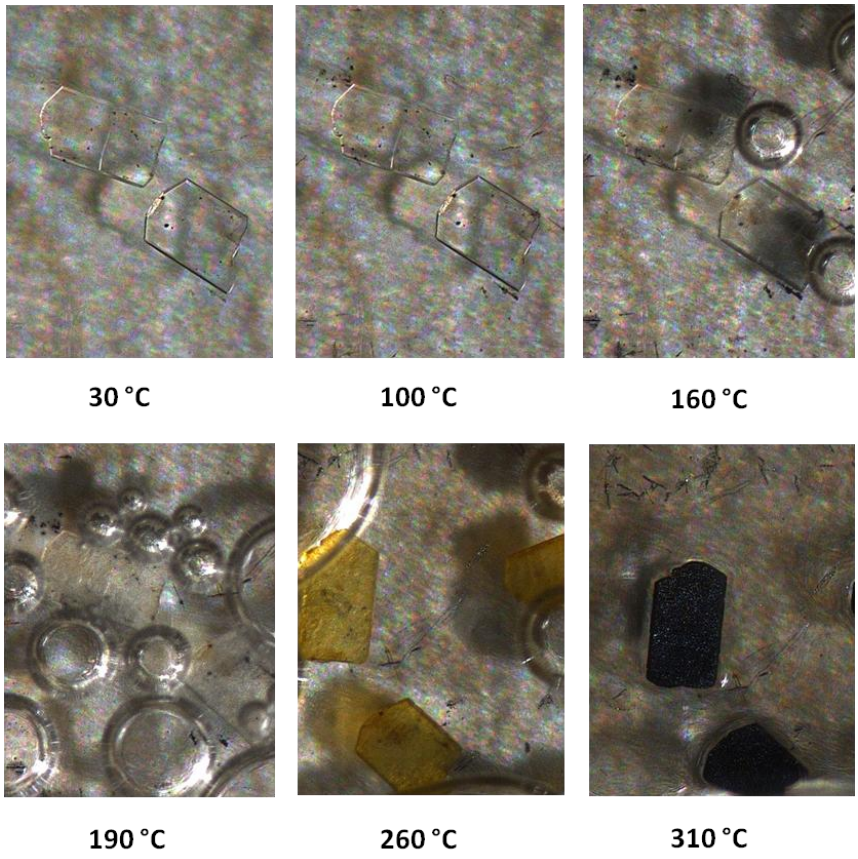

Figure 17. Hot stage microscopy images obtained for $\mathbf{2_{AC}}$. The sample was heated from room temperature to 310 °C. Bubbles in the oil surrounding the crystals correspond to solvent loss in the approximate temperature range of 155–195 °C. As the solvent is lost the crystals become opaque and no longer diffract. A stable intermediate phase is obtained between desolvation and decomposition and the crystals eventually become black as they decompose.

Between the exotherm at *ca* 190 °C and the decomposition exotherm at *ca*. 300 °C, two small exotherms at *ca* 250 °C and *ca* 270 °C are present in the DSC trace. As these temperatures extend beyond the upper limit of the VT cryostat it is not possible to determine, by VT-PXRD methods, whether these exotherms are indicative of a phase change. An attempt was made to identify the phase by simply heating the sample to 257 °C in the TGA (i.e. the temperature at which the first thermal event ends) and then recording the powder pattern; from these results it appears that this exotherm does not indicate a further phase change.[§] Similarly, a second sample was heated to 295 °C (the end of the second exothermic event) and a powder pattern was recorded. Unfortunately the diffractogram was of such poor quality that it is not possible to accurately identify whether

[§] We acknowledge that it is not possible to accurately determine the temperature:phase relationship by this method as the cooling process, as well as the time taken to load the sample from the TGA into the powder X-ray diffractometer, may have an affect on the phase obtained.

it is the same phase as previously obtained, although it does appear that traces of the HT phase are present at very low peak intensities.

3.2.1.5. Further attempts to obtain single crystals of the desolvated structures of $\mathbf{1}_{\mathbf{MeOH\cdot H2O}}$, $\mathbf{1}_{\mathbf{MeCN}}$, $\mathbf{1}_{\mathbf{AC}}$ and $\mathbf{2}_{\mathbf{AC}}$

Whilst monocrystallinity[**] is not a requirement for porosity studies, single crystals can provide us with information regarding intermolecular interactions that is not readily attainable by other methods. For this reason every effort was made to obtain crystals of the guest free phases of $\mathbf{1}_{\mathbf{MeOH\cdot H2O}}$, $\mathbf{1}_{\mathbf{MeCN}}$, $\mathbf{1}_{\mathbf{AC}}$ and $\mathbf{2}_{\mathbf{AC}}$. It is clear from the results above that the single crystals of the inclusion complexes do not survive the high temperatures needed to remove the solvent from the metallocyclic hosts despite the fact that the solvent molecules are located in open channels and only participate in weak hydrogen bonds or van der Waals interactions and should therefore be able to easily diffuse out of the host lattice. Therefore, in an effort to obtain the single-crystal structures of the apohost phases by means other than heating, single crystals of the guest-included phases of each were placed under a dynamic vacuum (10^{-3} Torr) for 24 hours. In all cases there was a discernable loss of monocrystallinity owing to fracturing of the crystals and in fact, in the majority of cases, the crystals converted to a white microcrystalline powder. However, for $\mathbf{1}_{\mathbf{MeCN}}$ and $\mathbf{1}_{\mathbf{AC}}$ a few larger crystals survived the process intact the solvent molecules could still be modelled with the same occupancy as that of the original structure. We also attempted to exchange the parent solvent with a more volatile guest and then to evacuate the channels by heating, but this also resulted in powdering of the sample (see section 3.2.2).

In a final effort to remove the solvent with retention of monocrystallinity, an attempt was made to 'supercritically activate' samples of $\mathbf{1}_{\mathbf{MeOH\cdot H2O}}$, $\mathbf{1}_{\mathbf{MeCN}}$, $\mathbf{1}_{\mathbf{AC}}$ and $\mathbf{2}_{\mathbf{AC}}$. This innovative and relatively new approach to increasing the gas-accessible surface areas in various MOF materials has been pioneered by Hupp and co-workers[15] and, very briefly, involves exchange of the solvent within the pores of the MOF with liquid CO_2. The sample is then taken above the critical point of CO_2 (T = 31 °C and P = 73 atm), and held under these conditions for a period of several hours; upon depressurisation the empty porous material is formed. Crystals of the inclusion complexes were treated with

[**] By this we mean crystals that are suitable for the technique of single-crystal diffraction analysis.

supercritical CO_2 for 24 hours and then slowly vented over several hours. A visual inspection of the crystals revealed no significant change to the external morphology and the crystals still extinguished plane polarised light uniformly. However, single-crystal structure analysis revealed that the solvent molecules had not been removed by this method.

3.2.1.6. A comparison of the interaction energies in the structures of $\mathbf{1_{MeCN}}$ and $\mathbf{M2_{MeCN}}$

In order to gain further insight into the high thermal stability of the Ag(I) metallocyclic hosts for their included guest molecules, a computational study[††] was carried out to investigate whether strong guest-guest and/or host-guest interactions could account for this observed stability. A range of interaction energies were calculated for the $\mathbf{1_{MeCN}}$ system and compared to that of a previously reported Ag(I) metallocycle, which does not retain its guests at high temperatures i.e. $\mathbf{M2_{MeCN}}$ ($[Ag_2(\mathbf{A2})_2](PF_6)\cdot 2CH_3CN$, where **A2** = 2,3,4,6-tetrafluoro-1,4-bis(2-methylimidazole-1-ylmethyl)benzene).[12] $\mathbf{1_{MeCN}}$ was chosen as a representative of this series for the computational studies owing to the structural similarities between $\mathbf{1_{MeCN}}$ and $\mathbf{M2_{MeCN}}$; both structures comprise of Ag(I)-containing metallocycles that stack on top of one another to form columns, with the apertures of the metallocycles aligned to form 1D channels. The aromatic spacer moieties of the ligands are fluorinated at positions 2, 3, 5 and 6 and both accommodate two MeCN molecules per host metallocycle, positioned in an up-down dimeric arrangement within the channels. The differences between the compositions of $\mathbf{1_{MeCN}}$ and $\mathbf{M2_{MeCN}}$ are that (i) the anion is NO_3^- in $\mathbf{1_{MeCN}}$ and PF_6^- $\mathbf{M2_{MeCN}}$ and (ii) the imidazole moieties in $\mathbf{M2_{MeCN}}$ contain a methyl substituent on the 2' position. The orientation and arrangement of the MeCN dimer relative to the metallocycles, as well as the shape of the 1D channels, also differ in the two structures: in $\mathbf{1_{MeCN}}$ an open, continuous 1D channel is formed with the MeCN dimers slightly tilted relative to the channel direction, whereas the channels in $\mathbf{M2_{MeCN}}$ consist of a series of bulges connected by smaller apertures and the MeCN dimers are secluded in the bulges of the channel arranged approximately perpendicular to the channel direction. The packing arrangement of the metallocyclic columns is also different: in $\mathbf{1_{MeCN}}$ the columns are arranged in a herringbone motif, which is stabilised by π–π interactions and in

[††] Calculations were carried out by D.P. van Heerden under the supervision of Dr C. Esterhuysen – see Section 3.4.2 for further details.

M2$_{MeCN}$ the columns are arranged in a rectangular fashion with neighbouring columns linked by argentophilic interactions (see **Figure 18** for the images associated with **M2$_{MeCN}$**).

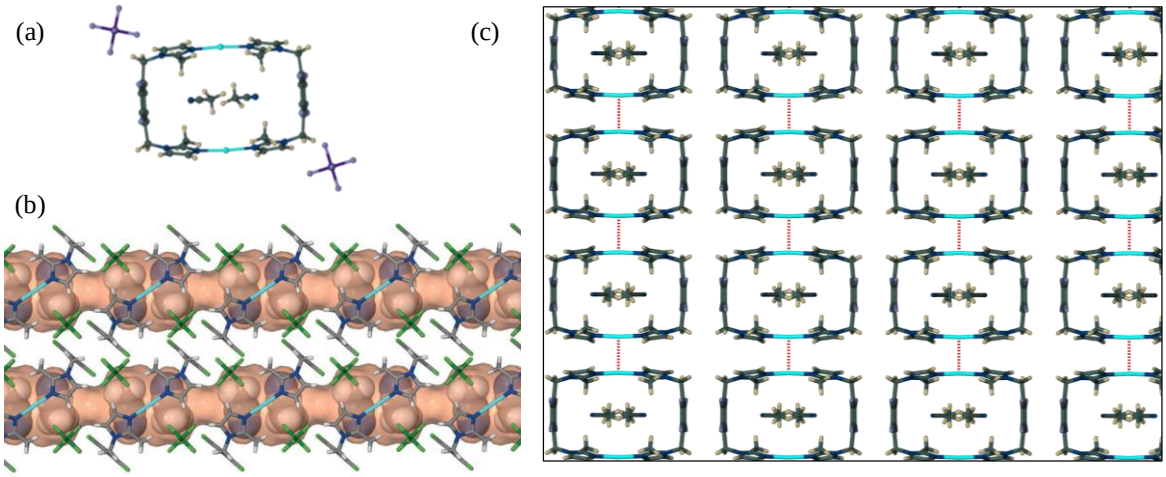

Figure 18. (a) The metallocyclic complex **M2$_{MeCN}$**. **(b)** Perspective view of **M2$_{MeCN}$** perpendicular to the 1D channel formed by the stacking of the metallocycles. Metallocycles are shown as capped-sticks and solvent molecules are shown in van der Waals representation. Solvent channel passing through the stacked metallocycles are shown as a semitransparent pink Connolly surfaces (using a probe radius of 1.4 Å). **(c)** Arrangement of the columns of metallocycles in **M2$_{MeCN}$** viewed along [100]. Solvent molecules and anions are omitted for clarity and argentophilic interactions are shown as fragmented bonds.[12]

In the calculations, the hydrogen atom positions of the models based on the diffraction data were optimised at the M06/CEP-31G level of theory (a density functional theory method utilising a double zeta basis set). The following interaction energies were calculated at the M06/CEP-121G (a triple zeta basis) level of theory for both the **1$_{MeCN}$** and **M2$_{MeCN}$** systems (see **Table 1** for the values associated with the various interactions and **Scheme 3** for a simplification of the models used in the calculations):

1) Guest-guest interaction, between the two MeCN molecules constituting a dimeric pair;
2) Guest-guest interaction, between one MeCN molecule and the next guest related by translation along [100] i.e. the next guest further along the channel;
3) Host-guest interaction, between one MeCN molecule and one $[Ag_2\mathbf{L}_2]^{2+}$ (**L** = **L1** for **1$_{MeCN}$** and **A2** for **M2$_{MeCN}$**) host metallocycle;

4) Guest counter-ion interaction, between one MeCN molecule and the counter-ion proximate to the methyl side of the guest;
5) Guest counter-ion interaction, between one MeCN molecule and the counter-ion proximate to the nitrile side of the guest;
6) Host-guest interaction, between one MeCN molecule and the host metallocycle proximate to the methyl side of the guest;
7) Host-guest interaction, between one MeCN molecule and the host metallocycle proximate to the nitrile side of the guest;
8) The interaction between a dimeric guest pair and the atoms located within a 4.5 Å sphere of inclusion.

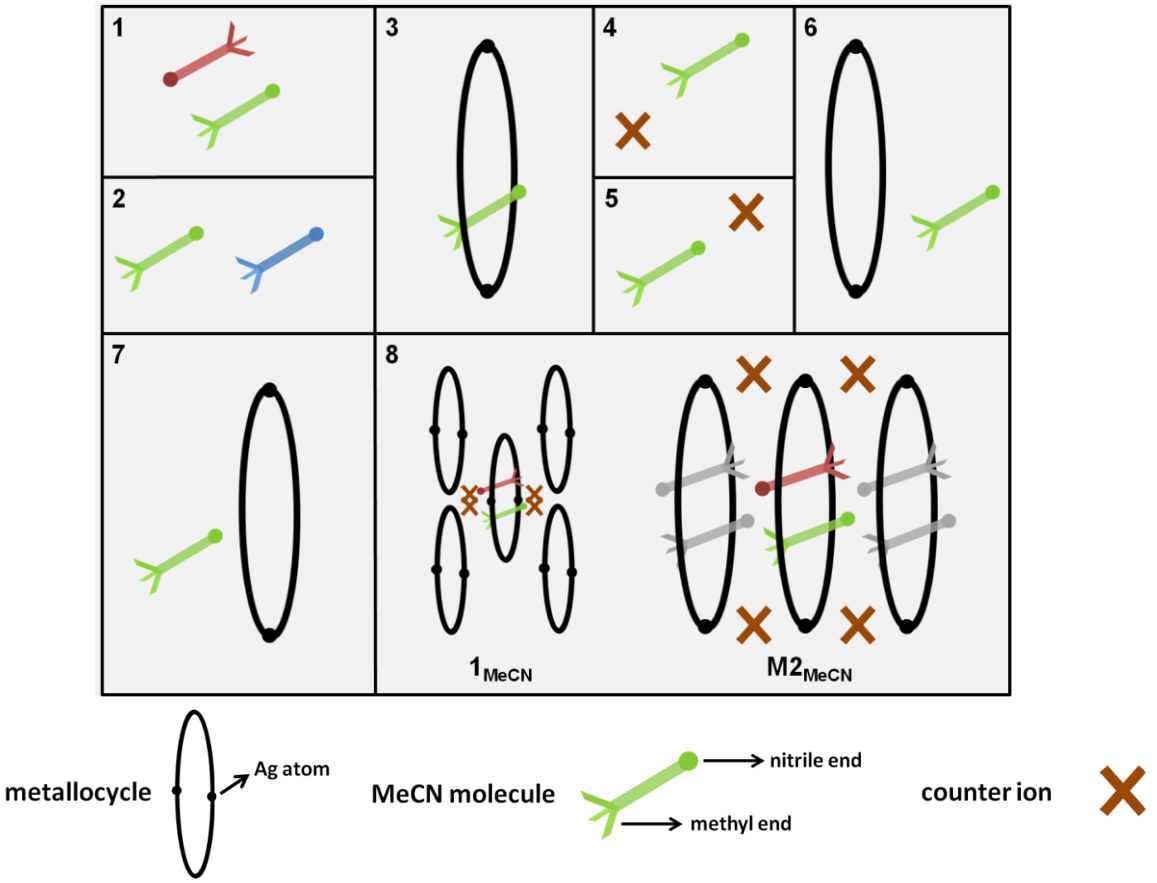

Scheme 3. Cartoon representation of the calculated interactions 1–8 described in the text.

Table 1. Comparison of the interaction energies between $\mathbf{1}_{\mathbf{MeCN}}$ and $\mathbf{M2}_{\mathbf{MeCN}}$.

Calculation number*	$\mathbf{1}_{\mathbf{MeCN}}$ (kcal mol^{-1})	$\mathbf{M2}_{\mathbf{MeCN}}$ (kcal mol^{-1})
1	–4.51	–3.29
2	–1.71	–0.42
3	–6.79	–9.96
4	–9.56	–4.48
5	2.59	1.89
6	4.55	4.01
7	–4.44	–4.95
8	–31.58	–29.39

*The description of the calculation associated with each reference is provided in Scheme 3 and in the text.

Table 1 shows that the guest-guest interactions in $\mathbf{1}_{\mathbf{MeCN}}$ are more stabilising than those of $\mathbf{M2}_{\mathbf{MeCN}}$. The MeCN guest has a greater stabilising interaction through its methyl extremity with the nitrate anion in $\mathbf{1}_{\mathbf{MeCN}}$ than with the PF_6^- anion in $\mathbf{M2}_{\mathbf{MeCN}}$ (–9.56 vs –4.48 kcal mol^{-1}), and it experiences a weaker interaction with the $[Ag_2(\mathbf{L1})_2]^{2+}$ metallocycle than with the $[Ag_2(\mathbf{A2})_2]^{2+}$ metallocycle (–6.79 vs –9.96 kcal mol^{-1}). In both structures, the MeCN has a repulsive interaction with neighbouring metallocycles through its methyl extremity (4.55 and 4.01 kcal mol^{-1} for $\mathbf{1}_{\mathbf{MeCN}}$ and $\mathbf{M2}_{\mathbf{MeCN}}$, respectively), while it has a stabilising interaction through its nitrile extremity with the same neighbours (–4.44 and –4.94 kcal mol^{-1} for $\mathbf{1}_{\mathbf{MeCN}}$ and $\mathbf{M2}_{\mathbf{MeCN}}$, respectively). This is opposite to the trend observed for the guest-counter-ion interactions. The interaction of a dimeric pair of MeCN guests within their 4.5 Å sphere of inclusion takes cooperative effects into account: in $\mathbf{1}_{\mathbf{MeCN}}$ the guest pair effectively 'sees' four counter-ions and two metallocycles with their included guests within a 4.5 Å sphere of inclusion, whereas the same pair in $\mathbf{M2}_{\mathbf{MeCN}}$ interacts with four counter-ions and four metallocyclic units but does not undergo an interaction with the included molecules in the 4.5 Å sphere, as they are too far away. This interaction is more stabilising in $\mathbf{1}_{\mathbf{MeCN}}$ than in $\mathbf{M2}_{\mathbf{MeCN}}$ by 2.2 kcal mol^{-1} and, although this appears to be a small difference in energy, taken in conjunction with a stronger guest-guest interaction of 1.2 kcal mol^{-1} (the first calculation in the list) could possibly provide an explanation for the observed stability of $\mathbf{1}_{\mathbf{MeCN}}$ with respect to its included guest molecules as compared to $\mathbf{M2}_{\mathbf{MeCN}}$.

Another factor to consider is that the magnitude of the stabilising energy observed for the interactions between the dimeric pair and the atoms located within a 4.5 Å sphere of inclusion is large for both systems i.e. –31.59 and –29.39 kcal mol^{-1} for $\mathbf{1}_{\mathbf{MeCN}}$ and $\mathbf{M2}_{\mathbf{MeCN}}$, respectively. This implies that $\mathbf{M2}_{\mathbf{MeCN}}$ should also have a high thermal stability

for its included guest molecules, yet it readily loses solvent under mild heating conditions. This led us to consider that the thermal stability may not only be due to guest-guest and host-guest interactions, but that host-host interactions may also play a role (i.e. the packing arrangement of the metallocyclic columns could stabilise the guest-free host framework). All of the Ag(I) metallocyclic structures in this chapter that exhibit high thermal stability for solvent-inclusion pack in the well-known herringbone motif, whereas the Ag(I) metallocycles in the literature are arranged in a rectangular fashion or a centred rectangular fashion. It is possible then that the arrangement of the metallocycles in $\mathbf{1}_{\mathbf{MeOH{\cdot}H2O}}$, $\mathbf{1}_{\mathbf{MeCN}}$, $\mathbf{1}_{\mathbf{AC}}$ and $\mathbf{2}_{\mathbf{AC}}$ is not such that the host framework can easily deform to a sufficiently stable guest-free conformation. As a consequence of this, removal of the solvent does not drive the system towards an energetically favourable state and much energy is needed to force the removal of the solvent molecules. This is in contrast to $\mathbf{M2}_{\mathbf{MeCN}}$ where the host metallocycles are arranged in such a manner that the host framework can subtly deform to create stronger host-host intermolecular interactions to compensate for the loss of host-guest intermolecular interaction and the host framework is thus stabilised, even in the absence of guests, and the energy barrier to solvent loss is much lower. It must be noted that calculations of this kind, i.e. probing the various host-host interactions in the absence of guest molecules, is a non-trivial undertaking and falls beyond the scope of this work.

3.2.2. SC-SC solvent exchange and thermal analyses

As is evident from the previous section, it is not possible to remove the original solvent of $\mathbf{1}_{\mathbf{MeOH{\cdot}H2O}}$, $\mathbf{1}_{\mathbf{MeCN}}$, $\mathbf{1}_{\mathbf{AC}}$ and $\mathbf{2}_{\mathbf{AC}}$ with retention of monocrystallinity by simply heating the sample under vacuum. We therefore decided to explore other methods of obtaining the apohost structure. A common alternative to thermally assisted evacuation of the parent solvent involves a liquid-phase exchange.[15,16] During this process the original solvent is replaced by a more volatile solvent that can then be removed under milder conditions, thereby increasing the possibility of obtaining the apohost structure by SC-SC methods. To this end crystals of $\mathbf{1}_{\mathbf{MeCN}}$ were immersed in the commonly used volatile organic solvent, dichloromethane (DCM). 24 hours later the single crystals appeared intact and SCD analysis revealed that a single-crystal to single-crystal (SC–SC) transformation had occurred in which the acetonitrile molecules had been replaced by the DCM molecules without causing significant rearrangement of the host molecules. Examples of SC–SC

transformations are uncommon, as crystallinity is difficult to retain when the system becomes strained as a result of reorganisation of molecules in the solid state.[17-22] During the solvent exchange process, images of the single crystals of $\mathbf{1_{MeCN}}$ were taken at various intervals (**Figure 19**). This was in order to exclude the possibility that the formation of $\mathbf{1_{DCM}}$ is as a result of the dissolution of $\mathbf{1_{MeCN}}$ in the excess DCM, followed by re-crystallisation of the new phase. The images show that there is no change in size, morphology, colour or transparency of the initial $\mathbf{1_{MeCN}}$ crystals over the 24 hour period.

Although attempts to remove the DCM from the channels of the $\mathbf{1_{DCM}}$ structure resulted in either powdering or decomposition of the single crystals, SC–SC exchange of solvent is intriguing.

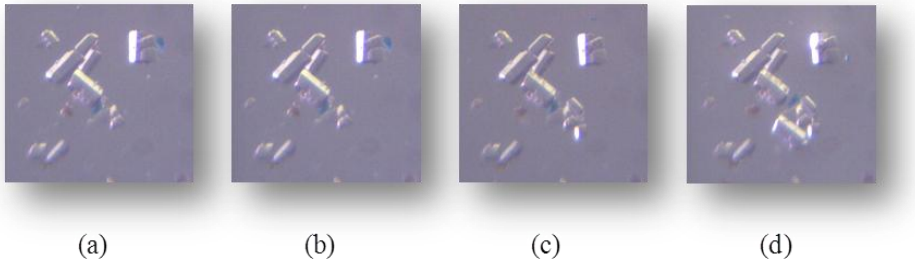

Figure 19. Photographs of single crystals of $\mathbf{1_{MeCN}}$ immersed in DCM. Images were taken after **(a)** 0 hrs, **(b)** 2 hrs, **(c)** 12 hrs and **(d)** 24 hrs.

The three categories of porosity were reviewed in Section 1.4; the second class of porosity involves guest exchange without there being a guest-free phase. The exchange of MeCN for DCM involves mass transport of guest molecules through the channels of the solid host medium and presumably involves a concerted mechanism in which the MeCN molecules simultaneously exit the channels as the DCM molecules enter; consequently, it would not be possible to isolate a guest-free phase at any point during the exchange process. The conversion of $\mathbf{1_{MeCN}}$ to $\mathbf{1_{DCM}}$ therefore renders $\mathbf{1_{MeCN}}$ a Class II porous system according to our classification in section 3.1. The guest exchange process can be generically described by the following equation:

$$\mathbf{HG}\,(s) + \mathbf{G'}(l) \rightarrow \mathbf{HG'}(s) + \mathbf{G}(l)$$

where **H** represents the host system, **G** the original guest and **G'** the potential new guest (present in excess during the reaction).

The successful exchange of MeCN for DCM in $\mathbf{1_{MeCN}}$ prompted a further investigation into the permeability of $\mathbf{1_{MeOH\cdot H2O}}$, $\mathbf{1_{MeCN}}$, $\mathbf{1_{AC}}$ and $\mathbf{2_{AC}}$ to a variety of common solvents. 10–15 mg of single crystals of the inclusion complexes were immersed in 2–5 mL of DCM, benzene (BZ), 1,4-difluorobenzene (DFB), 1,4-dioxane (DIOX), cyclohexane (CY) and water. After a period of one day to two weeks, single-crystal data were collected to determine if the parent solvent had been exchanged. If the SC data indicated that an exchange had occurred (see **Table 2** for the results of the exchange experiments), the sample was subjected to TGA and DSC to assess the thermal stability of the new inclusion complex. All reported weight loss percentages were recorded from the start of the TGA to the minimum in the first derivative of the weight-loss curve. As was previously the case, onset temperatures (T_{on}) of guest release were only noted for complexes in which a distinct endothermic desolvation step was observed in the DSC (**Table 3** at the end of this section). PXRD analysis was used to confirm the presence of any obvious secondary phases and in all cases the single-crystal data appeared to be representative of the bulk (Appendix B).[‡‡] The reversibility of the process was tested using the $\mathbf{1_{MeCN}} \rightarrow \mathbf{1_{DCM}}$ system i.e. the $\mathbf{1_{DCM}}$ crystals were re-immersed in MeCN for one day and the single-crystal structure was determined. The data indicate a slight degradation in the quality of the single crystal, but we were however able to obtain a reasonable structure showing that the DCM had been replaced by MeCN resulting in a recovery of the original $\mathbf{1_{MeCN}}$ phase. It can therefore be inferred that the exchange process is reversible in all systems, but single-crystal data would have to be collected for each system to verify this conjecture.

When exchange occurs in the $\mathbf{1_{MeOH\cdot H2O}}$, $\mathbf{1_{MECN}}$ and $\mathbf{1_{AC}}$ systems, the space-group symmetry remains the same as that of the parent systems and only small adjustments are apparent in the unit cell parameters of the new inclusion complexes. As has been mentioned before, the $\mathbf{1_G}$ parent structures are all isoskeletal; thus exchange of the respective parent solvents for the same new guest solvent results in three isostructural complexes that will all be allocated the same $\mathbf{1_{G'}}$ notation. For the analysis of the thermal data the parent guest will be included in brackets immediately following the $\mathbf{1_{G'}}$ notation to differentiate between the three sets of data (e.g. the thermal analysis of the $\mathbf{1_{MeCN}} \rightarrow \mathbf{1_{DCM}}$ exchange reaction will be denoted by $\mathbf{1_{DCM(MeCN)}}$.

[‡‡] The guest does not appear to contribute significantly to the diffraction profile. Therefore the peak positions in the diffractograms remained largely unaffected by the exchange process , necessitating SC as the primary tool for determining whether or not an exchange took place.

For the $\mathbf{2_{AC}}$ system, the exchange process removes the asymmetry of the two parent acetone molecules and the 2/*m* site symmetry is shifted to the centre of the metallocycle, resulting in a halving of the *a*-axis and similar stacking of metallocycles as seen in the $\mathbf{1_G}$ structures. The structures of the new inclusion complexes obtained from both $\mathbf{1_G}$ and $\mathbf{2_G}$ parent systems share many similarities with each another and it is therefore worthwhile to compare the structures with respect to the following parameters: the host:guest ratio (where the host is defined as the entire metallocyclic unit), the intramolecular Ag···Ag distance coupled with the aryl centroid-to-centroid distance, the stacking periodicity, the 'aromatic tilt' angle, the 'metallocycle tilt' angle and the total potential solvent volume. The values associated with these parameters can be found in **Table 3** at the end of this section – only outliers will be mentioned in the main body of the text.

Table 2. Summary of the exchange results obtained for the parent inclusion complexes.

G'	$\mathbf{1_{MeOH\cdot H2O}}$	$\mathbf{1_{MeCN}}$	$\mathbf{1_{AC}}$	$\mathbf{2_{AC}}$
Dichloromethane	$\mathbf{1_{DCM}}$	$\mathbf{1_{DCM}}$	$\mathbf{1_{DCM}}$	$\mathbf{2_{DCM}}$
Benzene	$\mathbf{1_{BZ}}$	$\mathbf{1_{BZ}}$	$\mathbf{1_{BZ}}$	$\mathbf{2_{BZ}}$
1,4-Difluorobenzene	$\mathbf{1_{DFB}}$	$\mathbf{1_{DFB}}$	$\mathbf{1_{DFB}}$	$\mathbf{2_{DFB}}$
1,4-Dioxane	$\mathbf{1_{DIOX}}$	$\mathbf{1_{DIOX}}$	$\mathbf{1_{DIOX}}$	$\mathbf{2_{DIOX}}$
Cyclohexane	$\mathbf{1_{CY}}$	no exchange[§§]	no exchange	$\mathbf{2_{CY}}$
Water	$\mathbf{1_{H2O}}$	no exchange	no exchange	no exchange

[§§] For the entries marked 'no exchange' the following procedure was carried out – structural elucidation by single-crystal methods revealed that no exchange had occurred after 24 hours of exposure to the guest solvent **G'**,,i.e. the parent solvent could still be modeled within the channels of the host in the same positions, with the same occupancy as that of $\mathbf{1_G}$. The crystal were then re-exposed to the solvent for a further 2 weeks, and the structure elucidated after this time period indicated that the exchange had still not occurred.

3.2.2.1. Exchange with DCM

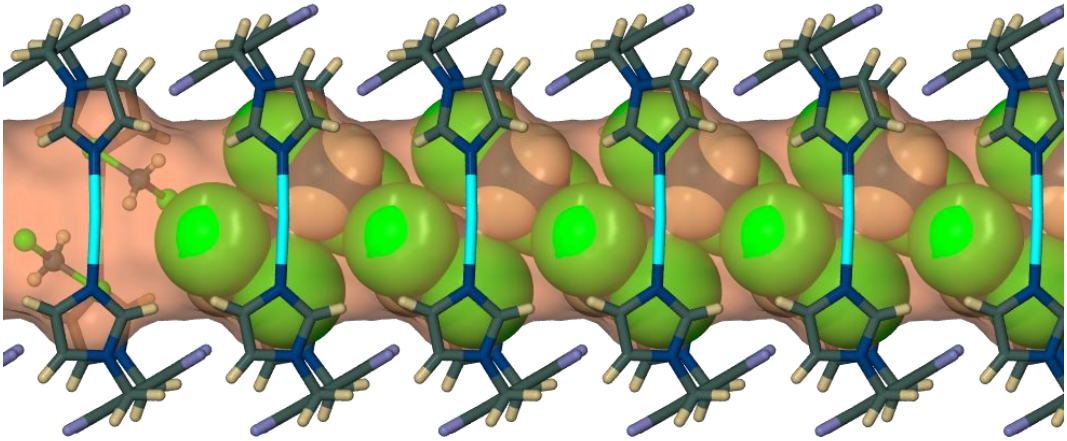

Figure 20. Projection of $\mathbf{1_{DCM}}$ (or $\mathbf{2_{DCM}}$) viewed perpendicular to (010). The host metallocycles are shown in capped-stick representation and the first pair of guest molecules (from the left) is shown in the ball-and-stick metaphor, and the remaining guest molecules are shown in van der Waals representation. The solvent channel passing through the stacked metallocycles is shown as a semitransparent solvent-accessible surface (using a probe radius of 1.4 Å). One of the chlorine atoms of each DCM molecule protrudes from the surface due to the C···O close contact between this chlorine atom and an oxygen atom of the nitrate anion.

The ASUs of $\mathbf{1_{DCM}}$ and $\mathbf{2_{DCM}}$ all consist of one half of a metallocyclic host complex, one counter-ion and one DCM molecule situated about a crystallographic inversion centre; this yields a host:guest ratio of 1:2. An examination of the structures reveals that there are no significant interactions between the host metallocycle and the guest. In $\mathbf{1_{DCM}}$ the DCM molecules and nitrate anions are associated by means of a short contact between a chlorine atom of a DCM molecule and an oxygen atom of the nitrate anion (C···O = 3.030(4) Å)[***], and in $\mathbf{2_{DCM}}$ this interaction is between a chlorine atom of a DCM molecule and a fluorine atom of the tetrafluoroborate anion (C···F = 2.992(6) Å)[†††].[23] The arrangement of the guest relative to the host metallocycles is similar in all four structures and only one figure has therefore been provided (**Figure 20**). The two large DCM molecules are accommodated along the length of the metallocycles, resulting in the largest value recorded for the packing periodicity, as well as the longest intra-metallocycle aryl distance and, correspondingly, the shortest intra-metallocycle Ag···Ag distance reported in the $\mathbf{1_{G'}}$ series (see **Table 3**).

[***] This interaction is within the sum of the van der Waals radii of Cl and O, which is 3.32 Å; we note that the sum of the radii should be slightly larger than 3.32 Å given that the O atom belongs to a negatively charged nitrate counter ion.[16]

[†††] The distance reported here is slightly longer than the sum of the van der Waals radii of F and O, which is 2.92 Å; however as mentioned above, the sum of the radii should be slightly larger than 2.92 Å as the F atom belongs to BF_4^-.

The TGA and DSC traces of $\mathbf{1_{DCM(MeOH\cdot H2O)}}$ in **Figure 21a** and $\mathbf{1_{DCM(AC)}}$ in **Figure 21c** reveal that their respective inclusion complexes are stable to *ca* 200 °C and then rapidly start to decompose as a multi-step process. As there is no mass loss before decomposition we infer that solvent loss is concomitant with decomposition of these two complexes. From the thermoanalytical data recorded for $\mathbf{1_{DCM(MeCN)}}$ (**Figure 21b**) it appears that the inclusion complex is also stable to *ca* 200 °C, but that the weight loss beyond this temperature is more gradual and step-wise than for the previous two complexes. The first weight loss step accounts for 8.4% of the total weight and does not appear to be due to a desolvation step as this value does not correspond to the loss of a stochiometric amount of solvent molecules per metallocycle (i.e. it is too high for the loss of one DCM molecule (calculated value 7.4%) and too low for the loss of two (calculated value 14.9%). One would also expect an endotherm to coincide with a desolvation step; however, the DSC trace for $\mathbf{1_{DCM(MeCN)}}$ shows a sharp exotherm in this region.

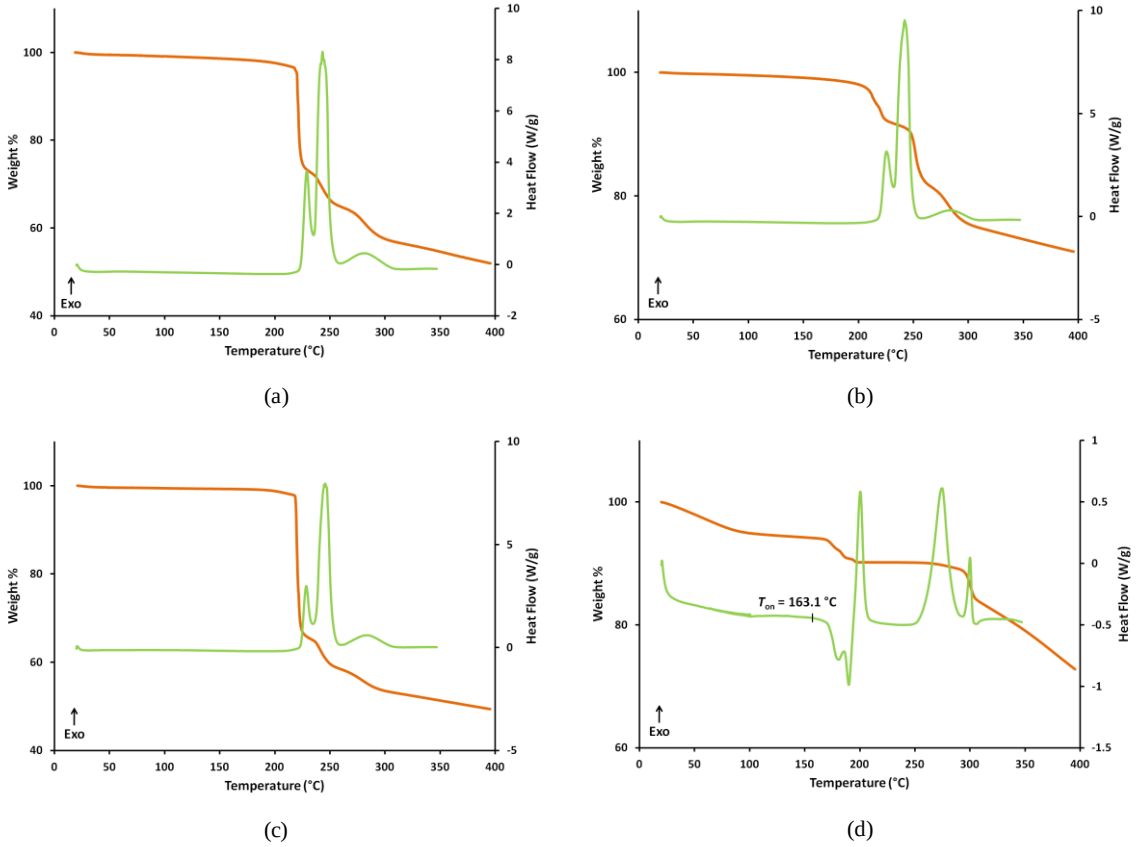

Figure 21. Thermoanalytical data for **(a)** $\mathbf{1_{DCM(MeOH\cdot H2O)}}$, **(b)** $\mathbf{2_{DCM(MeCN)}}$, **(c)** $\mathbf{1_{DCM(AC)}}$ and **(d)** $\mathbf{2_{DCM}}$; the TGA and DSC traces are orange and green, respectively.

The thermoanalytical data for $\mathbf{2_{DCM}}$ presented in **Figure 21c** are the most interesting in this series; from the TG trace it is apparent that solvent loss occurs gradually from room temperature until *ca* 160 °C and then more rapidly from *ca* 160–200 °C. The latter step coincides with an endothermic thermal event in the DSC trace with T_{on} = 163.1 °C. It is unclear whether this solvent loss is entirely due to loss of solvent from within the channels of the complex, or whether a certain percentage of the loss can be ascribed to solvent molecules adhered to the surface of the sample. If one considers the percentage mass loss of 9.8 % observed from room temperature to *ca* 200 °C (9.8%) vs. the percentage mass loss expected for a stochiometric loss of solvent (7.1% for one DCM and 14.2% for loss of two DCM molecules per metallocycle) into consideration, the latter explanation becomes more plausible. Beyond the desolvation endotherm three sharp exothermic events are observed in the DSC trace at approximate onset temperatures of 190, 250 and 290 °C. As the first exothermic event corresponds to a plateau region in the TG, it is likely that $\mathbf{2_{DCM}}$ follows the same trend observed for the parent $\mathbf{2_{AC}}$ i.e. there is a loss of one DCM per host with a concomitant rearrangement of the molecules to yield a new high temperature phase that is thermally stable for a further *ca* 50 °C. The exothermic events at *ca* 250 °C and *ca* 290 °C indicate that decomposition of $\mathbf{2_{DCM}}$ is a two-step process.

3.2.2.2. Exchange with benzene (BZ)

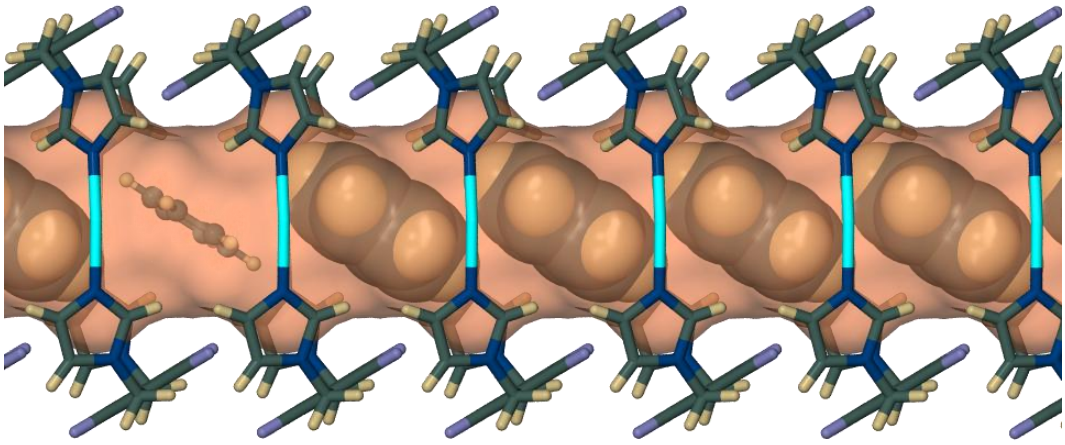

Figure 22. Projection of $\mathbf{1_{BZ}}$ viewed perpendicular to (010). The host metallocycles are shown in capped-stick representation and the first complete benzene guest (from the left) is shown in the ball-and-stick metaphor. The remaining guest molecules are shown in van der Waals representation. The solvent channel passing through the stacked metallocycles is shown as a semitransparent solvent accessible surface (using a probe radius of 1.4 Å).

The ASU of $\mathbf{1_{BZ}}$ consists of one half of a metallocyclic complex, a nitrate counter-ion and half of a benzene molecule situated about an inversion centre, yielding a host:guest ratio of 1:1. The most interesting feature of this structure is not the presence of certain interactions but rather the lack thereof. One might anticipate that the inclusion mode of an aromatic guest within a host structure so rich in aromatic moieties would involve either π–π stacking or C–H···π interactions, yet the benzene molecules align themselves in a manner such that all forms of these interactions are avoided. There are no significant interactions between the host metallocycles and guest molecules and it appears that the benzene guests are associated with the nitrate counter-ions by means of a weak C–H···O hydrogen bond between an aromatic hydrogen of the benzene ring and an oxygen atom of the nitrate counter-ion ($C_{donor}\cdots O_{acceptor}$ = 3.476(1) Å). **Figure 22** shows that the benzene molecules are situated on either side of the inversion centre in order to take part in this interaction i.e. they do not occupy the epicentre of the metallocyclic complex instead, they are located between two successive host rings in the metallocycle stacks.

In contrast, the ASU of $\mathbf{2_{BZ}}$ contains one half of a metallocycle, one BF_4^- anion and a benzene molecule with site occupancy of 0.5. The carbon atoms of the benzene rings were constrained as a rigid hexagon using the SHELX AFIX 66 command, and the overall structure converged to a final *R*1 = 0.0399. The space-group symmetry requires the guest molecule to be disordered over two sites of equal occupancy (**Figure 23**) and, upon inspection of the space-filled projections of the benzene molecules (**Figure 24**), it is apparent that only one of the orientations can be present within the channels i.e. either the pink molecules or the green molecules are present in one channel, resulting in a host:guest ratio of 1:1. The benzene guest molecules are stabilised over the two symmetry-related sites by a weak $Ag^+\cdots\pi$ interaction ($Ag^+\cdots\pi$ = 3.708 Å), (**Figure 23**).

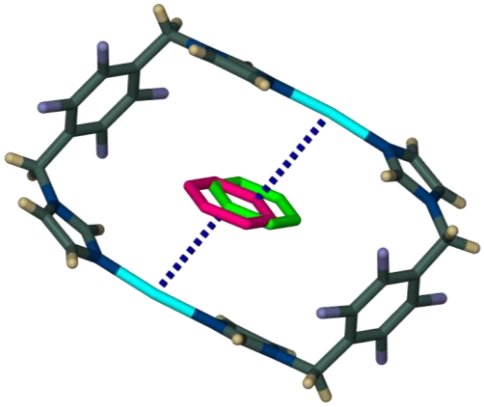

Figure 23. A complete metallocyclic host complex in $\mathbf{2_{BZ}}$. The disordered benzene molecules are shown as pink and green molecules; each guest molecule has a SOF of 0.5 and the two molecules are related to each other by a centre of inversion. The $Ag^{+}\cdots\pi$ interactions are indicated by the fragmented blue lines from the centroids of the aromatic guests to the Ag^{+} centre. All molecules are shown as capped-sticks and the H-atoms of the guest molecules have been omitted for clarity

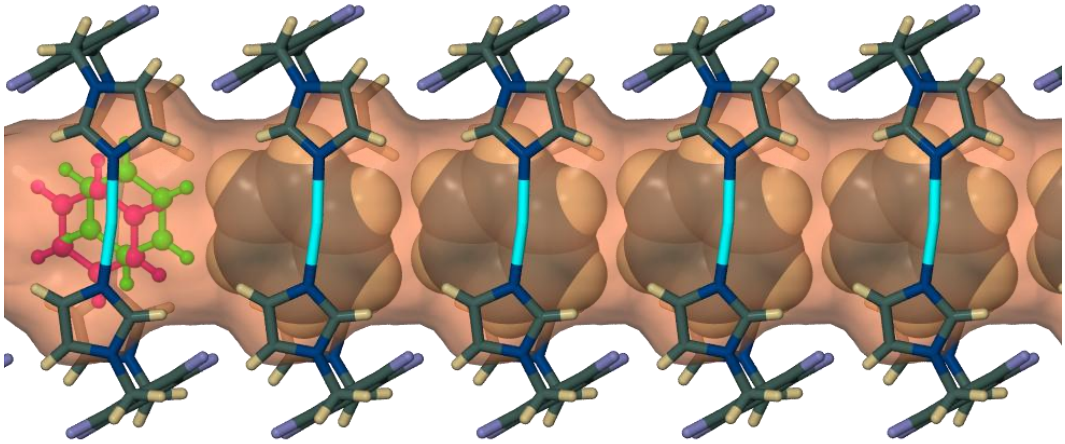

Figure 24. A perspective view of $\mathbf{2_{BZ}}$ viewed perpendicular to (010). The host metallocycles are shown in the capped-stick representation and the benzene molecules associated with the left-most metallocycle are shown in the ball-and-stick metaphor, and they are disordered over two positions. The remaining benzene guests are shown in space-fill in only one of the two possible orientations of the disordered guest within the 1D channel. The solvent channel passing through the stacked metallocycles is shown as a semitransparent accessible surface (using a probe radius of 1.4 Å).

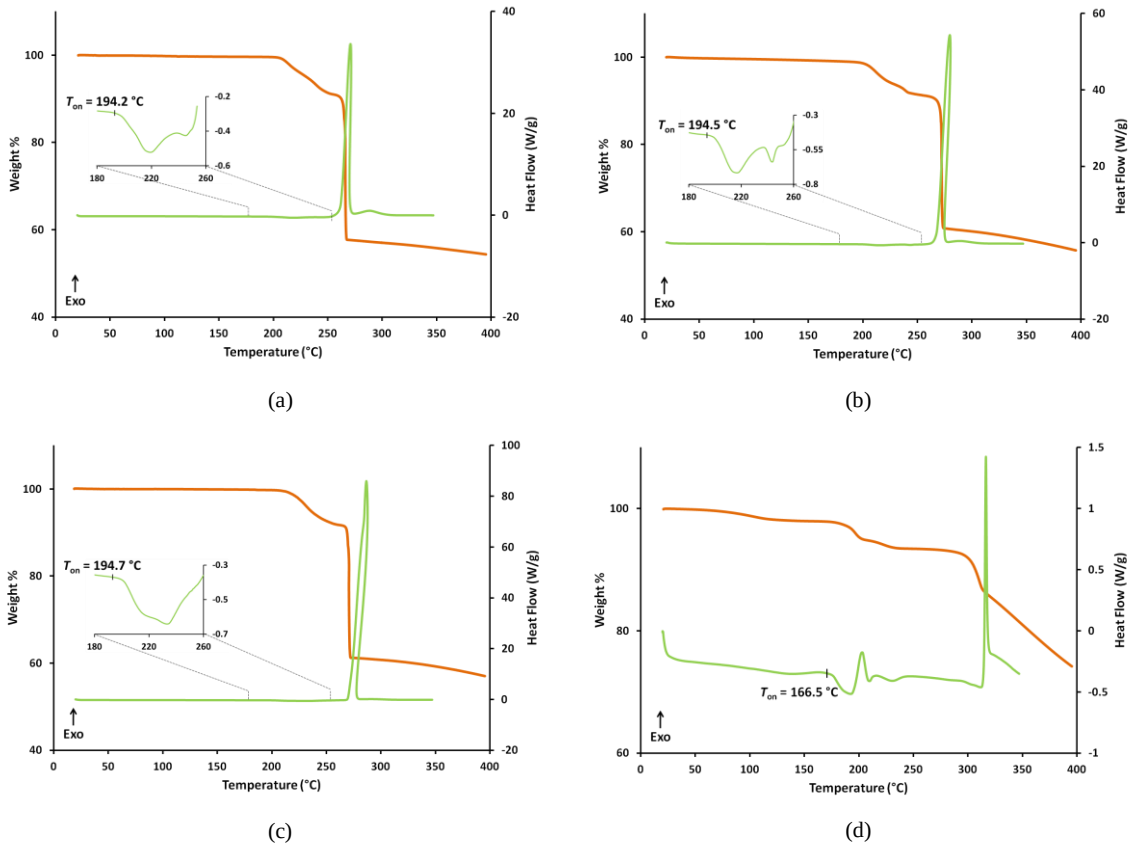

Figure 25. Thermoanalytical data for **(a)** $\mathbf{1}_{\mathbf{BZ(MeOH\cdot H2O)}}$, **(b)** $\mathbf{1}_{\mathbf{BZ(MeCN)}}$, **(c)** $\mathbf{1}_{\mathbf{BZ(AC)}}$ and **(d)** $\mathbf{2}_{\mathbf{BZ}}$. The TGA and DSC traces are orange and green, respectively.

The thermoanalytical data for $\mathbf{1}_{\mathbf{BZ(MeOH\cdot H2O)}}$, $\mathbf{1}_{\mathbf{BZ(MeCN)}}$ and $\mathbf{1}_{\mathbf{BZ(AC)}}$ are all remarkably similar (**Figure 25a–c**). The TGA traces display an almost horizontal line until 200 °C, after which a distinct weight-loss step occurs. This step corresponds to a 9.0%, 8.8% and 8.3% weight loss for $\mathbf{1}_{\mathbf{BZ(MeOH\cdot H2O)}}$, $\mathbf{1}_{\mathbf{BZ(MeCN)}}$ and $\mathbf{1}_{\mathbf{BZ(AC)}}$, respectively, and while these values are higher than the 7.5% calculated for the loss of one benzene molecule per host metallocycle we suggest that this thermal event must be a desolvation step that occurs simultaneously with a minor decomposition step. The endotherms corresponding to guest desolvation are lost in the baseline of the DSC when the highly exothermic decomposition step is taken into account; however these events can be clearly distinguished by merely rescaling the ordinate of the DSC. The inserts in **Figure 25**a–c reflect the distinct endothermic desolvation events and the T_{on} values of ~195 °C. An abrupt mass loss is observed in the TGA traces immediately following the desolvation step; this coincides with a sharp exotherm in the DSC and can be attributed to the major decomposition step of the complexes. The TGA of $\mathbf{2}_{\mathbf{BZ}}$ indicates that the sample starts to desolvate from room temperature until *ca* 240 °C, with the highest percentage of solvent

loss occurring between 170 and 240 °C. The entire solvent loss % from room temperature to 240 °C amounts to 6.5% of the total weight loss, which is slightly lower than the 7.2% calculated for the loss of one benzene molecule per metallocycle. This discrepancy in the mass loss % can easily be rationalised as solvent loss that had occurred before the thermal analysis.[‡‡‡] Again, this solvent loss is accompanied by an endotherm on the DSC (T_{on} = 166.5 °C), followed immediately by an exothermic event that could be due to a phase change. There are no further major thermal events until decomposition (marked by the sharp exothermic peak with an onset of approximately 320 °C).

3.2.2.3. Exchange with 1,4-difluorobenzene (DFB)

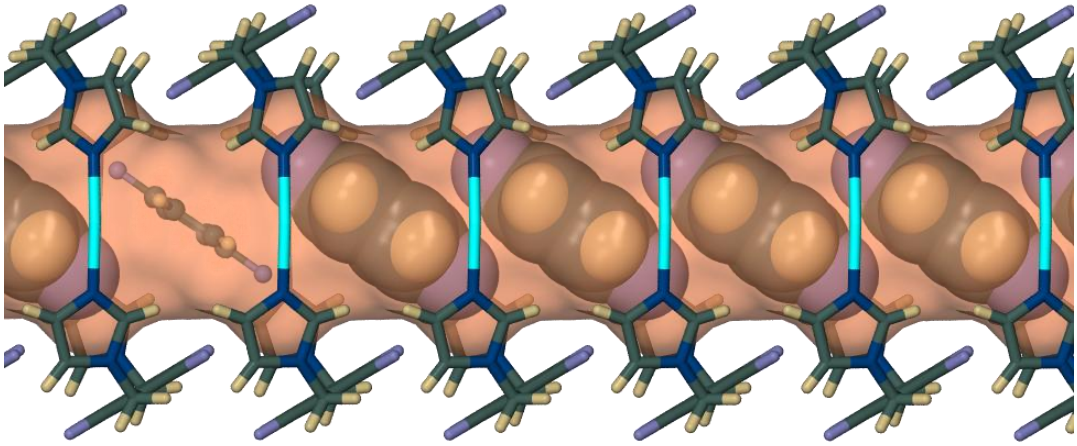

Figure 26. Projection of $\mathbf{1_{DFB}}$ viewed perpendicular to (010). The host metallocycles are shown in the capped-stick representation. The first complete 1,4-difluorobenzene guest (from the left) is shown in the ball-and-stick metaphor, and the remaining guest molecules are shown in van der Waals representation. The solvent channel passing through the stacked metallocycles is shown as a semitransparent accessible surface (using a probe radius of 1.4 Å).

[‡‡‡] The TGA trace indicates that $\mathbf{2_{BZ}}$ loses solvent from room temperature and the dried sample of $\mathbf{2_{BZ}}$ had been standing at room temperature for at least 2 hours before being loaded into the TGA instrument - so solvent loss should be slightly lower than expected.

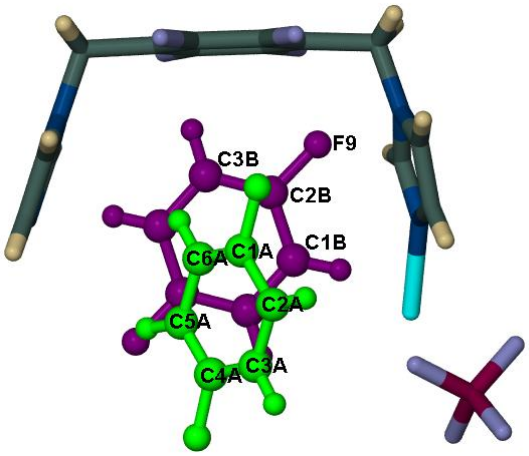

Figure 27. The two crystallographically unique DFB molecules are shown in green and purple in their positions relative to the ASU portion of the host in $\mathbf{2_{DFB}}$. The green molecule has a SOF of 0.5 and the entire molecule is present in the ASU, whilst only half of the purple guest is present in the ASU (SOF = 0.5) – the remainder of the molecule is generated by inversion symmetry. The guest molecules are shown in the ball and stick metaphor and the host as capped sticks. The non-hydrogen atoms of the guest molecules present in the ASU have been labelled for clarity.

The structure of $\mathbf{1_{DFB}}$ is remarkably similar to that of $\mathbf{1_{BZ}}$ with regard to the orientation of the guest molecules in the channels, as well as the host:guest ratio of 1:1, and as such does not require much discussion (**Figure 26**). A weak C–H···O hydrogen bond exists between the nitrate anions and the guest molecules occur with a $C_{donor}\cdots O_{acceptor}$ bond distance of 3.387(1) Å.

In contrast, the ASU of $\mathbf{2_{DFB}}$ contains one half of a metallocyclic complex with its corresponding BF_4^- anion, one DFB molecule with an occupancy of 0.5 (green molecule in **Figure 27**) and a half of a DFB molecule with an occupancy of 0.5 (purple molecule in **Figure 27**). Each green guest is symmetrically disordered across an inversion centre and the second half of the purple guest is generated by inversion symmetry, resulting in an overall host:guest ratio of $1:^3/_2$. From the packing arrangement and the site occupancies we infer that both of the crystallographically unique DFB molecules are present within a given 1D channel. **Figure 28(top)** shows the disordered DFB molecules with their symmetry-related guests; if one considers the two green molecules located in the centre of a particular metallocycle, it is clear that both molecules cannot be present at the same time (i.e. A and B cannot co-exist) as the molecules will overlap if the space-filled model is taken into account. Therefore, in order to maintain the host:guest ratio of $1:^3/_2$, only every alternating purple molecule (labelled C in **Figure 28**) is permissible within the channel. **Figure 28 (bottom)** shows one possible arrangement of the guest molecules. Both the green and purple guest DFB molecules interact with the BF_4^- anions *via* a weak H–bond; these parameters are $C_{donor}\cdots F_{acceptor}$ = 3.38(2) Å and $C_{donor}\cdots F_{acceptor}$ = 3.233(2) Å for the green and purple molecules, respectively. The fluorine atoms of the green DFB guest molecules in **Figure 28** protrude from the solvent-

accessible surface due to a close contact between these atoms and the carbon atoms of the host aryl ring (distance from the centroid of the aryl ring to the fluorine is *ca* 2.981 Å).

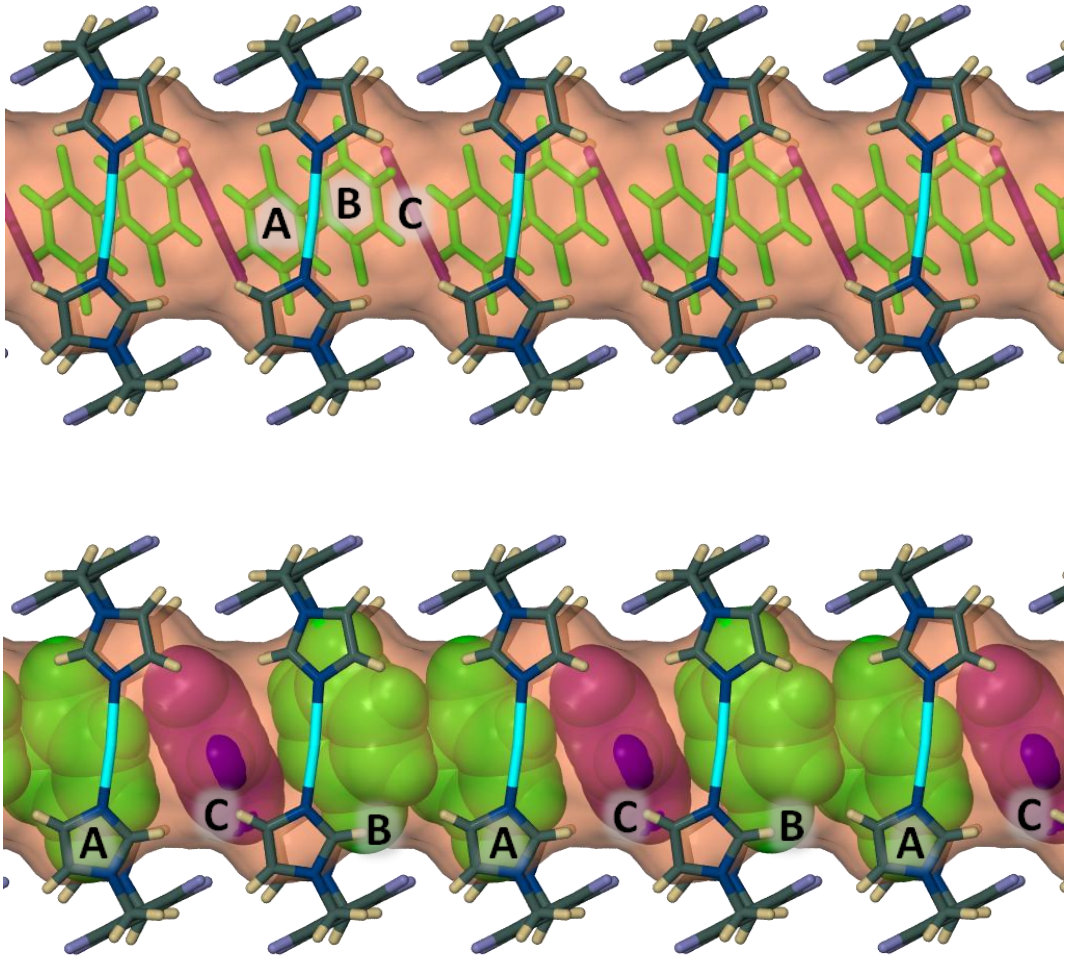

Figure 28. Projections of $\mathbf{2_{DFB}}$ viewed perpendicular to (010). The host metallocycles are shown in the capped-stick representation and the solvent channel passing through the stacked metallocycles is shown as a semitransparent solvent accessible surface using a probe radius of 1.4 Å. The same colouring scheme is employed for the guest molecules in both images. **(Top)** The disordered DFB guests are shown with their symmetry-related partners within the 1D channels as green and purple capped-stick molecules. The two symmetry related green molecules are labelled A and B and the purple molecule is labelled C. **(Bottom)** One possible arrangement of the guest molecules is shown with the DFB molecules displayed in the space-filled metaphor. Both the purple and the green molecules extend beyond the solvent accessible surface; in the case of the purple molecules this is due to the weak hydrogen bond between these molecules and the BF_4^- anion and in the case of the green molecules this is caused by the close contact between the fluorine atoms of the DFB molecules and the host aryl carbons.

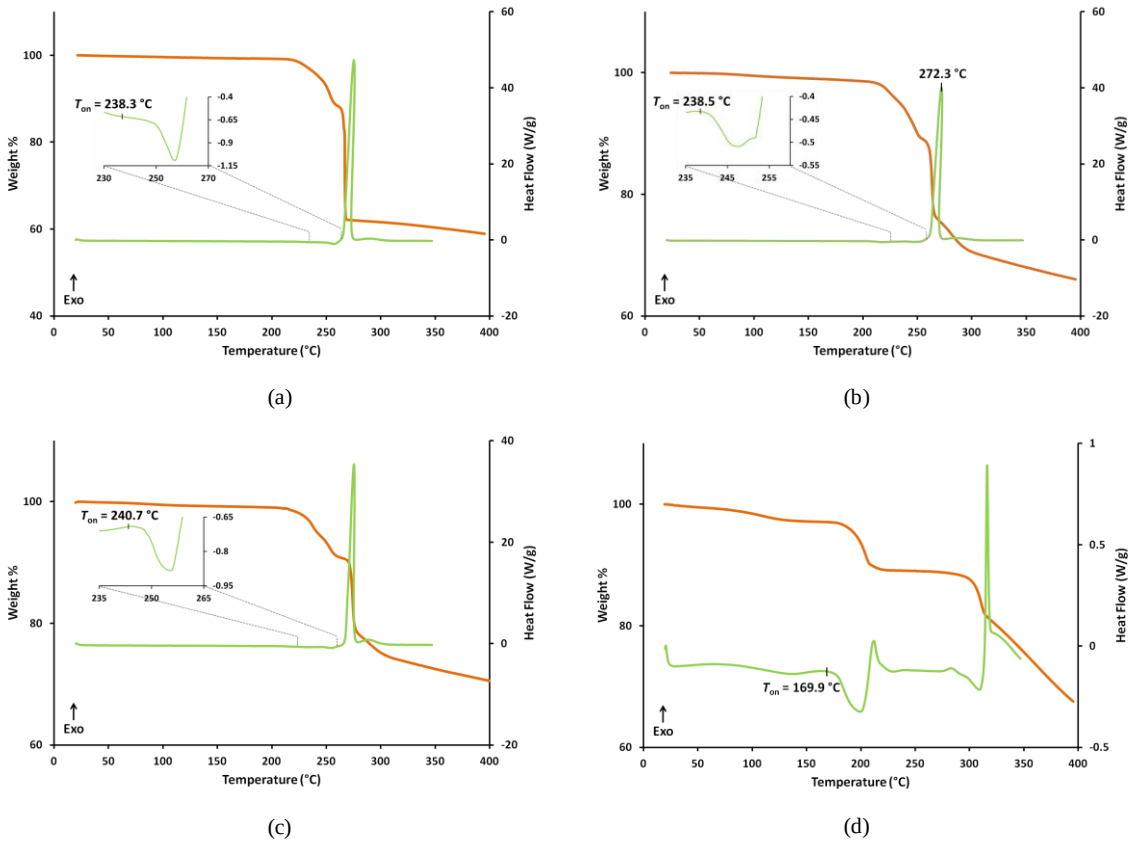

Figure 29. Thermoanalytical data for **(a)** $\mathbf{1}_{\mathbf{DFB(MeOH\cdot H2O)}}$, **(b)** $\mathbf{1}_{\mathbf{DFB(MeCN)}}$, **(c)** $\mathbf{1}_{\mathbf{DFB(AC)}}$ and **(d)** $\mathbf{2}_{\mathbf{DFB}}$; the TGA and DSC traces are orange and green respectively.

The thermoanalytical data for all of the 1,4-difluorobenzene solvates are highly reminiscent of their benzene solvate counterparts. The TGA thermograms of $\mathbf{1}_{\mathbf{DFB(MeOH\cdot H2O)}}$, $\mathbf{1}_{\mathbf{DFB(MeCN)}}$ and $\mathbf{1}_{\mathbf{DFB(AC)}}$ (**Figure 29a–c**) all display a wide plateau region from room temperature until *ca* 200 °C after which desolvation step of 11.3%, 10.9% and 10.9% are observed for $\mathbf{1}_{\mathbf{DFB}}$, $\mathbf{2}_{\mathbf{DFB}}$ and $\mathbf{3}_{\mathbf{DFB}}$, respectively. These values are slightly higher than the 10.6% calculated for the loss of one 1,4-difluorobenzene molecule per metallocycle, and, as mentioned above we attribute this to a concomitant minor decomposition step. The endotherms corresponding to the desolvation of $\mathbf{1}_{\mathbf{DFB(MeOH\cdot H2O)}}$, $\mathbf{1}_{\mathbf{DFB(MeCN)}}$ and $\mathbf{1}_{\mathbf{DFB(AC)}}$ can be seen in the inserts of **Figure 29a–c** (with T_{on} of approximately 239 °C). The abrupt mass loss in the TGA thermograms and the sharp exothermic peaks in the DSC traces indicate that the samples decompose rapidly beyond the desolvation step. $\mathbf{2}_{\mathbf{DFB}}$ gradually loses solvent from room temperature to *ca* 165 °C, and then more rapidly from 165–230 °C. The total solvent loss from room temperature to 230 °C is 10.9% of the total weight loss, which is slightly lower than the 11.4% calculated for the loss of one and a half 1,4-difluorobenzene molecules per metallocycle. This is most

likely due to loss of solvent from the sample before being loaded into the TGA. The major desolvation step is accompanied by an endotherm on the DSC (T_{on} = 169.9 °C) followed immediately by an exotherm, which we ascribe to a change in phase. The decomposition exotherm peak is evident with an onset temperature of approximately 300 °C.

3.2.2.4. Exchange with 1,4-dioxane (DIOX)

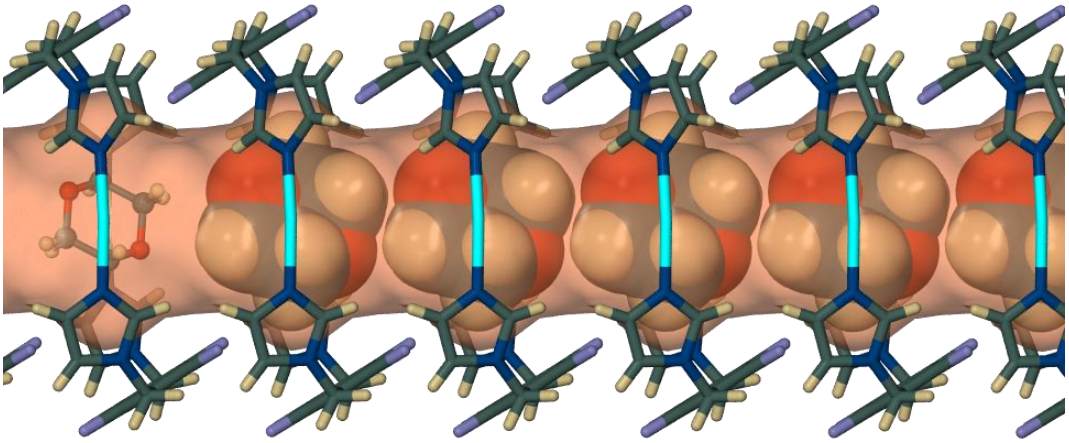

Figure 30. Projection of $\mathbf{1}_{\mathbf{DIOX}}$ viewed perpendicular to (010). The host metallocycles are shown in the capped-stick representation and the first 1,4-dioxane guest (from the left) is shown in the ball-and-stick metaphor. The remaining guest molecules are shown in van der Waals representation. The solvent channel passing through the stacked metallocycles is shown as a semitransparent solvent accessible surface (using a probe radius of 1.4 Å).

The structure of $\mathbf{1}_{\mathbf{DIOX}}$ features an ASU consisting of one half of a metallocyclic complex and a half a 1,4-dioxane molecule situated about an inversion centre, this yields a host:guest ratio of 1:1. The only interaction between the host and guest is a weak hydrogen bond donated by a host imidazolate carbon to an oxygen atom of the dioxane guest ($C_{donor}\cdots O_{acceptor}$ = 3.367(4) Å). This presumably plays a role in orientating the guest relative to the host and, interestingly, this is the first structure with a host:guest ratio of 1:1 in which the centre of mass of the guest molecule coincides with centre of mass of its metallocyclic host complex (**Figure 30**). Remarkably, there are no strong interactions or short contacts evident between the host and guest.

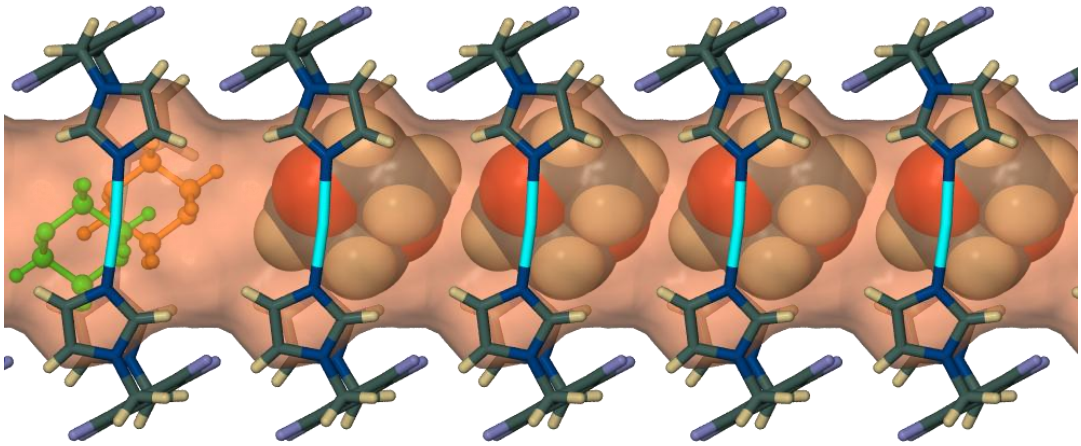

Figure 31. A perspective view of $\mathbf{2_{DIOX}}$ viewed perpendicular to (010). The host metallocycles are shown in capped-stick representation and the dioxane molecules associated with the left-most metallocycle are shown in the ball-and-stick metaphor, and are disordered over two positions. The remaining dioxane guests are shown in van der Waals representation in only one of the two possible orientations of the disordered guest within the 1D channel. The solvent channel passing through the stacked metallocycles is shown as a semitransparent solvent accessible surface (using a probe radius of 1.4 Å).

The ASU of $\mathbf{2_{DIOX}}$ consists of one half of a metallocycle, one BF_4^- anion and a disordered dioxane molecule. The SQUEEZE results are reasonably consistent with one dioxane molecule per metallocycle (i.e. the electron count is 53 electrons per metallocycle, and 48 electrons are expected for one dioxane molecule per metallocycle) resulting in a host:guest ratio of 1:1. The most reasonable crystallographic model involves one dioxane molecule with a site occupancy of 0.5 in the ASU. All bond lengths and angles of the dioxane molecule are constrained and it was not possible to treat the dioxane atoms anisotropically; the overall structure converged to a final $R1$ = 0.0748. Despite various attempts to choose crystals of higher quality or improve the data collection strategy, the constrained isotropic model presented here remains the best model to date for this system. The space group symmetry requires the guest molecule to be disordered over two sites of equal occupancy and upon inspection of the space-filled projections of the dioxane molecules (**Figure 31**) and taking the required host:guest ratio of 1:1 into account, it is apparent that only one of the two orientations can be present within the channels at any given time. The dioxane guest molecules are stabilised over the two symmetry-related sites by an electrostatic interaction between one of the oxygen atoms of the dioxane molecules and the silver centres ($Ag^+\cdots O$ = 3.09(5) Å).

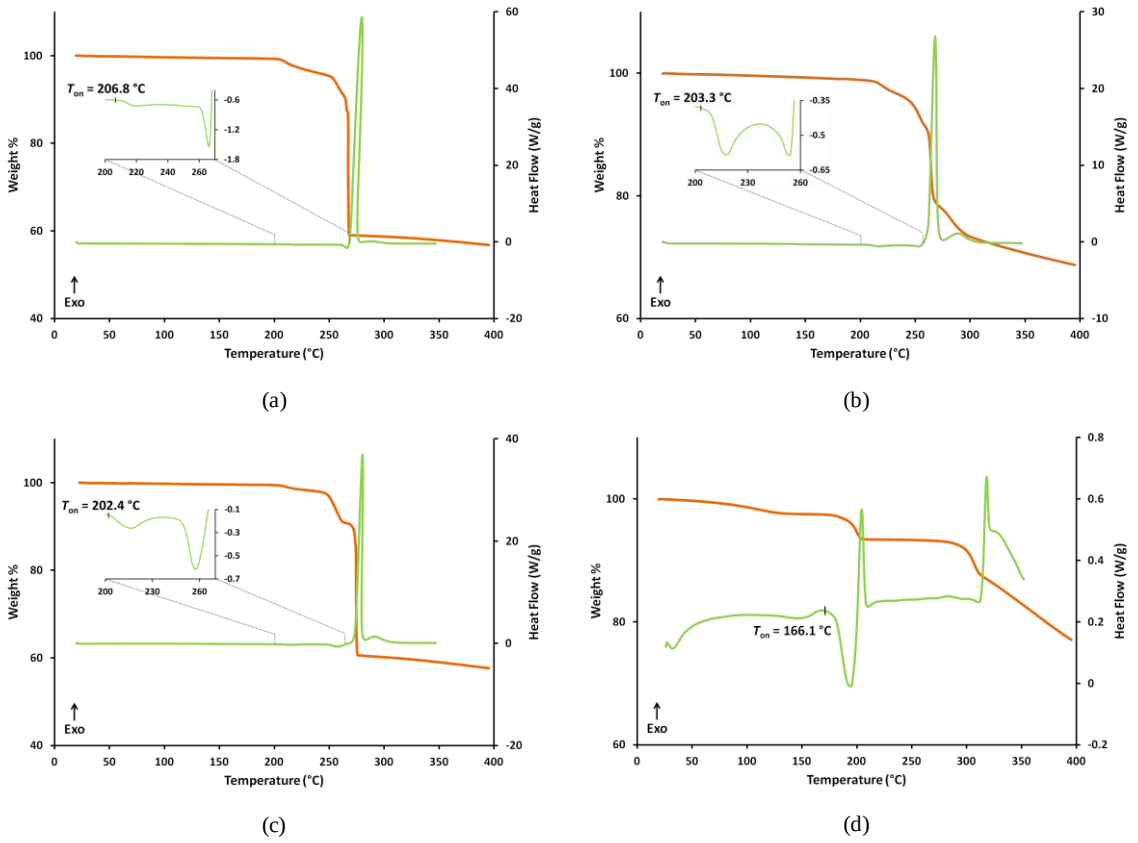

Figure 32. Thermoanalytical data for **(a)** $\mathbf{1}_{\mathbf{DIOX(MeOH\cdot H2O)}}$, **(b)** $\mathbf{1}_{\mathbf{DIOX(MeCN)}}$, **(c)** $\mathbf{1}_{\mathbf{DIOX(AC)}}$ and **(d)** $\mathbf{2}_{\mathbf{DIOX}}$; the TGA and DSC traces are orange and green, respectively.

The thermoanalytical data for $\mathbf{1}_{\mathbf{DIOX(MeOH\cdot H2O)}}$, $\mathbf{1}_{\mathbf{DIOX(MeCN)}}$ and $\mathbf{1}_{\mathbf{DIOX(AC)}}$ all suggest that solvent loss occurs *via* a two step process; the first step ends at approximately 230 °C and the second ends at approximately 260 °C. These steps correlate to two endotherms in the DSC traces: a very small endotherm at *ca* 220 °C and a larger one *ca* 255 °C (the smallest endotherm is almost imperceptible in the DSC of $\mathbf{1}_{\mathbf{DIOX}}$). The T_{on} values in the range of 202–206 °C shown in the inserts of **Figure 32** correspond to the onset temperatures of the first desolvation endotherm. It is very difficult to deconvolute the end of the second weight loss step from the start of decomposition. Therefore it is not possible to report sensible experimental solvent loss percentages to compare to the calculated value of 8.4% expected for loss of one 1,4-dioxane molecule per metallocycle. The abrupt mass loss and sharp exotherms above the temperatures of desolvation in the TGA and DSC traces respectively, indicate that decomposition directly follows desolvation. The thermal behaviour of $\mathbf{2}_{\mathbf{DIOX}}$ follows a very similar trend to that of $\mathbf{2}_{\mathbf{BZ}}$ and $\mathbf{2}_{\mathbf{DFB}}$, in that the sample appears to gradually lose solvent from room temperature to 155 °C and then more rapidly

from 155–215 °C. The cumulative solvent loss at 215 °C is only 6.6%, well below the 8.7% calculated for loss of one 1,4-dioxane per metallocycle. We hypothesis that this due to one of two reasons: (i) only a certain percentage of the sample has sufficient energy to be liberated of its solvent molecules at this temperature, resulting in a lower % weight loss than expected or, (ii) a large amount of solvent is lost before analysis. The major desolvation step is accompanied by an endotherm on the DSC (T_{on} = 166.1 °C), immediately followed by an exotherm, which again is indicative of a change in phase. The decomposition exotherm peak is evident with an onset of approximately 310 °C.

3.2.2.5. Exchange with cyclohexane (CY)

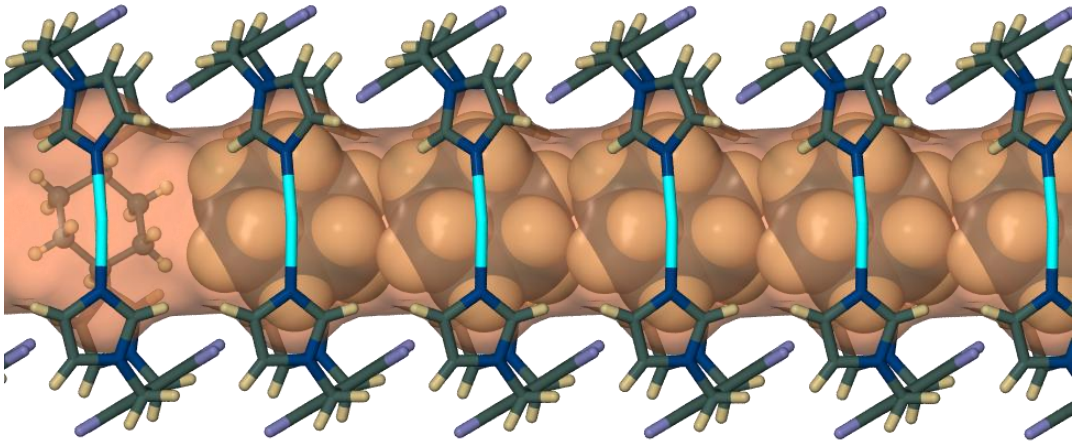

Figure 33. Projection of $\mathbf{1}_{\mathbf{CY(MeOH{\cdot}H2O)}}$ viewed perpendicular to (010). The host metallocycles are shown in capped-stick representation, the first cyclohexane guest (from the left) is shown in ball-and-stick and the remaining guest molecules are shown in van der Waals representation. The solvent channel passing through the stacked metallocycles is shown as a semitransparent solvent accessible surface (using a probe radius of 1.4 Å).

For reasons that are not entirely obvious, it appears that exchange of the 'parent' guest molecules for cyclohexane is a facile process for the $\mathbf{1}_{\mathbf{MeOH{\cdot}H2O}}$ and $\mathbf{2}_{\mathbf{AC}}$ systems but not for $\mathbf{1}_{\mathbf{MeCN}}$ or $\mathbf{1}_{\mathbf{AC}}$. For the $\mathbf{1}_{\mathbf{MeOH{\cdot}H2O}}$ and $\mathbf{2}_{\mathbf{AC}}$ systems; exchange occurred readily within a few days of exposure whereas no exchange was observed for $\mathbf{1}_{\mathbf{MeCN}}$ and $\mathbf{1}_{\mathbf{AC}}$, even after the crystals had been immersed in cyclohexane for more than two weeks, i.e. the respective acetonitrile and acetone guests could still be modelled exactly as they were in the original structures of $\mathbf{1}_{\mathbf{MeCN}}$ and $\mathbf{1}_{\mathbf{AC}}$. The ASU of $\mathbf{1}_{\mathbf{CY}}$ and $\mathbf{2}_{\mathbf{CY}}$ both consist of one half of a metallocycle, one anion and half a cyclohexane guest situated about an inversion centre to yield a host:guest ratio of 1:1. The cyclohexane molecules adopt the chair-shaped

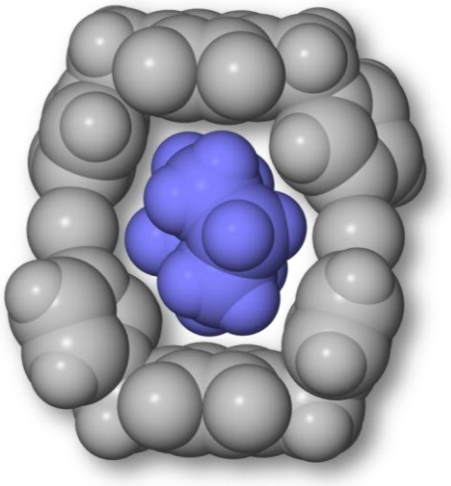

Figure 34. Space-filled representation of a guest cyclohexane molecule (blue) situated within the aperture of the metallocyclic host (grey) in $\mathbf{1_{CY}}$.

conformation when included within the channels of $\mathbf{1_{CY}}$ and $\mathbf{2_{CY}}$ and, as such, the orientation of the guest with respect to the host is very similar to that of the 1,4-dioxane-included structures above (**Figure 33**). Examination of the crystal structures of $\mathbf{1_{CY(MeOH·H2O)}}$ and $\mathbf{2_{CY}}$ reveals that there are no close contacts between the host metallocycles and the guest cyclohexane molecules. In fact, a space-filled projection of a guest molecule located within the aperture of a metallocycle in $\mathbf{1_{CY}}$ shows that the host and guest do not come into van der Waals contact with each other at all. The same is true for $\mathbf{2_{CY}}$ and therefore only one figure has been provided (**Figure 34**).

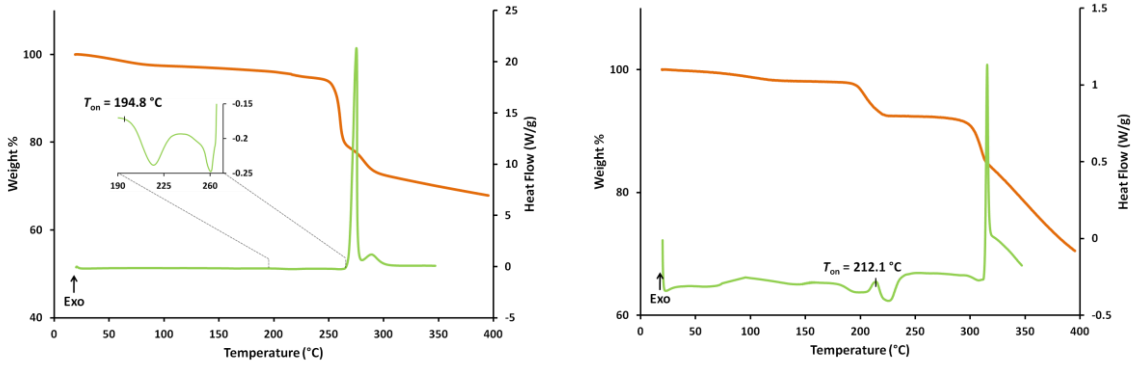

(a) (b)

Figure 35. Thermoanalytical data for **(a)** $\mathbf{1_{CY}}$ and **(b)** $\mathbf{2_{CY}}$; the TGA and DSC traces are orange and green, respectively.

The TGA for $\mathbf{1_{CY}}$ (**Figure 35a**) indicates that the sample gradually loses solvent from room temperature until *ca* 250 °C and then immediately starts to decompose above this temperature. The DSC trace indicates that there are two small, but discrete desolvation steps before decomposition. The first occurs with an onset of *ca* 195 °C and the second endotherm occurs just before decomposition with an onset of *ca* 245 °C. The exotherm associated with decomposition occurs with an onset of *ca* 260 °C. The weight loss recorded at 250 °C is a mere 5.7%, which is well below the 8.1% calculated for the loss of one cyclohexane per metallocycle. This observation, in conjunction with the single-crystal data, which indicates no strong interactions between the host and guest, initially lead us to

believe that a large percentage of the solvent loss must have occurred prior to thermal analysis. We therefore speculated that of all the solvates studied thus far, $\mathbf{1_{CY}}$ would be the most likely candidate to successfully liberate guest molecules from their positions within the host channels, with retention of monocrystallinity. In order to test if this is indeed the case, a sample of single crystals of $\mathbf{1_{CY}}$ were kept under a dynamic vacuum for 48 hours. A visual inspection of the crystals revealed that monocrystallinity had been maintained; however single-crystal analysis indicated that the solvent was still present. The same experiment repeated with heating resulted in a loss of single crystallinity. Thus, the only plausible explanation for the low percentage weight loss observed is that which has already been reached for $\mathbf{2_{DFB}}$ i.e. only a certain percentage of the sample loses solvent at this temperature and the rest of the solvent is lost concurrently with decomposition. Again, $\mathbf{2_{CY}}$ follows a very similar trend to that of $\mathbf{2_{BZ}}$ and $\mathbf{2_{DFB}}$ and $\mathbf{2_{DIOX}}$ (**Figure 35b**): the sample gradually loses solvent from room temperature to *ca* 180 °C and then rapidly from 180–230 °C. The total weight loss at 230 °C is 7.5%, which corresponds well to the 7.4% calculated for loss of one cyclohexane molecule per metallocycle. The major desolvation step is accompanied by an endotherm on the DSC at a T_{on} = 212.1 °C and there are no significant thermal events in the DSC trace until the onset of decomposition at *ca* 310 °C.

3.2.2.6. Exchange with water (H_2O)

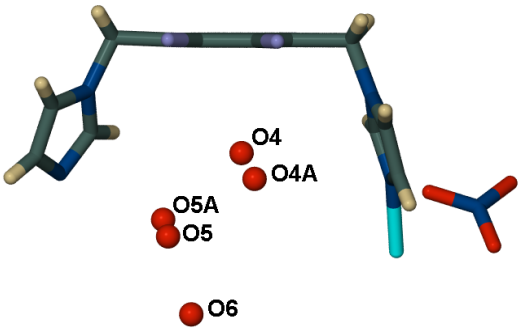

Figure 36. The ASU of $\mathbf{1_{H2O}}$; the host fragment is shown as capped-sticks and the disordered water molecules are represented as red spheres.

Interestingly the exchange of the 'parent' solvent only occurs for the $\mathbf{1_{MeOH\cdot H2O}}$ system. For the $\mathbf{1_{MeCN}}$, $\mathbf{1_{AC}}$ and $\mathbf{2_{AC}}$ systems the 'parent' guest molecules could still be modelled within the cavities of the metallocycles after exposure to water for two weeks. The ASU of $\mathbf{1_{H2O}}$ contains half a metallocyclic host and $2^1/_2$ water molecules situated over five positions i.e. in **Figure 36** O4 and O4A each have a site occupancy of 0.5 and cannot coexist, O5 and O5A also each have a site occupancy of 0.5 and cannot coexist and finally O6 has a site occupancy of 0.5. Both the host and the guest are situated about an inversion centre to yield a host:guest

ratio of 1:5. **Figure 37** shows a possible arrangement of the water guests within the host channel.

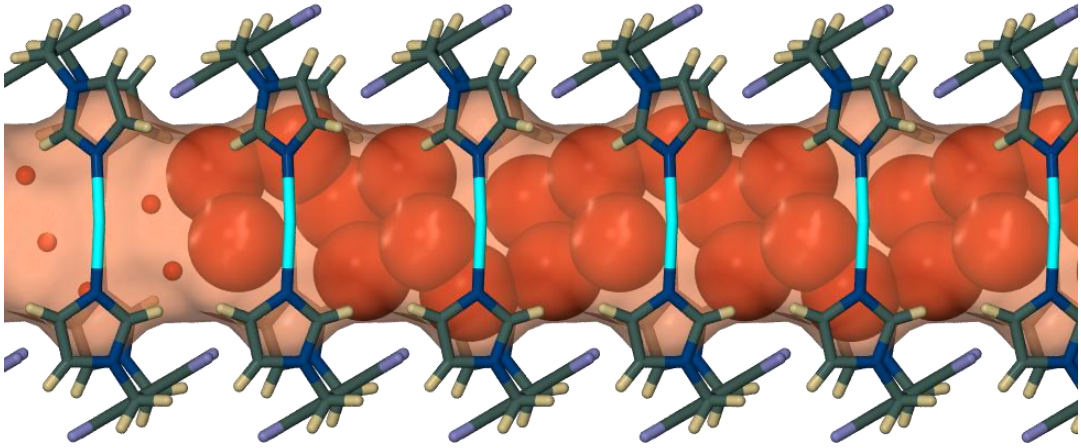

Figure 37. A perspective view of $\mathbf{1_{H2O}}$ viewed perpendicular to (010). The host metallocycles are shown in capped-stick representation and the water molecules associated with the left-most metallocycle are shown as spheres in one possible arrangement. The remaining water molecules are shown in space-fill in only one of the two possible orientations of the disordered guest within the 1D channel. The solvent channel passing through the stacked metallocycles is shown as a semitransparent solvent accessible surface (using a probe radius of 1.4 Å).

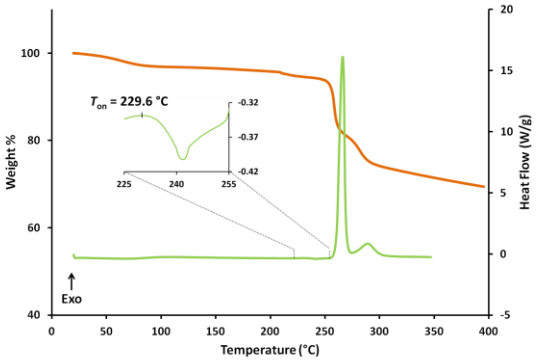

Figure 38. Thermoanalytical data for $\mathbf{1_{H2O}}$; the TGA and DSC traces are orange and green respectively.

The thermal behaviour of $\mathbf{1_{H2O}}$ is similar to that of $\mathbf{1_{DIOX}}$ in that the sample gradually loses solvent from room temperature until *ca* 240 °C and then immediately starts to decompose above this temperature. There is a small desolvation endotherm at T_{on} = 229.6 °C in the DSC trace and the exotherm associated with decomposition occurs at an onset of approximately 260 °C (**Figure 38**). As was the case for $\mathbf{1_{DIOX}}$, the weight loss recorded at 240 °C of 5.5% is significantly less than the 8.1% calculated for the loss of five water molecules per metallocycle, indicating that only partial desolvation occurs before decomposition.

Table 3. A summary of selected parameters for the 'parent' and exchanged complexes of the $\mathbf{1}_{\mathbf{G}}$ and $\mathbf{2}_{\mathbf{G}}$ systems.

Structure	Parent Guest	Host:Guest[a]	Ag···Ag (Å)	Intra-metallocycle aryl-aryl distance (Å)	Stacking periodicity (Å)[b]	Aromatic tilt angle (°)[c]	Metallocycle tilt angle (°)[c]	Total potential solvent volume/unit cell (Å^3)[d]	T_{on}	$T_{on} - T_b$
$\mathbf{1}_{\mathbf{MEOH\cdot H2O}}$		1 : 2	8.841	10.723	5.8633(13)	60.3	90.4	334		
$\mathbf{1}_{\mathbf{MECN}}$		1 : 2	8.703	10.799	5.8164(4)	57.9	86.9	335	192.9	111.3
$\mathbf{1}_{\mathbf{AC}}$		1 : 1	9.004	10.656	5.8183(7)	59.6	85.3	337		
$\mathbf{1}_{\mathbf{DCM}}$	MeOH·H_2O	1 : 2	8.469	10.945	5.9026(13)	58.7	87.5	346		
	MeCN	1 : 2	8.463	10.945	5.9020(8)	58.7	87.5	345		
	AC	1 : 2	8.457	10.930	5.8948(5)	58.8	86.9	344		
$\mathbf{1}_{\mathbf{BZ}}$	MeOH·H_2O	1 : 1	8.938	10.688	5.7869(9)	59.8	85.9	334	194.2	114.2
	MeCN	1 : 1	8.920	10.693	5.7718(9)	59.8	85.9	330	194.5	114.5
	AC	1 : 1	8.932	10.695	5.7637(3)	59.8	87.4	330	194.7	114.7
$\mathbf{1}_{\mathbf{DFB}}$	MeOH·H_2O	1 : 1	8.937	10.703	5.7890(4)	58.7	87.3	338	238.3	149.5
	MeCN	1 : 1	8.914	10.717	5.8211(7)	59.0	87.3	347	238.5	149.7
	AC	1 : 1	8.975	10.682	5.8054(6)	58.9	87.0	342	240.7	151.9
$\mathbf{1}_{\mathbf{DIOX}}$	MeOH·H_2O	1 : 1	8.912	10.661	5.7985(6)	59.4	85.0	325	206.8	105.5
	MeCN	1 : 1	8.887	10.624	5.7821(7)	59.2	84.6	316	203.3	102.0
	AC	1 : 1	8.905	10.611	5.7815(11)	59.3	84.5	318	202.4	101.1
$\mathbf{1}_{\mathbf{CY}}$	MeOH·H_2O	1 : 1	8.952	10.640	5.8533(3)	59.4	85.0	325	194.8	111.9
$\mathbf{1}_{\mathbf{H2O}}$	MeOH·H_2O	1 : 5	8.636	10.824	5.8710(2)	59.2	85.9	339	229.6	129.6
$\mathbf{2}_{\mathbf{AC}}$		1 : 2	7.864	11.027	12.9283(13)	68.9 43.6	96.2 98.9	821	155.7	99.4
$\mathbf{2}_{\mathbf{DCM}}$	AC	1 : 2	7.914	11.033	6.3342(6)	56.4	91.9	386	163.8	124.1
$\mathbf{2}_{\mathbf{BZ}}$	AC	1 : 1	7.887	10.997	6.3710(3)	55.5	92.1	372	166.5	86.5
$\mathbf{2}_{\mathbf{DFB}}$	AC	1 : $^3/_2$	8.057	11.059	6.5255(10)	56.7	97.4	431	169.9	81.1
$\mathbf{2}_{\mathbf{DIOX}}$	AC	1 : 1	7.870	11.017	6.3970(13)	55.4	93.0	386	166.2	65.1
$\mathbf{2}_{\mathbf{CY}}$	AC	1 : 1	8.323	10.838	6.3826(4)	54.5	92.1	392	212.1	131.4

[a] The 'host' is defined as the entire metallocyclic complex. [b] This determines the *a*-axis and is therefore known to a relatively high level of accuracy. [c, d] The method used to calculate these angles is depicted in **Figure 5**. [d] The total potential solvent accessible volume was determined using the command CALC SOLV from within the PLATON environment.[24,25]

3.2.3. Structure determination, thermal analysis and SC-SC solvent exchange of $\mathbf{3_{AC}}$

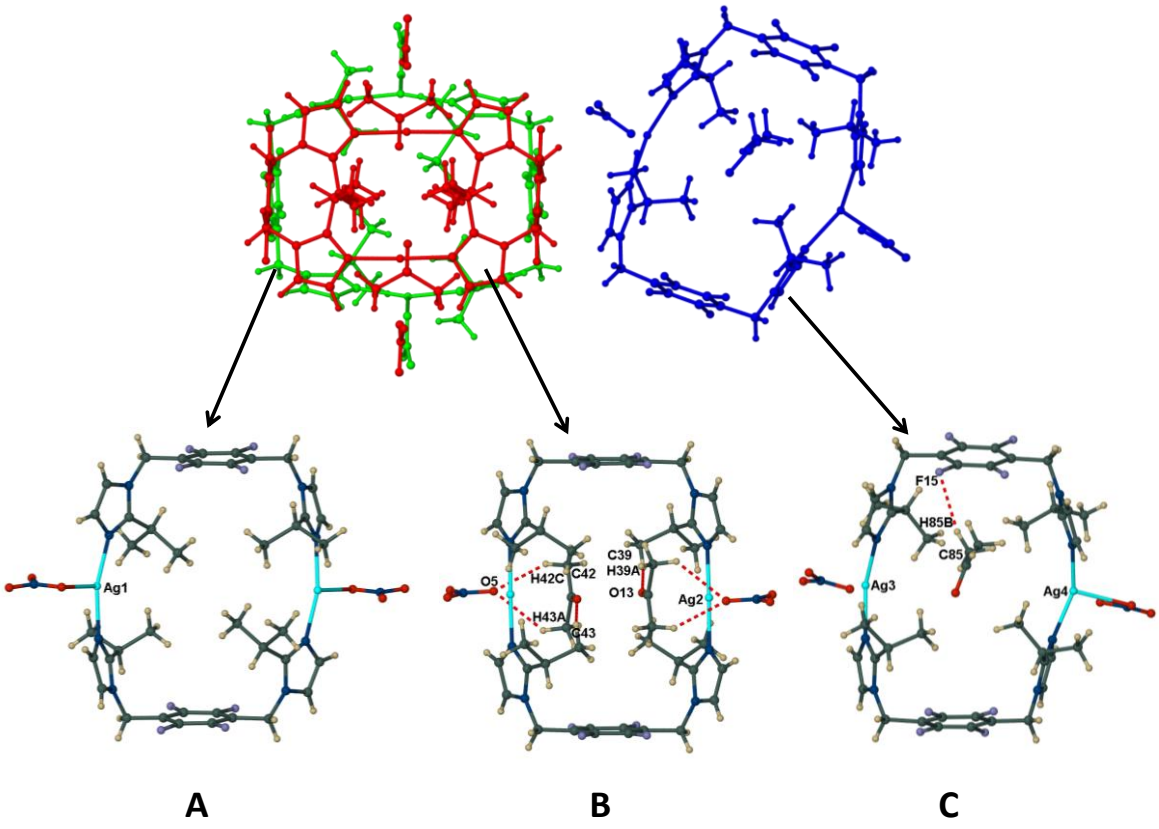

Figure 39. Ball-and-stick representation of the three crystallographically unique metallocycles in $\mathbf{3_{AC}}$; in the top half of the image the three metallocycles are viewed down [010] and are coloured green, red and blue to distinguish them from one another. The entire blue metallocycle is present in the ASU of $\mathbf{3_{AC}}$, whereas only half of the red and green metallocycles are present in the ASU - the complete metallocycles are shown for the sake of clarity. In the bottom half of the image, the three metallocycles have been separated from one another and are viewed perpendicular to the intra-metallocycle Ag···Ag vector. The metallocycle labelled **A** corresponds to the green molecule, **B** corresponds to the red molecule and **C** corresponds to the blue molecule. Hydrogen bonds are indicated as red fragmented lines.

As mentioned in Section 3.1, a fifth Ag(I) metallocyclic solvate was obtained in this series of thermally stable complexes. $\mathbf{3_{AC}}$ is formed by the reaction of **L2** (see Scheme 1) and $AgNO_3$ in acetone. Crystals suitable for single-crystal X-ray analysis were grown by slow evaporation of an equimolar solution of the ligand and metal salt. Unfortunately, difficulties were encountered in re-growing single crystals of suitable size and quality beyond those contained in the original reaction vial; most attempts resulted in the

formation of polycrystalline material. Single crystals formed in a few instances, but they were of such poor quality (i.e. they were very small and the diffraction profile consisted of weak, low-angle diffraction spots) that it was not possible to obtain reliable single-crystal data. A comparison of the diffractograms obtained by PXRD analysis of the material in each vial with the simulated PXRD pattern from the single-crystal structure of $\mathbf{3_{AC}}$ indicates that the bulk phase obtained in each case is that of the original $\mathbf{3_{AC}}$ phase; however, high quality single crystals are necessary to monitor the exchange experiments by single-crystal diffraction. Therefore all of the results contained in this section were obtained with the original batch of single crystals. As a consequence of this, the investigation of $\mathbf{3_{AC}}$ is not as comprehensive as that of $\mathbf{1_{MeOH{\cdot}H2O}}$, $\mathbf{1_{MeCN}}$, $\mathbf{1_{AC}}$ and $\mathbf{2_{AC}}$ but we feel it would be remiss to ignore this interesting result in the context of the present study.

Unlike the structures of $\mathbf{1_{MeOH{\cdot}H2O}}$, $\mathbf{1_{MeCN}}$, $\mathbf{1_{AC}}$ and $\mathbf{2_{AC}}$ that consist of only one type of metallocycle, single-crystal X-ray diffraction analysis reveals a far more complex structure for $\mathbf{3_{AC}}$. The ASU of $\mathbf{3_{AC}}$ consists of one complete metallocycle and two half metallocycles, four nitrate ions and two molecules of acetone, resulting in a total of three unique metallocycles, labeled **A**, **B** and **C** in **Figure 39**. In **A** and **B** the metallocycles are each situated on a crystallographic inversion centre with a half of the metallocycle unique in each case, whereas the entire dinuclear unit is unique in **C**. As previously shown,[26] it is convenient to describe the conformation of the ligands with regard to the positions of the substituents of the imidazole groups relative to the mean plane of the dinuclear complexes. In this regard the isopropyl groups can either be designated as "**U**" or "**D**" if they are oriented up or down, respectively. Therefore, if the upper left isopropyl group is taken as the starting position, proceeding in a clockwise direction yields **DUUD** for the conformation of **A** with respect to the orientations of the isopropyl groups. In an analogous manner the conformation of **B** is **UDDU** and **C** is **DDUU** (**Figure 40**). In all three of the metallocycles the Ag(I) ion is coordinated to two imidazole groups from two **L2** ligands. Yet interestingly, the coordination environment of the Ag^+ cation differs in all three cases depending on the proximity of the NO_3^- counter-ions. In **A** the NO_3^- anions are coordinated (Ag1–O = 2.580(5) Å) and, as a result of this coordination, the N–Ag1–N angle is 164.8(2)°; in **B** the nitrate ions are not close enough to form a coordination bond (closest Ag2–O distance = 2.826(5) Å)[§§§] and the N–Ag2–N angle of 177.9(2)° is

[§§§] Coordination bonds between Ag(I) ions and nitrate anions typically occur in the Ag-O bond distance range of 2.26–2.66 Å.[27]

approximately linear. In **C** the closest oxygen atom to Ag3 is situated 2.678(3) Å from the metal centre, and as such falls just out of the distance range reported for Ag–O coordination bonds.[27] The N–Ag3–N angle of 152.7(2)° deviates significantly from linearity. This can be attributed to the conformation of the metallocyclic ring and the steric constraints imposed by bulky isopropyl groups, whereas the closest oxygen atom to Ag4 can be located at a distance of 2.538(5) Å and therefore a coordination bond is formed, with a corresponding N–Ag4–N angle of 149.14(3)°. All three of the metallocycles therefore differ from one another with regard to the conformation of their ligands as well as the coordination geometry around each metal centre. This type of structural variation within one crystal structure is unprecedented in previous work involving analogous dinuclear complexes.

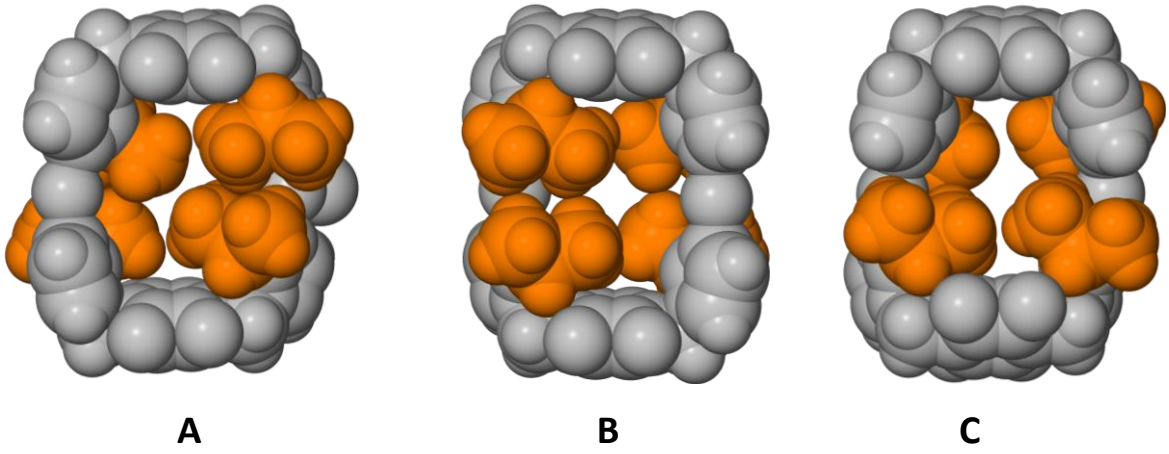

Figure 40. Space-filling projections of the three crystallographically unique metallocycles in $\mathbf{3}_{\mathbf{AC}}$ as viewed down [010]. The isopropyl groups on the imidazole rings have been coloured orange and the rest of the atoms are shown in grey to highlight the conformational differences between the three molecules.

As seen in **Figure 39**, metallocycle **B** encloses two symmetry-related acetone molecules that accept a hydrogen bond from an sp^3 carbon atom of an isopropyl substituent of the imidazole ring (C39···O13 = 3.385(1) Å). The solvent molecules also simultaneously function as bifurcated hydrogen bond donors and form hydrogen bonds with the uncoordinated nitrate anion (C42···O5 = 3.209(1) Å and C43···O5 = 3.342(1) Å). The dinuclear unit of **C** encloses a single acetone molecule, which is held in place by a weak hydrogen bond with a fluorine atom on the aromatic spacer (C85···F15 = 3.500(1) Å).

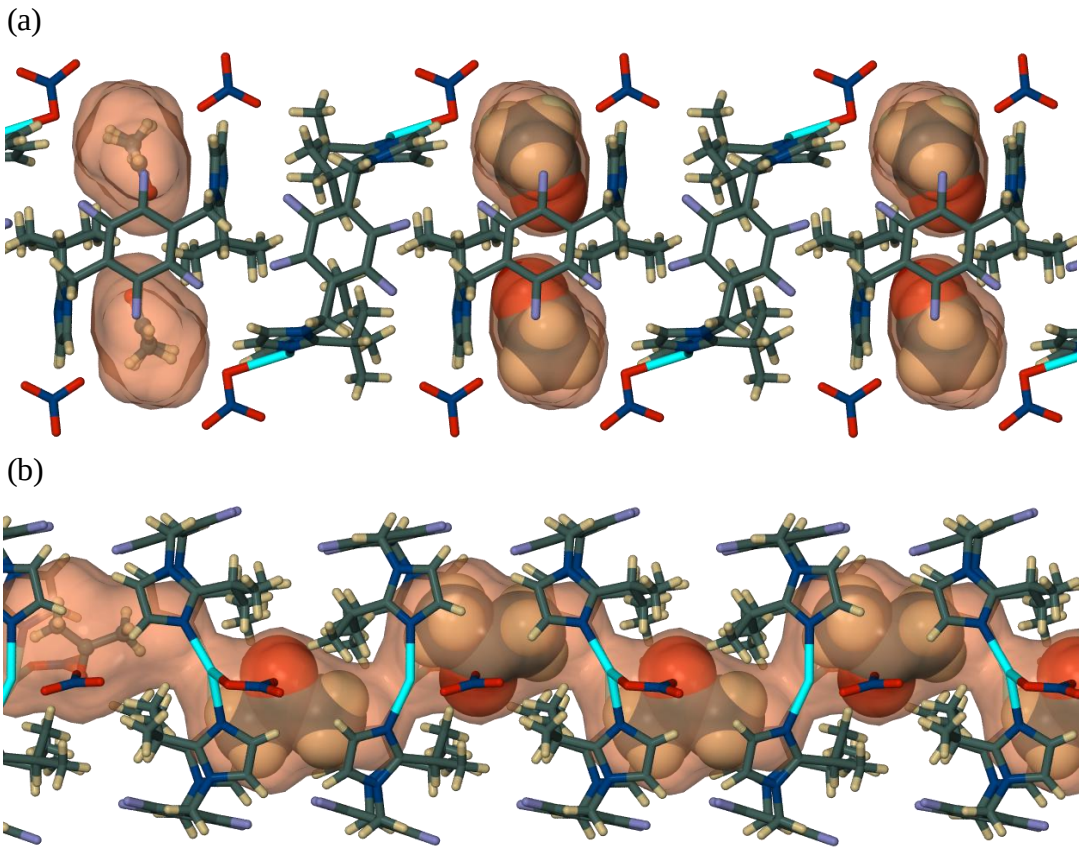

Figure 41. (a) Stacking of the metallocycles **A** and **B** along [010] in $\mathbf{3_{AC}}$. The host metallocycles are shown in capped-stick representation and the two solvent-filled pockets of 112 Å^3 associated with each metallocycle **B** are shown as a semitransparent solvent accessible surfaces (r_{probe} = 1.4 Å). The first two acetone molecules (from the left) are shown in the ball-and-stick metaphor, and the remaining guest molecules are shown in van der Waals representation. A methyl hydrogen atom from each solvent molecule protrudes from the solvent accessible surface in order to take part in a hydrogen bonding interaction with a nitrate anion. **(b)** A column of stacked **C** metallocycles in $\mathbf{3_{AC}}$ as viewed perpendicular to [010]. The host metallocycles are shown as capped-sticks and the first acetone guest (from the left) is shown in the ball-and-stick metaphor while the remaining guest molecules are shown in van der Waals representation. The solvent accessible channel passing through the stacked metallocycles is shown as a semitransparent surface (r_{probe} = 1.4 Å).

Metallocycles **A** and **B** stack one on top of another in an alternating fashion along the crystallographic *b* axis, and as can be seen from **Figure 41a**, the rings of **B** are tilted by approximately 73° with respect to **A** along [010]. This packing mode creates two solvent-filled pockets per metallocycle **B**, each with a cavity size of 112 Å^3 (r_{probe} = 1.4 Å). Metallocycles **C** also stack one on top of another along [010], but instead of forming discrete pockets they are stacked such that their apertures form continuous one-dimensional solvent-filled channels. Owing to the steric constraints imposed by the bulky isopropyl groups the channels consist of a series of bulges connected to one another by a

system of smaller apertures. The acetone molecules are accomodated within the bulges of the channels and are arranged in an up-down formation as viewed perpendicular to the channel direction (**Figure 41b**). The packing arrangement of the metallocycle columns in $\mathbf{3_{AC}}$ is that of a herringbone packing motif and, as such, is similar to the packing of $\mathbf{1_{MeOH\cdot H2O}}$, $\mathbf{1_{MeCN}}$, $\mathbf{1_{AC}}$ and $\mathbf{2_{AC}}$. The metallocyclic columns adjacent to one another in the direction parallel to [001] are all in the same orientation within the crystal and are comprised of identical stacks (**Figure 42**). The NO_3^- anions are located between the metallocycle columns associated with the Ag(I) centres by virtue of electrostatic interactions or coordination bonds.

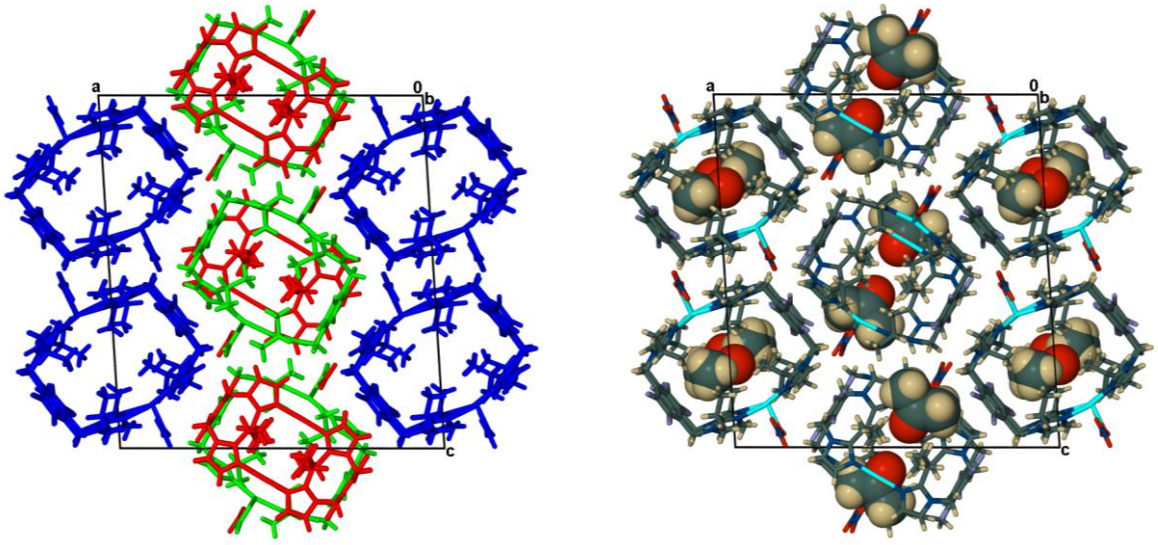

(a) (b)

Figure 42. Packing arrangement of the metallocycles in $\mathbf{3_{AC}}$, as viewed down [010]. **(a)** Metallocycles are shown in the capped-stick metaphor and solvent molecules have been omitted for clarity. The same colouring scheme has been employed for the metallocycles as that shown in **Figure 39** (i.e. metallocycle **A** is shown in green, **B** is shown in red and **C** is shown in blue). **(b)** Metallocycles are shown in the same view as (a) and are represented as capped-sticks; solvent molecules are shown in van der Waals representation.

In order to determine if the solvent molecules can be extracted from the host metallocycles with retention of monocrystallinity, single crystals of $\mathbf{3_{AC}}$ were subjected to TGA. As was observed for many of the inclusion complexes in this study, the loss of solvent occurs simultaneously with decomposition of the sample. The thermogram in **Figure 43** shows that $\mathbf{3_{AC}}$ is stable to *ca* 240 °C, after which the sample rapidly starts to decompose.

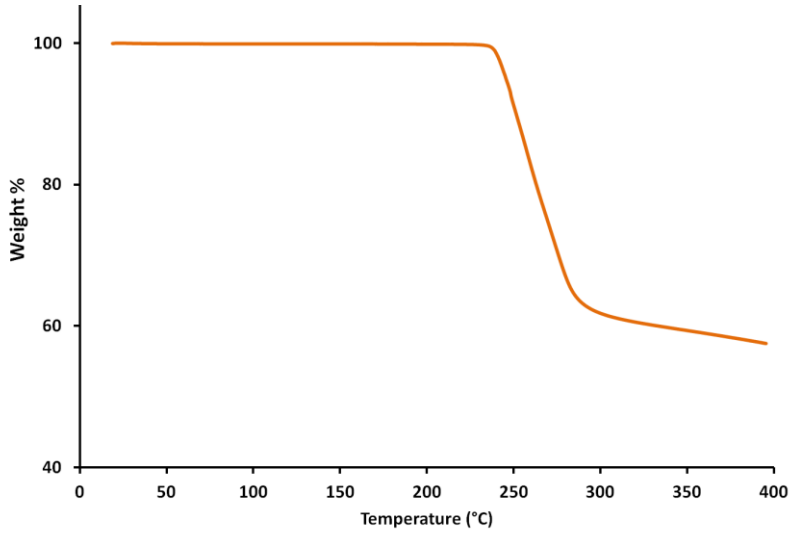

Figure 43. Thermogravimetric analysis of $\mathbf{3_{AC}}$.

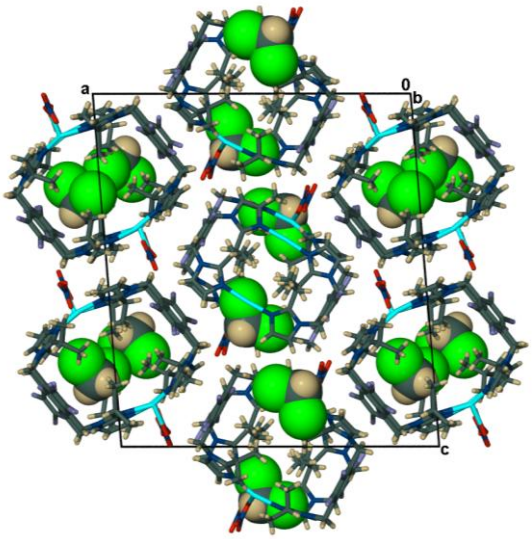

Figure 44. Capped-stick packing arrangement of $\mathbf{3_{DCM}}$ as viewed down [010]; solvent molecules are shown in van der Waals representation

The few remaining crystals in the vial were immersed in DCM to test if $\mathbf{3_{AC}}$ is capable of solvent exchange. After a period of one week a single crystal was harvested from the DCM mother liquor. Single-crystal X-ray analysis revealed that the acetone solvent molecules had indeed been replaced by the DCM molecules without significant disruption to the packing arrangement of the host metallocycles (**Figure 44**), to form $\mathbf{3_{DCM}}$. $\mathbf{3_{AC}}$ can thus be classed as a transiently porous system as the acetone molecules do not reside in open channels in the structure of $\mathbf{3_{AC}}$. Therefore the exchange of acetone for DCM would have to occur by means of a cooperative motion of the host molecules to create temporary openings to allow the acetone molecules to exit the host framework and the DCM molecules to enter.[8]

Figure 45a shows the two solvent-filled pockets per metallocycle **B** in $\mathbf{3_{DCM}}$, each pocket contains one DCM molecule. The inclusion of the larger solvent molecules increases the individual cavity sizes from 112 Å^3 in $\mathbf{3_{AC}}$ to 117 Å^3 in $\mathbf{3_{DCM}}$ (r_{probe} = 1.4 Å). The included DCM molecules donate two hydrogen bonds: one to the coordinated nitrate

anion on metallocycle **A** ($C_{donor}\cdots O_{acceptor}$ = 3.192(2) Å) and one to the uncoordinated nitrate anion associated with metallocycle **B** ($C_{donor}\cdots O_{acceptor}$ = 3.070(2) Å). The DCM molecules associated with **C** are located in discrete cavities of 171 Å^3 (r_{probe} = 1.4 Å); each cavity is shared between two successive metallocycles within the column of stacked **C** metallocycles and appears to overlap slightly with adjacent cavities (**Figure 45b**). This is in contrast to the 1D solvent-filled channels formed by the stacking of **C** in $\mathbf{3_{AC}}$. There are no significant interactions between the included DCM molecules and the host **C** metallocycles.

(a)

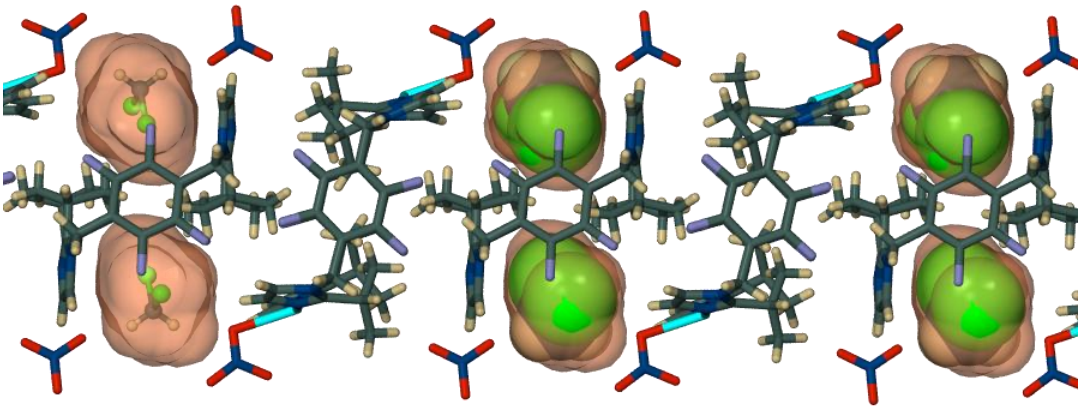

(b)

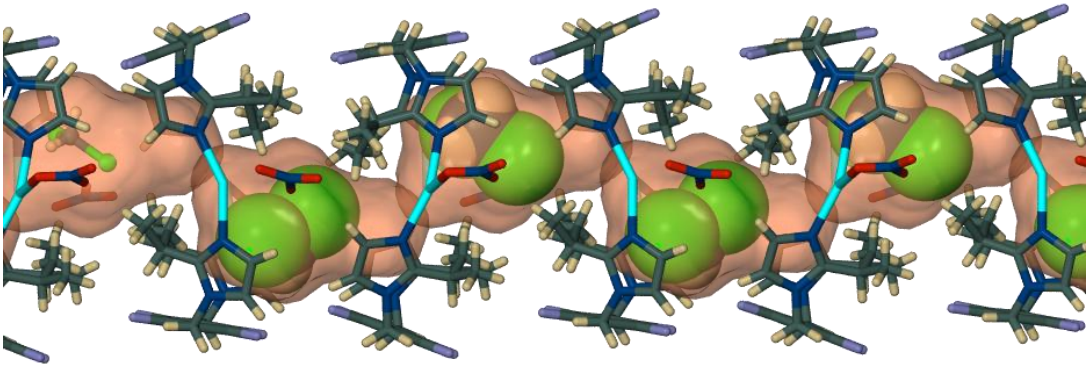

Figure 45.(a) Stacking of the metallocycles **A** and **B** along [010] in $\mathbf{3_{DCM}}$. The host metallocycles are shown in capped-stick representation and the two solvent-filled pockets of 117 Å^3 associated with each metallocycle **B** are shown as semitransparent accessible surfaces (r_{probe} = 1.4 Å). The first two DCM molecules (from the left) are shown in the ball-and-stick metaphor, and the remaining guest molecules are shown in van der Waals representation. The methylene hydrogen atoms of the DCM molecules protrude from the solvent accessible surface in order to take part in hydrogen bonding interactions with the nitrate anions. **(b)** A column of stacked **C** metallocycles in $\mathbf{3_{DCM}}$ as viewed perpendicular to [010]. The host metallocycles are shown as capped-sticks, the first DCM guest (from the left) is shown in the ball-and-stick metaphor and the remaining guest molecules are shown in van der Waals representation. The discrete solvent pockets of 171 Å^3 are shown as a semitransparent solvent accessible surface (r_{probe} = 1.4 Å).

3.2.4. Discussion of guest exchange and thermal analyses

In the preceding sections it has been demonstrated that the inclusion complexes $\mathbf{1}_{\mathbf{MeOH{\cdot}H2O}}$, $\mathbf{1}_{\mathbf{MeCN}}$, $\mathbf{1}_{\mathbf{AC}}$, $\mathbf{2}_{\mathbf{AC}}$ and $\mathbf{3}_{\mathbf{AC}}$ all have a high thermal stability and that removal of the solvent occurs either at temperatures well above the boiling point of the solvent, or simultaneously with decomposition of the host. As a consequence it can be inferred that the attractive interactions between these two components cannot easily be overcome – it is therefore somewhat perplexing that the occluded solvent can be so readily exchanged for other solvent molecules. It is clear that the mechanism by which this exchange occurs does not entail solvent loss followed by uptake of the incoming guest, but rather that it is a continuous and cooperative mechanism whereby an initial exchange occurs that facilitates successive interchanges with neighbouring guests.[17] This mechanism therefore involves the formation of several intermediate phases that contain both 'parent' molecules (**G**) and new guest molecules (**G'**) in the channels. We postulate that this state of flux will then continue, with the concentration of **G'** steadily increasing as the concentration of **G** decreases, until the new guest molecules have fully permeated the channels. In the case of $\mathbf{3}_{\mathbf{AC}}$, where some of the guests are located in discrete pockets rather than in infinite channels, the mechanism will additionally involve a cooperative movement of the host framework to create temporary openings between the discrete solvent-filled pockets to allow diffusion of the guests.[11] However, it is difficult to completely understand the mechanism by which this exchange takes place as the ephemeral nature of the intermediate phase excludes characterisation by means of single-crystal X-ray diffraction.

All exchange structures for the $\mathbf{1}_{\mathbf{G}}$ and $\mathbf{2}_{\mathbf{G}}$ 'parent' systems are based on a common isostructural framework comprising centrosymmetric metallocyclic complexes that stack one on top of another; the stacking periodicity of the columns span a narrow range and vary from ~5.76–5.90 Å for the $\mathbf{1}_{\mathbf{G}}$ systems and ~6.33–6.52 Å for the $\mathbf{2}_{\mathbf{G}}$ systems (**Table 3**). As a result of the stacking arrangement the structures all contain a common channel parallel to the crystallographic *a* axis that accommodates the various solvent molecules. The channels are amphiphilic as both water and organic aromatic guests can be accommodated within.

The $\mathbf{1}_{\mathbf{DCM}}$ and $\mathbf{2}_{\mathbf{DCM}}$ structures are the only structures to feature a host:guest ratio of 1:2; the remaining structures, with the exception of $\mathbf{1}_{\mathbf{H2O}}$, all have a host:guest ratio of 1:1. The two DCM molecules are located in the centre of the metallocycles and are associated with the counter-ions by means of a short contact between a chlorine atom and an oxygen

atom of the NO_3^- anions in $\mathbf{1_{DCM}}$, and a fluorine atom of the BF_4^- anions in $\mathbf{2_{DCM}}$. For the $\mathbf{1_G}$ series of structures $\mathbf{1_{DCM}}$ has the shortest intramolecular Ag···Ag distances and the longest intra-metallocycle aryl distances as a result of the shape and orientation of the DCM molecules within the channels (i.e. the two chlorine atoms of each DCM molecule are located on either side of the Ag(I) metal centres). In the $\mathbf{1_{BZ}}$ and $\mathbf{1_{DFB}}$ structures the guest molecules are located between successive metallocycles and are associated with the nitrate anions by virtue of a weak hydrogen bond between an aromatic hydrogen and the oxygen atom of the anion. In the $\mathbf{2_{BZ}}$ structure the benzene molecules are disordered and are oriented such that the major interaction between the host and guest molecules is a $Ag^+\cdots\pi$ contact. The guest molecules in $\mathbf{2_{DFB}}$ are also disordered, but are located between successive metallocycles and participate in weak hydrogen bonding interactions with the BF_4^- anions. The $\mathbf{1_{DIOX}}$, $\mathbf{1_{CY}}$ and $\mathbf{2_{CY}}$ systems are similar to one another in that the guest molecules are located in the centre of the metallocycles and there are no significant interactions between the host and guest. The guest molecules in $\mathbf{2_{DIOX}}$ are disordered over two positions and are associated with the host by a weak electrostatic $Ag^+\cdots O$ interaction. The $\mathbf{1_{H2O}}$ structure features a host:guest ratio of 1:5 and the water molecules are disordered over several positions within the channels.

As can be seen from in **Table 4**, the single-crystal structural analysis for the $\mathbf{1_{G'}}$ systems indicate that the host metallocyclic framework does not show significant guest-dependent cell volume variation i.e. the inclusion of the different guest species does not drastically alter the unit cell volume. This, in conjunction with the observation that (apart from the $\mathbf{1_{DCM}}$ structure, which has already been mentioned) the intra-molecular Ag···Ag distance, intra-metallocycle aryl distance, aromatic tilt angle and metallocycle tilt angles do not change significantly over the series of solvates, is an indication that the presence of different guests in the channels does not have a profound effect on the host framework i.e. the framework is rigid.

The thermal analyses of the exchange products indicate that all of the new inclusion complexes also have high thermal stability for their respective solvents. $\mathbf{1_{DCM}}$ is the only system in which desolvation occurs only as the sample decomposes; the rest of the solvates in the $\mathbf{1_{G'}}$ series all display endotherms associated with solvent loss before the major decomposition exotherm. The use of $T_{on} - T_b$ values recorded in **Table 3** as a parameter to assess the relative thermal stability of the host compounds for their respective guest molecules, shows that the $\mathbf{1_{DFB}}$ systems have the highest thermal stability and the

$\mathbf{1_{DIOX}}$ systems have the lowest. The entire $\mathbf{1_{G'}}$ series in descending order of thermal stability is thus: $\mathbf{1_{DCM}} > \mathbf{1_{DFB}} > \mathbf{1_{H2O}} > \mathbf{1_{Bz}} > \mathbf{1_{CY}} > \mathbf{1_{DIOX}}$.

The TGA traces of all of the solvates of the $\mathbf{2_{G'}}$ series indicate that loss of solvent occurs gradually from room temperature; however, there is a major desolvation step in which the majority of solvent is lost. This step has a corresponding endotherm in the DSC traces, and as a consequence of this we were able to note T_{on} values for the major desolvation step. According to the $T_{on} - T_b$ values recorded in **Table 3**, the $\mathbf{2_{G'}}$ series in descending order of thermal stability is: $\mathbf{2_{CY}} > \mathbf{2_{DCM}} > \mathbf{2_{BZ}} > \mathbf{2_{DFB}} > \mathbf{2_{DIOX}}$.

Both the $\mathbf{1_{G'}}$ and $\mathbf{2_{G'}}$ systems appear to have complex decomposition mechanisms as evidenced by the multiple-peak exotherms in the DSC traces in the region of decomposition.

3.3. CONCLUSION

This chapter describes five solvates of Ag(I) metallocycles, namely $\mathbf{1_{MeOH{\cdot}H2O}}$, $\mathbf{1_{MeCN}}$, $\mathbf{1_{AC}}$, $\mathbf{2_{AC}}$ and $\mathbf{3_{AC}}$, that are self-assembled from Ag(I) metal ions and the ditopic imidazole-derived ligands, **L1** and **L2**. Each solvate contains a different anion, guest and ligand combination as determined by single-crystal X-ray diffraction. These inclusion complexes were initially synthesised with a view to extending our portfolio of porous materials using zero-dimensional solvent-templated dinuclear metal complexes; we had initially hoped that removal of the solvent from the aperture of the host could be effected as a single-crystal to single-crystal transformation, yielding a porous single-crystal that could be exposed to a variety of guests. However, the thermal analyses of these compounds reveal that solvent loss occurs concomitantly with decomposition of the sample for $\mathbf{1_{MeOH{\cdot}H2O}}$, $\mathbf{1_{AC}}$ and $\mathbf{3_{AC}}$, and at temperatures well above the boiling point of the included solvent, with loss of single crystallinity for the $\mathbf{1_{MeCN}}$ and $\mathbf{2_{AC}}$ systems. This is particularly interesting in light of the fact that the solvent molecules are located in open channels and only interact with neighbouring guest molecules and the host framework through weak hydrogen bonds or van der Waals interactions and should, in principle, be able to easily escape the host lattice. Additionally, we found that the high-temperature phase obtained after desolvation of $\mathbf{1_{MeCN}}$ undergoes another phase change when re-exposed to MeCN and that the new phase retains some of the features of $\mathbf{1_{MeCN}}$, whereas the high temperature phase of $\mathbf{2_{AC}}$ does not undergo a phase change when re-exposed to acetone. The paucity in literature

accounts of systems that show high thermal stability towards their included solvent guest molecules indicates that this is a rare phenomenon that warrants further investigation.

In an attempt to rationalise the high thermal stability of these compounds, a computational study was carried out to investigate the guest-guest and host-guest interactions present in $\mathbf{1_{MeCN}}$ as compared to an analogous Ag(I) metallocycle host framework ($\mathbf{M2_{MeCN}}$) that readily loses its included MeCN guests with retention of monocrystallinity. The results of the computational investigation revealed that the guest-guest interaction energies between the guests constituting a dimeric pair were stronger in $\mathbf{1_{MeCN}}$ than $\mathbf{M2_{MeCN}}$ and that the interaction of a dimeric pair of MeCN guests within their 4.5 Å sphere of inclusion is more stabilising in $\mathbf{1_{MeCN}}$ than in $\mathbf{M2_{MeCN}}$, which could account for the observed stability of $\mathbf{1_{MeCN}}$ over $\mathbf{M2_{MeCN}}$. Furthermore, the latter interaction was found to be large for both systems, i.e. –31.59 and –29.39 kcal.mol^{-1} for $\mathbf{1_{MeCN}}$ and $\mathbf{M2_{MeCN}}$, respectively, indicating that $\mathbf{M2_{MeCN}}$ should also have high thermal stability for its included guest molecules. We rationalised that, since loss of solvent occurs for $\mathbf{M2_{MeCN}}$ under mild conditions, the host framework must be able to deform to create stronger host-host intermolecular interactions, thus compensating for the loss of host-guest intermolecular interactions, whereas $\mathbf{1_{MeCN}}$ cannot deform to a sufficiently stable guest-free conformation and therefore retains the included solvent molecules to much higher temperatures. It would be interesting to investigate the various host-host interactions; however, this would be computationally intensive and thus beyond the scope of the current study.

In a further attempt to remove the guest while maintaining the integrity of the host framework, a solvent exchange experiment was carried out in view of being able to thermally remove the new, more volatile solvent. Crystals of $\mathbf{1_{MeCN}}$ were immersed in DCM and single-crystal X-ray analysis revealed that 24 hours later the MeCN molecules had been exchanged for DCM in a single-crystal to single-crystal manner. Although thermal analysis indicates that it is not possible to remove the DCM with retention of monocrystallinity, we were intrigued by the facile exchange of the MeCN for the new guest. This prompted further investigation of all of the inclusion complexes as Class II porous systems and, to this end, single crystals of the $\mathbf{1_G}$ and $\mathbf{2_G}$ systems were exposed to a variety of common solvents and the exchange experiments monitored by SCD. The exchange occurs with only subtle adjustment of the host metallocycles to accommodate the new guests. Further studies can also be carried out to investigate the selective inclusion

behaviour of the original inclusion complexes when exposed to a mixture of guests. We postulated that the exchange occurs by a continuous and cooperative mechanism involving the formation of several intermediate phases containing both the 'parent' (**G**) and new guest (**G'**) molecules. It would be interesting to see if the mechanism of exchange and guest transport through the host lattice could be elucidated by future computational studies.

Thermal analysis again revealed high thermal stability of the solvent-exchanged complexes and it was therefore not possible to obtain a single-crystal structure of the apohost phase by removal of the new guests. The relative thermal stability of the host compounds for their respective guests for all solvent-exchanged complexes was additionally evaluated using the $T_{on} - T_b$ parameter. In accordance with the values of this parameter it was found that the thermal stability of the $\mathbf{1}_{\mathbf{G'}}$ series in descending order of stability is thus $\mathbf{1}_{\mathbf{DCM}} > \mathbf{1}_{\mathbf{DFB}} > \mathbf{1}_{\mathbf{H2O}} > \mathbf{1}_{\mathbf{Bz}} > \mathbf{1}_{\mathbf{CY}} > \mathbf{1}_{\mathbf{DIOX}}$ and the thermal stability of the $\mathbf{2}_{\mathbf{G'}}$ series is $\mathbf{2}_{\mathbf{CY}} > \mathbf{2}_{\mathbf{DCM}} > \mathbf{2}_{\mathbf{BZ}} > \mathbf{2}_{\mathbf{DFB}} > \mathbf{2}_{\mathbf{DIOX}}$.

Owing to the difficulty of obtaining crystals of $\mathbf{3}_{\mathbf{AC}}$ suitable for SCD it was not possible to explore this inclusion compound beyond the results obtained from the set of experiments carried out on the original vial of crystals. Ongoing studies are therefore aimed at optimizing the conditions of crystal growth so that high quality crystals can be re-obtained for this structurally interesting transiently porous system.

3.4. EXPERIMENTAL

3.4.1. Synthesis

3.4.1.1. $[Ag_2(L1)_2](NO_3)_2{\cdot}2CH_3OH{\cdot}H_2O$ ($\mathbf{1}_{\mathbf{MeOH{\cdot}H2O}}$)

0.03 mmol **L1** (9.5 mg) and 0.03 mmol $AgNO_3$ (5.4 mg) were each dissolved in 10 mL of aqueous methanol in separate vials. The ligand solution was slowly added to the metal salt solution and additional water was added (*ca* 5 mL) to prevent precipitation. The vial was capped and left in the dark. After five days crystals had grown that were suitable for single-crystal diffraction studies.

3.4.1.2. $[Ag_2(L1)_2](NO_3)_2{\cdot}2CH_3CB$ (1_{MeCN})

0.03 mmol **L1** (9.5 mg) and 0.03 mmol $AgNO_3$ (5.4 mg) were each dissolved in 10–15 mL of acetonitrile in separate vials. The ligand solution was slowly added to the metal salt solution. The vial was capped and left in the dark. After one day crystals had grown that were suitable for single-crystal diffraction studies.

3.4.1.3. $[Ag_2(L1)_2](NO_3)_2{\cdot}2(CH_3)_2CO$ (1_{AC})

0.03 mmol **L1** (9.5 mg) and 0.03 mmol $AgNO_3$ (5.4 mg) were each dissolved in 10 mL of acetone in separate vials. The ligand solution was slowly added to the metal salt solution and additional water was added (*ca* 5 mL) to prevent precipitation. The vial was capped and left in the dark. After one week crystals had grown that were suitable for single-crystal diffraction studies.

3.4.1.4. $[Ag_2(L1)_2](BF_4)_2{\cdot}2(CH_3)_2CO$ (2_{AC})

0.03 mmol L1 (9.5 mg) and 0.03 mmol $AgBF_4$ (5.8 mg) were each dissolved in 5 mL of acetone in separate vials. The ligand solution was slowly added to the metal salt solution. The vial was capped and left in the dark. After one week crystals had grown that were suitable for single-crystal diffraction studies.

3.4.1.5. $([Ag_2(L2)_2NO_3)(Ag_2(L2)_2(NO_3)_2)([Ag_2(L2)_2](NO_3)_2){\cdot}3(CH_3)_2CO$ (3_{AC})

0.03 mmol L2 (11.8 mg) and 0.03 mmol $AgNO_3$ (5.4 mg) were each dissolved in 10 mL of acetone in separate vials. The ligand solution was slowly added to the metal salt solution. The vial was capped and left in the dark. After two weeks crystals had grown that were suitable for single-crystal diffraction studies.

3.4.2. Computational methods

To assess the relative thermal stability of the $\mathbf{1}_{MeCN}$ and $\mathbf{M2}_{MeCN}$ inclusion complexes, various intermolecular interaction energies were calculated. The calculations were carried out by D.P. van Heerden under the supervision of Dr. C. Esterhuysen at the University of Stellenbosch using a parallel version of the program package Gaussian03.[28] Hydrogen atom positions of the models, based on diffraction data, were optimised at the M06/CEP-31G level of theory, where after single-point calculations were executed at the M06/CEP-

121G theory level[29-31] with counterpoise corrections[32] for the basis set superposition error. For each interaction, three single-point energy calculations were carried out and the interaction energy determined as the difference between (i) the energy of the whole model as described in **Scheme 3** and (ii) the sum of the energies of its constituents i.e. $\Delta E_{int} = E_{12} - (E_1 + E_2)$.

3.4.3. Crystallographic data

Table 4. Crystallographic data and refinement parameters for the all of the inclusion complexes in this chapter.

	$\mathbf{1}_{\mathbf{MeOH\cdot H2O}}$*	$\mathbf{1}_{\mathbf{MeCN}}$	$\mathbf{1}_{\mathbf{AC}}$	$\mathbf{2}_{\mathbf{AC}}$	$\mathbf{1}_{\mathbf{DCM(MeOH\cdot H2O)}}$
Empirical formula	$C_{29}H_{26}Ag_2F_8N_{10}O_8$	$C_{32}H_{26}Ag_2F_8N_{12}O_6$	$C_{31}H_{26}Ag_2F_8N_{10}O_7$	$C_{34}H_{32}Ag_2B_2F_{16}N_8O_2$	$C_{30}H_{24}Ag_2Cl_4F_8N_{10}O_6$
Formula weight	1010.34	1042.39	1018.36	1126.04	1130.13
Temperature (K)	100(2)	100(2)	100(2)	100(2)	100(2)
Wavelength (Å)	0.71073	0.71073	0.71073	0.71073	0.71073
Crystal system	monoclinic	monoclinic	monoclinic	monoclinic	monoclinic
Space group	$P2_1/n$	$P2_1/n$	$P2_1/n$	$P2_1/c$	$P2_1/n$
a (Å)	5.8633(13)	5.8164(4)	5.8183(7)	12.9283(13)	5.9026(13)
b (Å)	13.344(3)	13.2010(9)	13.4272(16)	12.2602(12)	13.264(3)
c (Å)	24.060(5)	24.2224(17)	23.910(3)	25.508(3)	23.941(5)
α (°)	90	90	90	90	90
β (°)	91.898(3)	92.4530(10)	91.589(2)	97.5140(10)	92.789(3)
γ (°)	90	90	90	90	90
V (Å^3)	1881.4(7)	1858.1(2)	1867.2(4)	4008.5(7)	1872.2(7)
Z	2	2	2	4	2
D_c (g/cm^3)	1.780	1.863	1.811	1.866	2.005
Absorption coefficient	1.141	1.157	1.149	1.097	1.431
F_{000}	996	1032	1008	2224	1112
Reflections collected	10643	10560	10656	23023	9949
Independent reflections	4048[R_{int} = 0.0438]	4067 [R_{int} = 0.0322]	4021 [R_{int} = 0.0222]	8637 [R_{int} = 0.0305]	4002 [R_{int} = 0.0420]
Goodness-of-fit on F^2	1.064	1.016	1.054	1.083	1.038
Final R indices [$I>2\sigma(I)$]	$R1$ = 0.0514, $wR2$ = 0.1300	$R1$ = 0.0301, $wR2$ = 0.0600	$R1$ = 0.0295, $wR2$ = 0.0754	$R1$ = 0.0575, $wR2$ = 0.1633	$R1$ = 0.0540, $wR2$ = 0.1424
R indices (all data)	$R1$ = 0.0787, $wR2$ = 0.1428	$R1$ = 0.0470, $wR2$ = 0.0669	$R1$ = 0.0363, $wR2$ = 0.0806	$R1$ = 0.0693, $wR2$ = 0.1710	$R1$ = 0.0736, $wR2$ = 0.1577

* This structure has previously been reported, however for the purposes of this study the crystal data was recollected and the values presented here may therefore differ slightly to those reported by *Gao et al.*[13]

	$\mathbf{1}_{DCM(MeCN)}$	$\mathbf{1}_{DCM(AC)}$	$\mathbf{2}_{DCM}$	$\mathbf{1}_{BZ(MeOH\cdot H2O)}$	$\mathbf{1}_{BZ(MeCN)}$
Empirical formula	$C_{30}H_{24}Ag_2Cl_4F_8N_{10}O_6$	$C_{30}H_{24}Ag_2Cl_4F_8N_{10}O_6$	$C_{30}H_{24}Ag_2B_2Cl_4F_{16}N_8$	$C_{34}H_{26}Ag_2F_8N_{10}O_6$	$C_{34}H_{26}Ag_2F_8N_{10}O_6$
Formula weight	1130.13	1130.13	1179.73	1038.39	1038.39
Temperature (K)	100(2)	100(2)	100(2)	100(2)	100(2)
Wavelength (Å)	0.71073	0.71073	0.71073	0.71073	0.71073
Crystal system	monoclinic	monoclinic	monoclinic	monoclinic	monoclinic
Space group	$P2_1/n$	$P2_1/n$	$P2_1/c$	$P2_1/n$	$P2_1/n$
a (Å)	5.9020(8)	5.8948(5)	6.3342(6)	5.7869(9)	5.7718(9)
b (Å)	13.2809(17)	13.2859(11)	12.2266(11)	13.489(2)	13.481(2)
c (Å)	23.926(3)	23.907(2)	25.772(2)	23.862(4)	23.860(4)
α (°)	90	90	90	90	90
β (°)	92.803(2)	92.8120(10)	95.9370(10)	91.618(3)	91.479(2)
γ (°)	90	90	90	90	90
V (Å^3)	1873.2(4)	1870.1(3)	1985.2(3)	1861.9(5)	1855.9(5)
Z	2	2	2	2	2
D_c (g/cm^3)	2.004	2.007	1.974	1.852	1.858
Absorption coefficient	1.430	1.433	1.369	1.153	1.156
F_{000}	1112	1112	1152	1028	1028
Reflections collected	10308	7671	11414	7138	10189
Independent reflections	4100 [R_{int} = 0.0537]	4568 [R_{int} = 0.0133]	4294 [R_{int} = 0.0247]	4278 [R_{int} = 0.0687]	4161 [R_{int} = 0.0275]
Goodness-of-fit on F^2	1.056	1.087	1.049	1.277	1.024
Final R indices [$I>2\sigma(I)$]	$R1$ = 0.0499, $wR2$ = 0.1145	$R1$ = 0.0268, $wR2$ = 0.0695	$R1$ = 0.0302, $wR2$ = 0.0678	$R1$ = 0.0656, $wR2$ = 0.1617	$R1$ = 0.0323, $wR2$ = 0.0796
R indices (all data)	$R1$ = 0.0859, $wR2$ = 0.1290	$R1$ = 0.0291, $wR2$ = 0.0710	$R1$ = 0.0395, $wR2$ = 0.0721	$R1$ = 0.0726, $wR2$ = 0.1647	$R1$ = 0.0401, $wR2$ = 0.0837

	$\mathbf{1}_{\mathbf{BZ(AC)}}$	$\mathbf{2}_{\mathbf{BZ}}$	$\mathbf{1}_{\mathbf{DFB(MeOH\cdot H2O)}}$	$\mathbf{1}_{\mathbf{DFB(MeCN)}}$	$\mathbf{1}_{\mathbf{DFB(AC)}}$
Empirical formula	$C_{34}H_{26}Ag_2F_8N_{10}O_6$	$C_{34}H_{26}Ag_2B_2F_{16}N_7$	$C_{34}H_{24}Ag_2F_{10}N_{10}O_6$	$C_{34}H_{24}Ag_2F_{10}N_{10}O_6$	$C_{34}H_{24}Ag_2F_{10}N_{10}O_6$
Formula weight	1038.39	1073.98	1074.37	1074.37	1074.37
Temperature (K)	100(2)	100(2)	100(2)	100(2)	100(2)
Wavelength (Å)	0.71073	0.71073	0.71073	0.71073	0.71073
Crystal system	monoclinic	monoclinic	monoclinic	monoclinic	monoclinic
Space group	$P2_1/n$	$P2_1/c$	$P2_1/n$	$P2_1/n$	$P2_1/n$
a (Å)	5.7637(3)	6.3710(3)	5.7890(4)	5.8211(7)	5.8054(6)
b (Å)	13.4998(8)	12.0878(5)	13.4613(9)	13.4049(16)	13.4559(14)
c (Å)	23.8821(14)	25.7534(8)	23.9568(17)	23.970(3)	23.949(3)
α (°)	90	90	90	90	90
β (°)	91.3950(10)	95.454(2)	92.2850(10)	92.423(2)	92.290(2)
γ (°)	90	90	90	90	90
V (Å^3)	1857.69(18)	1974.33(14)	1865.4(2)	1868.7(4)	1869.3(3)
Z	2	2	2	2	2
D_c (g/cm^3)	1.856	1.807	1.913	1.909	1.909
Absorption coefficient	1.155	1.104	1.161	1.159	1.159
F_{000}	1028	1054	1060	1060	1060
Reflections collected	9687	11869	8243	8057	7599
Independent reflections	4549 [R_{int} = 0.0146]	4903 [R_{int} = 0.0242]	4600 [R_{int} = 0.0229]	4495 [R_{int} = 0.0204]	4608 [R_{int} = 0.0245]
Goodness-of-fit on F^2	1.034	1.032	1.009	1.107	1.024
Final R indices [$I>2\sigma(I)$]	$R1$ = 0.0239, $wR2$ = 0.0618	$R1$ = 0.0399, $wR2$ = 0.1131	$R1$ = 0.0339, $wR2$ = 0.0783	$R1$ = 0.0466, $wR2$ = 0.1176	$R1$ = 0.0397, $wR2$ = 0.0887
R indices (all data)	$R1$ = 0.0265, $wR2$ = 0.0634	$R1$ = 0.0451, $wR2$ = 0.1165	$R1$ = 0.0431, $wR2$ = 0.0823	$R1$ = 0.0523, $wR2$ = 0.1207	$R1$ = 0.0507, $wR2$ = 0.0937

	$\mathbf{2_{DFB}}$	$\mathbf{1_{DIOX(MeOH\cdot H2O)}}$	$\mathbf{1_{DIOX(MeCN)}}$	$\mathbf{1_{DIOX(AC)}}$	$\mathbf{2_{DIOX}}$
Empirical formula	$C_{37}H_{26}Ag_2B_2F_{19}N_8$	$C_{32}H_{28}Ag_2F_8N_{10}O_8$	$C_{32}H_{28}Ag_2F_8N_{10}O_8$	$C_{32}H_{28}Ag_2F_8N_{10}O_8$	$C_{32}H_{28}Ag_2B_2F_{16}N_8O_2$
Formula weight	1181.02	1048.38	1048.38	1048.38	1097.98
Temperature (K)	100(2)	100(2)	100(2)	100(2)	100(2)
Wavelength (Å)	0.71073	0.71073	0.71073	0.71073	0.71073
Crystal system	monoclinic	monoclinic	monoclinic	monoclinic	monoclinic
Space group	$P2_1/c$	$P2_1/n$	$P2_1/n$	$P2_1/n$	$P2_1/c$
a (Å)	6.5255(10)	5.7985(6)	5.7821(7)	5.7815(11)	6.3970(13)
b (Å)	12.429(2)	13.3208(15)	13.2848(15)	13.301(3)	12.237(2)
c (Å)	25.312(4)	24.032(3)	23.985(3)	23.964(4)	25.475(5)
α (°)	90	90	90	90	90
β (°)	96.801(3)	90.880(4)	90.479(2)	90.622(3)	95.518(4)
γ (°)	90	90	90	90	90
V (Å^3)	2038.5(6)	1856.0(4)	1842.3(4)	1842.8(6)	1984.8(7)
Z	2	2	2	2	2
D_c (g/cm^3)	1.924	1.876	1.890	1.889	1.837
Absorption coefficient	1.090	1.161	1.170	1.169	1.105
F_{000}	1158	1040	1040	1040	1080
Reflections collected	9125	8749	15122	10758	8716
Independent reflections	5553 [R_{int} = 0.0321]	4559 [R_{int} = 0.0237]	4050 [R_{int} = 0.0248]	4558 [R_{int} = 0.0235]	4382 [R_{int} = 0.0422]
Goodness-of-fit on F^2	1.070	1.070	1.031	1.027	1.083
Final R indices [$I>2\sigma(I)$]	$R1$ = 0.0614, $wR2$ = 0.1281	$R1$ = 0.0410, $wR2$ = 0.1045	$R1$ = 0.0278, $wR2$ = 0.0680	$R1$ = 0.0309, $wR2$ = 0.0748	$R1$ = 0.0748, $wR2$ = 0.1814
R indices (all data)	$R1$ = 0.0921, $wR2$ = 0.1414	$R1$ = 0.0498, $wR2$ = 0.1089	$R1$ = 0.0321, $wR2$ = 0.0704	$R1$ = 0.0374, $wR2$ = 0.0780	$R1$ = 0.1026, $wR2$ = 0.1945

	$\mathbf{1_{CY}}$	$\mathbf{2_{CY}}$	$\mathbf{1_{H2O}}$	$\mathbf{3_{AC}}$	$\mathbf{3_{DCM}}$
Empirical formula	$C_{34}H_{32}Ag_2F_8N_{10}O_6$	$C_{34}H_{32}Ag_2B_2F_{16}N_8$	$C_{28}H_{20}Ag_2F_8N_{10}O_{11}$	$C_{172}H_{200}Ag_8F_{32}N_{40}O_{28}$	$C_{164}H_{184}Ag_8Cl_8F_{32}N_{40}O_{24}$
Formula weight	1044.44	1094.04	1040.28	4746.68	4854.07
Temperature (K)	100(2)	100(2)	100(2)	100(2)	100(2)
Wavelength (Å)	0.71073	0.71073	0.71073	0.71073	0.71073
Crystal system	monoclinic	monoclinic	monoclinic	monoclinic	monoclinic
Space group	$P2_1/n$	$P2_1/c$	$P2_1/n$	$P2_1/c$	$P2_1/c$
a (Å)	5.8533(3)	6.3826(4)	5.8710(2)	23.8025(8)	23.581(2)
b (Å)	13.4333(6)	12.3127(7)	13.3352(4)	15.4389(5)	15.4626(14)
c (Å)	23.6921(11)	25.5348(15)	23.9624(6)	25.9725(9)	26.291(3)
α (°)	90	90	90	90	90
β (°)	90.699(3)	95.562(3)	92.257(2)	93.58	94.5920(10)
γ (°)	90	90	90	90	90
V (Å^3)	1862.75(15)	1997.3(2)	1874.58(10)	9525.9(6)	9555.5(15)
Z	2	2	2	2	2
D_c (g/cm^3)	1.862	1.819	1.843	1.655	1.687
Absorption coefficient	1.152	1.094	1.154	0.914	1.020
F_{000}	1040	1080	1024	4800	4880
Reflections collected	7160	9119	9319	43953	57547
Independent reflections	4476 [R_{int} = 0.0279]	4840 [R_{int} = 0.0234]	4559 [R_{int} = 0.0240]	15030 [R_{int} = 0.0316]	22329 [R_{int} = 0.0703]
Goodness-of-fit on F^2	1.104	1.183	1.018	1.031	1.041
Final R indices [$I>2\sigma(I)$]	$R1$ = 0.0569, $wR2$ = 0.1326	$R1$ = 0.0707, $wR2$ = 0.1709	$R1$ = 0.0357, $wR2$ = 0.0944	$R1$ = 0.0618, $wR2$ = 0.1447	$R1$ = 0.0942, $wR2$ = 0.2525
R indices (all data)	$R1$ = 0.0673, $wR2$ = 0.1379	$R1$ = 0.0827, $wR2$ = 0.1771	$R1$ = 0.0448, $wR2$ = 0.0998	$R1$ = 0.0764, $wR2$ = 0.1552	$R1$ = 0.1514, $wR2$ = 0.3041

REFERENCES

(1) F. H. Herbstein, *Cryst. Growth Des.*, **2004**, *4*, 1419.

(2) M. R. Caira; L. R. Nassimbeni; M. L. Niven; W. D. Schubert; E. Weber; N. Dorpinghaus, *J. Chem. Soc. Perkin Trans. 2*, **1990**, 2129.

(3) L. R. Nassimbeni, *Acc. Chem. Res.*, **2003**, *36*, 631.

(4) G. D. Enright; K. A. Udachin; I. L. Moudrakovski; J. A. Ripmeester, *J. Am. Chem. Soc.*, **2003**, *125*, 9896.

(5) J. L. Atwood; L. J. Barbour; A. Jerga, *Science*, **2002**, *296*, 2367.

(6) L. J. Barbour; M. R. Caira; L. R. Nassimbeni, *J. Chem. Soc. Perkin Trans. 2*, **1993**, 1413.

(7) J. J. Vittal; T. Lu, *Cryst. Growth Des.*, **2006**, *6*, 822.

(8) L. J. Barbour, *Chem. Commun.*, **2006**, 1163.

(9) L. Dobrańska; G. O. Lloyd; L. J. Barbour, *New. J. Chem.*, **2007**, *31*, 669.

(10) L. Dobrańska; G. O. Lloyd; H. G. Raubenheimer; L. J. Barbour, *J. Am. Chem. Soc.*, **2005**, *127*, 13134.

(11) L. Dobrzańska; G. O. Lloyd; H. G. Raubenheimer; L. J. Barbour, *J. Am. Chem. Soc.*, **2006**, *128*, 698.

(12) L. J. Barbour; T. Jacobs; J. A. Gertenbach; D. Das, *Aust. J. Chem.*, **2010**, *63*, 573.

(13) J. M. Shreeve; Y. Gao; B. Twamley, *Inorg. Chem.*, **2006**, *45*, 1150.

(14) G. O. Lloyd; J. Alen; M. W. Bredenkamp; E. J. C. de Vries; C. Esterhuysen; L. J. Barbour, *Angew. Chem. Int. Ed.*, **2006**, *45*, 5354.

(15) J. T. Hupp; A. P. Nelson; O. K. Farha; K. L. Mulfort, *J. Am. Chem. Soc.*, **2009**, *131*, 458.

(16) M. Eddaoudi; J. Kim; N. Rosi; D. Vodak; J. Wachter; M. O'Keeffe; O. M. Yaghi, *Science*, **2002**, *295*, 469.

(17) Z. Huang; P. S. White; M. Brookhart, *Nature*, **2010**, *465*, 598.

(18) J. J. Vittal, *Coord. Chem. Rev.*, **2007**, *251*, 1781.

(19) J. L. Atwood; L. J. Barbour; A. Jerga; B. L. Schottel, *Science*, **2002**, *298*, 1000.

(20) D. X. Xue; W. X. Zhang; X. M. Chen; H. Z. Wang, *Chem. Commun.*, **2008**, 1551.

(21) M. Kawano; M. Fujita, *Coord. Chem. Rev.*, **2007**, *251*, 2592.

(22) M. A. Garcia-Garibay, *Angew. Chem. Int. Ed.*, **2007**, *46*, 8945.

(23) A. Bondi, *J. Phys. Chem.*, **1964**, *68*, 441.

(24) A. L. Spek, *J. Appl. Cryst.*, **2003**, *36*, 7.

(25) *PLATON, A multipurpose Crystallographic Tool*; U. Utrecth University, The Netherlands, **2008**.

(26) L. Dobrańska; G. O. Lloyd; C. Esterhuysen; L. J. Barbour, *Angew. Chem. Int. Ed*, **2006**, *45*, 5856.

(27) A. G. Orpen; L. Brammer; F. H. Allen; O. Kennard; D. G. Watson; R. Taylor, *J. Chem. Soc. Dalton Trans.*, **1989**, S1.

(28) *Gaussian 03, Revision B.05*; M. J. T. Frisch, G. W.; Schlegel, H. B.; Scuseria, G. E.; Robb, M. A.; Cheeseman, J. R.; Montgomery, Jr., J. A.; Vreven, T.; Kudin, K. N.; Burant, J. C.; Millam, J. M.; Iyengar, S. S.; Tomasi, J.; Barone, V.; Mennucci, B.; Cossi, M.; Scalmani, G.; Rega, N.; Petersson, G. A.; Nakatsuji, H.; Hada, M.; Ehara, M.; Toyota, K.; Fukuda, R.; Hasegawa, J.; Ishida, M.; Nakajima, T.; Honda, Y.; Kitao, O.; Nakai, H.; Klene, M.; Li, X.; Knox, J. E.; Hratchian, H. P.; Cross, J. B.; Bakken, V.; Adamo, C.; Jaramillo, J.; Gomperts, R.; Stratmann, R. E.; Yazyev, O.; Austin, A. J.; Cammi, R.; Pomelli, C.; Ochterski, J. W.; Ayala, P. Y.; Morokuma, K.; Voth, G. A.; Salvador, P.; Dannenberg, J. J.; Zakrzewski, V. G.; Dapprich, S.; Daniels, A. D.; Strain, M. C.; Farkas, O.; Malick, D. K.; Rabuck, A. D.; Raghavachari, K.; Foresman, J. B.; Ortiz, J. V.; Cui, Q.; Baboul, A. G.; Clifford, S.; Cioslowski, J.; Stefanov, B. B.; Liu, G.; Liashenko, A.; Piskorz, P.; Komaromi, I.; Martin, R. L.; Fox, D. J.; Keith, T.; Al-Laham, M. A.; Peng, C. Y.; Nanayakkara, A.; Challacombe, M.; Gill, P. M. W.; Johnson, B.; Chen, W.; Wong, M. W.; Gonzalez, C, Pittsburgh PA, Gaussian, Inc **2003**.

(29) W. J. Stevens; D. D. Konowalow; L. B. Ratcliff, *J. Chem. Phys.*, **1984**, *80*, 1215.

(30) W. J. Stevens; M. Krauss; H. Basch; P. G. Jasien, *Can. J. Chem.*, **1992**, *70*, 612.

(31) T. R. Cundari; W. J. Stevens, *J. Chem. Phys.*, **1993**, *98*, 5555.

(32) S. F. Boys; F. Bernardi, *Mol. Phys.*, **1970**, *19*, 553.

CHAPTER 4

INCLUSION OF THIAZYL RADICALS INTO A POROUS CRYSTALLINE MATERIAL

4.1. INTRODUCTION

The study of compounds with unique solid state properties and characteristics is one of the most active areas of research in the development and progress of materials chemistry. The challenges presented by future applications have been the driving force behind the extensive breadth of materials studied; from classical crystalline inorganic minerals to hybrid inorganic/organic systems and from crystalline organic materials to soft materials consisting of organic polymers. As yet, no single class of material completely satisfies all technological niches.[1-6] One approach to tackle this problem would be to design hybrid materials in which the synergic interplay between different classes of material may ultimately afford novel types of behaviour that are greater than the sum of the individual parts. This chapter reports the attempted gas-phase diffusion of two organic radicals into four porous crystalline materials, and shows that the inclusion is selective for a specific host material against the range of potential hosts tested. Furthermore, it is demonstrated that the properties of both the organic radicals as well as the host framework are modified in the new inclusion complexes and that the host framework acts as a radical storage vessel in which the organic radicals, which are normally highly reactive short-lived species, can be stored under ambient conditions within the cavities of the host material for a period of three months without degradation.

The past two decades have witnessed a growing interest in the study of porous materials, owing to their potential application in separation, storage, sensing and purification of molecular guests.[7-15] Many design strategies are employed in the synthesis of molecular porous materials (see Chapter 1) and of these, two have been used to generate porous materials as potential host systems for this study, i.e. porous materials comprised of 0D metallocyclic complexes that retain their shape upon desolvation to form empty voids or channels and metal-organic frameworks (MOFs). The variety of porous metallocycles obtained by the former method has been reviewed in Section 1.4.1.2 and the porous silver metallocycle[16] (**M1**) (**Figure 1**) and the transiently porous copper

metallocycle[17] (**M3**) (**Figure 2**) were selected as candidates for this study owing to their ability to retain their single crystal nature upon desolvation. In the second category, the porous MOF materials **ZIF-8**[18] and **MIL-53(Al)**[19] were chosen. As these materials have not thus far been treated in as much detail as the porous metallocyclic complexes, the following section provides a short overview as well as the reasons for the choice of these specific MOFs for this study.

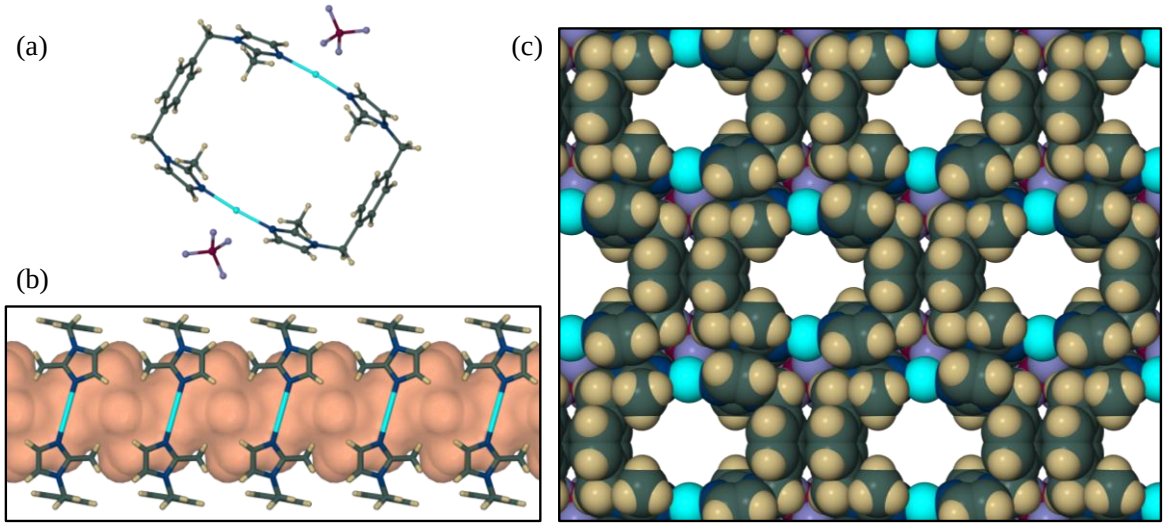

Figure 1. (a) The metallocyclic complex **M1** $[Ag_2\mathbf{A1}_2](BF_4)_2$, where **A1** = 1,4-bis(2-methylimidazol-1-ylmethyl)benzene. **(b)** View perpendicular to the 1D channels (semitransparent pink surface) formed by stacking of the $[Ag_2L'_2]^{2+}$ units (shown as capped-sticks). **(c)** Space-filling projection along [001], showing the arrangement of the 1D channels.

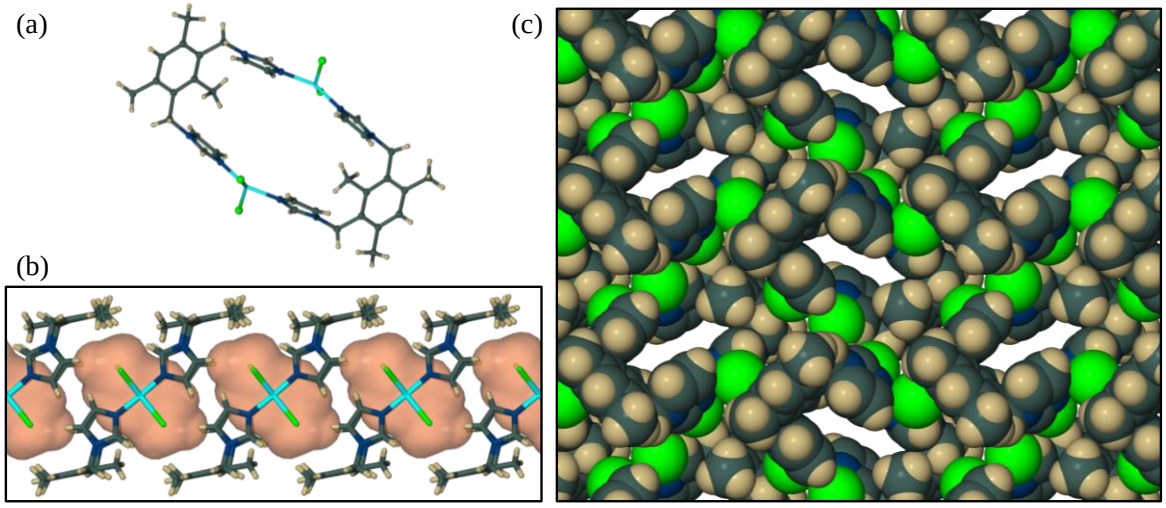

Figure 2. (a) The metallocyclic complex **M3** $[Cu_2\mathbf{A3}_2Cl_4]$, where **A3** = 1,3-bis(imidazol-1-ylmethyl)-2,4,6-trimethylbenzene. **(b)** View perpendicular to the $[Cu_2L''_2Cl_4]$ columns with host molecules shown in the capped stick representation and the guest-accessible pockets shown as semi-transparent pink surfaces. **(c)** Space-filling projection along [100], showing the arrangement of the metallocycle columns.

As the name suggests, MOFs are framework materials that are built up by connecting a series of rigid bi- or polydentate ligands (linkers) to one another by means of a system of metal clusters or metal ions (nodes) to create an open 3D framework with voids that can accommodate various guest molecules.[20] Judicious choice of both organic linkers and metal nodes can lead to a high degree of tunablity of the framework topology, which in turn affects the shape and size of the pores as well as having an influence on the chemical functionality of the framework.[21] Through the pioneering work of Yaghi, Kitagawa and Férey, the true versatility of these materials as dynamic vessels for the storage, separation and exchange of guests has been demonstrated.

Zeolitic imidazolate frameworks (ZIFs) are a new class of robust MOF materials developed by Yaghi. These porous materials have recently been thrust into the limelight because of their exceptional chemical stability in refluxing organic solvents and boiling alkaline water – an unprecedented finding in the field of MOF chemistry.[18] Their permanent porosity has also been demonstrated and it has been shown that they have an extremely high capacity for storing CO_2, as well as being selective for this gas from a mixture of CO_2 and CO. It has also been shown that they have high thermal stability and are able to survive temperatures of up to 550 °C.[22,23] ZIFs are structural analogues of zeolites, a well known and industrially fêted class of crystalline microporous materials that are widely used in the petrochemical industry for the production of gasoline.[24] In the zeolite framework, tetrahedral $Si(Al)O_4$ units are covalently joined by bridging oxygen atoms, whereas in the ZIF material the tetrahedral units are transition metals and the bridging groups are comprised of imidazolate units; thus the overall open framework structure is retained in the ZIF with the added advantage of being able to tailor the properties of the material by functionalisation of the organic linkers. To date more than 90 ZIFs have been structurally characterised,[23] and of these, **ZIF-8** (**Figure 3**) was chosen as a potential host material for this study owing to its large pore diameter (11.6 Å) and ease of synthesis on a gram scale.[22,25]

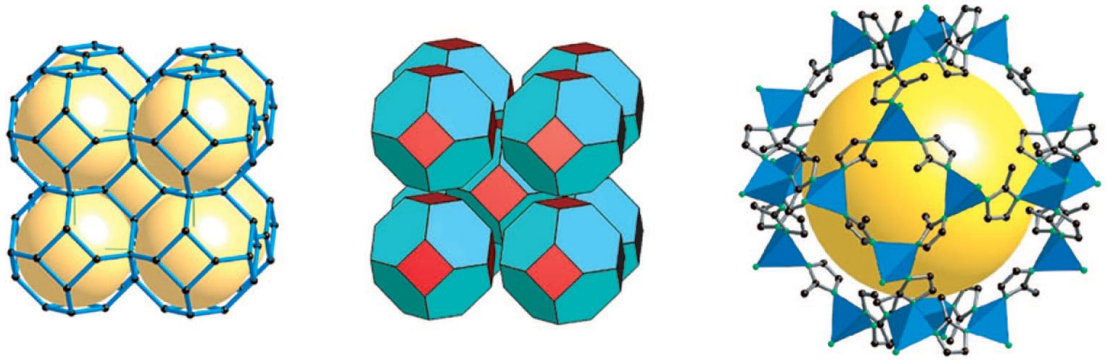

Figure 3. Various representations of the crystal structure of **ZIF-8**, which that has the sodalite (**sod**) type topology. **(Left)** the framework is represented as a simplified net with the nodes depicted as black dots and the linkers as blue sticks; **(middle)** the structure is shown as a tiling, which is a 3D representation of the subdivision of space by generalised polyhedra and **(right)** the largest cage in the **ZIF-8** structure is shown with the ZnN_4 tetrahedra represented in blue. The large yellow spheres represent the empty space within the framework. Figure adapted from reference 22.

The final host system in this chapter was selected from the MIL (MIL = Material of Institut Lavoisier) family of hybrid inorganic-organic nanoporous solids.[12,19,26,27] Whilst most synthetic procedures utilise clusters of divalent cations (e.g. Zn^{2+} and Cu^{2+}) as components in the assembly of MOFs, the MIL series contains cations in a range of oxidation states. In particular, the combination of certain trivalent metals (e.g. Al^{3+}, Cr^{3+}, Fe^{3+}, In^{3+}, V^{3+}, Ga^{3+}) with dicarboxylic acid derivatives has yielded a series of porous MOFs with unique and interesting structural features. It has been shown that these materials are permeable to a variety of guests; most noteworthy is the hydrogen storage capacity of 3.8 and 3.1 wt. % recorded for **MIL-53(Al)** and **MIL-53(Cr)** respectively, when loaded at 77 K under 1.6 MPa.[28] It has also been found that **MIL-53(Fe)** is capable of exchanging guest water molecules with a variety of organic solvents in a manner that is selective towards certain organic guests.[29] Similarly **MIL-47(V)** and **MIL-53(Al)** have shown promise as industrial adsorptive separation materials as they display a high degree of selectivity for styrene over ethylbenzene when exposed to a mixture of the two guests.[12] Of particular relevance to this study is the inclusion of ferrocene and other metallocene derivatives into the pores of **MIL-53(Al)** and **MIL-47(V)**,[30-33] as there are very few examples in the literature of materials that are solid at room temperature being included in a framework material *via* adsorption of the guest directly from the gas phase. It is interesting to note that in some cases the inclusion process results in a modification of certain properties of the original framework e.g. the redox-inactive **MIL-53(Al)** is converted into a redox-active species by a post-synthetic functionalisation of the

framework with 1,1′-ferrocenediyl-dimethylsilane.[31] However, the most remarkable feature of these materials is the exceptional framework flexibility demonstrated by certain members of the MIL family. For example, in the **MIL-53** series it has been found that the empty form (i.e. the phase devoid of any guest molecules) absorbs a stochiometric amount of water when exposed to the atmosphere; this process is fully reversible and the empty form can then be recovered by heating the hydrated form to temperatures exceeding 250 °C.[9,19,29,34-38] The absorption/desorption process is accompanied by a contraction and expansion of the pores with atomic displacements amounting to several angstroms, yet the underlying framework topology remains unaffected. Materials that exhibit this type of flexibility under the influence of an external stimulus are said to 'breathe'.[39] The breathing mechanism of the diamagnetic **MIL-53(Al)** framework has been examined extensively by ^{1}H, ^{13}C, ^{27}Al and ^{129}Xe NMR.[19,35,40] These studies have shown that the contraction and expansion of the framework depends on the presence of guest molecules and that the pore dimensions can be correlated to the nature, size and amount of guest molecules. We therefore decided to include the flexible **MIL-53(Al)** in our list of prospective host materials (**Figure 4**).

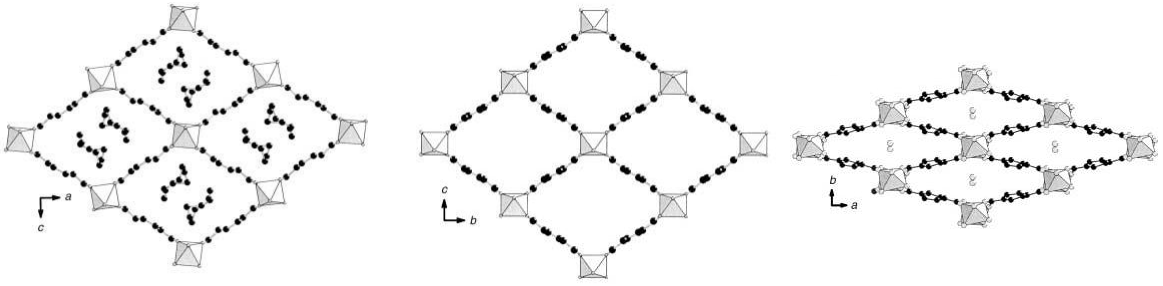

Figure 4. View of the 1D channels in the 3D frameworks of different forms of **MIL-53(Al)**: **(left)** the as synthesised form **MIL-53(Al)·terephthalic** acid, which contains unreacted disordered terephthalic acid molecules within the channels; **(middle)** the empty form and **(right)** the room temperature form, which contains water molecules absorbed from the atmosphere. Figure adapted from reference 19.

In recent years interest in paramagnetic materials has been on the rise as they form an integral part of modern technology, and it is in this regard that the production and physical properties of stable organic radicals has continued to be an active area of research.[4,41-44] Most organic radicals bear one unpaired electron in their π–systems and as such, they have been recognised as potential building blocks for molecule-based magnetic and conducting materials. Among these, thiazyl radicals (a member of the family of thermally stable sulphur-nitrogen heterocyclic radicals) have shown particular promise as

the inclusion of heavier p-block elements such as S and Se (in relation to O) offers greater dimensionality and magnetic anisotropy. These favour higher magnetic ordering and temperatures, and a range of both magnetic and conducting materials as well as spin-transition materials have been reported in the literature.[45] However, it has been shown that the ability of these organic radicals to act as conductive or magnetic materials is directly correlated to the arrangement of the molecules in the solid state structure (see Chapter 1), therefore significant research efforts have been aimed at implementing crystal engineering principles to control the solid state architectures of thiazyl radicals.[46-48] In single component systems these strategies mainly involve modifying the molecular structure of the radical so as to promote certain attractive or repulsive intermolecular interactions that will lead to a weakening of the spin-pairing solid state π*-π* dimerisation process and thereby intensify the magnetic properties of the material.[41,48-50] There have also been reports in the literature in which structural modification of the solid state structure is achieved through co-sublimation of two radicals with aromatic systems that have complementary electron distributions, to yield a co-crystal with a mixed dimer motif.[51] This is not the only report in which a second component is introduced into the crystallisation process; it has also been shown that is it possible for a thiazyl radical to act as a guest within a host lattice. Studies of this kind have been limited to two inclusion complexes obtained by co-sublimation of the radical guest molecules with the same molecular organic host framework, perhydrotriphenylene (**PHTP**).[52,53] In both of these cases the magnetic properties of the included radical were substantially modified, with the propensity for π*-π* dimerisation of the radical inhibited in both **NCC_6H_4CNSSN·** and **TTTA** (**TTTA** = trithiatriazenyl) included structures. These results indicate that there is potential for building more complex supramolecular architectures from thiazyl radicals in which the host fundamentally affects the supramolecular structure and subsequent behaviour of the radical and, conversely, to create systems in which the radical modifies the host.

The inclusion of thiazyl radicals into a porous coordination material has not previously been reported, but offers the potential for magnetic communication between the radical guest and a paramagnetic framework, thereby modulating the magnetic properties of the host lattice; e.g. recent studies by Pöppl *et al*.[54] have shown that the presence of a nitroxide radical modifies the magnetism of the copper framework **$Cu_3(btc)_2$** (**btc** = benzene-tricarboxylic acid). Furthermore, the presence of an unpaired electron in a radical

is generally associated with low stability and high reactivity, and as a result these compounds have a short lifetime if they are not synthesised and stored under strict inert conditions. It would therefore be highly advantageous if a system could be developed in which the radicals could be stored in air under ambient conditions, and then released in a controlled manner. In this vein promising results obtained by Dong *et al.* have indicated that it is possible to convert guest molecules that have been included in a porous coordination polymer to their corresponding organic radicals and stabilise them within the interior cavity in air for one month.[11]

Scheme 1. The two thiazyl radicals used in this study: (**left**) 5-methylbenzo-1,3,2-dithiazolyl (**MBDTA**) and (**right**) benzo-1,3,2-dithiazolyl (**BDTA**).

As an extension of these studies we report the investigation of the inclusion chemistry of thiazyl radicals within a porous coordination-based framework. For this work we have chosen the two known dithiazolyl radicals benzo-1,3,2-dithiazolyl (**BDTA**)[42] and 5-methylbenzo-1,3,2-dithiazolyl (**MBDTA**)[55] (**Scheme 1**) owing to the fact that their solid state properties are well understood. In this chapter we show that it is possible to include organic radicals into a porous material and we demonstrate that this inclusion process is selective for certain host systems and results in a modification of the original solid state structures of both the host and guest. In addition we show that, when contained within the pores of the host framework, these radicals can be stabilised as a guest and stored in air for a period of more than three months, and that by exposing the host-guest complex to a suitable solvent the radicals can be released in a controlled manner.

4.2. RESULTS AND DISCUSSION

4.2.1. Gas phase diffusion of MBDTA and BDTA into porous host materials

The four porous coordination materials that were examined as possible host systems were synthesised by methods documented in the literature. The two ligands, 1,4-bis(2-methylimidazol-1-ylmethylbenzene and 1,3-bis(imidazol-1-ylmethyl)-2,4,6-trimethyl

benzene, components of **M1** and **M3** respectively were synthesised (see Section 4.4.1) and single crystals of the metallocyclic complexes were obtained by slow evaporation of an equimolar solution of ligand and metal salt ($AgBF_4$ for **M1** and $CuCl_2$ for **M3**) in the relevant solvent. **M1** consists of a rectangular cationic complex comprised of two linearly coordinated silver ions doubly bridged to one another by means of two ligands; the rings stack on top of one another to form 1D channels occupied by occluded solvent molecules (**Figure 1**).[16] The structure of **M3** is similar to **M1** but differs in that it contains copper ions in a distorted square planar coordination environment that are coordinated to two ligands as well as two chloride anions. These complexes also stack linearly, but form discrete solvent filled voids instead of 1D channels (**Figure 2**).[17] Single crystals of the empty host structures were obtained by placing the materials under vacuum for 24 hours to ensure the removal of all solvent molecules. **ZIF-8** was formed in quantitative yields by the mechanochemical ion- and liquid-assisted grinding (ILAG) of ZnO, 2-methylimidazole (MeIM), DMF and an ammonium salt additive.[25] The framework of the **ZIF-8** structure is neutral and is built up from Zn^{2+} tetrahedral metal centres that are bridged to one another by virtue of the MeIM units. The metal centres are coordinated by the nitrogen atoms of the deprotonated MeIM only and form an angle of 145° at the Zn-MeIM-Zn centres (analogous to the Si-O-Si angle in zeolites). This material has been characterised as a sodalite (**sod**)* zeolite-type structure with modest pore apertures of 3.4 Å and large internal cavities that measure 11.6 Å in diameter (**Figure 3**).[18] The empty **ZIF-8** material was prepared by initially immersing a sample in methanol at room temperature for 48 hours to exchange all guest molecules for the more volatile methanol guest molecules; the evacuated form was then obtained by heating the sample to 300 °C under a dynamic vacuum. **MIL-53(Al)** was synthesised by the hydrothermal reaction of $AlCl_3 \cdot 6H_2O$ and terephthalic acid to initially form **MIL-53(Al)·terephthalic acid** which, with subsequent heating at 150 °C under vacuum, yields the empty **MIL-53(Al)** phase. The 3D framework is comprised of infinite trans chains of corner-sharing $AlO_4(OH)_2$ octehedra that are interconnected by the terephthalate units to form 1D rhombic shaped channels, with the hydroxyl groups protruding into the pores (**Figure 4**).[19] The organic radical guest materials **BDTA** and **MBDTA** were prepared according to the literature

* The three-letter symbol refers to a topological classification of the framework structure; for symbol definitions see the Reticular Chemistry Structure Resource available at http://rcsr.anu.edu.au/ (Date accessed 20/10/2011).

methods[46,55] under strict inert conditions and were purified by vacuum sublimation just below their decomposition temperatures.

Attempted loading of the radicals into the different host frameworks was carried out by direct adsorption of the radical from the vapour phase under reduced pressure. A sample of *ca* 50 mg of the host material was placed together with 50 mg of the radical in a Schlenk tube in separate glass vials. The pressure was then reduced to 10^{-3} mbar and the tube was sealed under static vacuum. The reaction tube was then heated to 50 °C to initiate sublimation of the radical. During this treatment a visual inspection of the host materials **M1**, **M1** and **ZIF-8** revealed that the samples did not appear to undergo any change when exposed to either **BDTA** or **MBDTA**. This was confirmed by further analysis, which showed only the presence of the host materials and not of the radical (electron impact mass spectrometry (EI–MS), powder X-ray diffraction (PXRD) and UV-Vis). In contrast, the white **MIL-53(Al)** powder underwent a clear change, forming a dark-brown material when exposed to **BDTA** and a reddish-brown material when exposed to **MBDTA** (**Figure 5**). For the purposes of this study we will refer to the inclusion complexes as **BDTA@MIL-53(Al)** and **MBDTA@MIL-53(Al)**.[56†]

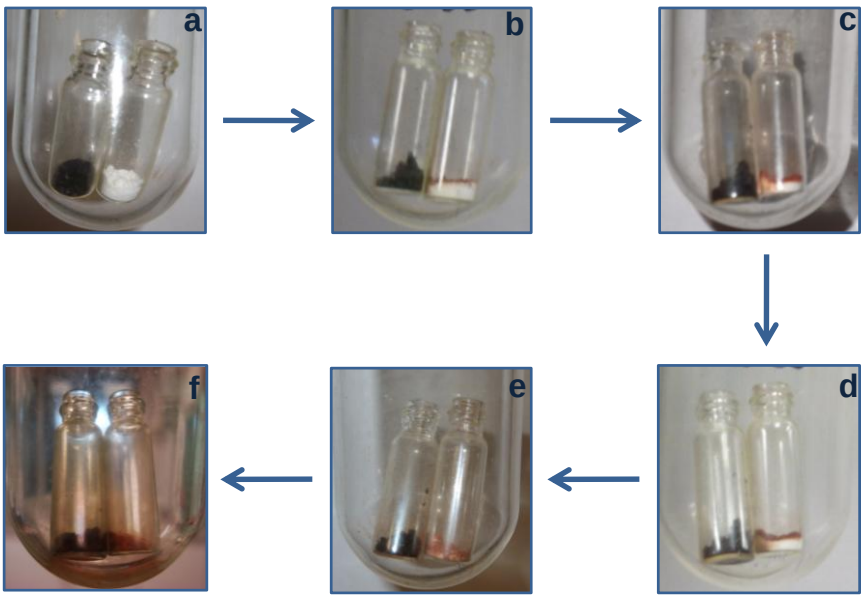

Figure 5. Photographs of the conversion of **MIL-53(Al)** to **MBDTA@MIL-53(Al)** showing the sublimation under vacuum of the **MBDTA** (black solid) into the **MIL-53(Al)** (white solid). Time exposed: **(a)** 0 hrs, **(b)** 24 hrs, **(c)** 48 hrs, **(d)** 72 hrs, **(e)** 96 hrs and **(f)** 4 weeks. Note the diffusion of the radical into the **MIL-53(Al)** sample characterised by an increasing depth of brown colouration at the top of the sample.

† This nomenclature is based on an adaptation of [ML_n]@MOF, which was originally used to annotate a family of organometallic inclusion compounds (ML_n = a volatile organometallic molecule).

The selectivity of the thiazyl guest for only the **MIL-53(Al)** host likely arises from a combination of factors. For the inclusion process to be favourable there must be a good correlation between the shape and size of the empty pore and prospective guest molecule, which was clearly not the case for **M1** and **M3** host systems. We note that studies of metallocyclic host structures of this kind have shown that it is possible for a host to adapt its shape to accommodate certain guest molecules;[57,58] however this process is tied to host-guest interactions i.e. the "shape-responsive fitting" will only occur when the guest can effectively take part in strong attractive interactions with the host.[34,59] We postulate that stabilising host-guest interactions could not form between the **M1** and **M3** host systems and the radicals, therefore no inclusion was observed. Furthermore, Dobrzańska *et al.*[57] and others[8,60] have speculated that host molecules may have the ability to cooperate with one another to facilitate the movement of guest molecules through the crystals - fundamental to this supposition is that the host molecules must be able to move. It is possible then that the rigidity of the **ZIF-8** framework is such that the small pore diameter could not be distorted so as to allow passage into the larger internal cavities whereas for the **MIL-53(Al)** material, the well known breathing mechanism may allow for diffusion of the radical into the channels.

UV/Vis transmission spectrometry, PXRD, electron paramagnetic resonance (EPR) spectroscopy and MS were used to characterise and elucidate the properties of the new inclusion complexes and the results of these analyses will be discussed in the following sections.

4.2.2. UV/Vis transmission spectrometry

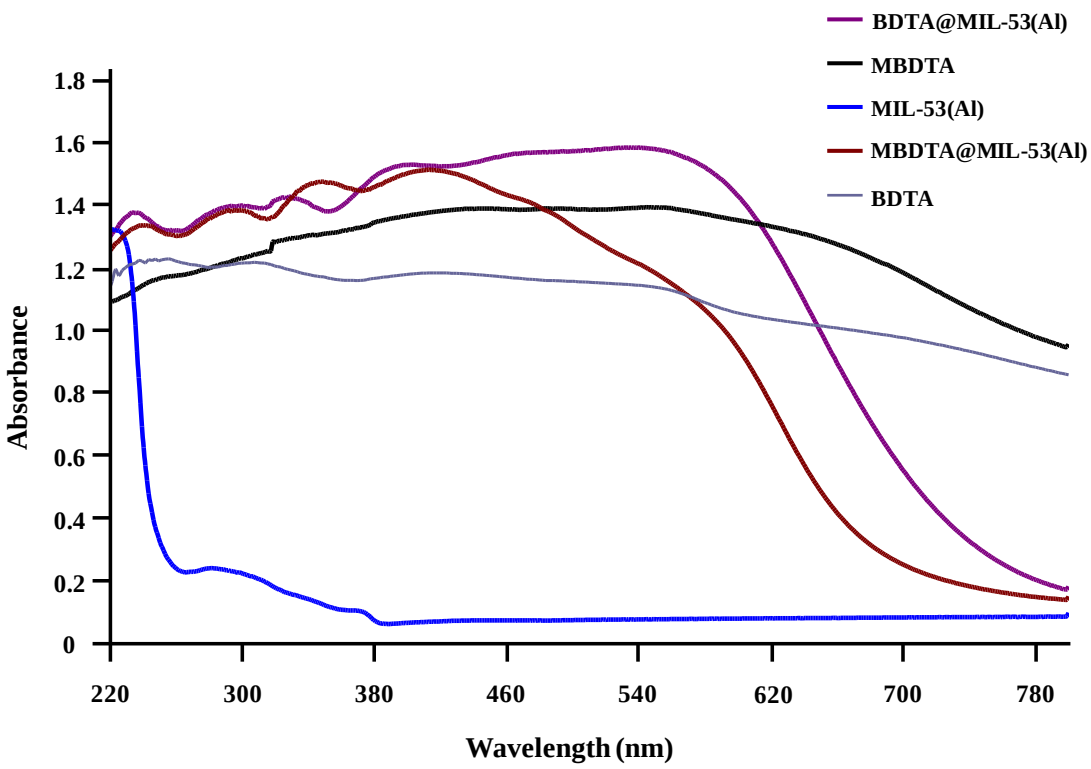

Figure 6. Solid-state UV/vis transmission spectra of the materials produced in this study.

The solid-state UV/Vis transmission spectra of **BDTA@MIL-53(Al)** and **MBDTA@MIL-53(Al)**, shown in **Figure 6**, are notably different from those of the pure **BDTA**, **MBDTA** and MIL-53(Al). samples and from the spectrum of pure **MIL-53(Al)**. This is indicative of an alteration in the packing of the radicals, which is to be expected in the confined environment of the **MIL-53(Al)** pores.[30-32,61-64] Newly sublimed pure **BDTA** and **MBDTA** both show broad peaks across the UV/Vis region, with no discernible fine structure, as would be expected for their general dark colour. The **BDTA@MIL-53(Al)** and **MBDTA@MIL-53(Al)** materials also contain broad bands, but some fine structure becomes apparent within the 200 to 500 nm range (the pure **MIL-53(Al)** material only exhibits a sharp terephthalate-based absorbance peak at approximately 220 nm). The absorbance peaks for **BDTA@MIL-53(Al)** (233, 295, 329 and 399 nm) are slightly blue-shifted in relation to the **MBDTA@MIL-53(Al)** (238, 293, 347 and 411 nm). In addition, **BDTA@MIL-53(Al)** shows greater average absorbance than **MBDTA@MIL-53(Al)**

above 450 nm. These observations are in accordance with the variation in colour between the two materials.

4.2.3. Structure solution by PXRD

It was not possible to grow single crystals of sufficient size for single-crystal diffraction analysis and therefore the structures of the inclusion complexes were solved from powder diffraction data. The advancements in *ab initio* structure solution methods, coupled with the development of user-friendly graphical user interfaces (GUI) have facilitated the process of structure determination from powder diffraction data and have allowed non-expert users to make use of this process almost routinely.[65] However, the collapse of the 3D information available from single-crystal data into the 1D of a powder diffractogram involves the loss of some information; therefore structure determination from powder diffraction data should only be attempted on powder patterns of the highest quality and in cases where the molecular connectivity of the system being studied is known.[66] The solution process is also greatly aided by comparing preliminary structure solutions of the system under investigation with literature structures of similar compounds.

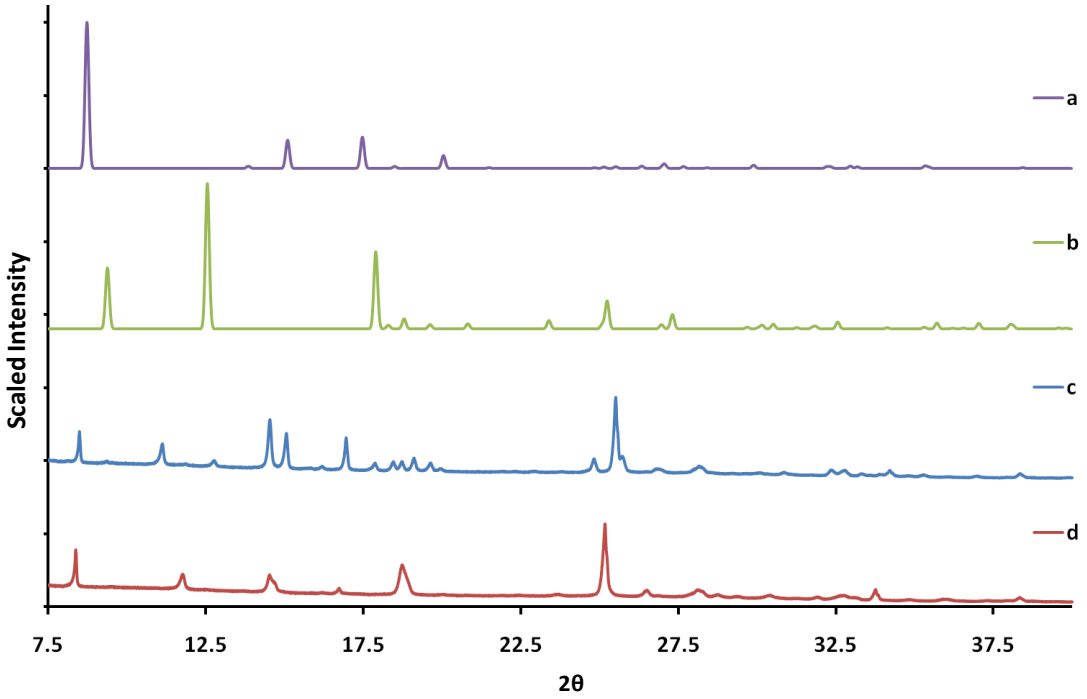

Figure 7. PXRD patterns **(a)** simulated from the single-crystal structure of the empty **MIL-53(Al)** (CCDC ref code: **SABVUN**), **(b)** simulated from the single-crystal structure of the hydrated **MIL-53(Al)** (CCDC ref code: **SABWAU**), **(c)** experimentally determined from **BDTA@MIL-53(Al)** and **(d)** experimentally determined from **MBDTA@MIL-53(Al)**.

Table 1. Unit cell parameters for **MIL-53(Al)**, **BDTA@MIL-53(Al)** and **MBDTA@MIL-53(Al)**.

	MIL-53(Al)	**BDTA@MIL-53(Al)**	**MBDTA@MIL-53(Al)**
space group	*Imma*	$P2_1/n$	$P2_1/n$
a (Å)	6.6085(9)	13.8911(7)	14.954(2)
b (Å)	16.675(3)	15.954(1)	15.089(2)
c (Å)	12.813(2)	6.6018(2)	6.6439(4)
α (°)	90	90	90
β (°)	90	91.699(4)	90.819(6)
γ (°)	90	90	90
V (Å^3)	1141.95	1462.5(1)	1499.0(3)

The PXRD analysis shown in **Figure 7** reveals that both the **BDTA@MIL-53(Al)** and **MBDTA@MIL-53(Al)** materials exhibit clearly distinct powder patterns from that of the empty or hydrated **MIL-53(Al)**,[19] which is indicative of a change in structure. Further information on the structure of these materials was obtained by performing Pawley refinement and simulated annealing on the powder patterns using the program DASH (version 3.2),[65] with final Rietveld refinement performed in Topas Academic.[‡67] This pointed to a change in unit cell dimensions and space group of the **MIL-53(Al)** framework for both inclusion materials, but no change in the chemical connectivity of the host framework (**Table 1**). This is consistent with the observations of Millange *et al.*[29] who stated that the pore dimensions of the MIL-materials are directly correlated to the nature of the guest molecules. The inclusion of the radical within the channels of the host framework results in a symmetry change from *Imma* (the empty phase of **MIL-53(Al)**) to $P2_1/n$ for both **BDTA@MIL-53(Al)** and **MBDTA@MIL-53(Al)**. The dimensions of the rectangular pores (defined by the Al-to-Al distances) coincide with the unit cell parameters and change from 16.675(3) and 12.813(2) Å in **MIL-53(Al)**, to 15.954(1) and 13.8911(7) Å in **BDTA@MIL-53(Al)** and finally to 15.089(2) and 14.954(2) Å in **MBDTA@MIL-53(Al)**, with the framework becoming progressively more square (see **Figure 8**). The third unit cell parameter corresponding to the periodicity of the Al chains remains largely unaffected.

‡ Structure solution and refinement was carried out by Prof J.M Rawson and Dr G.O. Lloyd at the Department of Chemistry at the University of Cambridge; full details of the solution process can be found in Section 4.4.2.

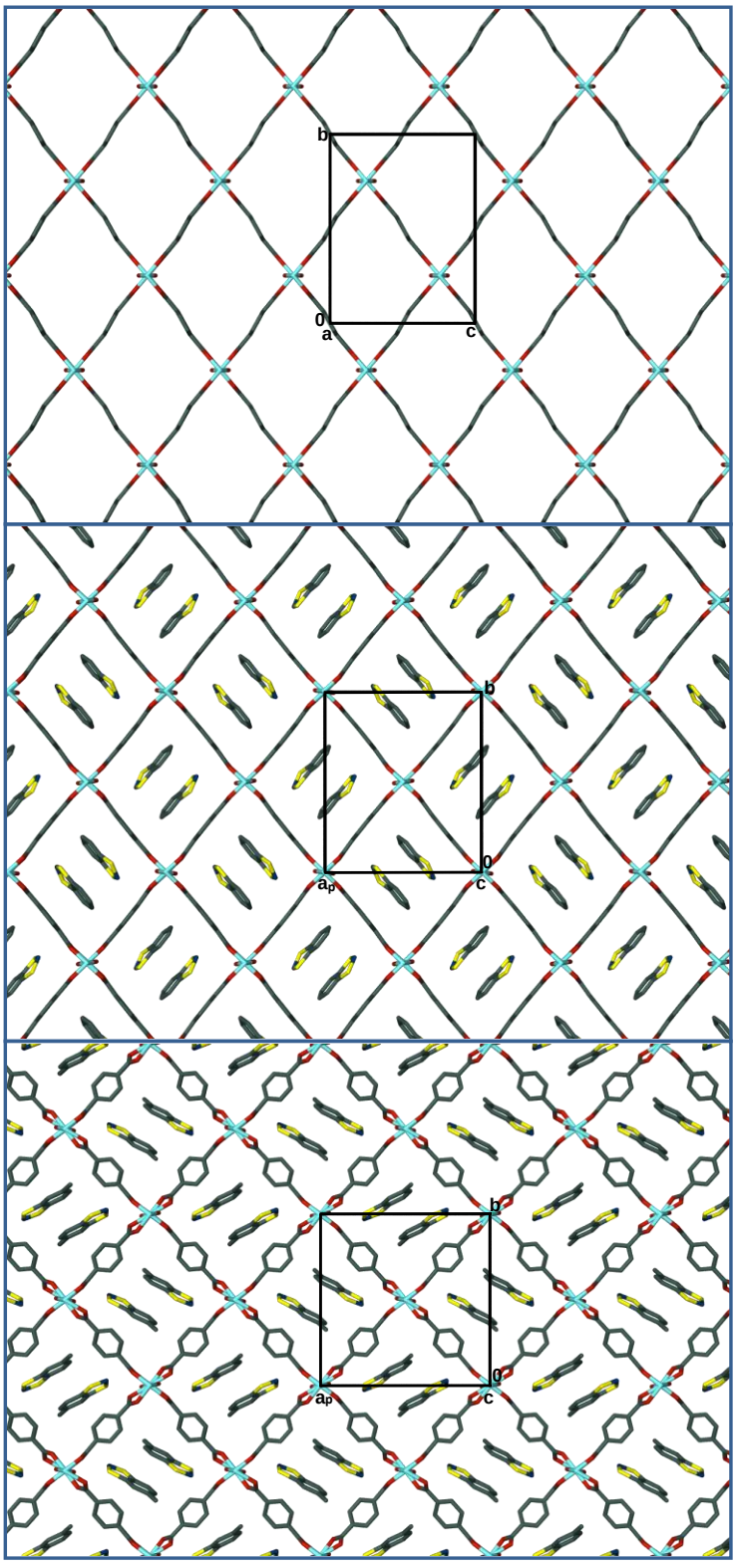

Figure 8. View along the 1D channels in the 3D framework structures of **(top)** the empty **MIL-53(Al)** as viewed down [100], **(middle) BDTA@MIL-53(Al)** viewed down [001] and **(bottom) MBDTA@MIL-53(Al)** viewed down [001]. The structure is initially open with the channels devoid of guest molecules thereby allowing for the diffusion of the radicals into the pore space. This results in a change in the shape of the framework and re-orientation of the phenylene group of the terephthalate, and consequently a change in the unit cell shape.

Owing to the significant contribution to the diffraction pattern by the sulphur-containing radicals, it was possible to extract some information on the packing of the radicals within the pores of **MIL-53(Al)**. The guest radicals in both **BDTA@MIL-53(Al)** and **MBDTA@MIL-53(Al)** appeared well-located at specific sites within the channels that offer a weak hydrogen bond interaction interaction between the nitrogen of the radical guest and the OH group of the host, as well as π–π interactions between the benzo-ring of the radical and a the phenylene ring of the terephthalate units. In addition, the peak intensities could only be accurately reproduced assuming a near full occupancy of the dithiazolyl radical sites (>85%). Both the simulated annealing and Rietveld refinement indicated that there may be some orientational disorder of the radical guests at those sites; however refinements with ordered **BDTA** or **MBDTA** molecules and with a 180° rotational disorder perpendicular to the molecular plane yielded essentially identical profiles. In both inclusion compounds, pairs of radicals are located around an inversion centre but their displacements with respect to the inversion centre lead to rather different structures.

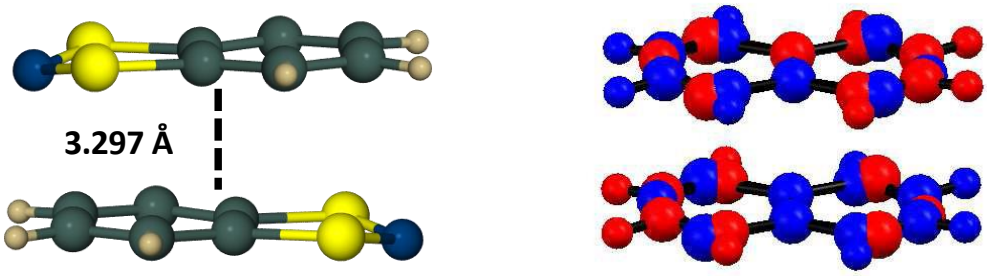

Figure 9. (Left) ordered **BDTA** π*–π* dimer in **BDTA@MIL-53(Al)** with interplanar separation of 3.297 Å and **(right)** disordered **BDTA** with the two components of disorder coloured red and blue.

As can be seen in **Figure 9**, in **BDTA@MIL-53(Al)** the two **BDTA** rings are almost eclipsed and separated by 3.297 Å, very close to the intramolecular distances observed in dimeric π*– π* dithiazolyl dimers (*cf.* 3.249 Å in **BDTA**; CCDC ref code: FAGRIO). Such π*– π* interactions occur *via* short intradimer S···S contacts (3.10 – 3.34 Å), and the location of the **BDTA** molecule with respect to the inversion centre in **BDTA@MIL-53(Al)** can only lead to such a π*– π* dimer formation if the structure adopts a *cis* π*– π* conformation, which is permissible provided the molecule is disordered over two orientations. Whilst the reported dimer in the pure **BDTA** crystal structure adopts a *trans*

conformation, several closely related **BDTA** derivatives adopt *cis* conformations[49,68-71] and the energy difference between them is very small.[§]

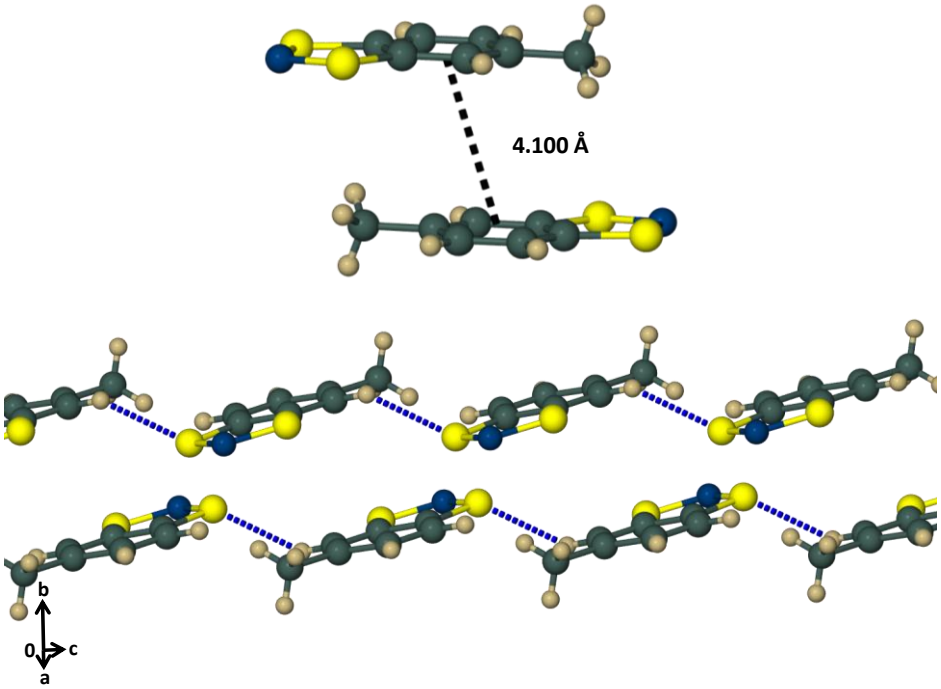

Figure 10. (Top) The distance between the **MBDTA** molecules within the pairs of radicals in **MBDTA@MIL-53(Al)** is too long to be considered π*–π* ($d_{centroid}$-$d_{centroid}$ of aryl rings = 4.100 Å) and **(bottom)** closest contact between radicals is a C–H···S contact (C_{donor}··· $S_{acceptor}$ = 3.442 Å)

In contrast, the **MBDTA** radicals in **MBDTA@MIL-53(Al)** are considerably more offset with respect to the crystallographic inversion centre, and there is no evidence for π*– π* dimerisation in the radical pairs ($d_{centroid}$–$d_{centroid}$ of aryl rings = 4.100 Å). The closest distances between the radicals is defined by a C–H···S contact (C_{donor} ··· $S_{acceptor}$ = 3.442 Å) (**Figure 10**). It is interesting to note that the single crystal structure of the pure **MBDTA** material reveals that the molecules are packed in a regularly spaced π–stack motif,[55] which stands in contrast to the arrangement of the radicals within the **MIL-53(Al)** channels (see **Figure 10**). The adoption of a π*– π* dimer motif in **BDTA@MIL-53(Al)** but not **MBDTA@MIL-53(Al)** is supported by EPR studies (see section 4.2.4).

In the case of **BDTA@MIL-53(Al)**, the **BDTA** interacts with the aromatic rings of the terephthalate through π–π interactions (distance between centroids on aryl rings 3.768 Å). The good fit between the size of the **BDTA** and the length of the terephthalate means

[§] DFT B3LYP/6-31G* indicates that the *cis* conformer is more stable by 14 kJ/mol than the *trans* conformer (see Section 4.4.2.2).

pairs of **BDTA** radicals are included into the pore space. The inclusion of **MBDTA** is similar to that of **BDTA**; however, the additional methyl-substituent on the aromatic ring of the guest molecule results in further distortion of the **MIL-53(Al)** framework and a rotation of the phenylene group of the terephthalate.

4.2.4. Electron paramagnetic resonance spectroscopy

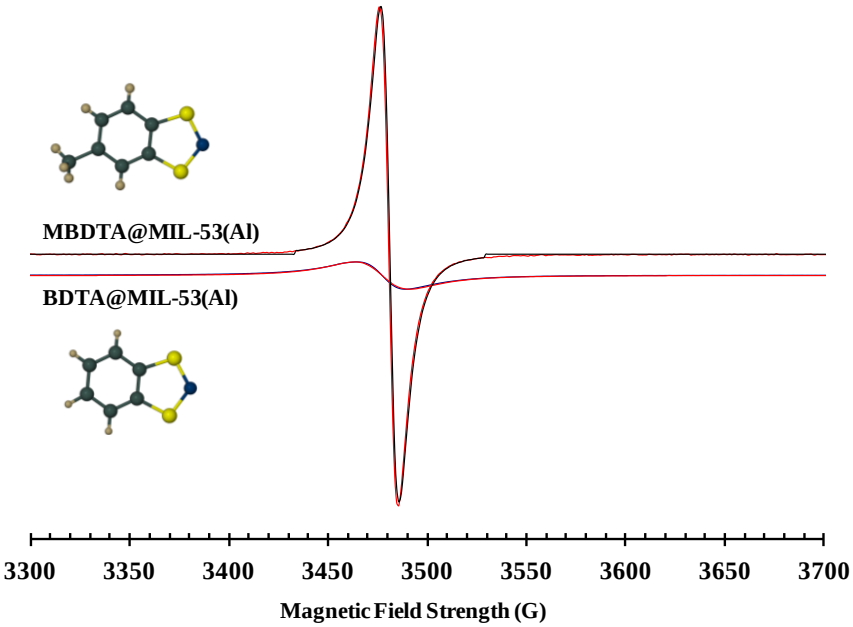

Figure 11. Room temperature EPR spectra of the **BDTA@MIL-53(Al)** material (g = 2.0108, ΔH_{pp} = 23.4 G) and the **MBDTA@MIL-53(Al)** material (g = 2.0095, ΔH_{pp} = 7.8 G) in red with simulated line shapes in black. The **BDTA@MIL-53(Al)** material exhibits a broader and less intense line width than the **MBDTA@MIL-53(Al)** material.

EPR spectroscopy was used to probe the structures of both the new radical-containing inclusion complexes. The room temperature X-band EPR spectra of **BDTA@MIL-53(Al)** and **MBDTA@MIL-53(Al)** reproduced in **Figure 11** both reveal isotropic singlet EPR spectra with g-values comparable to previous solution studies on dithiazolyl radicals.[72,73**] Both spectra exhibit Lorentzian line shapes but reveal significant differences in both intensity and line width; **BDTA@MIL-53(Al)** exhibits a significantly broader (ΔH_{pp} = 23.4 G) but less intense resonance (~5 %) than **MBDTA@MIL-53(Al)** (ΔH_{pp} = 7.8 G). The broader and less intense line width of **BDTA@MIL-53(Al)** is consistent with the structure determined by PXRD; disorder in the orientation of the **BDTA** molecules leads to either head-to-head or head-to-tail arrangements of radicals. When the radicals adopt a

** **MBDTA** in toluene g = 2.0065 and **BDTA** in $CFCl_3$ g = 2.008

head-to-head configuration then this generates a singlet π^*– π^* dimer which is EPR inactive.[46-48,55,72] Conversely head-to-tail association of **BDTA** radicals inhibits dimer formation and will contribute to the EPR spectral intensity. The short intermolecular contacts between radicals (distance between C_2S_2N ring centroids = 4.086 Å) and the resultant dipolar interactions (which vary as r^{-n}) are consistent with the broader nature of the EPR spectra. The steric demand of the additional methyl group in **MBDTA** appears to hinder dimerisation within the channels of **MBDTA@MIL-53(Al)**. The resultant distances between nearest neighbour C_2S_2N ring centroids now fall in the region 5.730 – 6.811 Å. As a consequence, the EPR spectrum is an order of magnitude more intense than the **BDTA**-included complex and the line width is considerably narrower – consistent with reduced dipolar broadening effects associated with the larger intermolecular contacts.[74] Additional studies at 77 K revealed no change in spectral features.

4.2.5. Radical regeneration - an EPR and MS study

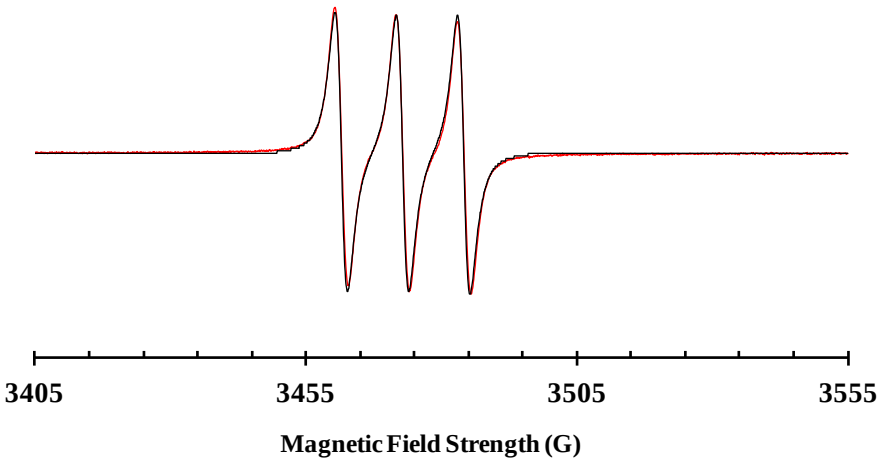

Figure 12. EPR spectrum of the recovered **BDTA** from **BDTA@MIL-53(Al)** after suspension in CH_2Cl_2 in red with the simulated line shape in black. An identical spectrum was recorded for the **MBDTA** recovered from **MBDTA@MIL-53(Al)**.

We noted that samples of the inclusion complexes stored under ambient conditions did not appear to undergo a colour change as would be expected for decomposition of the radicals within the framework channels. We then purposefully exposed the **BDTA@MIL-53(Al)** and **MBDTA@MIL-53(Al)** materials to air under ambient conditions for a period of at least three months in order to assess whether the radical species could be recovered from the pores of the **MIL-53(Al)** framework.

Remarkably, simple addition of CH_2Cl_2 (a solvent that will dissolve the radical but not the MOF) to **BDTA@MIL-53(Al)** or **MBDTA@MIL-53(Al)** produces the isotropic 1:1:1 triplet EPR spectrum in **Figure 12** [g = 2.0102, a_N = 11.3 G, ΔH_{pp} = 2.34 G (Lorentzian)],[††] which is consistent with the regeneration of the radicals from the porous materials and thereby confirms the release of the radical species from the host without degradation.

Additional evidence to support that the air sensitive radicals had been stabilised within the MOF is provided by EI-MS(+). Samples of the inclusion complexes were exposed to CH_2Cl_2 and the solutions were immediately analysed. In both cases the most intense peak observed corresponds to the molecular ion of the respective radical (**Figure 13**).

This enhanced stability of an adsorbed radical species within the pores of a MOF is in stark contrast to the pure radicals that degrade when not kept under an inert atmosphere. These findings are consistent with recent studies already mentioned in section 4.1, which show that it is possible to use a MOF material as a storage vessel for radical species; however, these radicals were generated *in situ* by UV irradiation of the already included guest molecules, and were only shown to be stable for a period of one month.[11]

[††] These spectra match the solution EPR for the as-synthesised **BDTA** and **MBDTA** reported in the literature.[46,55] The 1:1:1 triplets with no hyperfine splitting indicate that most of the spin density is localized on the heterocyclic ring, i.e. there is no spin coupling with the aromatic ring.

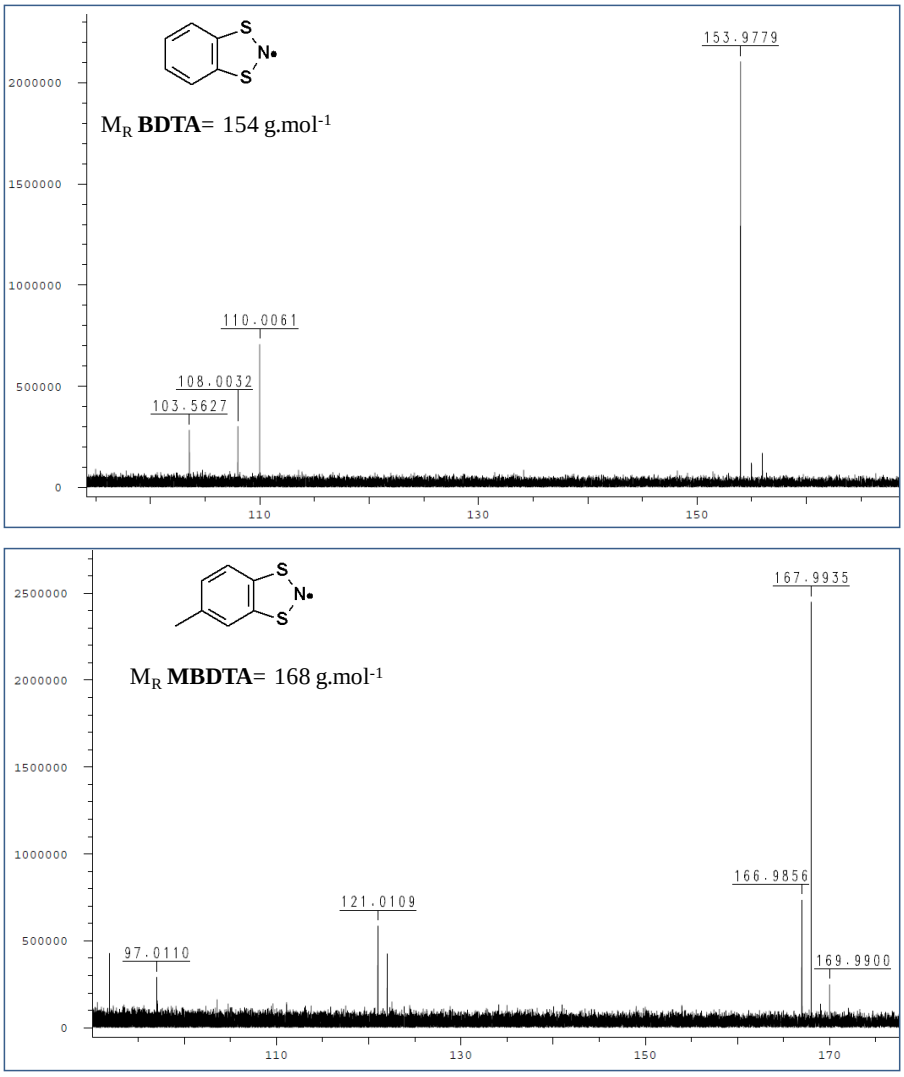

Figure 13. EI-MS(+) spectra of: **(top)** the recovered **BDTA** from **BDTA@MIL-53(Al)** and **(bottom)** the recovered **MBDTA** from **BDTA@MIL-53(Al)** after suspension in CH_2Cl_2.

4.3. CONCLUSION

Organic radicals are a class of materials chiefly studied for their application as magnetic materials, however the successful synthesis of a radical does not infer the formation of a magnetically ordered phase; careful control of the solid state at the molecular level is required to create a network of magnetic interactions that will result in bulk magnetic ordering. Endeavours to control the solid-state structure involve attempts to understand and manipulate intermolecular interactions, a non-trivial task. The confined volume within a porous material provides a platform of controlled space in which reactive radical species may be secluded for study, with the ultimate goal of incorporating magnetic behaviour with another desirable property provided by the host framework. In this chapter it has been

shown that it is possible to incorporate the known dithiazolyl radicals benzo-1,3,2-dithiazolyl (**BDTA**) and 5-methylbenzo-1,3,2-dithiazolyl (**MBDTA**) into the porous MOF material **MIL-53(Al)** *via* the gas phase diffusion of the guest molecules into the host material. We have demonstrated that this inclusion is selective for the **MIL-53(Al)** framework over the range of other potential host materials selected for this study i.e. the permanently porous silver metallocycle material **M1**, the transiently porous copper metallocycle **M3** and the highly stable porous material **ZIF-8**. We speculate that this selectivity arises as a result of a combination of factors, but that the major contributing factor is the ability of the **MIL-53(Al)** material to flexibly 'breathe' in response to certain stimuli, thereby facilitating diffusion of the radical into the pores of the host. The structures of the resulting two inclusion complexes, **BDTA@MIL-53(Al)** and **MBDTA@MIL-53(Al)** were elucidated by PXRD analysis, which revealed a modification of the original solid state structures of both the host and guest. For the host structures the 1D channels become progressively more square so as to optimise host-guest interactions; the two cell parameters affected by this process vary from 16.675(3) and 12.813(2) Å in the empty form to 15.954(1) and 13.8911(7) Å in **BDTA@MIL-53(Al)** and 15.089(2) and 14.954(2) Å in **MBDTA@MIL-53(Al)**. The packing of the guest molecules is also altered within the confined space of the pores; in the case of **BDTA** a disordered model is proposed in which the π*–π* mode of association is changed from *trans* in pristine **BDTA** to *cis* in **BDTA@MIL-53(Al)**, whereas the crystal structure of pure **MBDTA** consist of molecules packed in regularly spaced π–stacks and in **MBDTA@MIL-53(Al)** the radical molecules exist in pairs located around an inversion centre at a distance of *ca* 4.1 Å from each other, thereby negating the possibility of π*–π* dimerisation. The solid state EPR results reported in this chapter support the model provided by PXRD i.e. the broader and less intense resonance of the **BDTA@MIL-53(Al)** spectrum compared to the EPR spectrum obtained for **MBDTA@MIL-53(Al)**, which is an order of magnitude more intense with a considerably narrower line width, is consistent with a disordered π*– π* dimer motif in **BDTA@MIL-53(Al)** but not **MBDTA@MIL-53(Al).**

Furthermore, we have also shown that the radicals are stable within the interior of the **MIL53-Al** framework in air under ambient conditions for a period of more than 3 months and, with the addition of a suitable solvent, the guest molecules can readily be released from the host material. The integrity of the liberated guests was tested by EPR

and MS, which confirm the release of the radical without degradation. This result is remarkable in light of the fact that organic radicals are generally considered to be highly reactive species with short lifetimes, especially when they come into contact with air. In this regard the **MIL-53(Al)** host could be viewed as a radical storage vessel.

Future studies should be aimed at including these radicals into a paramagnetic MOF, such as **MIL-47(V)** or the paramagnetic isostructural analogues of **MIL-53(Al)**, **MIL-53(Cr)/(Fe)**, which are capable of the same breathing mechanism as that of **MIL-53(Al**). We believe that this inclusion process may aid the development of novel functional materials by offering unique possibilities for magnetic communication between the radical guest and the host framework.

4.4. EXPERIMENTAL

4.4.1. Synthesis and Characterisation

4.4.1.1. $[Ag_2$(1,4-bis(2-methylimidazol-1-ylmethyl)-benzene$_2](BF_4)_2$ (M1)

4.4.1.1.1. 1,4-bis(2-methylimidazol-1-ylmethyl)benzene

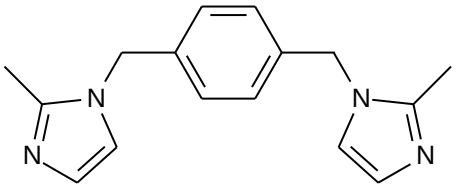

2-Methylimidazole (0.82 g; 10 mmol) and KOH (2.3 g; 40 mmol) were dissolved in DMSO (15 mL) and the solution was stirred for 2 hours at room temperature. α-α′-Dichloro-*p*-xylene (0.88 g; 5.00 mmol) was added and the solution was stirred for a further 3 hours at the room temperature. 15 mL of water was then added to the mixture and the aqueous solution was extracted with $CHCl_3$ (4 × 10 mL). The $CHCl_3$ solution was dried overnight over anhydrous Na_2SO_4. The solution was filtered and the solvent removed *in vacuo*. Excess diethyl ether was added to the residue and the solution was allowed to stand overnight at -10 °C. The resulting white powder was filtered and washed with diethyl ether and air dried.

Yield: 0.920 g, 71.9%.^{1}H-NMR ($CDCl_3$, 400 MHz): δ 2.29 (6H, s, CH_3), 5.00 (4H, s, CH_2), 6.80 (2H, s, H_{im}), 6.92 (2H, s, H_{im}), 7.00 (4H, s, H_{bz}); ^{13}C-NMR ($CDCl_3$, 100 MHz): δ 13.0, 49.3, 119.8, 127.2, 127.4, 136.3, 144.9.

*4.4.1.1.2. [Ag_2(1,4-bis(2-methylimidazol-1-ylmethyl)benzene)$_2$](BF_4)$_2$ (**M1**)*

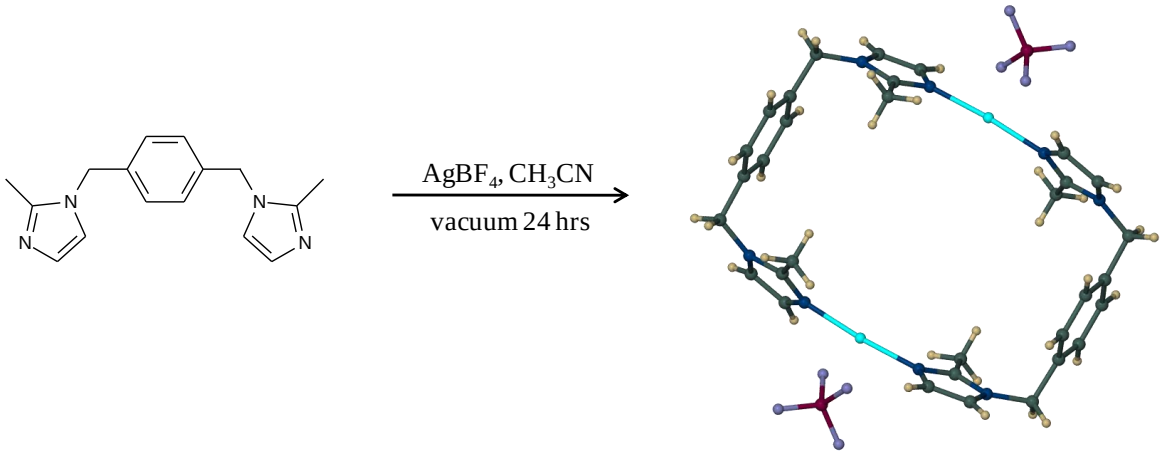

Scheme 2. Formation of $\mathbf{M_A}$ $[Ag_2L'_2](BF_4)_2$, where L′ = 1,4-bis(2-methylimidazol-1-ylmethyl)benzene.

1,4-Bis(2-methylimidazol-1-ylmethyl)benzene (10.7 mg; 0.04 mmol) was dissolved in CH_3CN and added to a solution of $AgBF_4$ (7.81 mg; 0.04 mmol) in CH_3CN. The solution was allowed to slowly evaporate over a period of 5 days to yield crystals suitable for single-crystal diffraction studies. This process was repeated several times to yield 50 mg of single crystals of **M1**·2CH_3CN. The empty structure **M1** was obtained by placing these crystals under vacuum for 24 hours.

4.4.1.2. [Cu_2(1,3-bis(imidazolyl-1-ylmethyl)-2,4,6-trimethyl-benzene)$_2Cl_4$ (M3)

4.4.1.2.1. 1,3-Bis(imidazol-1-ylmethyl)-2,4,6-trimethylbenzene

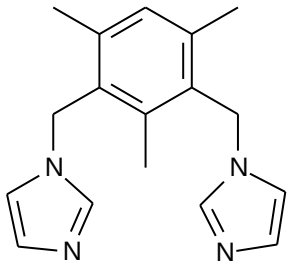

2,4-Bis(chloromethyl)-1,3,5-trimethylbenzene (1.09 g; 5.00 mmol) and imidazole (3.40 g; 50.0 mmol) were dissolved in 200 mL MeOH. The resulting solution was stirred under reflux for 18 hours. The solvent was removed *in vacuo* to yield a yellow oil. K_2CO_3 (6.91 g; 50 mmol) in 100 mL of water was added to the oil and the solution was stirred until the product precipitated. The white solid was then filtered, washed with 100 mL of water and left to air dry.

Yield: 0.876 g, 62.6%.^{1}H-NMR ($CDCl_3$, 400 MHz): δ 2.17 (6H, s, CH_3), 2.30 (3H, s, CH_3), 5.14 (4H, s, CH_2), 6.73 (2H, s, H_{im}), 7.01 (2H, s, H_{im}), 7.03 (1H, s, H_{bz}), 7.30 (2H, s,

H_{im}); ^{13}C-NMR ($CDCl_3$, 100 MHz): δ 15.3, 19.9, 45.3, 118.5, 129.5, 129.9, 131.4, 136.5, 137.8, 138.6.

*4.4.1.2.2. Cu_2(1,3-bis(imidazol-1-ylmethyl)-2,4,6-trimethylbenzene)$_2Cl_4$ (**M3**)*

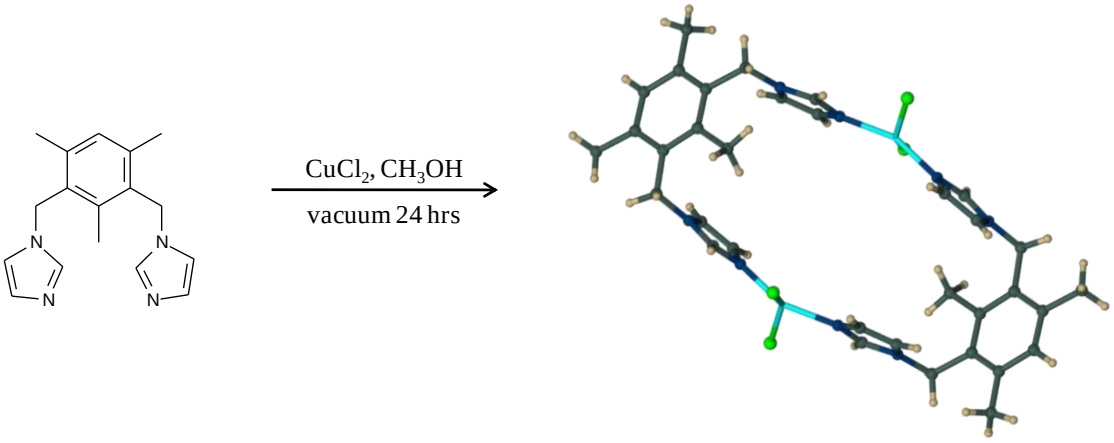

Scheme 3. Formation of $\mathbf{M_B}$ $[Cu_2L''_2Cl_4]$, where L″ = 1,3-bis(imidazol-1-ylmethyl)-2,4,6-trimethylbenzene

1,3-Bis(imidazol-1-ylmethyl)-2,4,6-trimethylbenzene (10.7 mg; 0.04 mmol) was dissolved in CH_3OH and added to a solution of $CuCl_2$ (7.81 mg; 0.04 mmol) in CH_3OH. The solution was allowed to slowly evaporate over a period of 5 days to yield crystals suitable for single-crystal diffraction studies. This process was repeated several times to yield 50 mg of single crystals of **M3**·CH_3OH·H_2O. The empty structure **M3** was obtained by placing these crystals under vacuum for 24 hours.

4.4.1.3. Zeolitic imidazolate framework (ZIF-8)

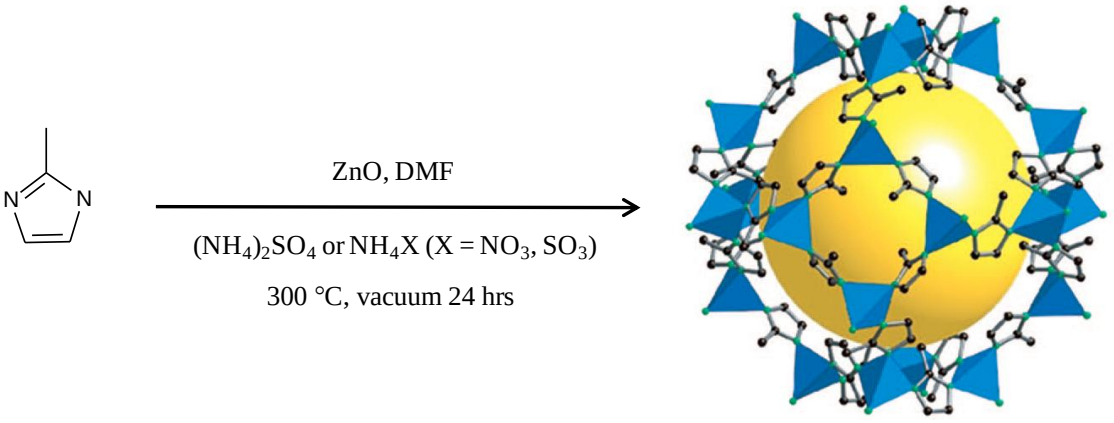

Scheme 4. Synthesis of **ZIF-8** by the mechanochemical method of ILAG.[22]

ZIF-8 was synthesised by the mechanochemical method of ion- and liquid- assisted grinding. ZnO and 2-methylimidazole, DMF and 10 mg of $(NH_4)_2SO_4$ or NH_4X (X = NO_3, SO_3) were loaded into a 10 mL stainless steel jar along with two 7 mm diameter stainless steel balls. The mixture was ground for approximately 30 mins in a Retsch MM200 mill at 30 Hz to yield **ZIF-8** in quantitative amounts. The phase purity of the sample was confirmed by comparison of its PXRD pattern with the one simulated for the known **ZIF-8** structure (CCDC ref code: VELVOY). The **ZIF-8** material in this study was synthesised by Tomislav Friščić at the University of Cambridge and was activated by immersing the sample in methanol at room temperature for 48 hours. The evacuated form was then obtained by heating the sample to 300 °C for 24 hours under a dynamic vacuum.

4.4.1.4. MIL-53(Al)

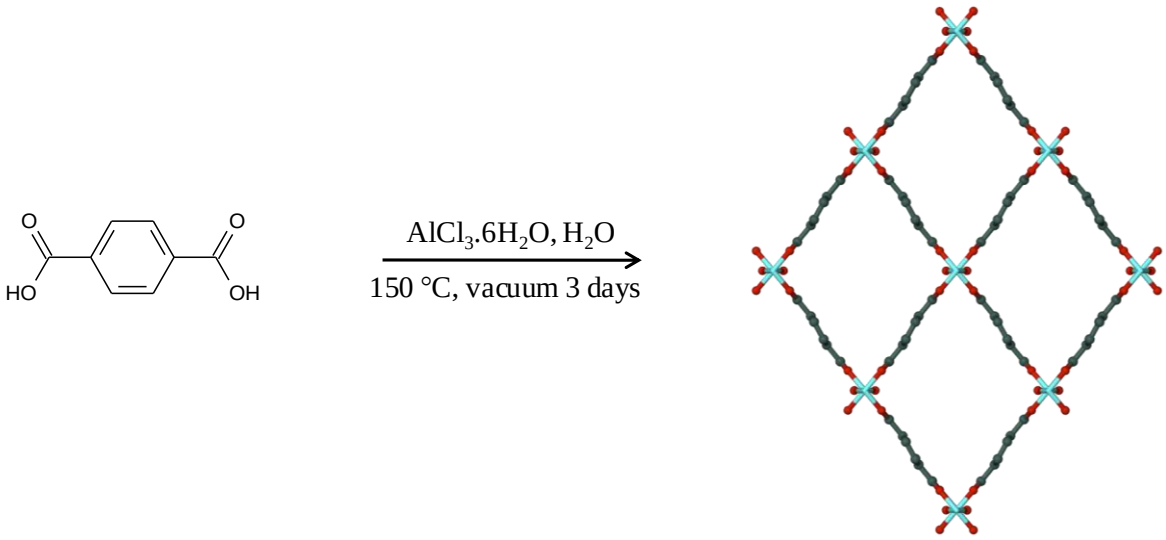

Scheme 5. Synthesis of **MIL-53(Al)** under solvothermal conditions.

MIL-53(Al) was synthesised under solvothermal conditions by reacting $AlCl_3.6H_2O$ (500 mg, 1.33 mmol) with terephthalic acid (400 mg, 2.41 mmol) in deionised water (5 mL). The reaction was carried out in a 27 mL Teflon-lined stainless steel Parr bomb apparatus under autogenous pressure for 5 hours at 150 °C. This yielded a white crystalline precipitate containing both terephthalic and **terephthalic@MIL-53(Al)** acid. The precipitate was washed with deionised water (3 × 5 mL) and DMF (3 × 5 mL), and then heated in DMF (10 mL) in a 27 mL Teflon-lined stainless steel Parr bomb apparatus overnight at 150 °C to afford **MIL-53(Al)·DMF**. This precipitate was washed with DMF (3 × 3 mL) and then activated by heating at 150 °C under vacuum for 3 days.

4.4.1.5. Benzo-1,3,2-dithiazolyl (BDTA)

4.4.1.5.1. Benzo-1,3,2-dithiazolylium chloride ([BDTA]Cl)

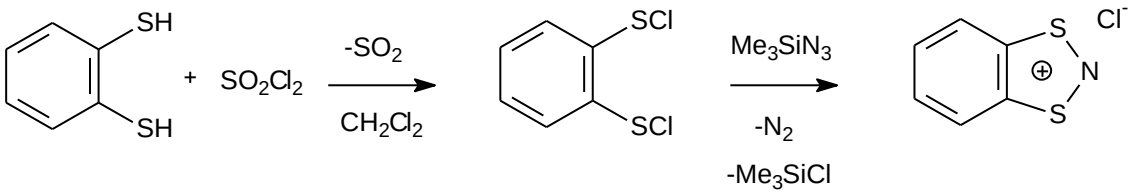

Scheme 6. Synthesis of benzo-1,3,2-dithiazolylium chloride.

A solution of 1,2-dimercaptobenzene (0.250 g, 0.200 mL, 1.80 mmol) in CH_2Cl_2 (10 mL) was added dropwise to a stirring solution of sulphuryl chloride (0.48 g, 0.28 mL, 3.6 mmol) in CH_2Cl_2 (5 mL). The orange solution was refluxed for 2 hours to ensure a complete reaction then the solvent was removed *in vacuo* to yield an orange oil. This oil was re-dissolved in CH_2Cl_2 (10 mL) and added dropwise to a solution of trimethylsilylazide (0.201 g, 0.220 mL, 1.80 mmol) in CH_2Cl_2 (6 mL) at 0 °C. CH_2Cl_2 (10 mL) was then added to the resulting yellow precipitate and the mixture was stirred for 1 hour at room temperature, filtered, and the yellow solid was washed with CH_2Cl_2, (2 × 5 mL) then dried *in vacuo*.

Yield: 0.212 g, 62.2%. Found: C, 38.92; H, 2.00; N, 6.85; required for $C_6H_4NS_2Cl$ C, 39.02; H, 2.13; N, 7.41.

4.4.1.5.2. Benzo-1,3,2-dithiazolyl (BDTA)

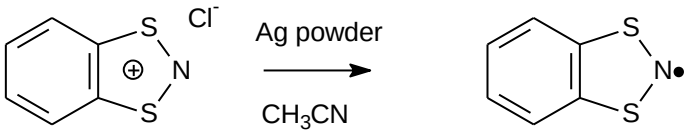

Scheme 7. Synthesis of benzo-1,3,2-dithiazolyl.

Benzo-1,3,2-dithiazolylium chloride (0.200 g, 1.00 mmol) and silver powder (0.134 g, 1.25 mmol) were stirred together in CH_3CN (25 mL) overnight. The red solution was

filtered and the solvent removed *in vacuo* to give a black solid. Sublimation (60–65 °C/10^{-3} Torr) afforded black rhombs of BDTA.

Yield: 0.065 g, 42.2%. Found: C, 46.47; H, 2.46 and N, 9.06; required for $C_6H_4NS_2$: C, 46.7; H, 2.6 and N, 9.09. MS (EI^+): m/z 154 (100%, $([M+H]^+$)

4.4.1.6. 5-Methylbenzo-1,3,2-dithiazolyl (MBDTA)

4.4.1.6.1. 5-Methylbenzo-1,3,2-dithiazolylium chloride ([MBDTA]Cl)

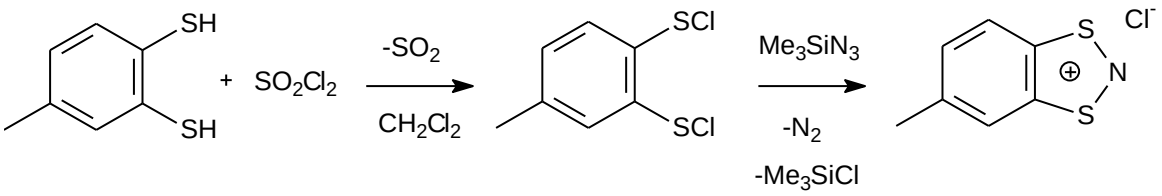

Scheme 8. Synthesis of 5-methylbenzo-1,3,2-dithiazolylium chloride.

A solution of 3,4-dimercaptotoluene (0.500 g, 3.20 mmol) in CH_2Cl_2 (10 mL) was added dropwise to a stirring solution of sulphuryl chloride (1.73 g, 1.0 mL, 128 mmol) in CH_2Cl_2 (5 mL). The orange solution was refluxed for 2 hours to ensure a complete reaction then the solvent was removed *in vacuo* to yield an orange oil. This oil was re-dissolved in CH_2Cl_2 (10 mL) and added dropwise to a solution of trimethylsilylazide (0.403 g, 0.45 mL, 3.50 mmol) in CH_2Cl_2 (6 mL) at 0 °C. CH_2Cl_2 (10 mL) was then added to the resulting yellow precipitate and the mixture was stirred for 1 hour at room temperature, filtered, and the yellow solid was washed with CH_2Cl_2, (2 × 5 mL) then dried *in vacuo*.

Yield: 0.447 g, 68.5%. Found: C, 41.14; H, 3.33 and N, 4.75; required $C_7H_6NS_2Cl$: C, 41.26; H, 2.94; N, 6.88.

4.4.1.6.2. 5-Methylbenzo-1,3,2-dithiazolyl (MBDTA)

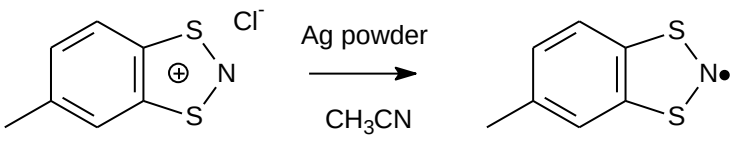

Scheme 9. Synthesis of 5-methylbenzo-1,3,2-dithiazolyl.

5-Methylbenzo-1,3,2-dithiazolylium chloride (0.380 g, 1.90 mmol) and silver powder (0.266 g, 2.50 mmol) were stirred together in CH_3CN (25 mL) overnight. The red solution

was filtered and the solvent removed *in vacuo* to give a black solid. Sublimation (50–55 °C/10^{-3} Torr) afforded black rhombs of MBDTA.

Yield: 0.120 g, 37.5%. Found: C, 48.26; H, 3.57 and N, 5.91; required for $C_7H_6NS_2Cl$: C, 50.0; H, 3.6; N, 8.3. MS (EI^+): m/z 167 (100%, ($[M+H]^+$). The disparity in the required microanalytical data and the data obtained was consistent over several analyses, indicating the present of an impurity. However, as EI-MS($^+$) and PXRD analysis (**Figure 14**) clearly identify **MBDTA** as the major product no further purification was attempted.

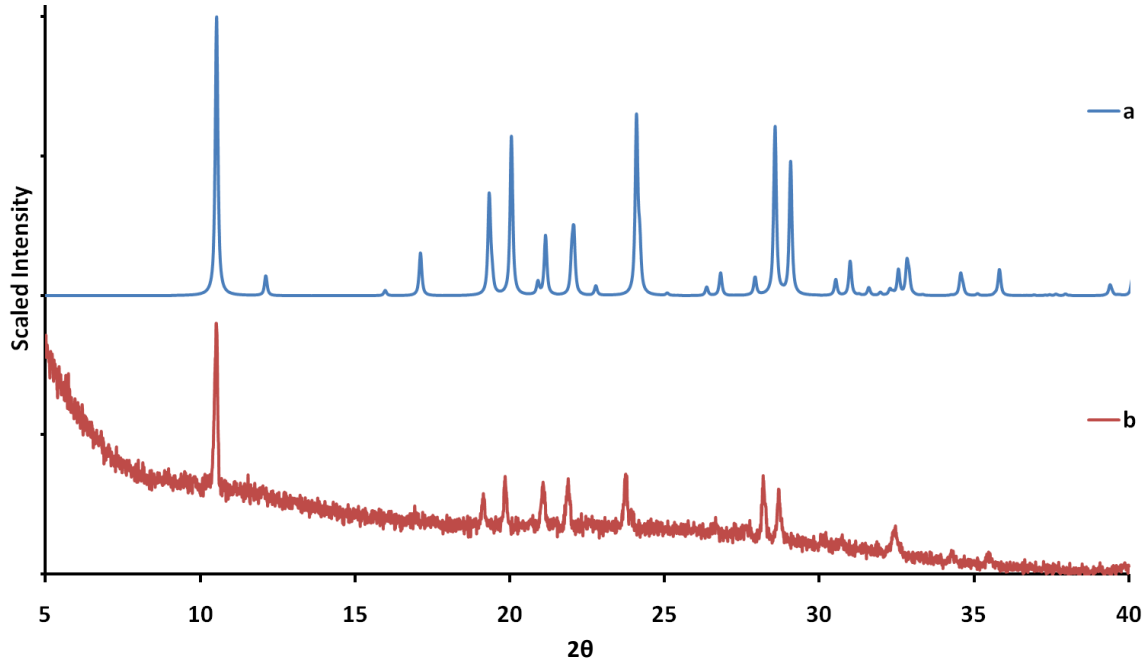

Figure 14. PXRD pattern **(a)** simulated from the single-crystal structure of pure **MBDTA** (CCDC ref code: **WOWCAM**) and **(b)** experimentally determined from a sample of freshly sublimed **MBDTA**.

4.4.2. Structure solution of BDTA@MIL-53(Al)‡‡

The PXRD pattern for **BDTA@MIL-53(Al)** was indexed with DICVOL[75-77] within the DASH software[65] using the 12 most intense peaks (2θ < 20°). This yielded a series of possible monoclinic cells with high figures of merit (**Table 2**) all of which exhibited a *c*-axis of *ca*. 6.6 Å, comparable with the shortest cell dimension in each of the three previously reported settings for **MIL-53(Al)** derivatives.[12,19,27] Of the three cells with the highest figure of merit [M(12) = 18.2 F(12) = 33.6], the structure with the smallest distortion from orthorhombic was selected (β = 91.72(8)°). Subsequent space group

‡‡ Structure solution and refinement was carried out by Prof J.M Rawson and Dr G.O. Lloyd at the Department of Chemistry at the University of Cambridge.

identification based on systematic absences in the powder pattern revealed $P2_1/n$ as the most probable setting and all subsequent structure solution and refinement was carried out in this setting. This exhibited a good fit to the diffraction profile (χ^2 = 5.35), although a number of low intensity features, which were observed in the difference profile, were not indexed by this $P2_1/n$ cell. Notably these could not be assigned to previously reported MIL phases or BDTA itself. It is possible that they correspond to a crystallographic super-cell or may be attributed to a small concentration of another phase. The structure of **BDTA@MIL-53(Al)** was solved in DASH using a simulated annealing technique.[65] Two independent Z-matrices were employed that were constructed from previous crystallographic data; one representing the core inorganic framework (CCDC ref code: SABVOH01) and the other the **BDTA** host (CCDC ref code: FAGRIO). Preliminary unconstrained solutions revealed that the Al centre lay on an inversion centre. Indeed a study of the previously reported structures of **MIL-53** host-guest complexes revealed a common 6.6 Å crystallographic axis which, in all cases which corresponds to the periodicity of the Al-O-Al framework with the Al located at the origin.[19] A second simulated annealing was subsequently undertaken constraining one Al centre to the origin (0,0,0) and the second to the special position (0,0,$^1/_2$) and with the Al···Al vector constrained to lie parallel to the *c*-axis. This offered a good fit to the PXRD pattern. Simulated annealing with a range of site occupancies for the **BDTA** guest revealed a best fit (χ^2 = 24.12) to the diffraction profile with **BDTA** assigned to full occupancy with a preferred orientation axis (-3 3 0). Significant deterioration in the fit to the PXRD pattern was noted with **BDTA** site occupancies less than 80%. The structure and diffraction profile is shown below in **Figure 15**.

Table 2. Possible monoclinic cell settings for **BDTA@MIL-53(Al)**. Highlighted cells offer the best figures of merit and the solution marked with an asterisk was implemented in the subsequent structure solution.

a	b	c	β	M(12)	F(12)
13.889(11)	15.924(15)	6.602(6)	91.72(8)	18.2	33.6*
15.923(20)	13.888(15)	6.498(7)	92.20(12)	13.8	27.5
15.199(12)	15.924(15)	6.602(6)	114.02(7)	18.2	33.6
16.947(28)	13.890(15)	6.500(7)	110.34(12)	12.8	25.1
17.427(23)	13.888(15)	6.498(7)	114.08(11)	13.8	27.5
16.965(22)	13.888(15)	6.498(7)	110.31(11)	13.8	27.5
15.556(13)	15.924(15)	6.602(6)	116.82(7)	18.2	33.6

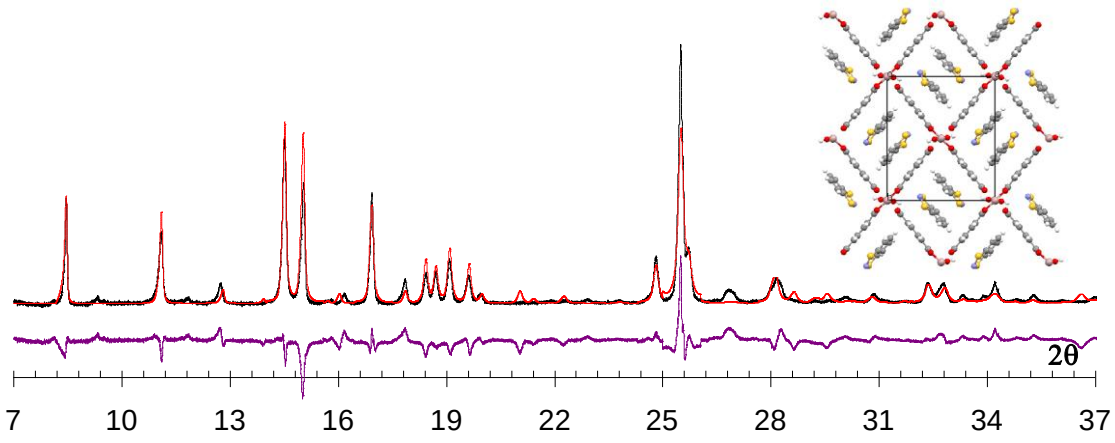

Figure 15. The best fit for the simulated annealing for **BDTA@MIL-53(Al)**. The black trace represents the experimental pattern, the red trace the calculated pattern and the purple trace represents the difference pattern.

An examination of this solution revealed a 'conventional' MIL framework with the **BDTA** guest adopting an eclipsed π-π dimer motif located around an inversion centre with an inter-plane separation of 3.305 Å, but which avoided both the 'conventional' cis-oid and trans-oid π*-π* interactions with close intermolecular S···S contacts (~3.0–3.2 Å) observed for some other thiazyl radicals. This suggested the presence of some disorder of the guest in the cavity. Further simulated annealing solutions were undertaken with two half-occupancy **BDTA** guests. This offered marginally improved fit (χ^2 = 23.25) and which might best be considered as a cis-oid π*–π* dimer (S···S distance = 3.4 Å), disordered around an inversion centre (**Figure 9**). Owing to the negligible improvement in

fit, the simple ordered model was used in the subsequent Rietveld refinement, but we acknowledge that disorder equivalent to a 180° rotation perpendicular to the molecular plane is most likely present. Rietveld refinement was carried out using the program Topas Academic[67] with fixed atomic coordinates to afford an R_{wp} factor of 9.69%. The final fit between the simulated and experimental powder patterns are given in **Figure 16** below.

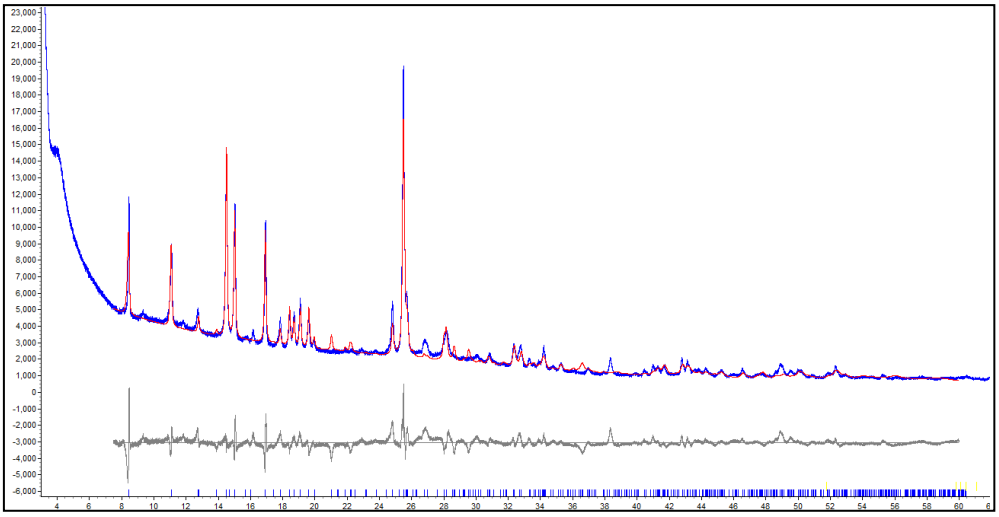

Figure 16. The fit of the PXRD pattern of **BDTA@MIL-53(Al)** after Rietveld refinement. The black trace represents the experimental pattern, the red trace the calculated pattern and the blue trace represents the difference pattern.

4.4.2.1. Structure solution of MBDTA@MIL-53(Al)

A similar approach was applied to solve the structure of **MBDTA@MIL-53(Al)** from its corresponding powder pattern. Cell indexing afforded similar cell settings to that of **BDTA@MIL-53(Al)** with the best two fitting results shown in **Table 3**. Simulated annealing with a range of site occupancies for the **MBDTA** guest revealed a best fit (χ^2 = 34.50) to the diffraction profile with full occupancy and with a preferred orientation axis of (3 3 0). The diffraction profiles are shown below in **Figure 17**. Rietveld refinement with fixed atomic coordinates yielded an R_{wp} factor of 11.1%; the fit is given below in **Figure 18**.

Table 3. Possible monoclinic cell settings for **BDTA@MIL-53(Al)**. Highlighted cells offer the best figures of merit and the solution marked with the asterisk was implemented in the subsequent structure solution.

a	b	c	β	M(12)	F(12)
13.889(11)	15.924(15)	6.602(6)	91.72(8)	18.2	33.6
14.954(15)	15.089(15)	6.643(4)	90.819(6)	12.5	14.6*

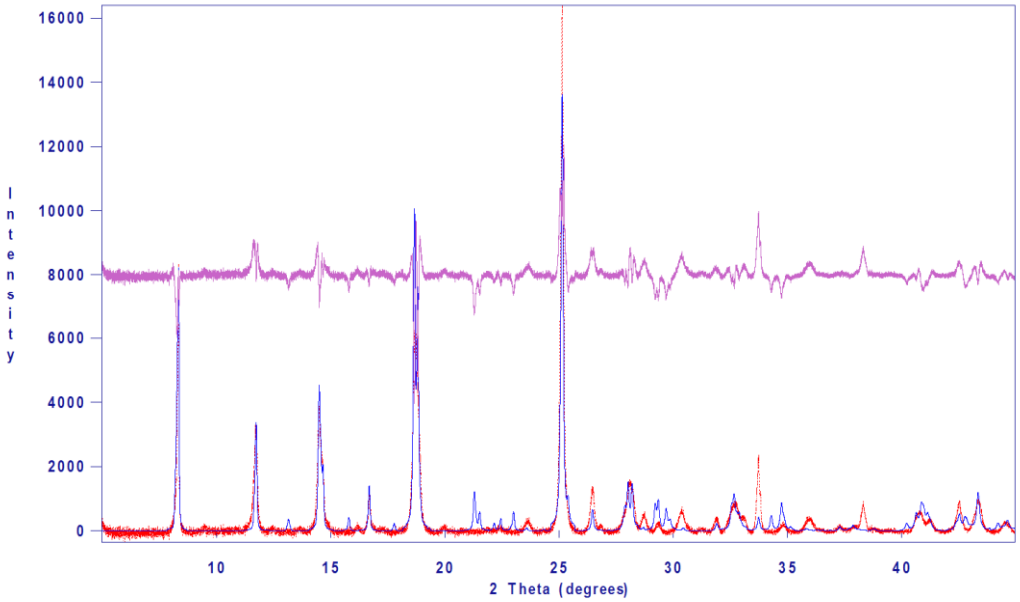

Figure 17. The best fit for the simulated annealing for **MBDTA@MIL-53(Al)**. The black trace represents the experimental pattern, the red trace the calculated pattern and the purple trace represents the difference pattern.

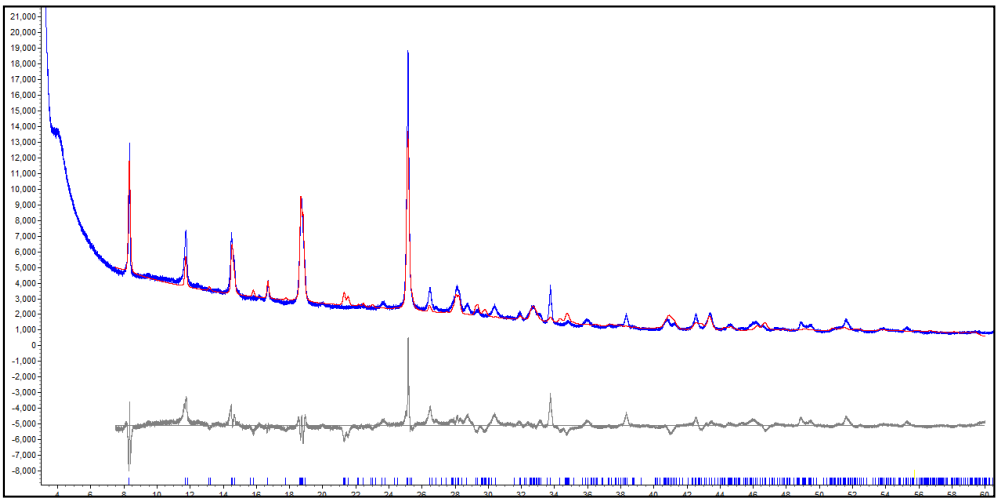

Figure 18. The fit of the PXRD pattern of **MBDTA@MIL-53(Al)** after Rietveld refinement. The black trace represents the experimental pattern, the red trace the calculated pattern and the purple trace represents the difference pattern.

4.4.2.2. DFT calculations

Full gas phase geometry-optimisations of *cis* and *trans* isomers of $(BDTA)_2$ were undertaken by J.M. Rawson using Jaguar[78] to estimate the energy difference between these models of π*– π* dimerisation. The B3LYP functional and 6-31G*+ basis set were employed and a closed shell singlet ground state configuration was assumed.

REFERENCES

(1) C. N. R. Rao; A. K. Cheetham; A. Thirumurugan, *J. Phys-Condens. Mat.*, **2008**, *20*, 1.

(2) A. V. Chubukov; D. V. Efremov; I. Eremin, *Phys. Rev. B*, **2008**, *78*, 134512.

(3) M. D. Ward, *Chem. Soc. Rev.*, **1995**, *24*, 121.

(4) C. Train; L. Norel; M. Baumgarten, *Coord. Chem. Rev.*, **2009**, *253*, 2342.

(5) A. R. Ruiz-Salvador; L. M. Rodriguez-Albelo; A. Sampieri; D. W. Lewis; A. Gomez; B. Nohra; P. Mialane; J. Marrot; F. Secheresse; C. Mellot-Draznieks; R. N. Biboum; B. Keita; L. Nadjo; A. Dolbecq, *J. Am. Chem. Soc.*, **2009**, *131*, 16078.

(6) D. Maspoch; D. Ruiz-Molina; J. Veciana, *Chem. Soc. Rev.*, **2007**, *36*, 770.

(7) F. Millange; N. Guillou; M. E. Medina; G. Ferey; A. Carlin-Sinclair; K. M. Golden; R. I. Walton, *Chem. Mater.*, **2010**, *22*, 4237.

(8) S. Kitagawa; K. Uemura, *Chem. Soc. Rev.*, **2005**, *34*, 109.

(9) S. Bourrelly; B. Moulin; A. Rivera; G. Maurin; S. Devautour-Vino; C. Serre; T. Devic; P. Horcajada; A. Vimont; G. Clet; M. Daturi; J. C. Lavalley; S. Loera-Serna; R. Denoyel; P. L. Llewellyn; G. Ferey, *J. Am. Chem. Soc.*, **2010**, *132*, 9488.

(10) L. Hamon; P. L. Llewellyn; T. Devic; A. Ghoufi; G. Clet; V. Guillerm; G. D. Pirngruber; G. Maurin; C. Serre; G. Driver; W. van Beek; E. Jolimaitre; A. Vimont; M. Daturi; G. Ferey, *J. Am. Chem. Soc.*, **2009**, *131*, 17490.

(11) Q. K. Liu; J. P. Ma; Y. B. Dong, *J. Am. Chem. Soc.*, **2010**, *132*, 7005.

(12) M. Maes; F. Vermoortele; L. Alaerts; S. Couck; C. E. A. Kirschhock; J. F. M. Denayer; D. E. De Vos, *J. Am. Chem. Soc.*, **2010**, *132*, 15277.

(13) S. L. James, *Chem. Soc. Rev.*, **2003**, *32*, 276.

(14) J. T. Hupp; G. Lu, *J. Am. Chem. Soc.*, **2010**, *132*, 7832.

(15) H. G. Zheng; Z. Z. Lu; R. Zhang; Y. Z. Li; Z. J. Guo, *J. Am. Chem. Soc.*, **2011**, *133*, 4172.

(16) L. Dobrańska; G. O. Lloyd; H. G. Raubenheimer; L. J. Barbour, *J. Am. Chem. Soc.*, **2005**, *127*, 13134.

(17) L. Dobrzańska; G. O. Lloyd; H. G. Raubenheimer; L. J. Barbour, *J. Am. Chem. Soc.*, **2006**, *128*, 698.

(18) O. M. Yaghi; K. S. Park; Z. Ni; A. P. Cote; J. Y. Choi; R. D. Huang; F. J. Uribe-Romo; H. K. Chae; M. O'Keeffe, *Proc. Natl. Acad. Sci. USA*, **2006**, *103*, 10186.

(19) T. Loiseau; C. Serre; C. Huguenard; G. Fink; F. Taulelle; M. Henry; T. Bataille; G. Ferey, *Chem.-Eur. J.*, **2004**, *10*, 1373.

(20) B. Moulton; M. J. Zaworotko, *Chem. Rev.*, **2001**, *101*, 1629.

(21) L. Carlucci; G. Ciani; D. M. Proserpio, in *Making Crystals by Design. Methods, Techniques and Applications*; D. Braga, F. Grepioni, Eds.; Wiley: New York, **2007**, p 58.

(22) R. Banerjee; A. Phan; B. Wang; C. Knobler; H. Furukawa; M. O'Keeffe; O. M. Yaghi, *Science*, **2008**, *319*, 939.

(23) A. K. Cheetham; J. C. Tan; T. D. Bennett, *Proc. Natl. Acad. Sci. USA*, **2010**, *107*, 9938.

(24) G. T. Kokotailo; S. L. Lawton; D. H. Olson; D. H. Olson; W. M. Meier, *Nature*, **1978**, *272*, 437.

(25) T. Friscic; P. J. Beldon; L. Fabian; R. S. Stein; A. Thirumurugan; A. K. Cheetham, *Angew. Chem. Int. Ed.*, **2010**, *49*, 9640.

(26) A. N. Neimark, A. V.; F. X. Coudert; C. Triguero; A. Boutin; A. H. Fuchs; I. Beurroies; R. Denoyel, *Langmuir*, **2011**, *27*, 4734.

(27) B. Slater; A. M. Walker; B. Civalleri; C. Mellot-Draznieks; F. Cora; C. M. Zicovich-Wilson; G. Roman-Perez; J. M. Soler; J. D. Gale, *Angew. Chem. Int. Ed.*, **2010**, *49*, 7501.

(28) G. Ferey; M. Latroche; C. Serre; F. Millange; T. Loiseau; A. Percheron-Guegan, *Chem. Commun.*, **2003**, 2976.

(29) F. Millange; C. Serre; N. Guillou; G. Ferey; R. I. Walton, *Angew. Chem. Int. Ed.*, **2008**, *47*, 4100.

(30) M. Meilikhov; K. Yusenko; R. A. Fischer, *Dalton Trans.*, **2009**, 600.

(31) M. Meilikhov; K. Yusenko; R. A. Fischer, *J. Am. Chem. Soc.*, **2009**, *131*, 9644.

(32) M. Meilikhov; K. Yusenko; A. Torrisi; B. Jee; C. Mellot-Draznieks; A. Poppl; R. A. Fischer, *Angew. Chem. Int. Ed.*, **2010**, *49*, 6212.

(33) M. Meilikhov; K. Yusenko; R. A. Fischer, *Dalton Trans.*, **2010**, 10990.

(34) E. J. Cussen; J. B. Claridge; M. J. Rosseinsky; C. J. Kepert, *J. Am. Chem. Soc.*, **2002**, *124*, 9574.

(35) M. A. Springuel-Huet; A. Nossov; Z. Adem; F. Guenneau; C. Volkringer; T. Loiseau; G. Ferey; A. Gedeon, *J. Am. Chem. Soc.*, **2010**, *132*, 11599.

(36) M. Vougo-Zanda; J. Huang; E. Anokhina; X. Q. Wang; A. J. Jacobson, *Inorg. Chem.*, **2008**, *47*, 11535.

(37) T. R. Whitfield; X. Q. Wang; L. M. Liu; A. J. Jacobson, *Solid. State. Sci.*, **2005**, *7*, 1096.

(38) T. K. Trung; P. Trens; N. Tanchoux; S. Bourrelly; P. L. Llewellyn; S. Loera-Serna; C. Serre; T. Loiseau; F. Fajula; G. Ferey, *J. Am. Chem. Soc.*, **2008**, *130*, 16926.

(39) G. Ferey; C. Serre, *Chem. Soc. Rev.*, **2009**, *38*, 1380.

(40) C. Lieder; S. Opelt; M. Dyballa; H. Henning; E. Klemm; M. Hunger, *J. Phys. Chem. C*, **2010**, *114*, 16596.

(41) A. Alberola; J. M. Rawson; A. Whalley, *J. Mater. Chem.*, **2006**, *16*, 2560.

(42) J. M. Rawson; G. D. McManus, *Coord. Chem. Rev.*, **1999**, *189*, 135.

(43) R. C. Haddon, *Nature*, **1975**, *256*, 394.

(44) D. Maspoch; D. Ruiz-Molina; K. Wurst; N. Domingo; M. Cavallini; F. Biscarini; J. Tejada; C. Rovira; J. Veciana, *Nat. Mater.*, **2003**, *2*, 190.

(45) S. Blundell, *Magnetism in Condensed Matter*; Oxford University Press: London, **2003**.

(46) G. Wolmershauser; M. Schnauber; T. Wilhelm, *J. Chem. Soc., Chem. Commun.*, **1984**, 573.

(47) T. M. Barclay; A. W. Cordes; R. H. deLaat; J. D. Goddard; R. C. Haddon; D. Y. Jeter; R. C. Mawhinney; R. T. Oakley; T. T. M. Palstra; G. W. Patenaude; R. W. Reed; N. P. C. Westwood, *J. Am. Chem. Soc.*, **1997**, *119*, 2633.

(48) D. A. Haynes; C. S. Clarke; J. N. B. Smith; A. S. Batsanov; J. A. K. Howard; S. I. Pascu; J. M. Rawson, *CrystEngComm*, **2010**, *12*, 172.

(49) A. Alberola; R. J. Collis; S. M. Humphrey; R. J. Less; J. M. Rawson, *Inorg. Chem.*, **2006**, *45*, 1903.

(50) A. Alberola; E. Carter; C. P. Constantinides; D. J. Eisler; D. M. Murphy; J. M. Rawson, *Chem. Commun.*, **2011**, *47*, 2532.

(51) D. A. Haynes; C. Allen; C. M. Pask; J. M. Rawson, *CrystEngComm*, **2009**, *11*, 2048.

(52) P. J. Langley; J. M. Rawson; J. N. B. Smith; M. Schuler; R. Bachmann; A. Schweiger; F. Palacio; G. Antorrena; G. Gescheidt; A. Quintel; P. Rechsteiner; J. Hulliger, *J. Mater. Chem.*, **1999**, *9*, 1431.

(53) H. I. Suss; T. Wuest; A. Sieber; R. Althaus; F. Budde; H. P. Luthi; G. D. McManus; J. Rawson; J. Hulliger, *CrystEngComm*, **2002**, 432.

(54) A. Poppl; B. Jee; K. Koch; L. Moschkowitz; D. Himsl; M. Hartman, *J. Phys. Chem. Lett.*, **2011**, *2*, 357.

(55) G. D. McManus; J. M. Rawson; N. Feeder; F. Palacio; P. Oliete, *J. Mater. Chem.*, **2000**, *10*, 2001.

(56) M. Meilikhov; K. Yusenko; D. Esken; S. Turner; G. Van Tendeloo; R. A. Fischer, *Eur. J. Inorg. Chem.*, **2010**, *2010*, 3701.

(57) L. Dobrańska; G. O. Lloyd; C. Esterhuysen; L. J. Barbour, *Angew. Chem. Int. Ed*, **2006**, *45*, 5856.

(58) A. Heyns, *PhD Thesis*; University of Stellenbosch, **2011**.

(59) R. Matsuda; R. Kitaura; S. Kitagawa; Y. Kubota; T. C. Kobayashi; S. Horike; M. Takata, *J. Am. Chem. Soc.*, **2004**, *126*, 14063.

(60) J. L. Atwood; L. J. Barbour; A. Jerga; B. L. Schottel, *Science*, **2002**, *298*, 1000.

(61) C. E. Willans; S. French; L. J. Barbour; J.-A. Gertenbach; P. C. Junk; G. O. Lloyd; J. W. Steed, *Dalton Trans.*, **2009**, 6480.

(62) P. Metrangolo; A. Abate; M. Brischetto; G. Cavallo; M. Lahtinen; T. Pilati; S. Radice; G. Resnati; K. Rissanen; G. Terraneo, *Chem. Commun.*, **2010**, *46*, 2724.

(63) J. Martí-Rujas; N. Islam; D. Hashizume; F. Izumi; M. Fujita; M. Kawano, *J. Am. Chem. Soc.*, **2011**, *133*, 5853.

(64) L. Yu, *Acc. Chem. Res.*, **2010**, *43*, 1257.

(65) W. I. F. David; K. Shankland; J. van de Streek; E. Pidcock; W. D. S. Motherwell; J. C. Cole, *J Appl Crystallogr*, **2006**, *39*, 910.

(66) B. M. Kariuki; D. M. S. Zin; M. Tremayne; K. D. M. Harris, *Chem. Mater.*, **1996**, *8*, 565.

(67) *Topas Academic V4.1*; A. Coelho, **2007**.

(68) J. L. Brusso; O. P. Clements; R. C. Haddon; M. E. Itkis; A. A. Leitch; R. T. Oakley; R. W. Reed; J. F. Richardson, *J. Am. Chem. Soc.*, **2004**, *126*, 8256.

(69) A. Alberola; R. J. Collis; R. J. Less; J. M. Rawson, *J. Organomet. Chem.*, **2007**, *692*, 2743.

(70) R. T. Oakley; A. Alberola; O. P. Clements; R. J. Collis; L. Cubbitt; C. M. Grant; R. J. Less; J. M. Rawson; R. W. Reed; C. M. Robertson, *Cryst. Growth Des.*, **2008**, *8*, 155.

(71) A. Alberola; D. Eisler; R. J. Less; E. Navarro-Moratalla; J. M. Rawson, *Chem. Commun.*, **2010**, *46*, 6114.

(72) E. G. Awere; N. Burford; R. C. Haddon; S. Parsons; J. Passmore; J. V. Waszczak; P. S. White, *Inorg. Chem.*, **1990**, *29*, 4821.

(73) S. R. Harrison; R. S. Pilkington; L. H. Sutcliffe, *J. Chem. Soc., Faraday Trans. 1*, **1984**, *80*, 669.

(74) Y. Kusaba; M. Tamura; Y. Hosokoshi; M. Kinoshita; H. Sawa; R. Kato; H. Kobayashi, *J. Mater. Chem.*, **1997**, *7*, 1377.

(75) D. Louer; M. Louer, *J. Appl. Crystallogr.*, **1972**, *5*, 271.

(76) D. Louer; R. Vargas, *J. Appl. Crystallogr.*, **1982**, *15*, 542.

(77) D. Louer; A. Boultif, *J. Appl. Crystallogr.*, **1991**, *24*, 987.

(78) *Jaguar V7.7*; Schrödinger, **2010**.

CHAPTER 5

SUMMARY

The investigation of inorganic porous materials has led to exciting advances in the field of supramolecular chemistry. Of particular relevance to this study are advances in the formation of hybrid materials, whereby the inclusion of a functional guest within the pores of a host framework modifies the properties of both the host and the guest.

The escalating number of potential applications of these systems is a clear incentive for indentifying new inclusion complexes capable of surpassing the reported properties of those systems that have already been reported. The intentional design and synthesis of materials with specific functions i.e. crystal engineering, implicitly requires control of the solid-state structure. This has been achieved, in part, through judicious choice of building blocks that, under the right conditions of crystallisation, may spontaneously assemble to form the required product. Crystal engineering endeavours involving coordination compounds are based on the design principle in which bidentate or polydentate ligands serve as the organic linkers between metal nodes to form discrete coordination complexes or coordination networks. The resulting structures can then be classified as discrete 0D coordination complexes or infinite 1D, 2D or 3D periodic structures. Unfortunately, owing to the limited control afforded by the self-assembly process and the many factors that can influence the process of crystallisation, it is still not possible to reliably predict the final structure based solely on the molecular structures of the building blocks. As a consequence many new porous materials are still obtained through serendipity.[1]

It has become apparent that the role of serendipity in the discovery of new porous materials can only be limited through an investigation of a wide parameter space (i.e. many different reaction conditions need to be investigated to determine the optimum crystallisation conditions for a given product). In this regard, X-ray diffraction analyses is an invaluable tool that can be used to characterise all intermediate products with a view to extrapolating trends that will ultimately lead to the formulation rules for structure prediction. The atomic level information provided by these techniques also allows the correlation of physical properties of the material with structural changes at the molecular level and, combined with the information obtained from computational methods, models of guest loss/uptake, exchange and egress can be proposed.[2] The work presented in this

thesis draws from these observations and attempts to address some of the issues stated here. The following sections summarise the major aspects covered in each chapter of this work.

Chapter 1 presents the fundamental concepts relevant to this work. A description of the structural features of the two metal-organic host frameworks pertinent to this study is also given; namely the 0D metallocyclic host materials that incorporate ditopic imidazole ligands and the 3D metal-organic frameworks assembled from rigid organic ligands. The brief literature survey of MOFs indicates that this class of materials shares structural similarities with the industrially fêted zeolite porous materials, but offer significant advantages over zeolites because structural variation can be introduced into the framework to tailor the properties of the material. The four metallocycles reported in the literature all stack to form solvent-filled channels or discrete solvent-filled pockets in the solid state and are classified as being either conventionally or transiently porous. In all cases the solvent could be removed as a single-crystal to single-crystal transformation to yield an empty phase capable of absorbing new guests and are thus categorised as Class I porous systems (as opposed to Class II porous systems that undergo guest exchange without the need for a guest-free phase).

With regard to ongoing studies of 0D metallocycles, six flexible ditopic ligands were synthesised with the aim of complexing these ligands to transition metal salts to produce novel porous 0D metallocycles. The ligands are: 2,3,5,6-tetrafluoro-1,4-bis(imidazol-1-yl-methyl)benzene (**L1**),[3] 2,3,5,6-tetrafluoro-1,4-bis(2-isopropylimidazole-1-yl-methyl)benzene (**L2**), 1,3-bis(2-isopropylimidazole-1-yl-methyl)-2,4,6-trimethylbenzene (**L3**), 1,4-bis(4,5-dichloroimidazole-1-yl-methyl)benzene (**L4**), 4,4'-bis(4,5-dichloroimidazole-1-yl-methyl)biphenyl (**L5**) and 4,4'-bis(2-isopropylimidazol-1-ylmethyl)biphenyl (**L6**). They all consist of two imidazole moieties tethered to a variable aromatic core by means of methylene linkers and are therefore able to adopt several conformations. **Chapter 2** describes the synthesis and characterisation of these six flexible ligands that were reacted with a variety of transition metal salts in a systematic manner. From these self-assembly reactions the structures of 29 novel coordination complexes were elucidated by means of single-crystal X-ray diffraction: 15 complexes contain **L1**, three contain **L2**, four contain **L3** and eight contain **L4**. No single-crystal structures were elucidated for systems containing **L5** or **L6**. Of the 29 structures obtained, 14 structures are classified as 1D strands, eight as 2D network structures, two as non-porous discrete

complexes and five as 0D metallocycles. The remainder of this chapter comprises two sections of suggested future work that could potentially increase the probability of obtaining desired metallocyclic hosts. In the first section it is suggested that the metal binding site should be pre-organised prior to reaction with the ligand. This could be achieved by reacting the metal with a suitable dicarboxylate chelating moiety, thereby forming a 'semi-protected' metal cation that is pre-organised and more likely to yield the desired discrete species upon reaction with the ditopic imidazole ligand. In the second section a high-throughput protocol is outlined that could be implemented as an efficient and systematic means of exploring a wide parameter space in a short period of time. This would effectively streamline further studies aimed at producing porous metallocyclic materials.

In **Chapter 3** the single crystal structures of the five metallocycles formed from the reaction conditions outlined in Chapter 2 are reported. They are, $[Ag_2(\mathbf{L1})_2](NO_3)_2{\cdot}2CH_3OH{\cdot}H_2O$ ($\mathbf{1_{MEOH{\cdot}H2O}}$), $[Ag_2(\mathbf{L1})_2](NO_3)_2{\cdot}2CH_3CN$ ($\mathbf{1_{MeCN}}$), $[Ag_2(\mathbf{L1})_2](NO_3)_2{\cdot}2(CH_3)_2CO$ ($\mathbf{1_{AC}}$), $[Ag_2(\mathbf{L1})_2](BF_4)_2{\cdot}2(CH_3)_2CO$ ($\mathbf{2_{AC}}$) and $([Ag_2(\mathbf{L2})_2NO_3)(Ag_2(\mathbf{L2})_2(NO_3)_2)([Ag_2(\mathbf{L2})_2](NO_3)_2){\cdot}3(CH_3)_2CO$ ($\mathbf{3_{AC}}$). Single-crystal analysis reveals that the metallocycles stack to form 1D channels in all five structures and that $\mathbf{1_{MeOH{\cdot}H2O}}$, $\mathbf{1_{MeCN}}$ and $\mathbf{1_{AC}}$ are isoskeletal. Their structures are consistent with two MeOH molecules and a disordered water molecule per metallocycle in $\mathbf{1_{MeOH{\cdot}H2O}}$, two MeCN molecules per metallocycle in $\mathbf{1_{MeCN}}$ and one acetone molecule per metallocycle in $\mathbf{1_{AC}}$. The structure of $\mathbf{2_{AC}}$ is similar to the isoskeletal series, differing with respect to the stacking periodicity of the metallocyclic columns. There are two acetone molecules per host metallocycle in $\mathbf{2_{AC}}$. The structure of $\mathbf{3_{AC}}$ is far more complex than the other four metallocycles, and single crystals of $\mathbf{3_{AC}}$ could only be obtained once. Hence it was not treated in the same detail as the other systems. Furthermore, all five structures are channel inclusion compounds with no appreciably strong host-guest interactions and the metallocyclic columns are arranged in a herringbone motif.

The thermal analysis (TGA, DSC and hot stage microscopy) of the inclusion complexes indicate that all five of the solvates have remarkably high thermal stability for their included solvent molecules, and that the single crystals do not survive the desolvation process. For the $\mathbf{1_{MeOH{\cdot}H2O}}$, $\mathbf{1_{AC}}$ and $\mathbf{3_{AC}}$ systems the thermoanalytical data shows that the solvent is lost only when the host decomposes. For the $\mathbf{1_{MeCN}}$ and $\mathbf{2_{AC}}$ systems, however, the TGA trace indicates that desolvation is a single step process

occurring in the temperature range of 180–220 °C for $\mathbf{1_{MeCN}}$ and 160–190 °C $\mathbf{2_{AC}}$ respectively. The weight loss events in the TGA traces correspond to the loss of two MeCN molecules per metallocycle in $\mathbf{1_{MeCN}}$ and only one acetone molecule in $\mathbf{2_{AC}}$. This indicates that $\mathbf{2_{AC}}$ does not desolvate fully before decomposition. The DSC of each reveals an endotherm coinciding with the guest-release process at onset temperatures (T_{on}) of 192.9 °C for $\mathbf{1_{MeCN}}$ and 155.7 °C for $\mathbf{2_{AC}}$. The relative stability of the host compounds for their respective guests was further analysed using the $T_{on} - T_b$ parameter (i.e. the difference between the onset temperature of desolvation and the boiling point) and these values are 111.3 °C for $\mathbf{1_{MeCN}}$ and 99.4 °C for $\mathbf{2_{AC}}$. This value, which for most solvates is a negative number, indicates that $\mathbf{1_{MeCN}}$ and $\mathbf{2_{AC}}$ show remarkable thermal stability with respect to the loss of their included solvent molecules. The nature of the desolvated phase in $\mathbf{1_{MeCN}}$ and $\mathbf{2_{AC}}$ was also investigated by VT-PXRD. The PXRD patterns in both cases indicate a phase change due to desolvation and it was concluded that the host molecules must subtly rearrange to a more densely-packed phase during this process. Interestingly, the original solvated phase could be recovered by immersing the high-temperature $\mathbf{1_{MeCN}}$ phase in the original parent solvent, whereas the original $\mathbf{2_{AC}}$ phase could not be recovered under the same conditions.

Chapter 3 also outlines the results of a computational study that was carried out to investigate whether strong guest-guest and/or host-guest interactions could account for high thermal stability. A range of interaction energies were calculated for the $\mathbf{1_{MeCN}}$ system and compared to that of a previously reported Ag(I) metallocycle $[Ag_2(\mathbf{A2})_2](PF_6)\cdot 2CH_3CN$ (where **A2** = 2,3,4,6-tetrafluoro-1,4-bis(2-methylimidazole-1-ylmethyl)benzene) that also includes two MeCN molecules per metallocycle, but does not retain its guest at high temperatures. It appears that the guest-guest interaction between two MeCN molecules of a dimer is more stabilising in $\mathbf{1_{MeCN}}$ than in the literature structure by 1.2 kcal mol^{-1}. Moreover, the interaction of a dimeric pair of MeCN guests within their 4.5 Å sphere of inclusion is more stabilising in $\mathbf{1_{MeCN}}$ by 2.2 kcal mol^{-1} than in the literature structure (values of -31.58 and -29.39 kcal mol^{-1} were obtained for $\mathbf{1_{MeCN}}$ and the literature structure, respectively). It was concluded that although the 2.2 kcal mol^{-1} may appear to be a small difference in energy, taken in conjunction with a stronger guest-guest interaction of 1.2 kcal mol^{-1} it could possibly provide an explanation for the observed thermal stability of $\mathbf{1_{MeCN}}$ with respect to its included guest molecules as compared to the literature structure. It was also noted that the packing arrangement of the

metallocyclic host columns could stabilise the guest-free phase and host-host interactions should therefore not be overlooked when attempting to rationalise the high thermal stability. It was suggested that further computational studies should be undertaken to probe the various host-host interaction energies.

Finally, in an attempt to obtain the guest-free phase of the metallocycles by means other than thermally-assisted evacuation, a liquid phase solvent exchange was attempted. In this experiment the parent solvent is exchanged for a more volatile solvent that can be removed under milder conditions. To this end, single crystals of $\mathbf{1_{MeCN}}$ were immersed in DCM. After 24 hours the crystals appeared intact and SCD analysis revealed that a single-crystal to single-crystal transformation had occurred in which the MeCN molecules had been replaced by DCM without significant disruption to the packing of the host framework. Unfortunately, attempts to remove the solvent resulted in extensive fracturing of the single crystals into a polycrystalline powder; however, the conversion of $\mathbf{1_{MeCN}}$ to $\mathbf{1_{DCM}}$ distinguishes this system as a Class II porous material. This prompted an investigation into the ability of $\mathbf{1_{MeOH\cdot H2O}}$, $\mathbf{1_{MeCN}}$, $\mathbf{1_{AC}}$ and $\mathbf{2_{AC}}$ to function as Class II porous systems. Single crystals of the metallocycles were immersed in DCM, benzene, difluorobenzene, dioxane, cyclohexane and water and the exchange processes were monitored by single-crystal X-ray diffraction. Exchange occurred readily in most cases, with only subtle adjustment of the host metallocycles to accommodate the new guest. The thermal stability of the resulting inclusion complexes was also investigated by TGA and DSC. These results indicated that the new inclusion complexes are also able to retain their included solvent molecules at temperatures well above their boiling points.

It was suggested that future work should involve exposing the metallocycles to a mixture of guests to determine whether the host material selectively includes one guest over the other. It would also be interesting to investigate whether the mechanism of guest exchange can be elucidated by further computational studies.

Chapter 4 details the gas-phase diffusion of the organic radicals 5-methylbenzo-1,3,2-dithiazolyl (**MBDTA**) and benzo-1,3,2-dithiazolyl (**BDTA**) into the porous MOF host material **MIL-53(Al)** to yield the two inclusion complexes **BDTA@MIL-53(Al)** and **MBDTA@MIL-53(Al)**. It was demonstrated that this inclusion process is selective for the **MIL-53(Al)** framework over a range of potential host materials. This selectivity was attributed to the well-documented 'breathing effect' of the **MIL-53(Al)** (i.e. the contraction and expansion of the pores in response to an external stimulus). The structures

of the two inclusion complexes were elucidated by PXRD analysis and indicate that the shape of 1D channels of the host framework adjust slightly, as compared to the empty **MIL-53(Al)**, so as to optimise host-guest interactions. The packing arrangement of the radicals is also altered within the pores of the framework. Both radicals are included as pairs located around an inversion centre. However, their displacement relative to the inversion centre differs. In the case of **BDTA@MIL-53(Al)** the radicals are eclipsed and a disordered model is proposed in which the π*–π* mode of association is altered from *trans* in pristine **BDTA** to *cis* in **BDTA@MIL-53(Al)**. In **MBDTA@MIL-53(Al)** the radicals are offset with respect to the inversion centre and there is no evidence for π*–π* dimerisation as the radicals are located *ca* 4.100 Å from each other. This is in contrast to the crystal structure of pure **MBDTA**, which consists of molecules packed in regularly spaced π–stacks. The solid state EPR of two inclusion complexes is also reported. Both show isotropic 1:1 singlets, and the **BDTA@MIL-53(Al)** resonance is much broader and less intense than the **MBDTA@MIL-53(Al)** resonance. This is an indication of disorder in the packing arrangement of the **BDTA** molecules within the channels of the host material and is consistent with the structure as determined by PXRD.

Furthermore, it was shown that the radicals could be stabilised as guests and stored in air for more than three months and that, by the addition of a suitable solvent, the radicals could be released in a controlled manner. EPR and MS were used to confirm the release of the radical without degradation. It was suggested that future work should involve the inclusion of the radicals into a paramagnetic host framework, which may offer opportunities for magnetic communication between host and guest species.

REFERENCES

(1) N. B. McKeown, *J. Mater. Chem.*, **2010**, *20*, 10588.

(2) M. J. Rosseinsky, *Micropor. Mesopor. Mat.*, **2004**, *73*, 15.

(3) J. M. Shreeve; Y. Gao; B. Twamley, *Inorg. Chem.*, **2006**, *45*, 1150.

APPENDIX A

GENERAL PROCEDURES AND INSTRUMENTS

1. INSTRUMENTS

1.1. SINGLE-CRYSTAL X-RAY DIFFRACTION ANALYSIS (SCD)

In all cases suitable single crystals (i.e. those found by inspection to have good morphology and that extinguished plane-polarized light uniformly) were placed on the end of a MiTeGen mount using paratone oil. Intensity data were collected on either a Bruker SMART[1] APEX single-crystal X-ray diffractometer equipped with a molybdenum fine-focus sealed tube, Monocap collimator and an APEXII detector or a Bruker APEX DUO single-crystal X-ray diffractometer equipped with Incoatec IμS molybdenum and copper microfocus X-ray sources and an APEXII detector. In both cases temperature control was maintained using an Oxford Cryogenics Cryostat. Data reduction was carried out by means of a standard procedure using SAINT[2] and empirical corrections were performed where necessary using SADABS.[3,4] Both programs were executed from within the APEX 2 software package. All crystal structures were solved using the SHELXS-97[5] suite of programs, either by direct methods or a combination of Patterson and partial-structure expansion. X-Seed[6] was used as a graphical interface for SHELX. Structures were expanded by iterative examination of difference Fourier maps following least-squares refinements of the earlier models. All ordered non-hydrogen atoms were refined anisotropically by means of full-matrix least-squares calculations on F^2 using SHELXL-97 within the X-Seed environment. The hydrogen atoms were all placed in calculated positions using riding models and assigned isotropic thermal parameters 1.2 - 1.5 times the U_{eq} of their parent atoms. According to the SHELX-97 manual:[7] “It is difficult to locate hydrogen atoms accurately using X-ray data because of their low scattering power, and because the corresponding electron density is smeared out, asymmetrical, and is not centred at the position of the nucleus. In addition hydrogen atoms tend to have larger librational amplitudes than other atoms. For most purposes it is preferable to calculate the hydrogen positions according to well-established geometrical criteria and then to adopt a refinement procedure which ensures that a sensible geometry is retained.” We believe that

the method used by SHELXL-97 to place hydrogen atoms in calculated positions is adequate for the purposes of this study.

1.2. POWDER X-RAY DIFFRACTION (PXRD)

Diffraction patterns of intensity *vs* 2θ were recorded on a PANalytical X'Pert PRO Multi-Purpose Diffractometer with Bragg-Brentano geometry, using Cu-K_α radiation (λ = 1.5418 Å). Intensity data were collected from multiple 2θ scans by an X'Celerator detector utilising the flat stage configuration. Variable-temperature PXRD patterns were collected using the capillary spinner configuration equipped with an Oxford Cryostream cooling system. All samples were first pulverised to minimise preferred orientation contributions to intensity data. A step size of 0.017 degrees and a scan-speed of 42 seconds per step, over a 2θ range of 3–50°, were used during data collection.

1.3. THERMOGRAVIMETRIC ANALYSIS (TGA)

TGA measurements were carried out using a TA Instruments Q500 thermograivmetric analyser. All TGA experiments were performed on the as-grown crystals with the sample in an open aluminium pan. Sample sizes typically ranged from 5 – 15 mg. N_2 gas was used to purge the furnace (flow rate 50 mL min^{-1}). Samples were typically heated at 10 °C min^{-1} from room temperature to 400 °C.

1.4. DIFFERENTIAL SCANNING CALORIMETRY (DSC)

DSC measurements were carried out using a TA Instruments Q100 differential scanning calorimeter on samples of the as-grown crystals. Samples of 3 – 10 mg were placed in crimped, vented aluminium pans. Both the reference and the sample pans were prepared using the same method. N_2 gas was used to purge the furnace (flow rate 50 mL min^{-1}). Samples were typically heated at 10 °C min^{-1} from room temperature to 400 °C.

1.5. INFRARED SPECTROSCOPY (IR)

IR spectra were recorded in the 4000–400 cm^{-1} region, using a Nexus 670 FT–IR instrument (Thermo Nicolet Instruments, USA) with a Golden Gate ATR accessory.

1.6. NUCLEAR MAGNETIC RESONANCE SPECTROSCOPY (NMR)

All samples were dissolved in deuterated chloroform ($CDCl_3$). ^{1}H-NMR and ^{13}C-NMR were performed on a Varian Unit INOVA (400 MHz) or a Varian VNMRS (300 MHz) NMR Spectrometer. All analyses were carried out by the Central Analytical Facility of the University of Stellenbosch.

1.7. LIQUID CHROMATOGRAPHY ELECTROSPRAY IONISATION MASS SPECTROMETRY (LC ESI-MS)

LC ESI–MS analyses for the ditopic imidazole ligands were carried out on a Waters API Quattro Micro mass spectrometer with an elecrospray ionization source in positive mode. All samples were dissolved in methanol at a concentration of 2 μM and introduced into the ESI–MS at a flow rate of 50 L h^{-1} during analysis. A capillary voltage of 3.5 kV was applied, with a source temperature of 100 °C and a cone voltage of 35 V. The desolvation temperature was set at 350 °C and the desolvation gas flow rate to 350 L h^{-1}. All data were acquired in the positive mode and scanning occurred through *m/z* = 100–1000 (where *m/z* is defined as the molecular mass to charge ratio).

1.8. ELECTRON IMPACT MASS SPECTROSCOPY

EI–MS analyses for the organic radicals were carried out on a Kratos Concept instrument in positive mode. All samples were dissolved in dry CH_2Cl_2 prior to incorporation in the matrix liquid.

1.9. ELEMENTAL ANALYSIS

Carbon, hydrogen and nitrogen microanalyses were carried out on an Exeter CE-440 Elemental Analyser. Approximately 1.5 mg of sample was sealed in a pre-weighed capsule under an atmosphere of dry nitrogen in a glove box. This analysis was carried out at the University of Cambridge.

1.10. ELECTRON PARAMAGNETIC RESONANCE SPECTROSCOPY (EPR)

Room temperature EPR spectra were collected on a Bruker ESP 300 X-band EPR spectrometer running at ~9.7 GHz with accurate microwave frequencies measured using a microwave counter at the University of Windsor (Canada). Linewidths and composition (Lorentzian/Gaussian) were determined using an isotropic solution model (Winsim).[8] Simulations of isotropic spectra were carried out using in-house software.[9]

1.11. UV–VIS SPECTROSCOPY

Solid-state UV-vis spectra were recorded on a Perkin Elmer Lambda 750 equipped with an integrating sphere at the University of Cambridge.

2. COMPUTER PROGRAMS

2.1. X-SEED[6,10]

X-Seed is a graphical user interface to several non-interactive utilities. This crystallographic software tool was utilised to facilitate the process of crystal structure solution, refinement, analysis and presentation of the resulting model. Some of these utilities and their primary functions are listed below:

SHELX-97[5] – this suite of programs was used for crystal structure solution and refinement. It comprises six computer programs (SHELXS, SHELXL, CIFTAB, SHELXA, SHELXPRO and SHELXWAT).

Lazy-Pulverix[11] – a program used for calculating X-ray and neutron diffraction powder patterns.

POV-Ray[12] – is a ray-tracing program that was used to produce high quality molecular graphics images. A set of unique and complex commands is used to render an image of a scene from the perspective of an imaginary camera. A scene comprises an object (or set of objects) and light sources. Unit cell and atom labels were embedded into the graphics using POV-Label.

MSROLL[13,14] is a program that was incorporated into X-Seed in order to calculate solvent-accessible surfaces. MROLL was developed by Michael Connolly to map the solvent-accessible areas of proteins and nucleic acids for graphical display. The solvent-accessible surface has been defined by Lee and Richards[15] as the surface area created by tracing the centre of a sphere with a known radius as it is rolled around the surface of interest (i.e. it is the surface that is reversibly accessible to solvents or other guest molecules). During this treatment a molecule or crystal is approximated as a set of fused spheres with van der Waals radii – the *contact* surface is then mapped out as a probe is rolled over this hard-sphere van der Waals surface.[16] The output of this method is a numerical value for this area and thus the approach needs to be modified in order to visualise the void and calculate the volume (i.e. to calculate the solvent *accessible* surface). After MSROLL was incorporated into X-Seed it was appropriately modified to give the option of mapping either type of surface. The modification entails adding the specified probe radius to the van der Waals radii of each of the atoms involved, once this is done the probe radius is then given as zero and the accessible surface is the "contact" surface traced by the centre of the probe.[17] For the purposes of calculating volumes and visualising cavities in the present study, the solvent guest molecules are removed from the atom list. A specific probe radius is then chosen and MSROLL is envoked. The cavity is mapped to generate a '.cav' file, which can be viewed in X-Seed and visualised as part of the structure using POV-Ray. The guest is then reinstated and the image thus rendered contains a visualisation of the position of the guest encapsulated within the guest-accessible voids.

2.2. PLATON[18,19]

The total potential solvent accessible volume was determined using the command CALC SOLV within the PLATON environment. During this treatment the guest molecules are

deleted from the .ins file and the structure is re-refined prior to the calculation. Upon completion of the calculation the value given is the void volume per unit cell.

REFERENCES

(1) *SMART Data Collection Software,Version 5.629*; Madison, WI, Bruker AXS Inc. **2003**.

(2) *SAINT Data Collection Software, Version 6.45*; Madison, WI, Bruker AXS Inc. **2003**.

(3) *SADABS, Version 2.05*; Madison, WI, Bruker AXS Inc. **2002**.

(4) R. H. Blessing, *Acta Crystallogr., Sect. A: Found. Crystallogr.*, **1995**, *51*, 33.

(5) G. M. Sheldrick, *Acta Crystallogr., Sect. A Found. Crystallogr.*, **2008**, *64*, 112.

(6) L. J. Barbour, *Journal of Supramolecular Chemistry*, **2001**, *1*, 189.

(7) G. M. Sheldrick, *Programs for crystal structure analysis* University of Göttingen, Germany, **1997**.

(8) *Public EPR software tools V0.98*; D. A. O'Brien; D. R. Duling; Y. C. Fann, **1998**.

(9) *Edinburgh University*; J. M. Rawson, **1993**.

(10) J. Atwood; L. J. Barbour, *Cryst Growth Des*, **2003**, *3*, 3.

(11) K. Yvon; W. Jeitshko; E. Parthe, *J. Appl. Cryst.*, **1997**, *10*, 73.

(12) *POV-Ray™ for Windows, Version 3.6*; Williamstown, Australia, Persistence of Vision Raytracer Pty. Ltd., **2004**.

(13) M. L. Connolly, *Science*, **1983**, *221*, 709.

(14) M. L. Connolly, *J. Mol. Graphics*, **1993**, *11*, 139.

(15) B. Lee; F. M. Richards, *J. Mol. Biol.*, **1971**, *55*, 379.

(16) M. J. Turner; J. J. McKinnon; D. Jayatilaka; M. A. Spackman, *CrystEngComm*, **2011**, *13*, 1804.

(17) F. M. Richards, *Annu. Rev. Biophys. Bio.*, **1977**, *6*, 151.

(18) A. L. Spek, *J. Appl. Cryst.*, **2003**, *36*, 7.

(19) *PLATON, A multipurpose Crystallographic Tool*; U. Utrecth University, The Netherlands, **2008**.